Simulation of Radiation in Non-Equilibrium and Expanding Hypersonic Flows

Joseph Graham Steer

Lincoln College

University of Oxford

A thesis presented for the degree of

Doctor of Philosophy

Michaelmas 2024

Study hard what interests you in the most undisciplined, irreverent, and original manner possible

Richard Feynman

Acknowledgements

In the words of the Hilltop Hoods – *"There ain't enough paper for the names I gotta mention"*. This thesis is already long enough, so here is an abbreviated acknowledgement of those who have been involved in making my DPhil the adventure it has been.

Firstly, many thanks to Matt 'Magpie' McGilvray for everything over the past few years. On the work front, though it is painful to admit, you are nearly always right. Thank-you for the tireless effort you put toward not only me but the entire group and for never being afraid to get your hands dirty. Here's to many victory beers in the future!

Secondly, thank-you to Luca Di Mare and Peter Collen, both of whom were extremely patient as they taught me their respective crafts. Luca, thanks for taking me under your wing as an unofficial student (at least until about a month ago). If brilliance is passed on via osmosis then all of those hours sitting together working on LASTA may save me yet. Pete, thanks for everything, but in particular somehow finding the time to help me design a hydrogen system while writing up your DPhil. I only realise now, after experiencing the write up first-hand, how extraordinarily generous this was.

A huge thanks to the wider hypersonics group. In particular Luke Doherty and Christopher Hambidge, without whom we might as well shut down the entire operation. You two have made me a much better, more thorough engineer. To Tristan 'Tug' Crumpton, thanks for being you. The days we had you in the control room were truly the glory days. Thanks to Matthew Satchell for his discussions, help with FROSST, and general happiness. To Alex 'Chai' Glenn and Justin 'Goose' Clarke, I wouldn't want to unravel the mysteries of non-equilibrium thermochemistry with anyone else. Thanks Chai in particular for teaching me most of what I know about spectroscopy, we will have no idea what to do with the mirrors downstairs when you leave[1].

I have also had the pleasure of working with an incredible capable group of people

[1]Maybe take them with you so you can view yourself from many angles?

at the Southwell Building who are worth their weight in gold and more. Thanks in particular to Bill & Hal for their pipework genius and Christmas drinks. Alex, Anna, and Kathryn for always accommodating my overly complex purchase orders and our general last-minute requests. Leo, Duncan, and Harry for working miracles with metal, and finally Andrea for producing a fantastic set of radiometers.

Thank-you to my beautiful fiancé Laura for coming on this journey with me. You have been on the roller-coaster for every peak and trough. Maybe one day, if you are crazy enough to do a DPhil, I will repay the favour. To my family and cheer-squad back in Australia, thank-you and I love you. The early morning / late night video calls while I walked back and forth to the lab meant a lot and always made the day better, see you all soon!

Finally, thanks to T6 for never failing me when it mattered. Even though you are nearly 60 years old, you keep getting faster – something to aspire to.

Abstract

The primary aim of this thesis was to develop new and improved methods to simulate radiation in expansion tubes and by extension, improve estimates of the freestream properties. Radiation in hypersonic flows arises as a consequence of particle excitation due to high velocities. Models of the phenomenon must account for many complex physical effects and hence predictions of radiation are often associated with high uncertainty. Additionally, such models are typically tuned to experimental results from ground test facilities which are also complex and behave non-ideally.

The work in this thesis contributed to solving the problem of radiation modelling primarily through the development of a new numerical method for impulse facilities named *LASTA 2.0*. The purpose of LASTA 2.0 is to decouple the non-ideal behaviour of impulse facilities from thermochemistry models by using experimental measurements as boundary conditions. LASTA 2.0 is the first numerical tool to simultaneously account for the effect of shock speed variation, upstream wave processes, and non-equilibrium thermochemistry on the test slug in an impulse facility. Additionally, the computational cost of running LASTA 2.0 is very low, with a typical test case taking approximately 15 minutes to solve on a laptop.

The LASTA 2.0 method was compared to established shock tube modelling tools FROSST and NESS to validate the fluid dynamic and thermochemical models respectively. A satisfactory agreement was seen, permitting application of LASTA 2.0 to a variety of historical cases. Coupled LASTA 2.0 / NEQAIR 15.2.2 radiation predictions showed excellent with shock tube experiments in N_2–O_2, N_2–CH_4, and H_2–He mixtures for wavelengths between 160 – 1450 nm.

To enable application of LASTA 2.0 to the expansion tube, a validation dataset was required. To this end, a series of intensified, wall-mounted radiometer probes were developed to measure radiation through the unsteady expansion downstream of the secondary

diaphragm. Spectrally integrated measurements of the oxygen 777 nm and hydrogen 656 nm atomic lines were made through unsteady expansion waves in the T6 Stalker tunnel for expansion pressure ratios between 2 – 200. The unsteady expansion was clearly visible and its size, as determined from the radiometer data, agreed well with conventional pressure measurements. The radiometer measurements constitute a novel dataset for expanding flows where historically, relatively few experimental measurements are available.

Finally, the LASTA 2.0 domain was modified to allow simulation of the expansion tube. LASTA 2.0 predictions agreed closely with ideal argon simulations of an expansion tube, demonstrating that valuable information can be obtained about the expansion tube using this approach. Coupled LASTA 2.0 / NEQAIR 15.2.2 simulations of the radiometer test cases compared favourably with the measurements through the unsteady expansion, indicating that the method was applicable in the presence of strong thermochemical non-equilibrium. Finally, the model was used to simulate a Titan entry experiment in the X3 expansion tube facility. The freestream was predicted to be highly non-uniform and thermochemically frozen, implying that conventional equilibrium state-to-state facility models are inadequate for this and similar test cases.

The work described in this thesis establishes LASTA 2.0 as a state-of-the-art impulse facility modelling tool with a unique capability to simultaneously model non-equilibrium and non-uniform shock trajectory effects. These capabilities combined with the low computational cost should allow for adoption of LASTA 2.0 (or a similar method) by the wider research community as the default post-processing approach for shock and expansion tubes.

List of Publications

Publications included in this thesis:

Incorporated as part of Chapter 3:

Steer, J., Clarke, J., McGilvray, M., and Luca, D. M. (2024a). LASTA 2.0: Validation of a reverse time integration method. In *AIAA SCITECH 2024 forum*, page 0447

Incorporated as part of Chapter 5:

Steer, J., Collen, P., and McGilvray, M. (2024c). Radiance Measurements Through Unsteady Expansion Waves in Relaxing Air and H_2 -He Mixtures. In *AIAA AVIATION FORUM AND ASCEND 2024*, Las Vegas, Nevada. American Institute of Aeronautics and Astronautics

Incorporated as part of Chapter 6:

Steer, J., Clarke, J., Collen, P. L., Satchell, M., Di Mare, L., and McGilvray, M. (2025c). Effect of Non-Uniform Shock Speed on Expansion Tube Flows. In *AIAA SCITECH 2025 forum*, page 2159

Other work published by the author during DPhil candidacy:

Steer, J., Collen, P. L., Glenn, A. B., Sopek, T., Hambidge, C., Doherty, L. J., McGilvray, M., Loehle, S., and Walpot, L. (2023b). Experimental study of a galileo sub-scale model at ice giant entry conditions in the T6 free-piston driven wind tunnel. In *AIAA SCITECH 2023 forum*, page 1339

Steer, J., Collen, P. L., Glenn, A. B., Hambidge, C., Doherty, L. J., McGilvray, M., Loehle, S., and Walpot, L. (2023a). Shock radiation tests for ice giant entry probes including CH4 in the T6 free-piston driven wind tunnel. In *AIAA SCITECH 2023 forum*, page 1729

Steer, J., Collen, P., Glenn, A., Hambidge, C., Doherty, L. J., McGilvray, M., Sopek, T., Loehle, S., and Walpot, L. (2024b). Commissioning of Upgrades to T6 to Study Giant Planet Entry. *Journal of Spacecraft and Rockets*

Loehle, S., Meindl, A., Poloni, E., Steer, J., Sopek, T., McGilvray, M., and Walpot, L. (2022). Experimental Simulation of Gas Giant Entry in the PWK1 Arcjet Facility including CH4. In *AIAA SCITECH 2022 Forum*, San Diego, CA & Virtual. American Institute of Aeronautics and Astronautics

McGilvray, M., Collen, P., Doherty, L., Steer, J., Leader, J., Glenn, A., and Hambidge, C. (2022). The Oxford T6 Stalker tunnel: performance, upgrades and new modes of operation. Publisher: European Space Agency

Leader, J., Steer, J., Collen, P., and McGilvray, M. (2022). Measurement of aeroheating of satellite components at true flight total enthalpies. Publisher: European Space Agency

Crumpton, T. J. (2024). Analysis of Mars Entry Shock Wave Radiance in the T6 Stalker Hypersonic Wind Tunnel. In *AIAA SCITECH 2024 Forum*, Orlando, FL. American Institute of Aeronautics and Astronautics

Clarke, J., Brody, S., Steer, J., McGilvray, M., and Di Mare, L. (2024a). Quasi-one-dimensional non-equilibrium method for shock tube and stagnation line flows. *Physics of Fluids*, 36(9):096140

Articles in preparation:

Steer, J., Clarke, J., Collen, P., McGilvray, M., and Di Mare, L. (2025a). Characteristic numerical method for shock tube flows with non-equilibrium thermochemistry and non-uniform shock speed. *Physics of Fluids*

Steer, J., Clarke, J., Collen, P., Satchell, M., McGilvray, M., and Di Mare, L. (2025b). Characteristic numerical method for expansion tube flows. *Physics of Fluids*

Steer, J., Collen, P., and McGilvray, M. (2025d). Radiance measurements of thermochemically relaxing N2-O2 and H2-He mixtures through unsteady expansion waves. *Journal of Thermophysics and Heat Transfer*

Contents

List of Figures

List of Tables

Nomenclature

Abbreviations

AST Aluminium Shock Tube

CARS Coherent Anti-Stokes Raman Spectroscopy

CCD Charge-Coupled Device

CEA Chemical Equilibrium with Applications

CFD Computational Fluid Dynamics

CWL Centre Wavelength

DHTG Diamond Heat Transfer Gauge

DPLR Data Parallel Line Relaxation

EAST Electric Arc Shock Tube

ESA European Space Agency

ESTCj Equilibrium Shock Tube Calculator junior

ExT Expansion Tunnel

FROSST FRamework for Overset Simulation of Shock Tubes

FWHM Full Width at Half Maximum

ICCD Intensified Charge-Coupled Device

ICP Inductively-Coupled Plasma

ILS Instrument Line Shape

IR Infrared

IS Integrating Sphere

JAXA Japanese Aerospace Exploration Agency

LASTA LAgrangian Shock Tube Analysis

MSL Mars Science Laboratory

MSR Mars Sample Return

NASA National Aeronautics and Space Administration

NEQAIR Non-EQuilibrium AIr Radiation

NRST Non-Reflected Shock Tube

OCEAN Oxford Chemical Equilibrium with Applications

OES Optical Emission Spectroscopy

PCB PicoCoulomB Piezotronics

PMT Photomultiplier

POSHAX POst SHock RelAXation

PWT Plasma Wind Tunnel

QSS Quasi Steady State

RST Reflected Shock Tunnel

sCMOS scientific CMOS

SRF Spatial Resolution Function

SST Steel Shock Tube

STS Shock Timing Station

TDLAS Tunable Diode LAser Absoption Spectroscopy

TOF Time of Flight

TPS Thermal Protection System

VUV Vacuum Ultraviolet

Greek Symbols

α Thermal diffusivity, $\mathrm{m}^2\,\mathrm{s}^{-1}$

β Shape factor, -

ℓ Test slug length, m

η Non-dimensional post-shock distance, -

η_e Frozen thermal conductivity for electronic energy due to collisions between electrons and all particles, $\mathrm{J}\,\mathrm{m}^{-1}\,\mathrm{s}^{-1}$

η_v Frozen thermal conductivity for vibrational energy due to collisions between molecules and all particles, $\mathrm{J}\,\mathrm{m}^{-1}\,\mathrm{s}^{-1}$

Γ Damköhler number, -

γ Ratio of specific heats, -

Λ Shock speed, $\mathrm{km}\,\mathrm{s}^{-1}$

μ Viscosity, $\mathrm{Pa}\,\mathrm{s}$

ω Relaxation factor

ϕ Length scale, m

ρ Density, $\mathrm{kg}\,\mathrm{m}^{-3}$

τ Test time, $\mu\mathrm{s}$

τ_s Translational-vibrational energy relaxation time for molecular species s, s

υ Radial velocity, $\mathrm{m}\,\mathrm{s}^{-1}$

Latin Symbols

$\dot{n}_{e,s}$ Molar rate of production of species n per unit volume by electron impact ionization, $\mathrm{kg}\,\mathrm{mol}\,\mathrm{m}^{-3}\,\mathrm{s}^{-1}$

$\hat{D}_s$ Average vibrational energy per unit mass of molecule s, which is destroyed or created at rate $\dot{w}_s$, $\mathrm{m}^2\,\mathrm{s}^{-1}$

$\hat{I}_s$ First ionization energy of species s per kg-mole, $\mathrm{J}\,\mathrm{kg}^{-1}\,\mathrm{mol}^{-1}$

$\mathbf{A}$	Jacobian
$\mathbf{Q}$	Solution vector
$\mathbf{R}$	Residual vector
$\mathbf{X}$	Correction to the primitive variables
a	Speed of sound, $\mathrm{m\,s^{-1}}$
$C_{v,V}$	Specific heat at constant volume for vibrational electronic energy, $\mathrm{J\,kg^{-1}\,K^{-1}}$
d	Diameter, m
e	Internal energy, J
f	Source term, -
h	Enthalpy, $\mathrm{J\,kg^{-1}}$
M	Molar mass, $\mathrm{kg\,mol^{-1}}$
m	Mass, kg
p	Pressure, Pa
p_e	Electron pressure, Pa
Q_{rad}	Radiative energy transfer rate, $\mathrm{J\,m^{-3}\,s^{-1}}$
R	Universal gas constant, $\mathrm{J\,kg^{-1}\,mol^{-1}\,K^{-1}}$
r	Radius, m
S	Core flow effective diameter, m
T	Temperature, K
t	Time, s
u	Velocity, $\mathrm{m\,s^{-1}}$
W	Velocity ratio across the shock, -
w	Characteristic variable, -
x	Distance, m

Subscripts

1	Shock tube fill condition
2	Post-shock condition
5	Acceleration tube fill condition
5	Post-shock accelerator gas condition
7	Expanded test case condition
e	Electron
e	In the core flow (Mirels)
eq	Equilibrium condition
n	Number of species
s	Species
V	Vibrational-electronic mode
w	At the wall

Chapter 1

Introduction

Contents

1.1 Motivation

The Vulnerable World Hypothesis is a thought experiment introduced by the academic and philosopher Nick Bostrom (Bostrom, 2019). In a vulnerable world, there is some level of technological development at which civilization cannot help but be destroyed. Bostrom conducts the thought experiment by reaching into the urn of possible inventions. From the urn, one may withdraw a ball that represents an idea, discovery, or technological advancement. The balls are coloured according to their benefit to humanity and crucially, one cannot see inside the urn before reaching in. Over the course of history we, as a species, have pulled mostly white (beneficial) and varying shades of grey (double edged swords), but never black (exclusively negative).

Generally speaking, hypersonic technologies and the space sector are excellent examples of grey balls. Research in this field has brought about some of humanity's greatest achievements such as the Apollo program, flying the space shuttle back from orbit, and landing robotic rovers on the surface of Mars. These feats are valuable intrinsically, but have been shown to provide a sustained benefit through commercialisation of spin-off technologies (Hertzfeld, 2002). Conversely, hypersonic weapons grant powerful nations

the ability to deliver nuclear payloads to any location on Earth within hours, a capability against which there is no reliable defence.

Whatever the colour of the ball, it seems certain that we will continue to reach into the urn for new discoveries as huge investments in hypersonics and the space industry continue to be made. Recently, the Australian, US, and UK governments jointly announced the AUKUS trilateral security partnership (Reuters, 2023) that will precipitate a 9.3 billion AUD investment in Australian hypersonics research and development (Macmillan, 2020). The UK will invest 1 billion GBP to develop their own hypersonic capability in the next 7 years (Allison, 2023), while the US continues to invest billions in its hypersonics research programs (USNI, 2024).

Civil and private investments in hypersonics are also increasing. The UK Space Agency (UKSA) estimate that 77% of the 469 billion USD space sector is commercially owned and the industry is expected to grow at a rate of 11% p.a. until 2030 (UKSA, 2024). 60,000 - 100,000 satellites launches are expected by 2030 compared to the 11,000 launched in the past 60 years. NASA, through the Artemis program, will put the first woman and person of colour on the moon by 2026 (Bowman, 2024) and plans to put astronauts on Mars in the 2030s (Bowman, 2023). SpaceX are continuing development of their Starship which aims to be the most powerful launch vehicle ever developed (SpaceX, 2024).

Efforts to explore the solar system through the use of unmanned interplanetary probes and robotic rovers continue. The OSIRIS-REx mission returned an asteroid sample to Earth for first time in late 2023 (Bolles, 2024b). NASA and ESA plan to launch missions to Titan (Bolles, 2024a), Mars (ESA, 2024), Venus (NASA, 2024), and the Ice Giants (Bayon, 2019) in the coming decade. These endeavours will all involve hypersonic entry into atmospheres that we have seldom visited and are, as a consequence, not well understood. These upcoming missions will require significant research support to ensure their success.

The following sections provide background to the reader and are intended to narrow the focus to the central themes of the thesis. Section 1.1.1 introduces the hypersonic shock layer and the challenges of modelling it. Section 1.1.2 highlights the problems associated with a subset of the hypersonic shock layer, the expanding wake region, and issues faced in trying to model it in ground based test facilities. These sections elucidate the choice of research direction for the thesis and are followed by the research objectives.

1.1.1 The Hypersonic Shock Layer

Hypersonic flight, whether it be sustained in Earth's atmosphere or during planetary entry, is characterised by the design challenge of aero-heating, that is, a significant increase in the surface temperature of the craft in flight. This phenomenon actually begins to manifest below speeds that might be considered hypersonic, a well known example being the Concorde supersonic airliner. The maximum temperature that the Concorde's aluminium airframe could safely withstand was 127 °C, a fact that limited the cruising speed of the Concorde to *only* Mach 2.04 (Eberhart, 1967). Sustained flight at higher speeds necessitates the use of exotic, difficult to manufacture materials such as titanium and composites. Another well known aircraft, the Lockheed SR-71 Blackbird, employed an 85% titanium airframe to withstand temperatures of up to 565 °C and cruise at speeds of at least Mach 3.2 (Merlin, 2009). In both of these cases, the mechanism of heat transfer into the vehicle was exclusively convective i.e. due to movement of air over the vehicle surface. This mechanism remains important as the speed of flight increases, however other heat transfer modes begin to emerge.

Vehicles that exceed a certain speed threshold[1] will begin to encounter so-called real gas effects. Here, the energy added to the gas molecules when interacting with the vehicle shock layer is large enough to induce chemical reactions. In this scenario, molecules may dissociate, ionize, emit energy as radiation, and the later recombine further downstream. These real gas effects introduce enormous complexity to the problem of accurately predicting heat transfer to the vehicle surface.

The craft that typically encounter real gas effects are those that travel at super-orbital speeds[2], a requirement to traverse inter-planetary distances in a reasonable time frame. Notable examples of such craft include the Space Shuttle (7.8 $\mathrm{km\,s^{-1}}$), the Apollo Spacecraft (11.1 $\mathrm{km\,s^{-1}}$), Mars 2020 (5.6 $\mathrm{km\,s^{-1}}$), and the Galileo Entry Module (47.4 $\mathrm{km\,s^{-1}}$) (Anderson Jr., 2006; Tibère-Inglesse et al., 2023a; Milos et al., 1999). These vehicles feature ablative heat shields and are characteristically blunted so as to increase drag and thus decelerate to a speed where at which they can land or a parachute may be safely deployed. During the deceleration phase, such vehicles encounter convective but also radiative heating due to chemical excitation and relaxation.

Depending on the velocity, gas composition, and vehicle geometry, radiative heating can constitute a significant fraction of the total vehicle heating. Figure 1.1 shows the maximum convective and radiative heat flux at the leading edge stagnation point for a range

[1] A speed that is dependent on the gas composition of the freestream

[2] A speed greater than the speed required to remain in orbit

of planetary entry missions reported by Parcero et al. (2022). These cases do not necessarily feature strong radiative heating and are selected to provide a representative overview of the aeroheating environment for planetary entry. The data is grouped according to the body into which the vehicle entered. It can be seen that the radiative component of heat transfer plays a major role in the majority of these missions. It is also clear that the magnitude of radiative heating is dependent on atmospheric composition, indicating that a strong understanding of the underlying thermochemical processes is important for accurate radiative heating predictions. It should also be noted that the values in Figure 1.1 also depend greatly on the vehicle geometry, heat shield design, and entry velocity, Gnoffo (1999) provides several figures illustrating this.

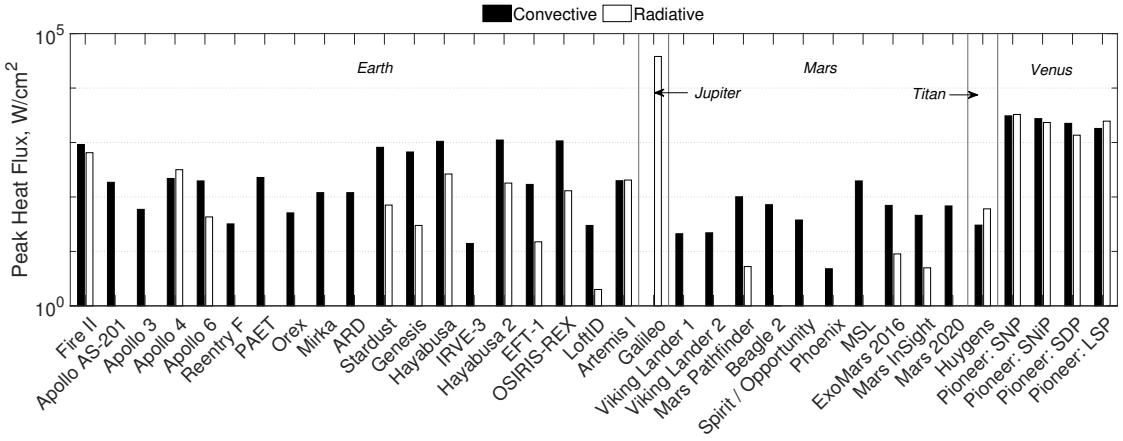

Figure 1.1: The maximum convective and radiative heat flux at the leading edge stagnation point for several planetary entry missions. All data is taken from Parcero et al. (2022) with the exception of the Huygens predictions which are taken from Hollis et al. (2005). The $t = 189$ s maximum coupled radiative and convective + coupled radiative values for DPLR + NEQAIR96 are quoted

Prediction of the radiative heat flux then requires accurate information about the shock layer gas temperature and composition. In high temperature applications, it is necessary to conceive of the temperature as a phenomenon at the microscopic scale. Here, the temperature is an expression of the distribution of energy within a mixture of particles and thus, an individual temperature may be assigned to each particle energy mode of which there are four: translational, vibrational, rotational, and electronic. These modes may be thought of as the degrees of freedom of a particle if it is modelled as a point mass (in the case of an atom) or two point masses attached by a spring (in the case of a diatomic molecule). On timescales encountered in everyday applications (on the order of seconds), it can be assumed that these mode temperatures have sufficient time to reach a state of equilibrium and their collective behaviour may be accurately described by a sin-

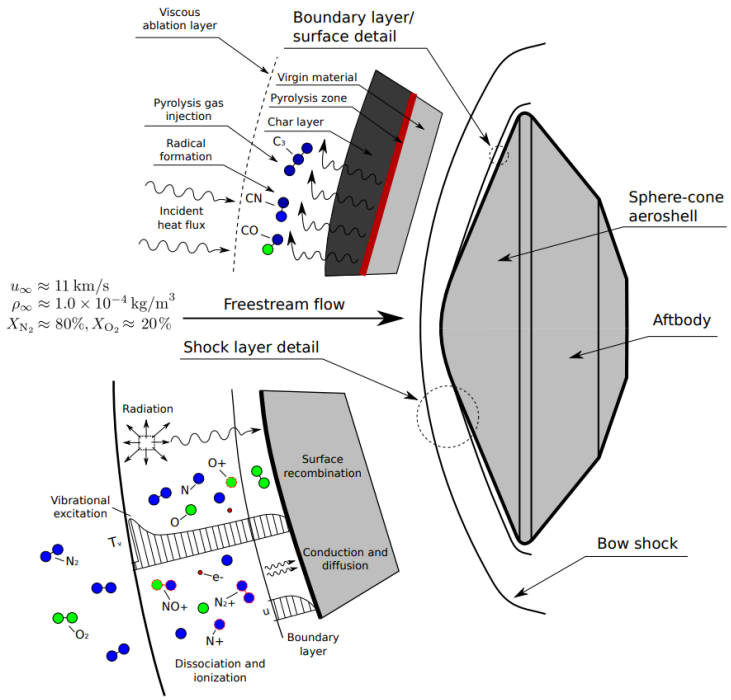

Figure 1.2: Phenomenology of a hypersonic shock layer (Potter, 2011)

gle temperature. This assumption in no longer valid in the shock layer of a hypersonic vehicle and more detail is required to make correct predictions.

To illustrate this with an example, refer to Figure 1.2 which shows the typical physical processes that occur at the surface of a super-orbital hypersonic vehicle during flight, in this case a blunt-body aeroshell in the Earth's atmosphere. Here, the freestream consists of diatomic O_2 and N_2[3] which become vibrationally excited upon crossing into the shock layer and colliding with other energetic molecules. This establishes a state of thermal non-equilibrium, where the energy modes of the molecules behave according to a temperature that is distinct from the other modes. These molecules will begin to emit radiation as individual molecules transition between excited vibrational states. Progressing deeper into the shock layer, further collisions between particles cause molecules to dissociate, individual atoms to become excited, and finally ionization of atoms to occur. Electronic transitions within atoms contribute further to the radiative heat flux incident on the vehicle surface. During this time, when the quantity of species concentrations are in flux, the flow is said to be in a state of chemical non-equilibrium.

The gas in shock layer will reach a state of thermal and chemical equilibrium if sufficient collisions between species occur. At this point, the rate of creation and destruction of species is equal and thus the bulk species fractions do not change, and the mode tem-

[3]In reality, trace species such as Argon and CO_2 are also present

peratures may be modelled by a single equilibrium temperature. It is important to note that although thermal and chemical non-equilibrium are often referred to collectively as *non-equilibrium* they do not necessarily arise and dissipate simultaneously.

The picture becomes significantly more challenging upon proceeding to the vehicle surface. Here, the shock layer gas, in some complex thermochemical state, interacts with the boundary layer and ablation products generated by the heat shield recession. The ablation products are typically long-chain hydrocarbons that themselves form elaborate reaction schemes with the shock layer gas, become chemically excited, and emit radiation (Erb et al., 2020). It is likely that at this point the flow will be optically thick, meaning that it is not accurate to model the shock layer at a perfect transmitter of radiation and re-absorption of radiation must be considered (McGuire et al., 2020). Additionally, the surface of the craft is typically made of a material that serves to catalyse chemical reactions (Loehle et al., 2014). The degree to which thermochemical rates are altered depends on a variety of factors and is generally considered to be a poorly understood phenomenon (Anderson Jr., 2006). This is to say nothing of the bulk material behaviour of the heat shield, typically a woven fibre composite, which may not recess or ablate uniformly due to its non-homogeneity (Grigat et al., 2023).

The gas ultimately leaves the windward side of the vehicle, expanding rapidly around the edge of the forebody and enters the wake flow. The rapid expansion of the gas to a low temperature and pressure can lead to so-called chemical freezing, where there are insufficient collisions between particles to allow chemical and thermal equilibrium to be reached (Beck and Mackie, 1978; Holbeche, 1964a). This gas will continue to emit radiation, albeit significantly less than the gas on the stagnation point of the vehicle, as it proceeds to equilibrium that the vehicle aftbody must withstand. The aftbody must accommodate design features that are not necessary on the forebody such as radio-transparent materials to facilitate communications with Earth during cruise and a mechanism to house the parachute for the descent phase. It is also desirable to minimise the thermal protection system (TPS) thickness on the aftbody so as to maintain aerodynamic stability during entry. Consequently, the aftbody can be vulnerable to relatively low radiative heat loading and accurate models of the expanding flow processes are required to ensure sufficient safety margins.

The flow in the wake is the last link in a chain of highly complex physical processes and this has made it a comparatively difficult subject of study (Johnston, 2015). Processes in the wake are highly coupled which leads to large uncertainties in predictions for ra-

diative heat flux. Johnston et al. (2012) found error bounds for radiative heat flux to the aftbody of a Martian entry to be -78% to 262%. The size of the wake can be many times greater than the vehicle in many cases which leads to a large integrated heat load (Brandis et al., 2020). West et al. (2017) estimate a radiative heating uncertainty bound of up to 125% in the aftbody region for Lunar return case.

The same expansion processes that occur in the wake of hypersonic vehicles may be leveraged in ground based wind tunnel facilities to produce high enthalpy flow conditions. Study of the phenomenon in a wind tunnel provides a controlled environment for a variety of flow conditions to be explored and offers a new opportunity for the problem to be addressed. This opportunity is the focus of the next section.

1.1.2 Relevance of the Expanding Flow Problem

Flight testing of hypersonic vehicles is an expensive endeavour on Earth, and an even more expensive one on other planets. As a result, significant research attention has been devoted to methods of recreating planetary entry conditions in ground test facilities. Ground-based experiments facilitate the use of advanced instrumentation and provide information to vehicle designers that is used to de-risk the flight.

The full complexity of planetary entry flows is difficult to recreate in its entirety in a single ground test facility, which has led to the develop of a range of facilities to study different aspects of the problem separately[4]. A summary of the typical performance capabilities of several types of ground test facilities is shown in Figure 1.3. These facilities can be as complex as the phenomenon they simulate which motivates a degree of introspection before assertions about flight can be made with confidence. The expansion tube, a central subject of this thesis, is one such facility.

As the name suggests, the expansion tube shock heats and then unsteadily expands a slug of gas (analogous to flow entering the wake of a flight vehicle) to generate some of the highest enthalpy test conditions possible in a ground test facility. Expansion tubes have been widely used since their inception for hypersonics research and to provide support for vehicle design (Morgan, 1997). Expansion tubes, by their nature, inherit many of the issues associated with wake flow in flight vehicles, particularly thermochemical freezing of the freestream test gas, leading to uncertainty about the generated test conditions. Large changes to the magnitude (> 100 %) and temporal variation of flow properties occur depending on the degree of freezing occurring. This effect has been observed in

[4]Further details are provided in Chapter 2

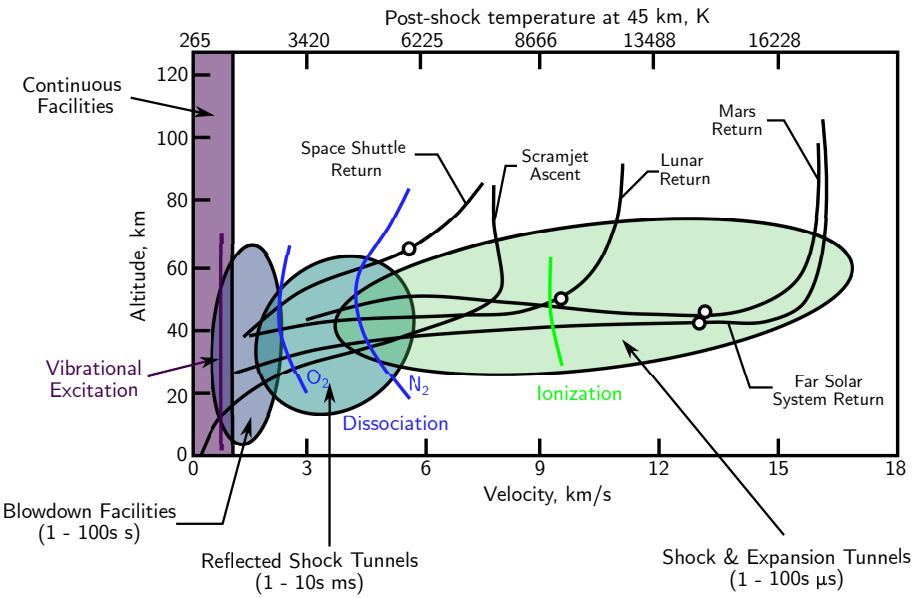

Figure 1.3: Typical performance envelopes of several types of ground test facilities, adapted from Collen (2021)

a variety of gas mixtures and test conditions (Beck and Mackie, 1978; Holbeche, 1964a; Nasser and Cleaver, 1977; Wei et al., 2017; Appleton, 1966) and success in predicting them or recreating them numerically has been limited (Gildfind et al., 2018a,b).

The difficulty in predicting expansion tube behaviour must in part be attributed to uncertainty in shock tube modelling. Expansion tubes function essentially as an extension to the shock tube (the shock tube output might be considered as the input to the expansion tube unsteady expansion) which causes uncertainty to propagate through the process. Improved understanding of the causes of discrepancies between shock tube facilities have been provided in recent work (Satchell et al., 2022c; Collen et al., 2022; Clarke et al., 2023b), however robust predictions of non-equilibrium behaviour remain elusive (Clarke et al., 2023a). New approaches are needed to model the shock tube and expansion tube to improve confidence in experimental data and to ultimately address the large uncertainties associated with radiative heat flux predictions in wake flows.

1.2 Research Objectives

The contents of the previous section highlighted the design challenges posed by planetary entry missions and the need for improved non-equilibrium thermochemistry modelling in the context of an expanding flow in a vehicle wake. This problem is strongly linked to modelling of the freestream of expansion tube/tunnel facilities which remain the best available option in many cases for ground testing of planetary entry missions. Our relatively poor understanding of the expanding flow problem limits our confidence in expansion tube/tunnel facilities and thus, in our ability to design successful missions to explore the solar system. To address these uncertainties, the following objectives were selected for this thesis:

A: Develop a Non-Equilibrium, Lagrangian Shock Tube Solver

Previous attempts to accurately model the shock tube, a necessary precursor to expansion tube modelling, have highlighted the importance of accounting for non-uniform shock speed during the experiment. Such non-uniformity results in an enthalpy gradient in the shock tube test slug which the experimenter must account for, or else be in error. It has also been found that, particularly in strongly accelerating shock speed cases, pressure waves originating from the facility driver affect the test gas and must be modelled. State-of-the-art shock tube models consider a subset of non-equilibrium effects, shock speed non-uniformity, or driver effects, but never all. Thus, the first objective of this thesis is to produce a numerical model that can account for all of these effects simultaneously. This will be achieved by developing a new numerical method. When developed, this method will provide new insight into shock tube experiments and provide a platform to model the expansion tube, which is essentially an extension of the shock tube.

B: Characterise Historical Shock Tube Test Cases

The cause of discrepancies in historical shock tube data from several different experimental facilities has been attributed to shock speed non-uniformity. To date, numerical models that account for this phenomenon have not considered non-equilibrium and driver effects which has limited their utility. Equipped with an updated shock tube solver, the second objective of this thesis is to apply the tool to historical data and shed light on previous inconsistencies. This will be achieved by applying the code to tests from the EAST and T6 facilities where cases with a variety of complex shock speed profiles are available.

Comparisons to experiment will serve to benchmark the code and highlight its strengths and weaknesses.

C: Produce a Validation Dataset for the Expansion Tube

Measurements of the freestream of any hypersonic facility are difficult to obtain non-intrusively. Optical measurements that are commonplace for a shock tube are complicated when applied to the expansion tube because of the relatively low temperature and thus low radiative emission of the freestream. This perhaps explains the paucity of data for the expansion tube freestream in the literature, which is a serious obstacle to understanding expanding flows. The third objective of this thesis then is to measure the freestream thermochemical state of an expansion tube as it evolves from secondary diaphragm. This will be accomplished by developing a sensitive radiometer probe and test conditions that are conducive to relatively strong radiative emission. Conditions relevant to Lunar return and Ice Giant entry will be targeted. These results will serve as a validation dataset for numerical models of expanding flows and will enable completion of the final thesis objective.

D: Extend the Shock Tube Solver to the Expansion Tube

The final objective of this thesis is to produce a numerical tool that can provide improved predictions of the expansion tube freestream. This objective will be achieved by manipulating the boundary conditions imposed on the shock tube solver to include a low pressure acceleration tube. Adjustments to the boundary layer model and treatment of the secondary diaphragm behaviour are required. Flow properties predicted by the model will be used to simulate the expected radiative emission and thus allow direct comparison to the experimental validation dataset. The comparison will ideally validate the numerical model and allow statements about the expansion tube freestream to be made with reduced uncertainty.

1.3 Thesis Structure

This document consists of six further chapters, the contents of which are briefly summarised below:

Chapter 2: Literature Review

Here, the relevant literature is compiled and discussed to provide a justification for the choice of thesis direction. Previous experimental results that suggest the presence of thermal and chemical non-equilibrium in the freestream of expansion tube/tunnel facilities are highlighted, particularly where this is thought to have increased experimental uncertainty. Experimental techniques that may be of use in the study of expanding flows are reviewed and compared. Approaches to numerical modelling of impulse facilities are reviewed with particular attention paid to their ability to account for non-uniform shock trajectories.

Chapter 3: A Novel Non-Equilibrium, Lagrangian Shock Tube Solver

In this chapter, the development of an improved shock tube solver known as LASTA 2.0 is presented. The basic structure, governing equations, and method of solution are detailed. New features of the code such as the inclusion of a non-equilibrium model and a backwards time integration scheme are discussed. Agreement between the method and results from a viscous, axisymmetric Navier-Stokes solution is found to be within 1% in pressure and temperature in the majority of cases. Improved agreement with experimental data is evident when compared to LASTA 1.0, particularly where there is strong shock speed non-uniformity.

Chapter 4: The Effect of Shock Speed Variation on Non-Equilibrium Processes

Now that LASTA 2.0 has been validated, it is applied to historical shock tube data. Previous methods have operated under an equilibrium assumption and have not modelled pressure waves originating from the driver gas which has led to error. Test cases in relevant to Lunar return, Titan entry, and Ice Giant entry from the EAST and T6 shock tube facilities are analysed, with particular attention paid to radiance from the oxygen 777 and hydrogen 656 nm lines.

Chapter 5: Radiance Measurements Through Unsteady Expansion Waves

Measurements of the freestream thermochemical state of expansion tunnels are difficult to obtain non-intrusively and for this reason, are relatively scarce, especially when compared to shock tubes measurements. In this chapter, the development, validation, and use of a wall mounted radiometer probe in the T6 expansion tube are presented. The developed radiometers are shown to be in excellent agreement with conventional shock tube optical emission spectroscopy and thus their application to the expansion tube is justified. Measurements of oxygen 777 nm and hydrogen 656 nm radiance through the unsteady expansion wave at several locations in the tube show the reduction in temperature that occurs for a range of acceleration tube pressures (expansion strengths).

Chapter 6: Modelling Expansion Tube Flows with LASTA 2.0

In the final *content* chapter, the new features of LASTA 2.0 are put to use to model the effect of shock speed non-uniformity on freestream non-equilibrium in an expansion tube. NEQAIR simulations of the LASTA 2.0 predicted species number densities and temperatures are compared to the experimental results from Chapter 5.

Chapter 7: Conclusion

Finally, the complete findings of thesis are summarised. Limitations of the approaches taken to addressing the thesis objectives are discussed and form the basis for recommendations of future work. These include possible improvements to the radiometer probes, LASTA 2.0, and the T6 facility.

Appendix A: LASTA 2.0 Guide

A quick start guide for use of the LASTA 2.0 software is provided with an example input file. A table summarising the input files used for each simulation in the thesis is provided as well as the GitHub code version and date.

Appendix B: Governing Equations and for the Two-Temperature Plasma

Here, the governing equations and method of solution for the LASTA 2.0 code are rigorously defined. The implementation of the Park two-temperature model is presented as well as the mathematical operations necessary to transform the equations for a conservative to a characteristic basis.

Appendix C: Reaction Rates

The reaction schemes used for modelling thermochemical non-equilibrium throughout the thesis are summarised here.

Appendix D: Further Analysis of E65

Comparisons between LASTA 2.0 / NEQAIR 15.2.2 full spectrum radiation predictions and experiment for 5 additional test cases are presented here.

Chapter 2

Literature Review

Contents

2.1 Introduction

The aim of this chapter is to provide context for the direction taken in the remainder of the thesis and to summarise the state of art in the relevant literature. Firstly, the use of shock and expansion tubes as tools in high temperature gas dynamics research will be reviewed with a particular focus on the non-ideal effects that are present. Next, a summary of experimental diagnostics for hypersonic flows is presented. Attention will be paid to the comparative strengths and weaknesses of different techniques. Finally, a review of simulation approaches to the shock and expansion tube is presented.

2.2 Shock Tubes

Shock tubes are currently one of the best available platforms for shock layer radiation measurements because of their relative simplicity and versatility. Shock tubes are to the expansion tube what the forebody flow field is to the aftbody flow field in flight. A robust, comprehensive model of the shock tube is a pre-requisite for accurate expansion tube modelling and thus, the operating principles of shock tubes are reviewed first.

2.2.1 Background

A shock tube experiment aims to match gas composition, density, and shock speed to flight, thereby obtaining similarity between the flight stagnation line and the shock tube flow. Shock tube flows are considered *chemically clean* meaning that the test gas is chemically undisturbed before the experiment takes place. This offers a significant advantage over other experimental facilities and makes shock tubes highly informative for the investigation of non-equilibrium chemical kinetics. Figure 2.1 shows a distance-time plot of the typical wave processes occurring in a generic shock tube during a test. Initially, the test gas, matching the density and composition of the free stream flight condition of interest, resides in the region denoted *Shock Tube*. The high pressure driver gas ruptures the primary diaphragm and drives a strong shock wave through the test gas. To obtain similarity with flight, the shock speed should match the flight case. The region of useful test gas, denoted τ, grows until it reaches a maximum value governed by the boundary layer growth (Mirels, 1963). Measurements of radiation behind the shock wave can be made at any point along the length of the shock tube, but they are typically obtained at a measurement window located at the downstream end of the facility where the test time is maximised (Cruden and Brandis, 2020; Collen, 2021).

A complete review of the historical development of shock tubes, beginning in 1899 (Vincenti et al., 1966), is not attempted here. However, several facilities active in the study of shock layer radiation for hypersonics applications are highlighted. The facility with the greatest capability is the NASA Electric Arc Shock Tube (EAST) which is described in detail by Cruden et al. (2021). The EAST driven tube has a bore diameter of 10.16 cm[1] and is 12.5 m in length. The facility is driven by means of an electric arc, which discharges 1.2 MJ of energy from a 40 kV capacitor bank into the gas in a buffer tube. The buffer tube typically contains hydrogen or helium and is separated from the driven tube by a thin diaphragm. This driver approach affords EAST a large performance en-

[1] A 60 cm tube is also used

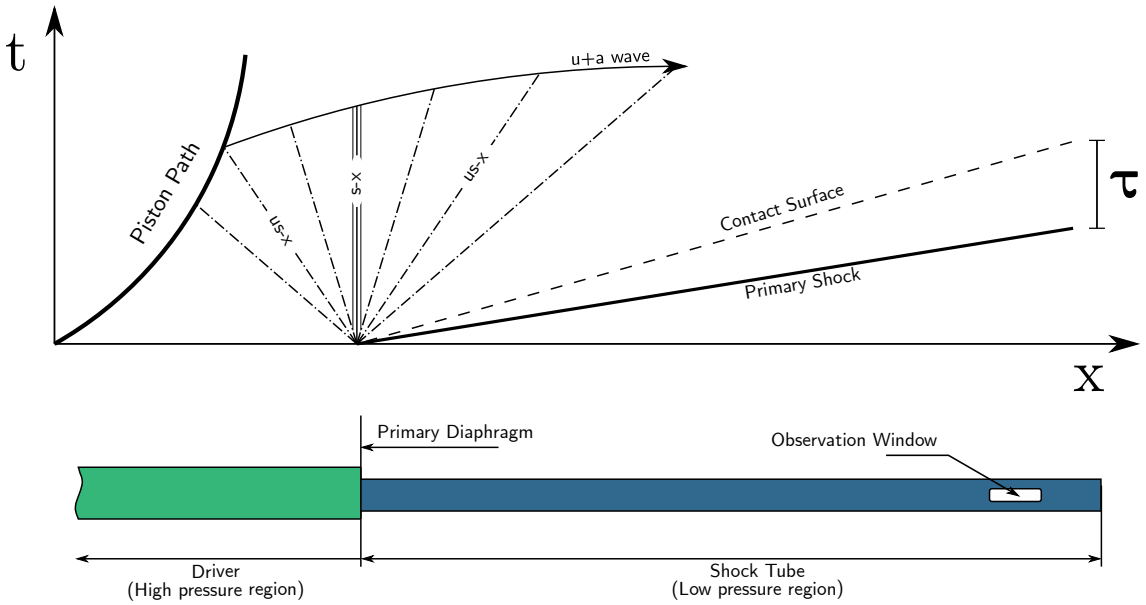

Figure 2.1: Position-time diagram of ideal wave processes in a generic shock tube

velope with shock speeds between 1.3 and 46 $\mathrm{km\,s^{-1}}$ possible depending on the driven gas. Measurements of post-shock radiation in the EAST are made with up to four independent spectrographs coupled to intensified CCD cameras. The spectrographs view the test gas through slot windows in the driven tube just before the dump tank. The use of many spectrometers allows a wide spectral range to be captured for each experiment from the vacuum ultraviolet (VUV) to the near infrared (NIR). EAST has provided support for the design of many NASA planetary entry missions and thus benchmark datasets for a large number of atmospheres and speed ranges are available. These include Venus (Cruden et al., 2012), Mars (Cruden et al., 2016; Brandis et al., 2013; Cruden et al., 2018; Cruden, 2014; Tibère-Inglesse et al., 2023a), Earth (Brandis and Cruden, 2017a; Cruden and Brandis, 2020; Brandis and Cruden, 2018), Saturn, Uranus, Neptune, Jupiter (Cruden and Bogdanoff, 2017; Cruden and Tibere-Inglesse, 2024), and Titan (Bose et al., 2006; Brandis and Cruden, 2017c; Tibère-Inglesse et al., 2023b).

The Japanese Aerospace Exploration Agency (JAXA) operate the free-piston driven Hyper-Velocity Shock Tube (HVST). The HVST driven tube is square in cross section and has dimensions of 70 x 70 x 4175 mm (Yamada et al., 2011). Similarly to EAST, measurements of shock layer radiation are made through a window located just before the dump tank. HVST has been used to make measurements for Earth (Yamada et al., 2012; Takayanagi et al., 2014) and Mars entry (Takayanagi and Fujita, 2013). HVST may also be operated as an expansion tube, which is discussed further in Section 2.3.1.

The X2 super-orbital expansion tube at the University of Queensland may be operated

in so called non-reflected shock tube (NRST) mode. X2 has a bore diameter of 85 mm and typically operates as an expansion tube, which is discussed further in Section 2.3.1. In the NRST configuration, the test gas is imaged as it exits the shock tube and enters the test section, rather than through a window in the side of the tube. This approach requires that the core flow is viewed through a steady expansion which increases uncertainty in the freestream state. However, results from X2 in NRST mode have been shown to compare favourably with results from other facilities (McGilvray et al., 2024). Measurements of shock layer radiation for Mars and Titan entry environments have been made in this fashion (Brandis, 2009a).

The Oxford T6 Stalker tunnel has recently been established as a tool for the study of shock layer radiation (Collen, 2021). The facility is free-piston driven and generates pressures on the order of 50 MPa during a shot. The driver may be coupled to a range of downstream components to allow operation of the facility as either a shock tube (ST), expansion tube or expansion tunnel (ExT), or reflected shock tunnel (RST). T6 offers the only expansion tube capability in Europe with test times between 20 and 150 $\mu\mathrm{s}$. During an experiment, a piston weighing either 36 or 90 kg is accelerated to speeds of approximately 300 $\mathrm{m\,s^{-1}}$ by high pressure air known as the reservoir gas. The piston compresses the driver gas which, upon rupturing the primary diaphragm, unsteadily expands into the driven tube, forming the shock wave that is studied at the end of the facility. Measurements of conditions relevant to Earth (Collen et al., 2019; Glenn et al., 2022), Mars (Crumpton, 2024), Titan (Sopek et al., 2024), and Giant Planet entry (Steer et al., 2023a) have been made.

2.2.2 Non-Ideal Effects

Despite their ostensibly simple operation, several subtle complexities inherent in shock tube operation conspire to make accurate a priori simulations difficult. These arise from a variety of sources but ultimately result in a non-uniform shock speed profile in the driven tube which can strongly affect the state of the test gas at the time of measurement. These sources of complexity in the shock tube are reviewed here.

Boundary Layer Effects

The primary non-ideal effect is growth of the boundary layer in the test slug and driver gas, which serves to attenuate the shock by entraining mass from the core flow. Mirels (1963) developed a model of the shock tube boundary layer by assuming that it behaved

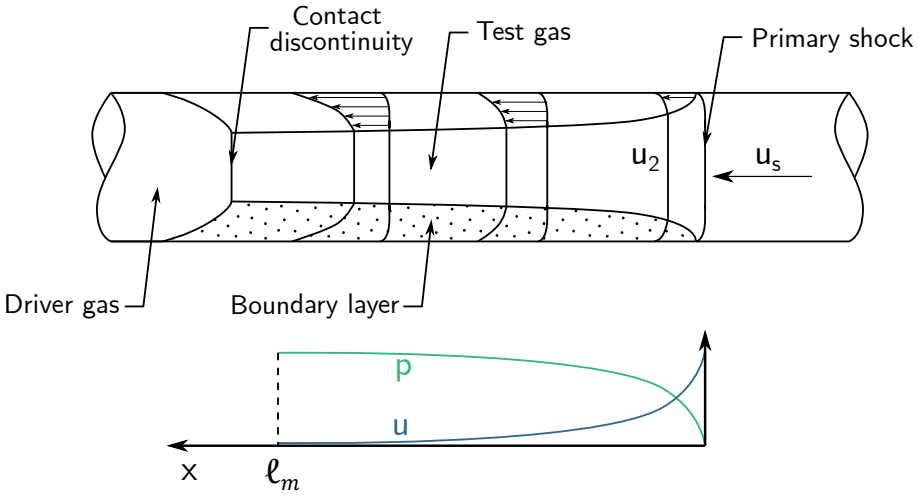

Figure 2.2: Flow processes in a shock tube

according to laminar flat plate theory as if in a uniform external freestream in the shock frame of reference. Mirels then considered the boundary layer to behave self-similarly according to a shape factor, β. Under this assumption, the length of the test slug grows until the mass flow rate it entrains from the core flow is equal to the mass flow rate entering the test slug through the shock. This length is known as the maximum separation distance or *Mirels length* (ℓ_m) and may be determined using only the tube fill pressure, fill composition, and shock speed. Figure 2.2 illustrates boundary layer development in a shock tube in the shock attached frame of reference.

Mirels (1966) then further examined the implications of the model, with particular attention paid to the variation in flow properties that occur as a result of the growth of the boundary layer. Mirels showed that the post-shock flow in a shock tube is analogous to flow through a converging duct with area ratio governed by:

$$\frac{A_{2s}}{A_2} = 1 - \left(\frac{\ell}{\ell_m}\right)^{1/2} \tag{2.1}$$

Where state 2_s is the immediate post-shock state, state 2 is the gas state a distance ℓ behind the shock wave, and ℓ_m is the maximum separation distance. This variation changed the post-shock properties (ρ, u, p, T) as a function of distance behind the shock by up to 35% when compared with a no-boundary layer case for shock waves with $M > 3$. Mirels found that this applied for both laminar and turbulent boundary layers (Mirels, 1966). Mirels only considered ideal gas behaviour in these two publications, however the implications for study of real gas effects and shock layer radiation are significant[2]. In light of these findings, it is clearly not appropriate to assume constant post-shock properties.

[2]Mirels (1961) finds that the inclusion of real gas effects does not significantly change the conclusions

Clarke et al. (2023b) provide similarity transformations to account for the effect of the shock tube boundary layer on the test flow. These results demonstrate the in many circumstances, the variation in flow properties differs significantly from the ideal assumptions.

Mirels theory provides a satisfactory result in many experimental cases, however it is limited by the assumption of constant shock speed. In cases where strong shock attenuation is present, the boundary layer shape factor β will vary strongly depending on the local shock speed, leading to error. Improvement can be achieved by treating the model as unsteady (i.e. calculate the shape factor locally assuming an instantaneous shape change) or by fully coupling a boundary layer solver to a numerical model that accounts for the non-uniform shock behaviour.

Driver & Diaphragm Opening Effects

The motion of the contact surface, the interface between the expanded driver gas and test gas, produces waves which affect the shock speed and test slug (Morgan and Gildfind, 2013). The behaviour of the contact surface is itself dependent on many factors including the driver technology employed, the driver condition chosen for the experiment, and the primary diaphragm rupture behaviour. Bowman (1966) provides an extensive study of the wave processes in shock tube experiments and finds that, particularly at high pressures, the shock behaviour is dependent on transverse waves produced by the diaphragm opening and other upstream disturbances. Jacobs (1998) and McGilvray et al. (2013) both show the necessity of accounting for driver wave effects when modelling the shock tube test slug.

A variety of driver technologies are employed to produce the high pressure and temperature ratios required for shock tube operation. Notable examples include electric arc heated drivers (Menard, 1971), free-piston drivers (Stalker, 1972), and combustion drivers (Lu, 2002). These technologies achieve the required conditions via different mechanisms which will inevitably result in different wave patterns, even for nominally identical diaphragm rupture conditions.

The primary diaphragm in a shock tube are often assumed to rupture instantaneously. These diaphragms are typically scored metal plates of thickness > 1 mm and thus in practice, the opening process occurs over a non-negligible time (≈ 100 µs). White (1958) analysed the effect of diaphragm opening time on shock tube flows and found that it leads to an appreciable difference versus the ideal case, with significantly stronger shocks

in cases with monotonic driver/diatomic driven gas combinations. Rothkopf and Low (1974) studied the opening characteristics of several diaphragm configurations, materials, and experimental conditions. They found that diaphragm opening behaviour is strongly dependent on ductility. Detailed modelling of diaphragm rupture on a test-to-test basis is not practically possible and hence the effect of the diaphragm rupture on the test gas is typically considered stochastic.

Thermochemical Non-Uniformities

The non-equilibrium thermochemistry taking place in the shock layer is seen to affect the shock speed (Kotov et al., 2014; Chandel et al., 2018). Spence (1961) examined the effect of dissociation and vibrational relaxation on shock propagation in air mixtures. They considered that local disturbances may propagate at either the frozen or equilibrium sound speed and found that, given sufficient time, the shock tends to propagate at the equilibrium sound speed. Clearly, there is a *non-equilibrium* sound speed at which disturbances propagate between the immediate post-shock state and equilibrium state and thus the thermochemistry itself will influence the shock trajectory. These effects are also found to be dependent on the disturbance frequency.

Shock Speed Variation

The non-uniform wave processes from the sources discussed so far in this section each contribute to the experimentally observed phenomenon of non-uniform shock speed. Variation in shock speed can have a significant effect on the observed experimental results. Mirels (1963) postulated that this may be the case, but chose to focus on the limiting case of fully developed flow and constant shock speed. Holbeche (1964b) experimentally observed temperature discrepancies on the order of 200 K via sodium-line-reversal in air shocks and attributed this to shock attenuation. More recently, Collen et al. (2022) shows that for two test with the same shock speed at the measurement window, the post-shock oxygen 777 nm equilibrium radiance can vary by over 100 %. This effect has been shown to be present irrespective of the experimental facility or driver technology employed, having been observed and quantified in results from the EAST (Collen et al., 2023) and T6 (Collen et al., 2022) facilities.

Shock Curvature Effects

Shock curvature in a shock tube arises as a consequence of the boundary layer formation behind the shock wave. Hartunian (1961) developed a two-dimensional, linearized analytical model of the interaction between a normal shock wave and boundary layer. Hartunian assumed a semi-infinite boundary layer but considered real gas effects, which were found to exert considerable influence on shock curvature. De Boer (1963) later extended the analysis to cases with two parallel walls, a rectangular duct, and a circular shock tube. De Boer also included the effect of a finite length boundary layer which was found to be negligible provided that the boundary layer length was greater than the tube radius. De Boer developed expressions for the axial extent of the curved shock (θ), the expression for the laminar case being:

$$\theta_L = 1.030 \left(\frac{h\eta_1}{\rho_1 a_1} \right)^{1/2} M_1^{-0.5+\omega} C_L(M_1, \sigma, \omega, \gamma) \tag{2.2}$$

where h is the distance from the tube centreline, ρ_1 is the pre-shock density, a_1 is the pre-shock sound speed, η_1 is the pre-shock viscosity, and M_1 is the shock Mach number. C_L is a complex function of the Mach number and gas properties (for argon $\sigma = 0.70$, $\omega = 0.70$, $\gamma = 1.67$). This expression yields an increasing shock curvature for a decreasing fill pressure ($\theta \propto p^{-1/2}$) which has also been observed experimentally.

Optical diagnostics used in shock tubes often obtain an integrated measurement across the full width of the tube. Typically, the boundary layer is assumed to be cold and optically thin and thus its influence may be neglected. However, the implication of shock curvature theory is that under certain circumstances, the radiating test gas itself is radially non-uniform and therefore integrated measurements may not be appropriate for extracting accurate thermochemical rate data.

Contamination

The primary purpose of the shock tube (in the context of hypersonics research) is to produce high temperature gas mixtures from which thermochemical reaction rates may be deduced. Reaction rates are highly dependent on temperature, the species present, and their respective concentrations. Measurement of accurate thermochemical rates in a shock tube requires that the composition of the pre-shock gas is known to a high accuracy, lest unwanted chemical species influence the thermochemistry.

Ensuring the pre-shock gas is of sufficient purity is difficult in practice for several

reasons. Firstly, even minute quantities of common contaminants have been shown to significantly affect the thermochemistry. Clarke et al. (2024b) find that the presence of 0.08% C_2 in a nominal 79% N_2-21% O_2 test gas increases the nonequilibrium peak radiance by nearly 100% for a shock speed of 7.3 $\mathrm{km\,s^{-1}}$ in 33 Pa. The presence of contaminants has been postulated as a cause for the disagreement between experimental results and numerical predictions by several authors (Glenn et al., 2022; Cruden and Brandis, 2020). This is attributed to the formation of cyanogen (CN) which is a strong radiator. Incidentally, the cleanliness of the tunnel bore has been shown to affect boundary layer transition in the T5 Reflected shock tube facility (Jewell et al., 2017), implying a similar phenomenon may occur in the free stream of an expansion tunnel.

2.3 Expansion Tubes

In this section, the history, operating principles, and non-ideal effects in the expansion tube are presented.

2.3.1 Background

As the capacity of humanity to explore the solar system increased there developed a need for the ability to simulate superorbital flight speeds in ground test facilities. Shock tubes are limited, independently of driver considerations, in the total enthalpy they can simulate because all energy is added to the flow across a shock (Morgan, 1997). The addition of more energy serves to dissociate and then ionize the test gas, increasing the internal energy rather than the kinetic component of enthalpy. Additionally, the maximum test time in a shock tube is limited by the facility geometry and is typically on the order of µs (Mirels, 1963), meaning they are not ideal for testing of aerodynamic models where several flow lengths are required to establish steady processes

The expansion tube concept circumvents these limitations by adding total enthalpy to the test gas through an unsteady expansion wave (see Figure 2.3). The expansion tube is identical to the shock tube but an *acceleration tube* is added downstream of the tube containing the test gas. The acceleration tube contains low pressure gas, typically lab air, and is separated from the test gas via a secondary diaphragm. The secondary diaphragm can be made of any material in principle, but is typically a thin Mylar sheet. When the shock reaches the secondary diaphragm it ruptures, allowing the high-pressure, shock heated test gas to unsteadily expand into the acceleration tube, resulting in an increase in total enthalpy without significant dissociation of the test gas. The expansion tube may by coupled with an expansion nozzle at the acceleration tube outlet to further expand the test gas - this arrangement is known as an expansion *tunnel*.

Expansion tubes/tunnels offer the capability to establish steady flow over sub-scale models at true flight total enthalpies with relatively low freestream chemical non uniformity[3]. Similarity between the sub-scale vehicle and flight is achieved via binary scaling (De Crombrugghe, 2017). In a binary scaled experiment, the total enthalpy (essentially $\frac{U^2}{2}$) and the ρL product are matched to flight. This scaling replicates most of the desired properties from flight around the model, apart from radiation which does not scale directly (Andrianatos et al., 2015).

[3]Compared to, for example, a reflected shock tunnel which requires that the test gas stagnates before passing over the model

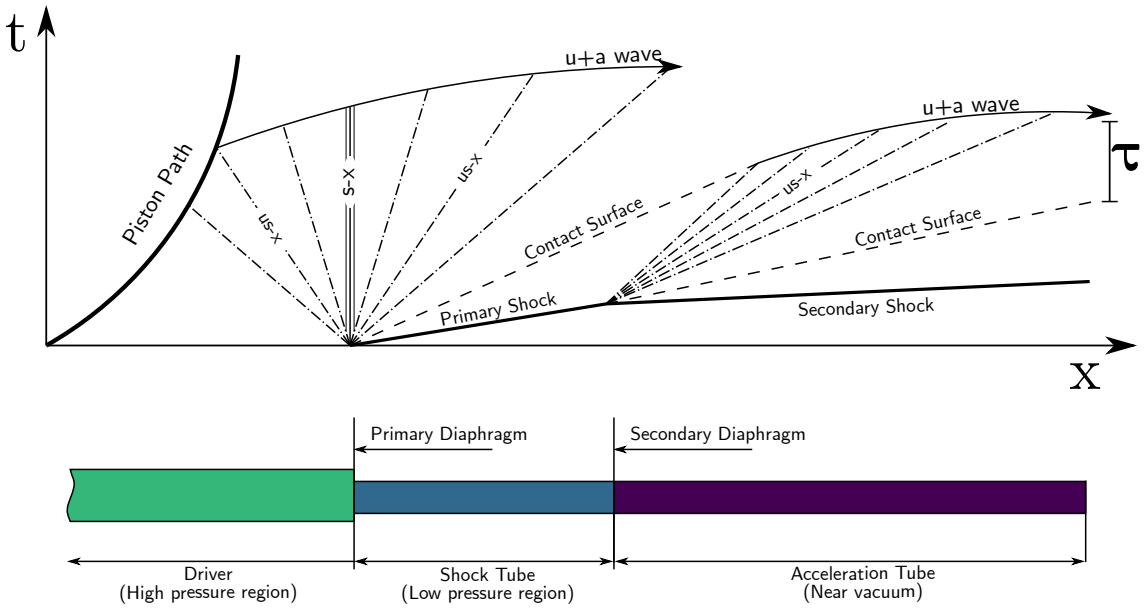

Figure 2.3: Position-time diagram of wave processes occurring in an ideal expansion tube

For point-to-point radiative transmission in an optically thin flow (transparent, the average photon will pass through without absorption) then similarity between flight and experiment is conserved because attenuation scales in proportion to mass traversed in the line of sight (Morgan et al., 2008). However, similarity is lost if the heat removed by radiation is significant. The heat removed from the shock layer scales in proportion to the mass of gas in the shock layer, ρL^3, whereas the mass flux into the shock layer scales in proportion to ρL^2. This means that observed radiative heating in the lab will be higher than in the flight case. The significance of this discrepancy depends on how strongly the radiative effects are coupled to the macroscopic flow properties, which is defined by the Goulard number, Γ, shown in Equation 2.3 (Goulard, 1961).

$$\Gamma = \frac{2q_R}{\frac{1}{2}\rho_\infty v_\infty^3} \tag{2.3}$$

Flows with $\Gamma > 0.1$ are considered to have non-negligible radiative coupling (Anderson Jr., 2006). Leyland et al. (2013) provides approximate values of Γ during peak radiative heating for several entry trajectories which are summarised in Table 2.1. In practice, this means that direct scaling between expansion tunnel flows and flight is not possible in circumstances where radiative coupling is significant. However, useful information about non-equilibrium thermochemistry can still be gleaned.

Table 2.1: Values of Γ for several entry trajectories provided by Leyland et al. (2013)

Trajectory	Γ
Lunar Return	0.01
Hayabusa	0.013
Jupiter	0.1
Titan	0.4

Expansion tunnels can be used to study non-equilibrium thermochemistry by interrogating the stagnation line of the sub-scale vehicle. Expansion tunnels can offer a superior signal to noise ratio to an equivalent shock tube experiment as the test times are much longer, allowing camera gating times to be larger. To obtain similarity between flight and experiment for non-equilibrium thermochemistry necessitates matching the Damköhler number, defined as:

$$\Delta = \frac{\rho_\infty \phi}{U} \approx \frac{\rho L}{\sqrt{2H_t}} \tag{2.4}$$

where ρ_∞ is the freestream density, ϕ is an appropriate length scale, and U is the freestream velocity (Inger et al., 2003). Matching the Damköhler number ensures that the rate of binary reactions is the same between the two flows, thus allowing thermochemical rates to be measured in an expansion tube. However, this scaling methodology does not extend to three-body reactions and is typically only appropriate for study of dissociation processes at the start of the shock layer.

The concept of the expansion tube was first proposed by Resler and Bloxsom (1952) and examined in detail by Trimpi (1962). The first expansion tubes were operated successfully at NASA Langley by Miller (1978) and Miller and Jones (1984) but they were limited in their research capability because few usable operating conditions had been developed. This facility was ultimately decommissioned in 1983 because of the poor performance envelope and financial issues at NASA, presumably caused in part by the shuttle program happening in parallel.

Paull et al. (1988) returned to the concept by constructing a free piston driven expansion tube at the University of Queensland in 1988, named X1. Their facility had comparable driver and shock tube dimensions to the Langley facility, but their acceleration tube was significantly shorter (3.18 m vs 19 m). Using this facility, they were able to diagnose the causes of the limited performance envelope seen at Langley which were primarily:

1. Extinction of the test time by arrival of the reflected unsteady expansion wave

2. Transmittance of noise from the driver gas to the test gas for small expansion ratio

cases

They found that these factors could be mitigated by ensuring a sufficient *acoustic buffer*, meaning that the speed of sound in the shocked test gas was considerable larger than the speed of sound in the driver gas. Paull and Stalker found that as a result, satisfactory expansion tube operation was only possible at high enthalpy conditions unless a method for decreasing freestream noise could be found.

The use of an intermediate shock-heated secondary driver had been proposed as a means of developing a sufficient acoustic buffer (Henshall, 1956). Stalker and Plumb (1968) were the first to demonstrate the technique using a standard shock tube arrangement. Morgan (2001) showed that the secondary driver could indeed be used to reduce noise transmission to the test gas, thus increasing the performance envelope of the expansion tube to encompass lower enthalpy test conditions. Additionally, Morgan and Stalker (1992) were able to use a secondary driver to increase the total enthalpy performance of the X1 facility, achieving maximum shock speeds of 18.7 $\mathrm{km\,s^{-1}}$. These findings significantly improved the usability of the expansion tube and provided justification for construction of a larger, more powerful facility.

The X2 and X3 facilities were developed during the 1990's by Morgan (1997) with total lengths of 25 and 65 m respectively. The larger sizes offered the ability to test larger, higher fidelity models and longer test times. The X2 facility was commissioned in 1995 (Scott et al., 2005) with a singe piston driver and was fitted with a contoured expansion nozzle in 2006 (Scott, 2006). Since then, the facility has enabled a plethora of testing including scramjet development (McGilvray, 2008), Titan entry (Capra, 2007; Capra and Morgan, 2012; Brandis, 2009a), Mars entry (Gu, 2018), Giant Planet entry (Higgins, 2005; James et al., 2017; Liu, 2021), and many others. X2 has a total enthalpy capability of 75 $\mathrm{MJ\,kg^{-1}}$ and is the fastest expansion tube in the world. The X3 facility was designed to operate with driver burst pressure of 100 MPa (Morgan, 2000) and has operated with total enthalpies exceeding 100 $\mathrm{MJ\,kg^{-1}}$. Since its commissioning, X3 has been upgraded with a Mach 10 and Mach 12 expansion nozzle (Davey and Litster, 2006; Toniato et al., 2020), a larger dump tank to facilitate scramjet testing, and a larger reservoir. X3 is the largest high performance expansion tube in the world.

Several expansion tubes/tunnels are in operation in the United States. The HYPULSE facility was based at the General Applied Science Laboratory (GASL). Originally the Langley expansion tube, it was (re)commissioned in 1989. The facility has since been transferred to Purdue University where it has been used for various hypersonic air-

breathing propulsion studies and some Mars entry probe configurations. The LENS-X shock-expansion tunnel has been operated by Calspan and University of Buffalo (CUBRC) since the 1990's. The facility has mainly been used for defence purposes such as development of missiles, interceptors, and strike/cruise vehicles. The facility has also been used by the Space Shuttle and Orion programs (Holden, 2015). The California Institute of Technology (CalTech) operate the High Enthalpy Tunnel (HET). This facility has primarily been used for University research problems and NASA planetary entry studies such as MSL (Mars Science Laboratory) and Orion. Recent studies have included attempts to characterise the freestream of the facility (Schwartz et al., 2021). Recently, Texas A&M University (TAMU) commissioned their Hypervelocity Expansion Tunnel (HXT) (Dean et al., 2022). The facility produces test times on the order of 1 $\mathrm{m\,sec}$ and has been used again as a platform to characterise the freestream (Dean et al., 2024).

2.3.2 Non-Ideal Effects

As an extension of the shock tube, expansion tubes inherit all of the issues with shock tubes in addition to their unique complexities. For this reason, only the expansion tube specific non-ideal effects are discussed in this section.

Unsteady Expansion & Thermochemical Freezing

Expansion tubes leverage the unsteady expansion phenomenon to achieve a large increase in the freestream total enthalpy. The unsteady expansion begins at the instant of secondary diaphragm rupture, after which the expansion head propagates through the shock heated test gas at the local speed of sound in the inertial reference frame. Through the expansion fan, the gas undergoes a rapid decrease in pressure and temperature until, the rate and duration of the decrease depending on the point at which the gas enters the fan. Rate dependent processes (such as chemical reactions and thermal relaxation) therefore proceed to different points depending on the residence time in the fan.

Figure 2.4 illustrates this point. A wave diagram of a one-dimensional, centred expansion fan is shown with three different particles which enter the fan at different times. Path 1 represents a particle that is close to the secondary diaphragm at the instant of rupture. The residence time in the fan is short and thus rate controlled processes have insufficient time to proceed to equilibrium and are *frozen*. In contrast, path 3 spends a relatively long time in the expansion fan and will have enough time to reach an equilibrium state. The gas that passes between these two paths will be in an intermediate, non-equilibrium

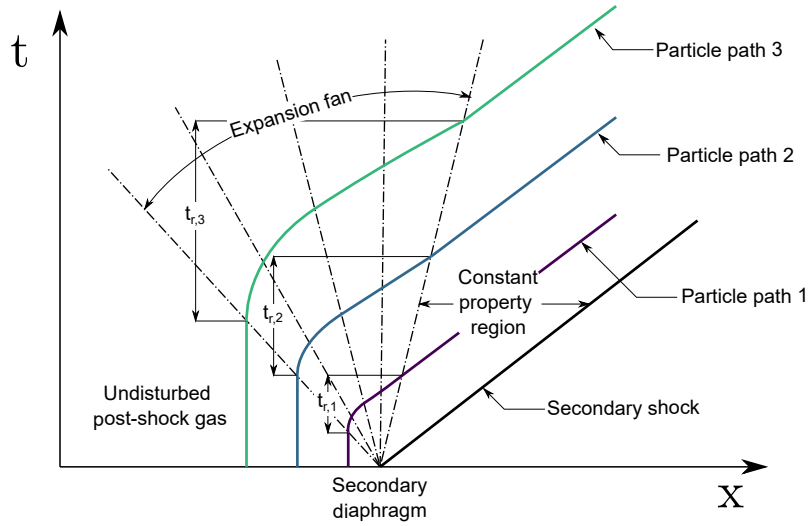

Figure 2.4: Wave process diagram of a centred, one-dimensional unsteady expansion fan adapted from Connor (1967)

chemical and thermal state. This picture is further complicated by the fact that, in the expansion tube, the gas entering the expansion fan is a complex, potentially unknown, non-equilibrium state.

Several authors have studied thermochemistry in expanding flows experimentally and numerically. Initial experimental evidence seemed to suggest that rates of recombination in the expansion fan were different than the corresponding dissociation rates. Until the early 1960's it had been assumed that rates of molecular excitation and relaxation were the same and followed the theory of Landau and Teller (1936). Their model proposed that the vibrational degree of freedom behaves like a harmonic oscillator and was of the form:

$$\frac{dE_v}{dt} = \frac{E_v(T) - E_v}{\tau}$$

Where E_v is the energy contained in vibration and $E_v(T)$ is the vibrational energy which would exist if it were in equilibrium with the translational temperature. τ is an experimentally determined time characteristic. Hurle et al. (1964) published data that appeared to demonstrate that this was not the case in a study of nitrogen chemistry in the context of a reflected shock tunnel. Measurements of vibrational temperature in their nozzle showed that the probability of N_2 vibrational de-excitation was 15 times greater than that predicted by theory.

Holbeche (1964a) was the first to study non-equilibrium phenomena in an unsteadily expanding flow. The apparatus was an expansion tube, though, this description was not in use at the time, that featured a cold H_2 driver which burst a copper diaphragm at 220

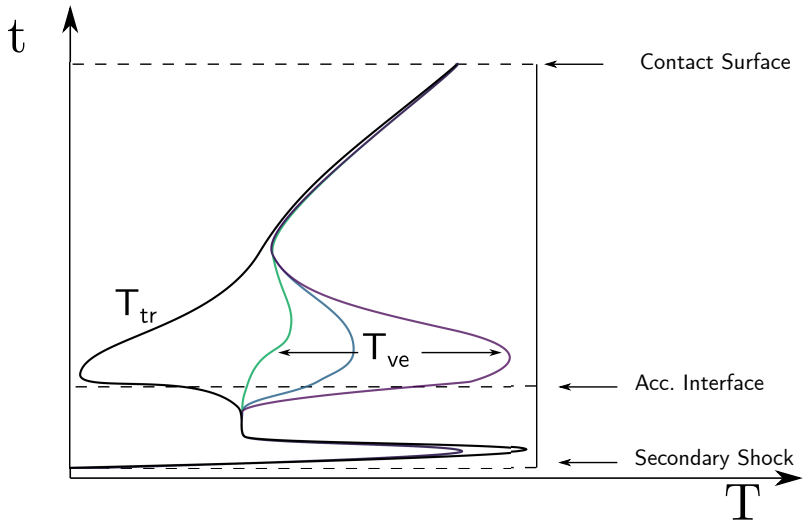

Figure 2.5: Observed shock layer radiation temperature variation through an unsteady expansion wave in shock-heated oxygen, reproduced from Holbeche (1964a)

psi. The test gas, pure O_2 at an initial pressure of 10 torr, was separated from the acceleration tube by a 7 μm aluminium diaphragm. The acceleration tube and dump tank were evacuated to pressures between 10^{-6} and 10^{-5} torr (0.1 to 1 mPa). These experiments were focused on measurement of the vibrational temperature profile of pure oxygen through the expansion wave.

The generalised vibrational temperature behaviour of O_2 as described by Holbeche is that of a *breakaway and subsequent rise* from the frozen to the equilibrium temperature through the expansion wave, which is shown in Figure 2.5. This phenomena occurs because the time constant of the vibrational energy mode is much greater than that of the translational mode and so the vibrational mode requires many more collisions between molecules to equilibrate. Particles at the front of the unsteadily expanded test slug undergo a rapid expansion to a low density and translational temperature where there are relatively few opportunities to collide with other molecules and distribute vibrational energy, thus freezing the vibrational temperature. Progressing upstream through the test slug, the local density and translational temperature increase and sufficient collisions between molecules occur to allow the vibrational temperature to decrease and approach the local equilibrium value. Molecules at the head of the unsteady expansion will be very near to a state of vibrational and translational equilibrium. It should be noted that such qualitative observations must be specific to the test gas and test conditions in use. After these initial experiments demonstrating departures from Landau-Teller, the theory was revised and the vibrational degree of freedom was modelled as anharmonic (Bray, 1968). This model predicted enhanced de-excitation rates which are only significant un-

der extreme non-equilibrium conditions.

In Holbeche's initial experiments, the low density of the flow immediately behind the secondary shock prohibited temperature measurement in the fully-frozen region. It was noted that this issue could be addressed by running with a higher initial fill pressure, however Holbeche did not attempt this as he was concerned about the risk of detonation[4]. The difference between experiment and theory was attributed to the sodium iodide spectrum-line-reversal temperature measurement technique, believed to be *collision limited* at low densities. Holbeche believed that by improving the sensitivity of this technique the issue could be eliminated and also allow extension of the observable temperature range.

It is not clear why Holbeche chose to run with such a low pressure in the acceleration tube in this particular study. Impulse facilities (particularly expansion tubes) were in their infancy at this time and so it is reasonable to conclude that issues with rapid boundary layer growth at low pressures were not well understood. It is likely that Holbeche's measurements were obstructed by large boundary layers (the effects were doubled given that the measurement technique was that of interferometry).

McLaren and Appleton (1970) focused on the fundamental infrared emission band of CO in expanding flows. These authors used an unusual experimental apparatus, effectively a shock tube within but separated from an evacuated chamber by an annular diaphragm. The facility generated a slug of gas in thermochemical equilibrium via a reflected shock process. The pressure rise caused by the reflected shock was sufficient to rupture the diaphragm, allowing the shock heated test gas to unsteadily expand into the vacuum chamber. The authors argued that their technique reduced uncertainty when compared to that of Holbeche since it allowed them to observe a stagnant gas sample rather than one that was in motion (i.e. in the process of being convected downstream past the observation station). McClaren also cited departures from the ideally assumed unsteady, one-dimensional, centred rarefaction wave, caused by the non ideal rupture of the secondary diaphragm and possible boundary layer effects as sources of uncertainty in Holbeche's work. Despite this, they arrived at compatible conclusions, namely that the ratio between forward and backward reaction rates for CO (ϕ_{CO-CO}) was approximately 1 (McClaren reported $1 \leq \phi_{CO-CO} \leq 5$).

Just and Roth (1971) ran CO relaxation rate experiments using an expansion tube setup and found no deviations from values predicted using the Landau-Teller theory.

[4]Due to the usage of pure oxygen as a test gas

These experiments were run at different conditions to other authors, which may have contributed to the agreement with Landau-Teller. They proposed that discrepancies observed by other authors could be caused by the presence of contaminants in the flow (H_2, CO_2, H_2O, etc.) and noted that the purpose of their paper was to report *data having contaminant levels possibly the lowest quoted in the literature*. The was achieved by passing the test gas through a liquid oxygen cooled trap to remove metal carbonyls and by minimising the shock tube leak rate, presented as 7 ppm (presumably per second, although this was not stated). It is noted that diffusion of evaporated H_2O from the shock tube walls could not be measured, however it is likely that this was a significant source of contamination unless preventative measures were taken.

Cleaver and Crow (1973) found no difference between compressing and expanding reaction rates in a study of O_2. Their arrangement was an expansion tube and their measurement technique was that of absorption spectroscopy. These authors also ran with a very low pressure in the acceleration tube, on the order of 10^{-5} torr. This work was extended to CO relaxation by Nasser and Cleaver (1977) in the same research group, where the de-excitation of vibrational energy was found to proceed twice as fast as that behind normal shocks.

Beck and Mackie (1978) performed the first study of a species other than O_2, CO_2, or N_2, namely, I_2 recombination in the presence of an Ar heat bath. The concentration of Iodine molecules formed by recombination in the expansion fan were monitored as a function of time via transmittance measurements. A multi-pass cell was used to obtain four pass of light from a xenon arc lamp across the tunnel centreline which was then focused on the entrance slit of a monochromator set to a wavelength of $493\ \mathrm{nm}$. The authors reported Iodine three-body recombination rate coefficients that were generally in agreement with results obtained via study in the compressing case below temperature of $700\ \mathrm{K}$, however deviations began above this temperature.

Expanding flow experiments have been performed at the University of Queensland (Wei et al., 2017; Gu, 2018; Kelly, 2020) in the X2 expansion tunnel facility. The aim of these experiments was to interrogate the thermochemical behaviour of the test gas, either air, a Mars entry relevant mixture, or Argon, as it passed through a Prandtl-Meyer expansion formed around the corner of a wedge model in the test section. Emission spectra were obtained were obtained in the VUV through to the IR at flow speeds between 2.8 - 4.0 $\mathrm{km\,s^{-1}}$. Gu (2018) reported no complex thermal non-equilibrium effects in the Prandtl-Meyer expansion for the Mars relevant mixture, however it was speculated that

this is because the complex non-equilibrium states form much further downstream than could be measured in the experiment. It was also noted that at lower freestream speeds, the CO_2 number densities derived from Pitot pressure measurements were factors of 4 – 5 greater than those obtained from the spectroscopy measurements. Gu suggests that this is due to a poor understanding of the non-equilibrium processes occurring through the unsteady expansion.

Tibère-Inglesse et al. (2022) have recently examined expanding air flows in the EAST facility. Measurements of the radiating test gas were made via emission spectroscopy through a rectangular window installed downstream of a conical expansion nozzle. The test conditions targeted high speed Earth entry with a freestream pressure of 0.2 torr and final shock speeds between 9.47 and 11.11 $\mathrm{km\,s^{-1}}$. Large shock curvature was observed with two spatial *peaks* in radiance evident due to this effect. Species number densities were deduced by spectrally fitting the experimental data at several spatial points. These were compared to results from an axisymmetric CFD simulation of the facility. Under prediction of radiation in the UV region was attributed to a under prediction of N_2^+ number density by the CFD, in turn caused by incorrect temperature predictions. The authors also cited difficulty in determining the extent of the test time due to uncertainty in the arrival time of the driver gas. This flow-field shares many of the complexities encountered in the X2 NRST mode, however it is perhaps the most complete spectral dataset for expanding flows with data available from 162 - 1423 nm for some tests. It seems plausible that some of the temperature discrepancy observed could be attributed to shock deceleration in the driven tubes, with a static inflow (presumably equilibrium although this is not stated) inflow condition at 10.2 $\mathrm{km\,s^{-1}}$ used. The authors also cite the need for improved thermochemical rates as a possible cause for the discrepancy.

Finally, Gu et al. (2023) performed a purely numerical study of the effect of thermochemical non-equilibrium in the expansion tube freestream. Gu used the L1d code to examine several expansion ratios in a fictitious expansion tube. Gu named non-equilibrium in the unsteady expansion as the most influential process affecting the expansion tube test flow. Large changes to the magnitude (> 100 %) and temporal variation of flow properties occur depending on the degree of freezing occurring. The simulations in this work were entirely inviscid which is acknowledged by the author as a major disadvantage given the importance of boundary layer growth on the test slug properties, particularly in the low pressure acceleration tube. For this reason it is questionable what applicability these results have to a real expansion tube.

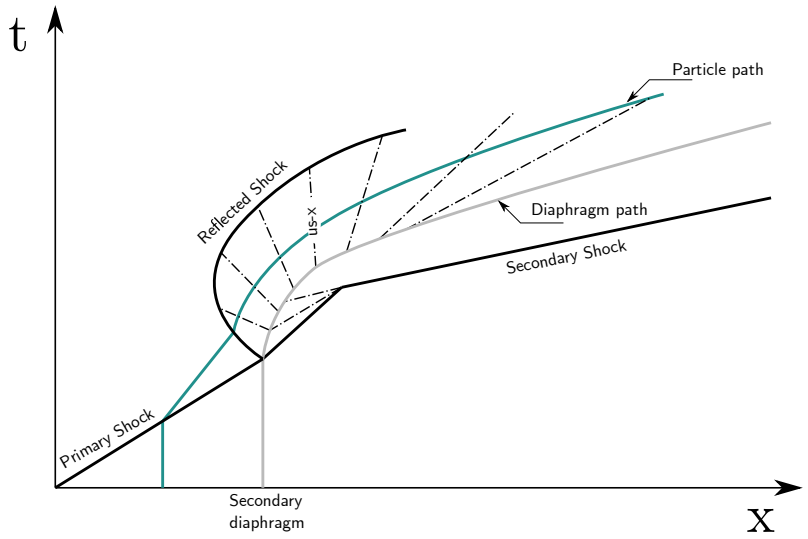

Figure 2.6: Wave process diagram of an expansion tube with a reflected shock formed at the secondary diaphragm, adapted from Bakos and Morgan (1994)

Non-Ideal Secondary Diaphragm Behaviour

Much like the primary diaphragm discussed in Section 2.2.2, the secondary diaphragm is also known to behave non-ideally. A variety of materials may be used for the secondary diaphragm with perhaps the most common being Mylar, cellophane, and aluminium foil. The secondary diaphragm needs only to withstand the static loading of the pressure differential between the shock tube and acceleration tube pre-test (typically no more than $1\ \mathrm{bara}$) and so can be relatively light (thickness on the order of $< 25\ \mu\mathrm{m}$). Nevertheless, the interaction between the diaphragm and the flow can cause significant deviations from ideal theory.

Miller III (1975) observed in early experiments in the Langley expansion tube that it was necessary to account for the test gas momentum losses caused by entrainment of secondary fragments in the core flow to accurately predict test gas properties. The possibility that the secondary diaphragm could cause a reflected shock to form was also considered. Neely and Morgan (1994) developed a one-dimensional wave diagram for the secondary diaphragm rupture and later Bakos and Morgan (1994) showed that reflected shock formation at the secondary diaphragm affected the recombination thermochemistry in the unsteady expansion. Figure 2.6 shows a representative wave process diagram for an expansion tube where a reflected shock forms at the secondary diaphragm. Here, some portion of the test slug is shocked a second time and undergoes more chemical dissociation and excitation before entering the unsteady expansion fan and relaxing to the final freestream state.

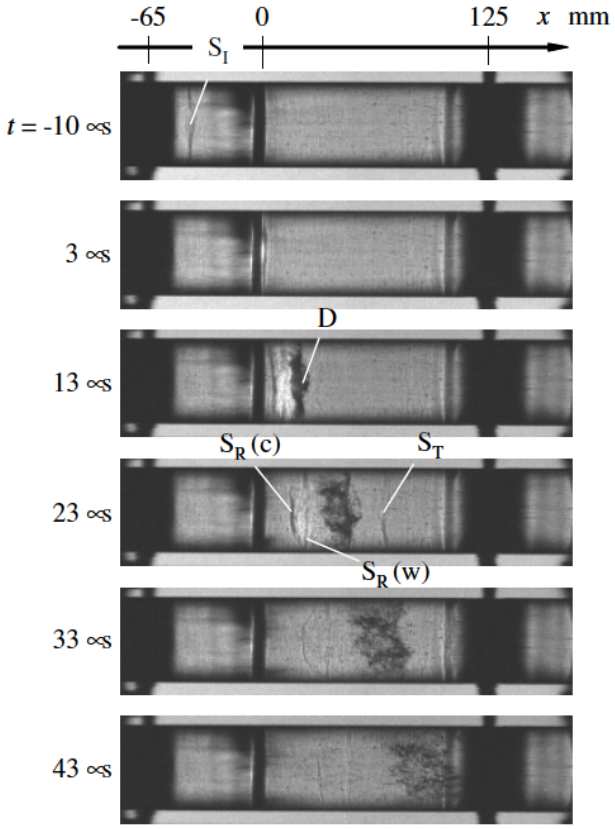

Figure 2.7: Shadowgraph images of the rupture of a 23 µm cellophane secondary diaphragm in the JX-1 expansion tube. S_I denotes the incident shock, $S_R(c)$ is the centre of the reflected shock, $S_R(w)$ is the reflected shock at the tube wall, S_T is the transmitted shock.

This phenomenon has been investigated experimentally by several authors. Roberts et al. (1995) studied the effect of secondary diaphragm thickness on flow quality in expansion tubes, finding that minimizing diaphragm thickness minimized the level of free stream disturbances. Wegener et al. (2000) visualised the rupture of a cellophane diaphragm in the X1 expansion tube by means of holographic interferometry. The found that the diaphragms tended to fail by shear at the periphery rather than rupture at centre due to the impulse nature of the loading by the primary shock. Furukawa et al. (2007) used a shadowgraph technique in the JX-1 expansion tube to visualise the diaphragm rupture process, an excerpt of their work is shown in Figure 2.7.

Figure 2.7 shows the complex interaction between the primary shock and the secondary diaphragm as it progresses with time. It is interesting to note that the reflected shock is highly two-dimensional, a fact that introduces further complexity to the problem of determining the freestream properties. Furukawa et al. observed qualitatively smaller free stream disturbances when using thinner diaphragms which is consistent with the

findings of Roberts et al. Furukawa et al. also made pressure measurements via transducers located perpendicular to the flow in the wall of the facility. Significantly lower pressures were observed in the immediate post-shock state when thinner diaphragms were used (the region affected by the reflected shock) but pressures further downstream were consistent between tests for a given test condition.

The use of a secondary diaphragm can also chemically contaminate the free stream in cases where real gas effects are large. Miller et al. (2014) find that secondary diaphragm fragments may readily entrain in the flow, increasing noise in pressure sensor measurements. It stands to reason that, given sufficient residence time in the test gas, small fragments are particulates originating from the secondary diaphragm may react chemically with the free stream gas and in doing so change the free stream chemical state.

Complex Boundary Layer Growth & Transition

The initial pressure in the acceleration tube tends to be low to facilitate the unsteady expansion which can lead to formation of a thick boundary layer. In extreme cases, expansion tubes are susceptible to the phenomenon of *test gas necking*. Gildfind et al. (2018a) provide a complete description of this process. Gas from the accelerator slug tends to be swept past the test/accelerator gas contact surface and into the boundary layer. This can cause the boundary layer to grow so large that the core flow completely collapses. Gildfind et al. find that, as might be expected, the effect worsens the further the test gas travels from the secondary diaphragm, making it desirable to truncate the acceleration tube before the core flow collapses.

The growth of the boundary layer is likely to have an effect on the core flow properties (even before complete collapse occurs) due to the reasons presented by Mirels (1966). To the author's knowledge, no validated analytical correlation or numerical tool exists for prediction of the expansion tube boundary layer state.

Boundary layer transition is also known to occur in the acceleration tube under certain circumstances. This can significantly change the boundary layer thickness and further influence the test slug properties, as shown in Figure 2.8. Prediction of boundary layer transition in hypersonic flow is an active research area for even a uniform free stream, however the problem is further complicated in the expansion tube due to the non-uniform unsteady expansion process. In practice this means that it is not appropriate to predict transition based on a Reynolds length as may be done for a flat plate. Weilmuenster (1974) developed an integrated approach to calculating Reynolds number

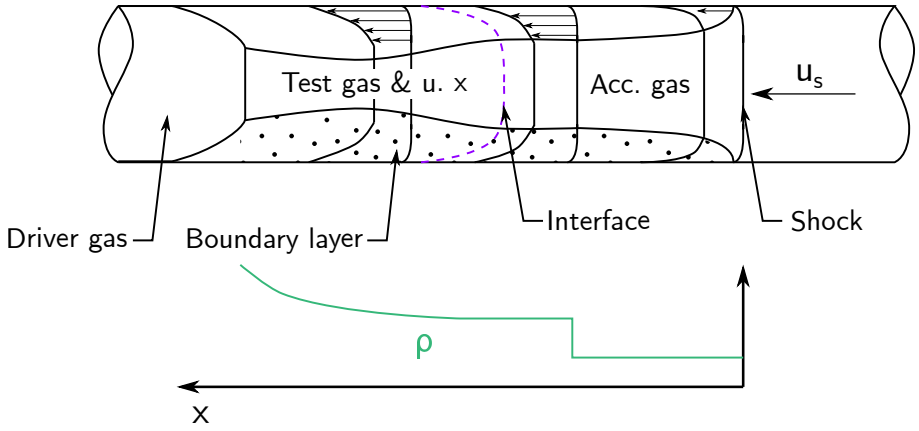

Figure 2.8: Boundary layer development in an expansion tube, adapted from McGilvray (2008)

in the context of an expansion tube in an effort to explain experimental Pitot pressure measurements in the Langley expansion tube. This approach indicated that a constant transition Reynolds number of 40×10^6 was appropriate to predict transition in the facility, although the authors cautioned against extrapolating this finding to other facilities with different geometries and surface roughnesses.

Upstream Wave Processes

Expansion tube test flows can be strongly influenced by waves originating from the driver. Under certain circumstances, these waves can shorten or destroy the test time. Paull and Stalker (1992) provide a complete summary of the factors limiting test time in an expansion tube. At high-enthalpy expansion tube test conditions[5], the test time is limited either by the downstream edge of the unsteady expansion or the downstream edge of the reflection of the upstream edge of the expansion off the driver-test gas interface. In the first case, assuming constant shock speed, the test time can be calculated with:

$$\tau = \frac{x_A a_7}{u_7(u_7 - a_7)} \tag{2.5}$$

Where x_A is the length of the acceleration tube, u_7 is the unsteadily expanded test gas velocity in the lab reference frame, and a_7 is the unsteadily expanded test gas speed of sound. In the second case, the test time is dependent on the time taken for the reflected expansion wave to emerge from the expansion. This time is given by:

$$t_1 = t_0 \left(\frac{a_7}{a_2}\right)^{\frac{\gamma+1}{2(1-\gamma)}} \tag{2.6}$$

[5]A threshold for *high-enthalpy* is not defined in the reference

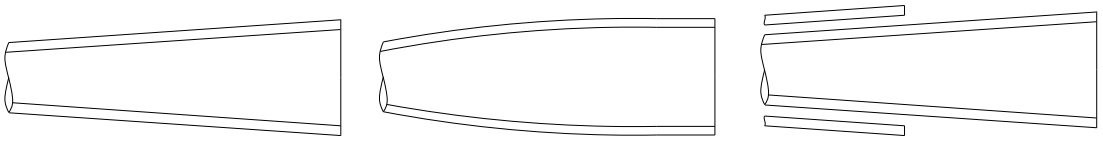

(a) Conical nozzle (b) Contoured nozzle (c) Skimmer nozzle

Figure 2.9: Common nozzle geometries

Here, the subscript 2 represents the shocked (but not expanded) test gas state and γ is assumed to be the quiescent value. The parameter t_0 represents the time between rupture of the secondary diaphragm and arrival of the unsteady expansion at the driver/test gas contact surface. This value can be estimated by calculating the Mirels slug length of the test slug at the point of secondary diaphragm rupture and then assuming that the contact surface moves with constant velocity, u_2, after diaphragm rupture. As discussed in Section 2.3.1, a failure to design test conditions with a sufficient acoustic buffer (the ratio a_7/a_2) severely limited the utility of early expansion tubes.

Expansion Nozzle

Inclusion of an expansion nozzle in the expansion tube flow cycle offers the experimenter an improved core flow size, allowing larger, higher fidelity models to be tested. Some typically expansion nozzle geometries are shown in Figure 2.9. This allows the experimenter to directly increase L in the ρL scaling parameter (discussed in Section 2.3.1), thereby increasing the performance envelope of the facility. Such a device adds another layer of complexity to the flow as it is now processed by a steady expansion. These nozzles are modelled on a test-to-test basis by using an ideal expansion process through an effective area ratio[6]. Axisymmetric CFD simulations are also tuned to match experimental observations of Pitot pressure, an example of this is included in Steer et al. (2024b).

[6]To account for the boundary layer in the nozzle

2.4 Diagnostic Techniques for Non-Equilibrium Flows

A variety of experimental techniques and instrumentation are available to characterise impulse facilities. Techniques for determining properties of particular interest in non-equilibrium flows, such as temperature and species number density, are reviewed in this section.

2.4.1 Emission

At the simplest level, measurements of the radiation emitted by a gas in the laboratory provide direct information about the level of radiative heating that might be expected in flight. However, the emission spectrum of a radiating gas also provides a wealth of information about chemical composition and thermal state. A complete summary of the possibilities of spectroscopy is provided by Thorne et al. (1999), only a brief discussion is presented here.

Spectrally Integrated Techniques

Perhaps the simplest way to measure radiative heat flux is with an integrated technique. *Spectrally Integrated* refers to a measurement that is summed or averaged over a range of wavelengths, rather than being specific to a single wavelength. Measurements from a high speed or conventional camera, shown in Figure 2.10, constitute spectrally integrated measurements. These techniques can be calibrated against a light source of known intensity and if the solid angle of the measurement device is known, the radiative heat flux may be determined. If coupled with a bandpass filter or similar the system can be used to target a particular spectral feature, provided that the measurement device responds adequately in the region of interest. Spectrally integrated techniques are useful for flow visualisation and for high level validation of numerical models, however they cannot be used to deduce the detailed thermochemical state of the flow. Spectrally integrated measurement techniques are commonplace in the literature and many examples are available.

Spatially Integrated Techniques

Measuring radiation at a single point[7] is desirable when a direct line of sight is not possible. This may be due to geometrical limitations, for example a desire to measure inside the bore of a shock tube, or because reabsorption of radiation is strong, for example the

[7] In the context of this chapter, a *single point* measurement is a measurement of the radiation or heat transfer incident on the surface of a measurement device that is not spatially resolved

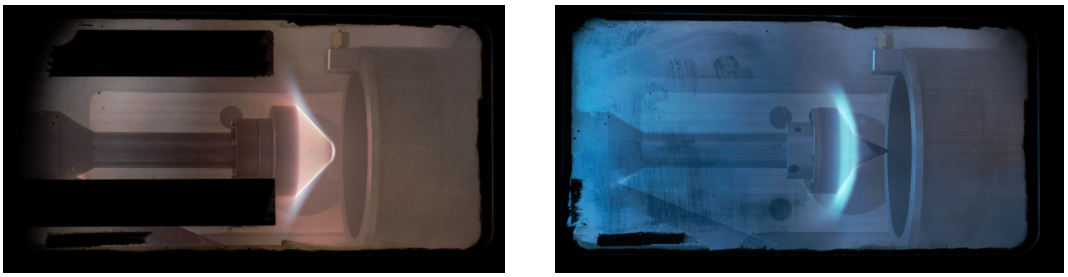

(a) H_2-He at 18 $\mathrm{km\,s^{-1}}$ (b) N_2-O_2 at 9 $\mathrm{km\,s^{-1}}$

Figure 2.10: Example images of radiating flow fields around sub-scale models in the T6 expansion tunnel taken by the author

need to measure radiative heat flux on a model surface when the flow is optically thick[8]. Single point measurement devices can be compact, allowing them to be installed in flight vehicles.

Photodiodes and photomultipliers (PMTs) offer the ability to make measurements at a high sampling frequency and signal to noise ratio. These devices convert incident photons into a voltage or current via the photoelectric effect which may be recorded by an external data acquisition system. The incident light may be filtered to target a particular spectral feature, or can be broadband to provide a bulk radiance measurement. PMTs offer superior sensitivity to photodiodes by means of an electron multiplier. An electron multiplier is comprised of numerous electrodes known as dynodes. When electrons are emitted from the photo-cathode, they are accelerated by the voltage across the focusing electrodes, striking the secondary emissive surface of the initial dynode, which generates secondary electrons. This cycle recurs across all dynodes within the electron multiplier, resulting in signal amplification of up to a million times.

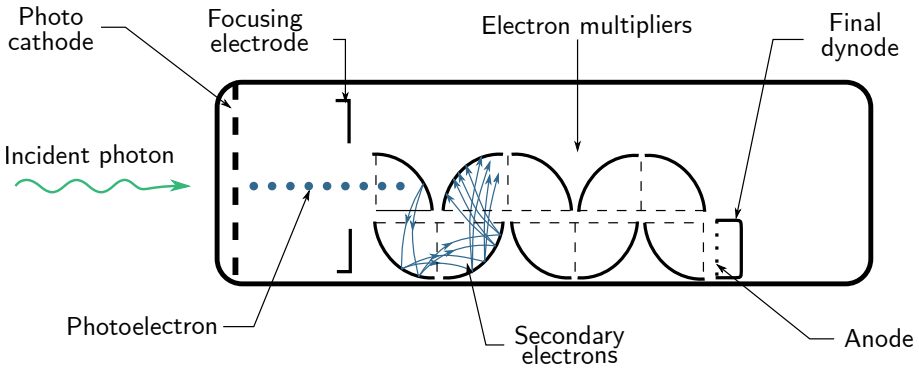

Figure 2.11: Operating principle of a photomultiplier tube.

Photodiodes and photomultipliers have been used extensively in high speed flow applications and a full review of this is not attempted here, however several studies are

[8] A medium is considered optically thick if it absorbs or scatters most of the radiation passing through it, preventing significant transmission

referenced as examples. James et al. (2021) have used photodiodes in place of pressure transducers to determine shock arrival in impulse facilities. This offers an advantage in high speed, low pressure flows. In this regime, the response time of the pressure transducer (typically ≈ 2 µs) can be large compared to the flow timescale and the post-shock pressure is small, resulting in a small signal to noise ratio in the pressure measurements. Such a system may be intensity calibrated to provide point measurements that can be compared to an OES system (Cooper and Borucki, 1973). Spectral filters may also be used to target a particular spectral feature.

Fibre optic cables can be readily used as collective optics. Fibre optics may be installed in difficult to reach areas but then be coupled to a higher fidelity, spectrally resolved measurement system. This technique has been used by Leibowitz and Austin (2019) to measure mid-wave infrared CO_2 radiation incident on the surface of a subscale MSL model in the HET. Fibre optics were embedded in the model at 0° at 16° angle of attack and then coupled to an infrared spectrometer. The data showed good agreement with numerical simulation, however they were limited by the relatively large solid angle of the fibre optics. Leibowitz also used this technique to make measurements of the expansion tube freestream and noted a significant decrease in radiance as the expansion fan passed through the field of view.

Integrated measurements need not utilise a photodiode or photomultiplier as a detector. Capra and Morgan (2012, 2013) developed total heat transfer gauges to be used in the X1 expansion tube. The gauges consisted of type-E thermocouples recessed below the model surface behind a transparent window and air gap. By accounting for the geometry of the installation and thus deducing the field of view (solid angle) of the thermocouple, the incident radiative heat flux could be determined. This technique is attractive because of its relative simplicity, however it does not offer an option to spectrally resolve the data save for using a spectral filter. A similar technique has been used to provide data for flight cases, most recently for the MSL (White et al., 2013) and Mars 2020 (Hwang et al., 2016) missions.

Optical Emission Spectroscopy

Optical emission spectroscopy (OES) is a commonplace technique for examination of radiating flows. OES has been used successfully for many years in shock tubes (Cruden et al., 2009; Collen, 2021), expansion tubes/tunnels (Collen et al., 2019), remote observations (Birch et al., 2022), and many other applications. OES systems are relatively simple,

provide spatially and spectrally resolved information, and can be applied in a variety of facilities.

OES systems typically consist of collective optics, a spectrometer, and a camera. The collective optics may be an arrangement of mirrors to provide a wide field of view of the area of interest, or a fibre optic cable to interrogate a single location[9]. Light reaching the spectrometer passes through the entrance slit, which functions as an aperture and allows the user some control over the ultimate spectral resolution of the system. The object light then interacts with a diffraction grating which disperses the light into its component wavelengths. The resolution that can be resolved by a given diffraction grating is determined by the density of grooves on the reflecting surface, typically given per mm. A higher groove density results in a finer spectrum. Finally, the dispersed light is recorded, typically an intensified CCD camera. Given a camera sensor with sufficient pixel density, it is possible to resolve both spatial and spectral axes. Calibrated results from an OES system may then be three dimensional, having a spatial, spectral, and intensity axis.

OES systems are limited in terms of achievable signal to noise ratio and spatial resolution by the camera. These are determined in large part by the camera exposure time or gating time. Modern intensified sCMOS cameras limited to relatively low frame rates[10] and are only able to capture a single frame during a typical test time for an impulse facility. To achieve sufficient signal during this single exposure, it is often necessary to select a gating time that is large, however in a shock tube, this can lead to spatial smearing of the image as the shock moves during the gating time. This fact is less relevant when applied to a model test where the shock is not expected to move significantly relative to the camera during the exposure time. Spatial smearing on the order of 2 - 3 mm is typical for a shock tube (Collen, 2021).

Techniques to circumvent this limitation are presently of interest in the hypersonics community. Ravichandran et al. (2021) coupled an intensifier to a high speed camera to resolve flow in the PWK1 plasma wind tunnel facility. Later, Lu et al. (2022) used a similar arrangement and coupled a V2012 Phantom camera to HiCATT 25 intensifier and SP2300 spectrograph to image flow in the X2 expansion tunnel at 100 kHz. The exposure time of the camera was 9.5 $\mu\mathrm{s}$, sufficient to interrogate the stagnation line of a sub-scale model but not applicable to a shock tube where test times are typically less than 10 $\mu\mathrm{s}$.

Streak cameras provide an option to capture temporally and spectrally resolved data at a single point. Streak cameras feature a photo-cathode and electron multiplier, similar

[9]For example, mounted in a sub-scale model to measure the radiation incident on the surface

[10]The Andor iStar sCMOS has a maximum from rate of 50 Hz

to that used in the photomultiplier tube (see Figure 2.11). The electrons produced by the photo-cathode then pass through a voltage divider before registering on a phosphor screen. By changing the voltage across the divider with time, the path of electrons is deflected depending on the time of entrance to the streak camera. When the streak unit is coupled to a spectrometer, this results in an image with wavelength as one axis and time as the other. Rond et al. (2007) used a streak camera in the TCM2 shock tube to measure post-shock radiation for Titan entry relevant conditions. This method offers superior temporal resolution with a minimum streak time of 10 ns.

With a sufficiently resolved emission spectrum, it is possible to deduce information about the temperature and species number densities of the sample (Thorne et al., 1999). These properties can then be used to determine reaction rates for a given gas mixture. The translational temperature, T_T, describes the kinetic energy of particles in the sample. The translational temperature is usually found by examining the Doppler broadening of a spectral line. The width of this broadening (often characterized by the full width at half maximum, FWHM) is directly related to the translational temperature of the gas. By fitting the observed line profile with a Gaussian function and comparing it to the known rest wavelength of the line, the translational temperature can be calculated.

The rotational temperature, T_R, reflects the distribution of molecules among different rotational energy levels. In molecular gases, rotational transitions are observed as a series of closely spaced lines in the emission spectrum, often in the microwave or far-infrared regions. By examining the relative intensities of these rotational lines, one can determine the rotational temperature. A similar technique can be applied to determine the vibrational temperature, T_V, except of course using vibrational emission features.

The intensity of a spectral line in emission is determined by the population of the excited state and the probability of transition to a lower level. The state populations are related to temperature [11] and the transition probability is determined by the Einstein coefficient (which is known). Thus, if the intensity of a spectral line is known it is often possible to deduce the number density of the species associated with that transition. This is usually achieved by comparing the result to a radiation modelling tool.

Finally, the electron number density may be determined by measuring the Stark broadening of a given atomic line. Stark broadening is the broadening of an atomic line due to the non-homogeneous distribution of charge in a plasma and resulting electric field. This field changes the electrostatic potential between states in an atom, leading to slight

[11] In equilibrium they can be modelled by a Boltzmann distribution

deviations in the wavelength of photon emitted if an electron transitions between these states. The shape of the distribution of change in wavelength for some atoms, such as the H atom, is known and is directly related to the electron number density. Cruden et al. (2012) gives an approximate relation between the Lorentzian width of the distribution and the electron number density:

$$n_e = 9.87 \times 10^{16} w_{L,\alpha}^{1.65} \tag{2.7}$$

It should be noted that several other broadening mechanisms are at play that must be accounted for. A summary is provided in Appendix C of Collen (2021).

2.5 Effect of Non-Ideal Fluid Mechanics on Thermochemical Rate Measurements

A major application of both shock and expansion tubes is the study of thermochemical reaction rates for use in large scale numerical models. The reaction rates, k[12], are a strong function of temperature and are often expressed in the Arrhenius form:

$$k = AT^n e^{-\frac{E}{RT}} \tag{2.8}$$

Where A is a pre-exponential coefficient, n is a non-dimensional power, E is the activation energy for the reaction, R is the universal gas constant, and T is a temperature. The temperature used in this equation depends on the chemical reaction. In practice, the parameters A and n are obtained by performing many 1D, inviscid post-shock chemical relaxation simulations and selecting the best fit to experimental observations. The simulation methodology and the definition of *best fit* varies depending on the source.

This approach requires knowledge of the particle time of flight which can be significantly altered from the constant value that is assumed by an inviscid simulation approach due to the effects discussed in Sections 2.2.2 and 2.3.2. Consider Figure 2.12a which shows the time of flight of a particle versus distance post-shock for several prediction methodologies. All cases assume freestream conditions of a 10 $\mathrm{km\,s^{-1}}$ shock wave in 13.3 Pa of air. The diameter is 100 mm for the shock tube cases. The inviscid or Rankine-Hugoniot approach, i.e. assuming constant post-shock velocity, is shown to under-predict the time of flight calculated considering boundary layer effects. For example, the viscous time of flight is underpredicted by 36 µsec at 30 mm post-shock or by 42%. If reaction rates were optimised against real shock tube data[13] using an inviscid 1D model for this case, a particle at 30 mm post-shock would erroneously be believed to have been in flight for 42% less time than in reality, leading to a deduced reaction rate that is 42% faster than required.

Non-uniform shock speed also significantly change the particle time of flight (Tibere-Inglesse et al., 2024) and is this effect is shown in Figure 2.12. Two cases of linear shock acceleration and deceleration of 500 $\mathrm{m\,s^{-1}\,m^{-1}}$, but still arriving at the same final speed of 10 $\mathrm{km\,s^{-1}}$, are presented. The particle time of flight is 45% lower and 120% higher than the constant value by the end of the test slug for the decelerating and accelerating cases, respectively. However, the start of the test slug is not as strongly affected. It should be noted that other variables such as the diameter of the shock tube, the fill pressure, and

[12] Usually expressed in units of $\mathrm{cm^3/mol/sec}$

[13] Assuming the shock speed is constant throughout the trajectory

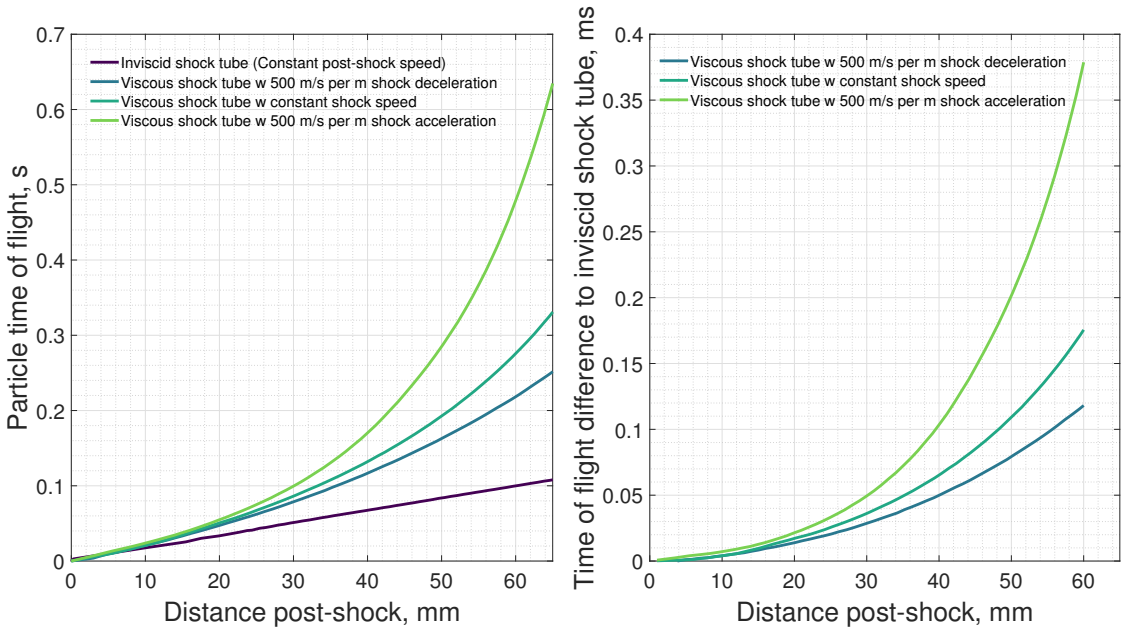

(a) Time of flight

(b) Difference

Figure 2.12: Time of flight of particles post-shock predicted by several methods. Reproduced from Clarke et al. (2023b)

test gas composition can strongly affect the particle time of flight. The reader is directed to Clarke et al. (2023b) for a comprehensive demonstration of these effects.

In a real shock or expansion tube experiment, the particle time of flight is more complex than shown in Figure 2.12 as the shock trajectory is often not well described by a linear trend. Therefore, the use of numerical modelling that includes as much detail as possible is required to account for the complex hydrodynamic processes taking place and thus allow accurate determination of thermochemical reaction rates. The next section is dedicated to a review of some methods available for impulse facility modelling in the open literature.

2.6 Numerical Modelling of Impulse Facilities

In light of the discussion so far in this chapter it is clear that shock and expansion tube flows are not straightforward. It follows that a variety of approaches to numerical simulation of these machines have been taken, each with strengths and weaknesses. Major objectives of this thesis are to develop an improved shock tube solver that can later be extended to expansion tubes, hence a review of the state of the art in numerical impulse facility modelling is required.

This section is comprised of two parts entitled *a-priori* and *a-posteriori*. These terms refer to two approaches to simulation of impulse facilities. A-priori tools use measurements of the facility before the experiment takes place as inputs whereas a-posteriori tools use experimental results as inputs, hybrid approaches are also possible.

2.6.1 A-priori

A variety of approaches have been taken to model shock tube flows, a summary of the key features of several is include in Table 2.2. Perhaps the simplest approach is state-to-state[14] or 0D modelling. These codes use a minimum number of inputs, for example initial pressure and shock speed, and make an ideal gas or equilibrium assumption to define the full flow properties. One of the earliest examples of these codes is the Equilibrium Shock Tube Conditions (ESTC) code which was later re-implemented in ESTCj (Jacobs et al., 2014). This code utilises CEA (McBride, 1996) for thermochemical properties and allows modelling of many simple flow processes found in pulse facilities including normal shocks, oblique shocks, steady and unsteady expansions. The capabilities of ESTCj form the basis for PITOT (James et al., 2018), which is intended as a *virtual facility* state-to-state code to allow rapid flow condition development. PITOT began as an equilibrium gas expansion tube solver but it now allows modelling of many types of facilities including shock tubes/tunnels and reflected shock tunnels. State-to-state solvers are convenient for simple calculations but by definition cannot and are not intended to account for additional complexities arising in impulse facilities. For example, state-to-state solvers assume constant shock speed in all processes, which is not the case in reality.

1D models offer improved resolution of the test slug properties at a higher computational cost. L1d (Jacobs, 1994), a quasi-one-dimensional Lagrangian CFD code designed to simulate free-piston driven impulse facilities, is one such example. This code simu-

[14] In this thesis *state-to-state* is intended to mean, unless otherwise stated, a method for modelling a thermodynamic cycle where the properties at each stage or state in the cycle are considered constant and transitions between stages or states are assumed to occur via ideal thermodynamic processes

lates transient flow processes in the facility including piston dynamics. Gas slugs along the length of the tube are discretized axially into fixed mass *slices* whose properties are tracked over the course of the simulation. Heat transfer and friction are modelled at the tubes walls, although the boundary layer is not simulated explicitly. L1d may be tuned to match experimental results, for example static pressure traces, by variation of one or more loss factors which account for non-ideal processes such as primary diaphragm rupture and flow through the orifice constriction between the driver and driven tubes. This approach has proved successful in many cases, examples include McGilvray et al. (2009); Gildfind et al. (2018b), however difficulty has been encountered in accurately matching properties at the acceleration tube exit.

Sharma Priyadarshini et al. (2018) developed a quasi-one-dimensional shock tube methodology and applied to the EAST facility. The methodology employs a source term to model the boundary layer growth that is scaled on a case by case basis to match the shock deceleration seen in the experiment. Results from these simulations provided an improved agreement with experiment when compared to a constant shock speed, equilibrium assumption, however the slug length predictions were incorrect due to the boundary layer source term implementation.

Full facility, 2D axisymmetric and 3D simulations offer the highest fidelity models of impulse facilities. Many codes with these capabilities are in use, such as Eilmer 4 (Gollan and Jacobs, 2013) and US3D (Candler et al., 2015). In general terms, these codes solve compressible Navier-Stokes equations over the flow domain subject to customizable user defined boundary conditions. Many turbulence models, reaction schemes, grid structures, and numerical methods are at the disposal of the user. Excellent agreement is obtained between experiment and simulation for a wide variety of test cases with such codes and they are an indispensable tool in hypersonics research, particularly for interplanetary vehicle design. Despite these advantages, like the other methods mentioned, these codes struggle to predict shock speed non-uniformity in impulse facilities.

Gildfind et al. (2018b,a) provide an excellent example of the typical approach taken to high-fidelity expansion tube/tunnel modelling for the X3 facility. Nompelis et al. (2004) provide an example for the LENS-XX facility. Chandel et al. (2019) provide an example of full facility modelling of the EAST using US3D. In these three example cases and generally speaking, the full-facility a-priori approach does not produce a shock speed profile that matches the experimental observations. This occurs because an a-priori approach fundamentally cannot accurately model all of the non-ideal processes that take

place in the facility, in particular the highly complex driver behaviour and boundary layer growth. This reality motivates the development of *a-posteriori* numerical methods.

2.6.2 A-posteriori

A-posteriori approaches use experimental observations use experimental observations such as the shock speed as boundary conditions for the simulation. This is done in an effort to decouple the thermochemistry from the underlying fluid mechanics. Several examples of a-posteriori numerical simulations are discussed in this section.

Several methods have been developed specifically to address modelling of the thermochemical non-equilibrium in shock tubes. Such methods typically solve one dimensional Navier-Stokes equations coupled to a finite rate chemistry model with the immediate post-shock, frozen gas state as a boundary condition. The gas is then allowed to thermochemically relax to an equilibrium state over a time governed by the chemistry model utilised. The POst SHock relAXation solver or POSHAX (Gollan, 2007, 2008) solves for post-shock thermochemistry subject to a Rankine-Hugoniot assumption or constant post shock velocity. This tool has been used by a variety of sources to analyse experimental results (Glenn et al., 2022; Potter, 2011; Collen et al., 2022), however boundary layer growth in shock tubes is seen to strongly affect the post shock velocity profile which limits the applicability of the code to experimental cases (Clarke et al., 2023b). The approach of relaxing the gas from a predetermined post shock state also neglects the effects of diffusion and does not allow the user to resolve the shock structure. The Non-Equilibrium Shock Solver (NESS) is a similar tool models the shock tube in cylindrical coordinates and solves the two-dimensional, two-temperature Navier-Stokes equations to resolve the post shock state. This approach allows the shock structure to be resolved and direct comparison to experiment is possible by implementation of a radial source term that mimics mass removal by the boundary layer. By variation of the radial velocity source term, the code may be applied to other geometries, such as the stagnation line of a blunt body with the correct particle time of flight achieved. In the shock tube case, NESS operates under the assumption of constant shock speed, which means that in cases of strong shock speed non-uniformity its predictions are likely to deviate from experiment.

Bensassi and Brandis (2019) illustrate a popular approach to modelling post-shock non-equilibrium relaxation known as the *stagnation-line* approach. Here, the stagnation line of flow over a cylinder is taken to be equivalent to the flow behind a shock wave in a shock tube. The radius of the cylinder is chosen to be large enough that edge effects

do not influence the stagnation line. This approach is independent of the physical model used, however the citation in question used the CoolFluid (Lani et al., 2005) package. The approach has been utilized in a variety of publications (Cruden et al., 2012; Brandis and Cruden, 2018; Brandis et al., 2010) with generally mixed agreement with the experimental measurements seen. This has been attributed to measurement error, the effect of shock speed uniformity, and fundamental limitations of the approach. Clarke et al. (2023b) later showed the discrepancy to be due in part to incorrect time of flight.

Petersen and Hanson (2001) developed a time-marching model to account for the effects of non-uniform shock speed and boundary layer development on the entropy in a shock tube experiment. Only small variations in shock speed were considered toward the end of the experimental trajectory, with a constant value assumed for the first 80% of the simulation. This severely limited the results, however qualitative agreement was seen with the experiment.

Satchell et al. (2022b,c) developed a model known as LASTA 1.0 specifically to account for shock speed non-uniformities in shock tube flows. LASTA 1.0 predictions show excellent agreement with experimental data and confirm the importance of shock speed variation in shock tube experiments. LASTA 1.0 solves coupled mass and energy conservation equations for each Lagrange, however conservation of momentum is never ensured. For a constant shock speed case, post-shock momentum is constant and so this treatment does not lead to error. However, for a strongly decelerating shock trajectory this can manifest as a non-physical drop in pressure toward the rear of the slug as slices at the rear travelling faster are not able to communicate their momentum for pressure with other slices toward the front. This is addressed indirectly in LASTA 1.0 by imposing a constraint on the Lagranges that pressure must not decrease moving upstream from the shock, which follows the observation in Satchell et al. (2022a) that static pressure traces behind shocks increase monotonically until the contact discontinuity, even for strongly accelerating or decelerating trajectories. While this approach is adequate for many shock tube cases, it precludes the use of LASTA 1.0 to model expansion tube experiments where test gas properties are strongly affected by expansion waves originating from the driver. LASTA 1.0 is also limited to an assumption of thermochemical equilibrium.

Table 2.2: Comparison of the capabilities of several widely used shock tube modelling tools

Code	A-priori / A-posteriori	Dimensionality	Non-Eq	Boundary Layer	Shock Trajectory	Cost
ESTCj [1]	Both	0D	N	N	N	$
PITOT [2]	Both	0D	N	N	N	$
L1d [3]	Pre	1D	Y	~	N	$$$
NESS [4]	Both	Quasi-1D	Y	~	N	$
POSHAX [5]	Pre	Quasi-1D	Y	~	N	$$
Eilmer 4 [6]	Pre	2D / 3D	Y	Y	N	$$$$$
US3D [7]	Pre	2D / 3D	Y	Y	N	$$$$$
FROSST [8]	Pre	2D	N	Y	N	$$
LASTA 1.0 [9]	Post	Quasi-1D	N	~	Y	$

[1] Jacobs et al. (2014), [2] James et al. (2018), [3] Jacobs (1998), [4] Clarke et al. (2023a), [5] Gollan (2007), [6] Gibbons et al. (2023), [7] Candler et al. (2015), [8] Satchell et al. (2021), [9] Satchell et al. (2022b,c)

2.7 Summary

This chapter contained a review of shock tubes, expansion tubes, and methods of their characterisation, both experimental and numerical. Although appearing simple at a surface level, test flows produced by shock and expansion tubes are complex and affected by a number of non-ideal processes. These non-ideal processes have the cumulative effect of significantly changing the hydrodynamic behaviour of the experiment and as a result, the thermochemistry in the test gas. Approaches to reconstruct experiments numerically have overwhelmingly been a-priori and have subsequently been unable to satisfactorily account for the non-ideal processes. This is a clear need for a new numerical tool that can account for both non-equilibrium and shock speed non-uniformity, as well as improved experimental measurements of the thermochemical state of the expansion tube freestream.

Chapter 3

A Novel Non-Equilibrium, Lagrangian Shock Tube Method

Contents

3.1 Introduction

In this chapter a novel, Lagrangian shock and expansion tube solver is introduced. The software that comprises the method will be referred to as *LASTA 2.0*. LASTA is an abbreviation of LAgrangian Shock Tube Analysis. The primary purpose of this tool is to account for the effects of non-uniform shock trajectory on the test flow in impulse facilities. The tool includes thermochemical non-equilibrium effects with a Park 2T approach. It has been shown experimentally by Collen et al. (2022) that non-uniform shock speed,

This chapter contains FROSST simulations performed by Matthew Satchell and NESS simulations performed by Justin Clarke. These have been indicated and cited where relevant

resulting from a number of hydrodynamic and thermodynamic processes, can significantly affect the thermochemical state of the test gas. This is discussed in more detail in Section 2.2.2. Satchell et al. (2022b) developed a method to account for shock trajectory which for simplicity, will be referred to for the remainder of this document as *LASTA 1.0*. Satchell's method used equilibrium thermochemistry to model the test slug based on the experimental shock trajectory alone. This approach assumed that entropy and enthalpy were constant in the Lagrangian reference frame and that the pressure and enthalpy were algebraically related, or that sound wave relaxation within the slug is instantaneous. Additionally, a restriction on the pressure behind the shock wave was imposed such that it could only increase monotonically with the intention of preventing non-physical pressure profiles. This is referred to in the rest of this chapter as the *pressure-limiter* effect. Though this was undoubtedly an improvement, the tool relied on an assumption of thermochemical equilibrium and did not enforce conservation of momentum which limited its applicability to complex shock tube cases and the expansion tube.

The model presented in this chapter addresses the shortcomings of Satchell's model and thus significantly expands its capability. The tool is recast as a method of characteristics solver and provides the full time history of the experiment as a solution rather than just the final time. Experimental data, namely the shock trajectory and additionally static pressure traces, are utilised to extract information about the test slug via reverse time integration. The rigorous solution of the governing equations ensures conservation laws are enforced within the discretization error of the scheme and permits inclusion of thermochemical source terms to model thermal and chemical non-equilibrium as well as the expansion tube.

In this chapter, the governing equations and model methodology are presented, followed by results and validation against experimental data other established numerical tools. The implementation of the non-equilibrium thermochemistry model is then validated against canonical test cases.

3.2 Methodology

LASTA 2.0 idealises the test slug as a one dimensional, inviscid core surrounded by a growing boundary layer, as shown in Figure 3.1. The model is conceived in the shock reference frame with x representing the distance behind the shock, $x \in [0, \ell]$, where 0 is the shock front and ℓ is the contact surface. The shock travels left to right at speed $-\Lambda$ in the lab frame. The test gas travels at speed u in the lab frame and $u + \Lambda = u'$ in the

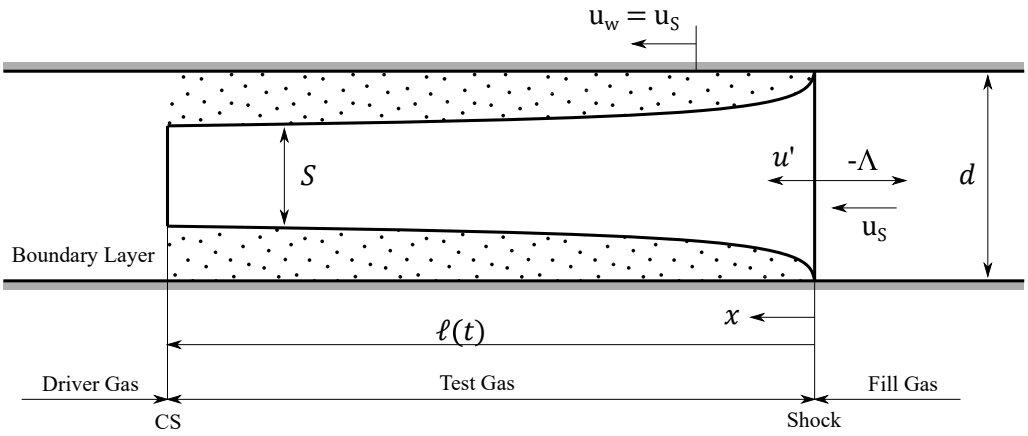

Figure 3.1: Diagram of the model domain, shown in the shock attached reference frame

shock frame. The one dimensional Euler equations are solved at each time point t along the supplied experimental shock trajectory with a source term to represent mass removal by the boundary layer. The domain size or slug length, ℓ, is allowed to vary along the length of the shock trajectory based on the mass balance between the shock addition and boundary layer subtraction. The size of the test slug and hence the test time is determined by the location where the mass flow consumed by the boundary layer matches the mass flow processed by the shock. Two boundary conditions are imposed on the model:

1. The primitive variables (ρ, u, p) immediately behind the shock at each time point are set by the shock trajectory

2. The pressure profile (in space) at the final time point is set by the user, ideally experimental values obtained from a static pressure transducer

3.2.1 Core flow governing equations

The program solves the one-dimensional species, momentum, vibrational-electronic energy, and total energy conservation equations in characteristic form. Because the system is solved in Lagrangian form, a frame transformation between the stationary and inertial frames is required. Define the following:

$$dx = dy - \Lambda dt \tag{3.1}$$

$$d\phi = \frac{\partial \phi}{\partial x} dx + \frac{\partial \phi}{\partial t} dt \tag{3.2}$$

$$d\phi = \frac{\partial \phi}{\partial x} (dy - \Lambda dt) + \frac{\partial \phi}{\partial t} dt \tag{3.3}$$

$$d\phi = \frac{\partial \phi}{\partial x} dy + \left(\frac{\partial \phi}{\partial t} - \Lambda \frac{\partial \phi}{\partial x} \right) dt \tag{3.4}$$

Time derivative measured by an observer bound to the frame of the shock:

$$\frac{\partial \phi}{\partial t'} = \frac{\partial \phi}{\partial t} - \Lambda \frac{\partial \phi}{\partial x} \tag{3.5}$$

$$\frac{D}{Dt} = \frac{\partial}{\partial t} + \left(u' + \Lambda\right) \frac{\partial}{\partial x} = \frac{\partial}{\partial t} + u \frac{\partial}{\partial x} \tag{3.6}$$

Thermochemistry follows the Park two-temperature model (Park, 1989), although this is not a requirement as any thermochemical model could be utilised with the same approach. This model assumes that the rotational and translational temperatures of heavy particles are in equilibrium at a temperature T, while the vibrational temperature of molecular species, the electron translational temperature, and the electronic excitation of atoms and molecules are in equilibrium at temperature T_V. The three-dimensional conservation equations are published by Gnoffo et al. (1989). For n species, the one-dimensional system is:

$$\underbrace{\frac{\partial}{\partial t'} \begin{bmatrix} \rho_s \\ \vdots \\ \rho_n \\ \rho u \\ \rho e_V \\ \rho E \end{bmatrix}}_{1} = \underbrace{-\frac{\partial}{\partial x} \begin{bmatrix} \rho_s u \\ \vdots \\ \rho_n u \\ \rho u u + p \\ \rho e_V u + p_e \\ \rho H u \end{bmatrix}}_{2} \underbrace{- \frac{2v}{r} \begin{bmatrix} \rho_s/\rho \\ \vdots \\ \rho_n/\rho \\ u \\ e_V \\ H \end{bmatrix}}_{3} + \underbrace{\begin{bmatrix} \dot{f}_s \\ \vdots \\ \dot{f}_n \\ 0 \\ \dot{f}_V \\ 0 \end{bmatrix}}_{4} \tag{3.7}$$

In Equation 3.7 the terms labelled 1 are the conserved variables. ρ_s denotes the density of species s with the bulk density given by:

$$\rho = \sum_{s=1}^{n} \rho_s \tag{3.8}$$

u is the velocity, e_V is the mixture vibrational-electronic energy per unit mass, E is the mixture total energy per unit mass. The terms labelled 2 comprise the flux-vector where H is the mixture total enthalpy per unit mass and p is the pressure. The pressure obeys Boyle's law:

$$p = \sum_{s=1}^{n} p_s = R \left(\sum_{s=2}^{n} \frac{\rho_s T}{M_s} + \frac{\rho_e T_V}{M_e} \right) \tag{3.9}$$

The source terms labelled 3 are included to model the removal of mass from the core flow by the boundary layer. Here, v is the radial component of velocity and r is the radius of the tube. The boundary layer model is presented in greater detail in Section 3.2.2.

The source terms labelled 4 account for the effect of thermochemistry. The terms $\dot{f}_s, \dot{f}_n$ account for the creation or destruction of a particular species due to chemical reactions. The term $\dot{f}_V$ is comprised of several contributions:

$$\begin{aligned}\dot{f}_V = &\underbrace{\frac{\partial}{\partial x}\left[(\eta_v + \eta_e)\frac{\partial T_V}{\partial x}\right]}_{5} + \underbrace{\sum_{s=mol.} \rho_s \frac{(e^*_{v,s} - e_{v,s})}{<\tau_s>}}_{6} \\ &+ \underbrace{2\rho_e \frac{3}{2}\bar{R}(T - T_V)\sum_{s=1}^{n-1}\frac{\upsilon_{es}}{M_s}}_{7} + \underbrace{\sum_{s=mol.}\dot{f}_s\hat{D}_s}_{8} - \underbrace{\sum_{s=mol.}\dot{n}_{e,s}\hat{I}_s}_{9} - \underbrace{Q_{rad}}_{10}\end{aligned} \tag{3.10}$$

Term 5 represents the conduction of energy through the test slug due to a gradient of vibro-electronic temperature. Term 6 represents the energy exchange or relaxation between trans-rotational and vibro-electronic energy modes, where τ_s is the relaxation time. τ_s is obtained from correlations in the literature[1] and is dependent on the gas mixture. Term 7 represents the energy exchange between modes due to elastic collisions between electrons and heavy particles. Term 8 is the energy lost or gained due to dissociation reactions and, similarly, term 9 is the energy lost or gained due to electron impact ionization. Finally, term 10 represents the energy lost due to radiation which is assumed to be zero for this study.

It is desirable to manipulate the governing equations such that they are expressed in terms of a set of variables of interest or so called *primitive variables*, shown below:

$$\frac{\partial}{\partial t'}\begin{bmatrix}\rho_s \\ \vdots \\ \rho_n \\ u \\ T_V \\ p\end{bmatrix} = -\begin{bmatrix} u & \dots & 0 & \rho_1 & 0 & 0 \\ \vdots & \ddots & \vdots & \vdots & \vdots & \vdots \\ 0 & \dots & u & \rho_n & 0 & 0 \\ 0 & \dots & 0 & u & 0 & 1/\rho \\ 0 & \dots & 0 & \frac{p_e}{\rho C_{v,V}} & u & 0 \\ 0 & \dots & 0 & \rho a^2 & 0 & u \end{bmatrix}\frac{\partial}{\partial x}\begin{bmatrix}\rho_s \\ \vdots \\ \rho_n \\ u \\ T_V \\ p\end{bmatrix} - \rho\frac{2v}{r}\begin{bmatrix}\rho_s/\rho \\ \vdots \\ \rho_n/\rho \\ 0 \\ 0 \\ a^2\end{bmatrix} + \begin{bmatrix}\dot{f}'_s \\ \vdots \\ \dot{f}'_n \\ 0 \\ \dot{f}'_V \\ 0\end{bmatrix} \tag{3.11}$$

Here, the electron pressure p_e appears which may be readily obtained from the vibrational-electronic temperature:

$$p_e = \frac{T_V R \rho_e}{M_e} \tag{3.12}$$

Where M_e is the electron molar mass and ρ_e is the electron density which is its self a primitive variable. The thermochemical source terms are marked with a prime to il-

[1] For example, Gnoffo et al. (1989)

lustrate that a transformation between conservation and primitive form has occurred. Finally, the system can be expressed in a characteristic basis by solving the eigenvalue problem. The details of these steps are included in Appendix B and only the final system is presented here.

$$\frac{\partial}{\partial t'}\begin{bmatrix} w_1 \\ \vdots \\ w_n \\ w_{n+1} \\ w_{n+2} \\ w_{n+3} \end{bmatrix} = -\begin{bmatrix} u & \dots & 0 & 0 & 0 & 0 \\ \vdots & \ddots & \vdots & \vdots & \vdots & \vdots \\ 0 & \dots & u & 0 & 0 & 0 \\ 0 & \dots & 0 & u+a & 0 & 0 \\ 0 & \dots & 0 & 0 & u & 0 \\ 0 & \dots & 0 & 0 & 0 & u-a \end{bmatrix} \frac{\partial}{\partial x}\begin{bmatrix} w_1 \\ \vdots \\ w_n \\ w_{n+1} \\ w_{n+2} \\ w_{n+3} \end{bmatrix} - a\frac{2v}{r}\begin{bmatrix} 0 \\ \vdots \\ 0 \\ 1 \\ 0 \\ -1 \end{bmatrix} + \begin{bmatrix} \dot{f}_s'' \\ \vdots \\ \dot{f}_n'' \\ 0 \\ \dot{f}_V'' \\ 0 \end{bmatrix} \tag{3.13}$$

Here, w_s are the characteristic variables. The characteristic variables provide a clear representation of the underlying fluid processes influencing the test slug properties, namely, wave processes travelling back and forth through the gas.

3.2.2 Boundary layer governing equations

The boundary layer is represented through its effects on the core flow. This is included by assuming the radial velocity v behaves according a local similarity approximation proposed by Mirels (1963). Using this approximation, the radial velocity at the edge of the boundary layer can be evaluated as:

$$v = \frac{\rho_{e,0} u_{e,0}}{4\rho\sqrt{\ell \ell_m}} \tag{3.14}$$

where ℓ is the distance from the shock, $\rho_{e,0}$, $u_{e,0}$ are the immediate post-shock density and velocity in the shock reference frame, ρ is the density in the test slug evaluated at ℓ, and ℓ_m is the maximum slug length. The maximum slug length is given by Mirels as:

$$\ell_m = \frac{d^2}{16\beta^2}\left(\frac{\rho_{e,0}}{\rho_{w,0}}\right)^2 \frac{u_{e,0}}{\Lambda - u_{e,0}} \frac{u_{e,0}}{\upsilon_{w,0}} \tag{3.15}$$

where d is the tube diameter, β is a calculated shape factor, $\rho_{w,0}$ and $\upsilon_{w,0}$ are the density and kinematic viscosity evaluated at the tube wall temperature, and Λ is the shock speed as before. Mirels' analysis provides estimates of the shape factor β behind a shock wave:

$$\beta = C_M^{\alpha} 1.59 \left(1 + \frac{1.796 + 0.802W}{WZ - 1}\right) \tag{3.16}$$

where

$$C_M = \frac{\rho_{sh}\mu_{sh}}{\rho_{w,sh}\mu_w} \tag{3.17}$$

Here, $W = \Lambda/u_{e,0}$ and $Z = \frac{\gamma+1}{\gamma-1}$. C_M corrects for boundary layer shape to account for changes in the freestream properties. α is an empirical constant, 0.48 here. These equations are evaluated to obtain the radial velocity profile along the test slug which can then be used to evaluate the source term. It should be noted that Mirels' analysis was developed for a steady, constant shock speed case, whereas here it is applied for a non-uniform, unsteady shock speed, the physical implication being that it is assumed that the entire boundary layer shape is instantly resized for changing shock speed. Previous work has shown that this assumption is sufficient for many typical shock tube cases (Satchell et al., 2022b).

3.2.3 Treatment of the characteristics

The characteristics $w^{(2)}$ and $w^{(3)}$ represent sound waves travelling through the test slug, $w^{(2)}$ originating from the shock front and $w^{(3)}$ originating from the driver gas. Figure 3.2a illustrates the directions of propagation for the $w^{(2)}$ and $w^{(3)}$ waves in a shock tube experiment where time progresses from top to bottom. Accurate numerical modelling of the effect of the $w^{(3)}$ characteristic on the test slug properties with forward time integration would require a pressure boundary condition at the contact discontinuity. Unfortunately, experimental information about the position and pressure of the contact surface is difficult to obtain non-intrusively and is typically unavailable, thus, the effect of $w^{(3)}$ on the test slug cannot be calculated via forward time integration. However, $w^{(3)}$ waves will ultimately propagate through the test slug to the shock front, so $w^{(3)}$ is known indirectly through its effect on the future trajectory. By integrating $w^{(3)}$ backwards in time, the approach taken here and shown in Figure 3.2b, the test gas is within the domain of influence of the shock with respect to $w^{(3)}$ and the full test slug history may be calculated using the shock trajectory and final pressure profile as boundary conditions.

The $w^{(3)}$ characteristic waves travel at a finite speed and thus their inclusion via the pressure boundary condition will influence only a subset of the solution domain. This is illustrated by Figure 3.3, an x-t diagram of a shock tube experiment in the shock reference frame. Figure 3.3a shows the wave processes modelled by Satchell's method, and Figure 3.3b shows the additional wave processes modelled by LASTA 2.0 as a result of the new boundary condition. It can be seen that the influence of the $u + a$ waves on the slug properties becomes more significant toward the rear of the slug as more waves have had

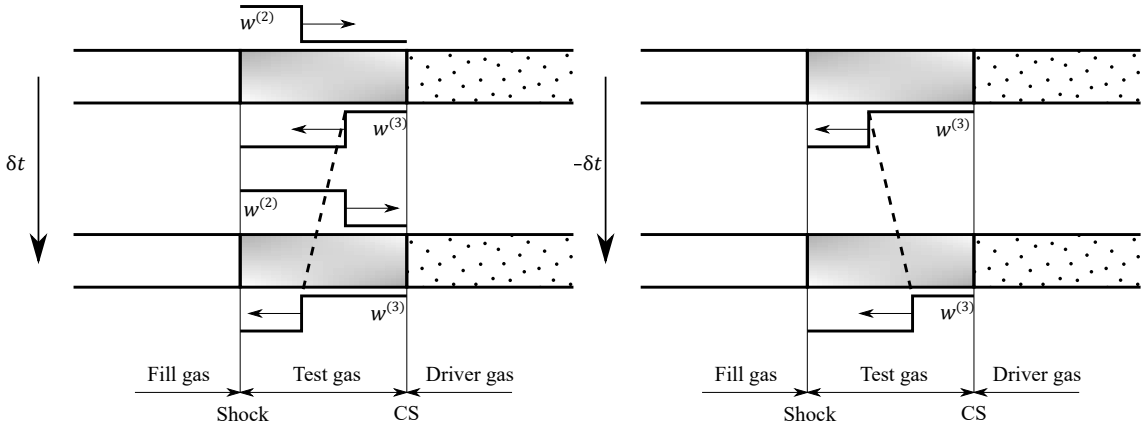

(a) Forward integration (b) Backward integration

Figure 3.2: Time integration for the $w^{(3)}$ characteristic

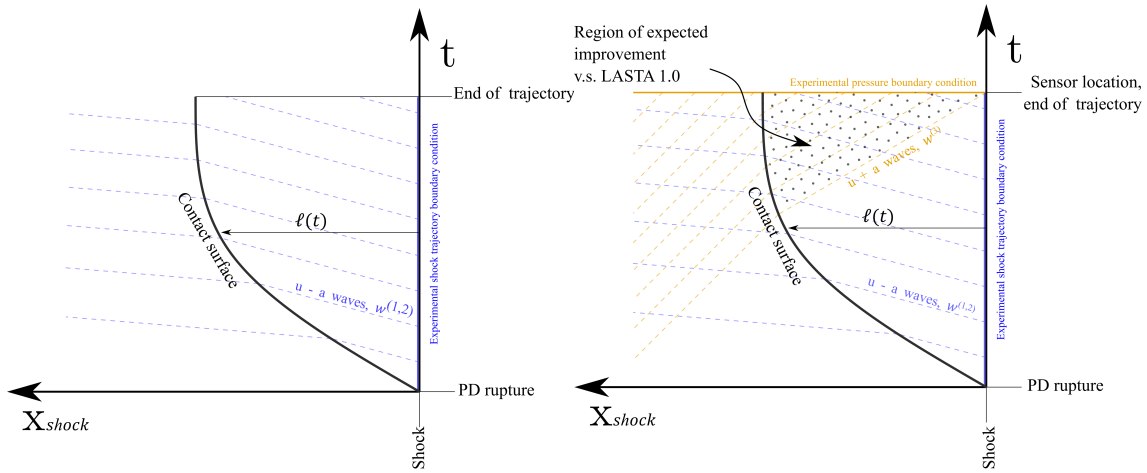

(a) LASTA 1.0 (b) LASTA 2.0

Figure 3.3: Diagrams of the wave processes modelled explicitly in each version of LASTA. The diagrams are representative of the processes occurring in a real experiment, but are not drawn to scale

time to pass through this region. Necessarily, the influence of $u - a$ waves, although still significant, becomes less important toward the rear of the slug. Satchell's method assumes that the relative flow within the test slug is low subsonic and that the time it takes for sound waves to propagate along the slug length is negligible compared to the duration of the trajectory, or more precisely that within a typical acoustic propagation time variations in shock speed are negligible. This assumption is addressed by LASTA 2.0 and improvement is expected in the region where the $u + a$ waves may propagate.

It should be noted that, although pressure measurements are used as a boundary condition here, it is possible in principle to use other experimental data, such as temperature inferred from heat transfer gauge measurements. It is also possible to move the boundary condition upstream or downstream, assuming experimental data is available, to the

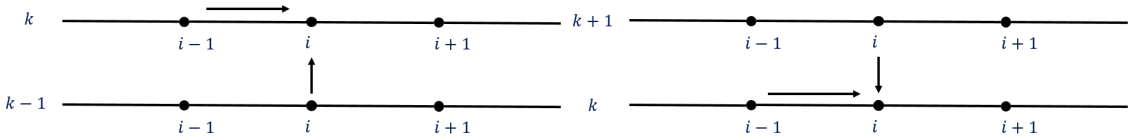

(a) entropy and right running sound wave (b) left running sound wave

Figure 3.4: Finite difference scheme

location of greatest interest.

3.2.4 Numerical scheme

The system of governing equations is solved using a finite difference method. The forward characteristics are evaluated at the ith spatial point and kth time point as:

$$\delta^t w_{i,k}^{(1)} + \frac{\Delta t}{\Delta x} u'_{i,k} \delta^+ w_{i,k}^{(1)} = 0 \tag{3.18}$$

$$\delta^t w_{i,k}^{(2)} + \frac{\Delta t}{\Delta x} \left(u'_{i,k} + a_{i,k}\right) \delta^+ w_{i,k}^{(2)} + 2\frac{a_{i,k} v_{i,k}}{r} = 0 \tag{3.19}$$

where

$$\delta^t w_{i,k}^{(1)} = \rho_{i,k} - \rho_{i,k-1} - \frac{1}{a_{i,k}^2}\left(\rho_{i,k} - \rho_{i,k-1}\right) \tag{3.20}$$

$$\delta^+ w_{i,k}^{(1)} = \rho_{i,k} - \rho_{i-1,k} - \frac{1}{a_{i,k}^2}\left(\rho_{i,k} - \rho_{i-1,k}\right) \tag{3.21}$$

$$\delta^t w_{i,k}^{(2)} = u_{i,k} - u_{i,k-1} + \frac{1}{\rho_{i,k} a_{i,k}}\left(p_{i,k} - p_{i,k-1}\right) \tag{3.22}$$

$$\delta^+ w_{i,k}^{(2)} = u_{i,k} - u_{i-1,k} + \frac{1}{\rho_{i,k} a_{i,k}}\left(p_{i,k} - p_{i-1,k}\right) \tag{3.23}$$

The backward characteristic is evaluated as:

$$\delta^t w_{i,k+1}^{(3)} + \frac{\Delta t}{\Delta x} \left(u'_{i,k} - a_{i,k}\right) \delta^+ w_{i,k}^{(3)} + \frac{2 a_{i,k} v_{i,k}}{r} = 0 \tag{3.24}$$

where

$$\delta^t w_{i,k+1}^{(3)} = u_{i,k+1} - u_{i,k} - \frac{1}{\rho_{i,k} a_{i,k}}\left(p_{i,k+1} - p_{i,k}\right) \tag{3.25}$$

$$\delta^+ w_{i,k}^{(3)} = u_{i,k} - u_{i-1,k} - \frac{1}{\rho_{i,k} a_{i,k}}\left(p_{i-1,k} - p_{i,k}\right) \tag{3.26}$$

The grid spacing Δx in equations 3.18,3.19 and 3.24 is constructed as

$$\Delta x = \ell \Delta \eta \tag{3.27}$$

where η is a non-dimensional coordinate with value 0 at the shock and 1 at the contact discontinuity. In order for the model to be solvable, an additional relation is needed to determine the slug length ℓ. The additional equation is obtained by imposing that at the contact discontinuity the relative velocity in the shock frame of reference matches the rate of change of the test slug length:

$$u' = \frac{d\ell}{dt} \tag{3.28}$$

The system is solved using an exact Jacobian where the inverse is approximated by a incomplete factorisation method. Let the solution vector and the residual be partitioned as follows:

$$\boldsymbol{Q} = \begin{bmatrix} \boldsymbol{Q}_B \\ \boldsymbol{Q}_T \end{bmatrix}, \ \boldsymbol{R} = \begin{bmatrix} \boldsymbol{R}_B \\ \boldsymbol{R}_T \end{bmatrix} \tag{3.29}$$

Where:

$$\boldsymbol{Q}_B, \boldsymbol{R}_B \in \mathbb{R}^{\mathcal{T}\times\mathcal{N}\times(\mathcal{M}+1)}, \ \boldsymbol{Q}_T, \boldsymbol{R}_T \in \mathbb{R}^{\mathcal{T}\times(\mathcal{M}+1)} \tag{3.30}$$

Let the Jacobian of the residual be:

$$\boldsymbol{A} = \begin{bmatrix} \dfrac{\partial \boldsymbol{R}_B}{\partial \boldsymbol{Q}_B} & \dfrac{\partial \boldsymbol{R}_B}{\partial \boldsymbol{Q}_T} \\ \dfrac{\partial \boldsymbol{R}_T}{\partial \boldsymbol{Q}_B} & \dfrac{\partial \boldsymbol{R}_T}{\partial \boldsymbol{Q}_T} \end{bmatrix} = \begin{bmatrix} \boldsymbol{A}_{BB} & \boldsymbol{A}_{BT} \\ \boldsymbol{A}_{TB} & \boldsymbol{A}_{TT} \end{bmatrix} \tag{3.31}$$

The solution vector is obtained via Newton iterations with:

$$\boldsymbol{Q} \to \boldsymbol{Q} - \tilde{\boldsymbol{A}}^{-1}\boldsymbol{R} \tag{3.32}$$

$\tilde{\boldsymbol{A}}^{-1}$ is an approximation of A^{-1} constructed via an incomplete factorisation method.

$$\boldsymbol{X}_B \to \boldsymbol{X'}_B = \boldsymbol{X}_B + \boldsymbol{A}_{BB}^{-1}(\boldsymbol{R}_B - \boldsymbol{A}_{BB}\boldsymbol{X}_B - \boldsymbol{A}_{BT}\boldsymbol{X}_T) \tag{3.33}$$

$$\boldsymbol{X}_T \to \boldsymbol{X'}_T = \boldsymbol{X}_T + \omega\boldsymbol{A}_{TT}^{-1}(\boldsymbol{R}_T - \boldsymbol{A}_{TB}\boldsymbol{X}_B - \boldsymbol{A}_{TT}\boldsymbol{X}_T) \tag{3.34}$$

where $\omega < 1$ is a relaxation factor.

3.3 Treatment of Experimental Inputs and Resulting Uncertainty

In this section, the use of experimental boundary conditions in LASTA 2.0 is discussed in detail. Firstly, the method for determining the shock arrival time, shock speed, and associated uncertainty for T6 experiments is presented. Second, the process of converting the experimental measurement of shock speed into a usable boundary condition is discussed. Finally, the optional use of experimental pressure data is discussed.

3.3.1 Determination of time of arrival

The approach to determination of shock arrival time and uncertainty varies between research groups. This includes the measurement technique used (James et al., 2021; Dufrene et al., 2015) and the post-processing approach (Brandis, 2009b; James, 2019).

The method used for determination of shock arrival time and uncertainty for all T6 test cases presented in this thesis is summarised in Appendix G of James (2018). Given the fundamental importance of the experimental shock speed measurement to the LASTA 2.0 simulation approach, this method is summarised here. The shock speed is simply calculated as:

$$V_s = \frac{x_2 - x_1}{t_2 - t_1} = \frac{\Delta x}{\Delta t} \tag{3.35}$$

where x_1 and x_2 are the axial locations of two adjacent sensors and t_2 and t_1 are the shock arrival times at the respective sensors. Here, subscript 2 denotes the downstream sensor and 1 the upstream. The uncertainty in shock speed is calculated using:

$$\delta V_s = V_s \sqrt{\left(\frac{\delta \Delta x}{\Delta x}\right)^2 + \left(\frac{\delta \Delta t}{\Delta t}\right)^2} \tag{3.36}$$

where $\delta \Delta x$ represents the uncertainty in Δx and $\delta \Delta t$ represents the uncertainty in Δt, the difference in arrival times between adjacent sensors. The uncertainty in Δx is comprised of:

1. Uncertainty in the measurement of the sensor locations
2. Uncertainty in the response of the pressure sensor due to its finite size
3. Uncertainty in the curvature of the shock

These three contributions are assigned a single uncertainty of $\pm 2.0 \times 10^{-3}$ m for each

sensor location. Given that the distance uncertainties at each sensor location are independent, the total distance uncertainty ($\delta\Delta x$) is given by:

$$\delta\Delta x = \sqrt{\delta x_1^2 + \delta x_2^2} \tag{3.37}$$

Similarly, one source of time uncertainty and one source of error are considered for $\delta\Delta x$:

1. Uncertainty in the shock time of arrival due to the post-processing approach
2. Sampling rate error from the data acquisition system

The time of arrival is determined manually to avoid the often large uncertainty and unreliability associated with an automated process. During post-processing, the user is presented with a graphical interface showing the time history for each sensor and they are prompted to select the data points immediately before and after they believe the shock arrived. This results in a range of possible arrival times, from which the midpoint is treated as the nominal value and half the width is treated as the uncertainty. This is illustrated in Figure 3.5

The sampling rate error is accounted for by including the size of a single sample (δt_{sr}) since the shock may arrive at any point during the sample. This must be considered for both sensors. The T6 data acquisition samples at 2.5 MHz so $\delta t_{sr} = 0.4$ µs. The final time uncertainty is then given by:

$$\delta\Delta t = \sqrt{\delta t_1^2 + \delta t_2^2 + 2\delta t_{sr}^2} \tag{3.38}$$

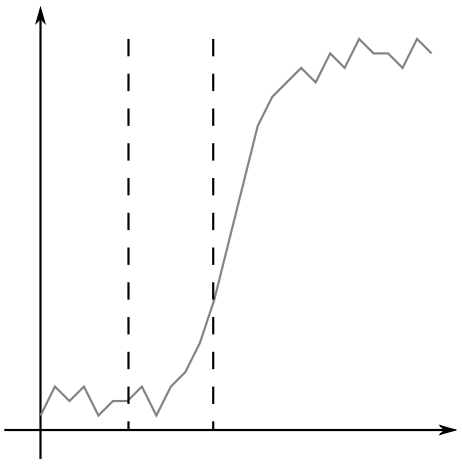

Figure 3.5: Window method

3.3.2 Treatment of the experimental shock speed

After processing as described in the previous section, the shock speed trajectory is available in the form of $x - t$ data where x is a vector of timing station locations and t is the arrival time of the shock at each location. In order to discretise the shock trajectory a high order polynomial ($n = 3 - 5$) or cubic spline is fitted to the shock speed vector and average arrival time i.e. a time between two station arrival times equidistant from each. The polynomial is evaluated at each simulation time point and the resulting shock speed is used to determine the flow properties via a normal shock relation, either ideal, equilibrium, or Rankine-Hugoniot depending on the user's preference.

It should be noted that, in many cases, the spatial resolution of experimental shock speed measurements is sufficiently low and/or the variation in shock speed is sufficiently high to mean that the choice of fit has an appreciable effect on the final test slug prediction. Consider Figure 3.6, which shows experimental measurements of shock speed for an experiment in the EAST facility. As with many impulse facilities, the density of time of arrival measurements increases toward the test section or observation window. This is always accompanied by an increase in the standard deviation of the shock speed measurements. This is because the uncertainty in Δx and Δt does not depend on the sensor spacing (Δx) and thus the uncertainty in the shock speed measurement (δV_s) is inversely proportional to Δx and Δt. Put simply, decreasing sensor spacing inherently increases shock speed uncertainty.

The increased shock speed variation toward the end of the shock tube poses a problem when the trajectory needs to be discretised for a LASTA 2.0 simulation. Figure 3.6 shows five different approaches to discretisation, namely four polynomials of increasing order and a piecewise cubic spline fit. The coefficient of determination (r^2) associated with each method is shown in the legend. A naive approach would be to simply select the method with the largest r^2 value, in this case the piecewise cubic spline fit, however this clearly results in a non-physical description of the shock behaviour as the sensor spacing decreases. This line of reasoning also applies to the polynomial fits, with perhaps $n = 1 - 3$ fits providing a plausible description of the physical behaviour of the shock.

The example is presented to illustrate that when analysing test cases with LASTA 2.0 where shock speeds have been determined by a time-of-arrival method there is often a need for the user to rely on their judgement in specifying the shock trajectory fit. The choice of polynomial fit also has implications for inclusion of experimental shock speed uncertainties, such as those discussed in the previous section, in LASTA 2.0 mod-

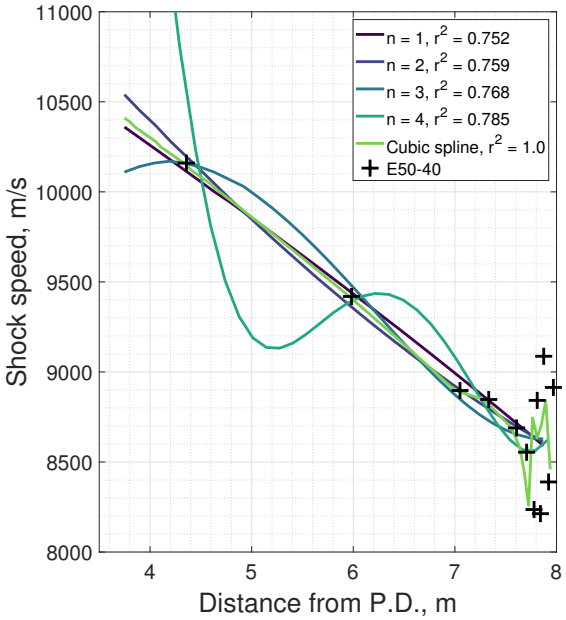

Figure 3.6: Experimentally measured shock speeds and several possible fits for E50-40, an example test case from the EAST facility

elling. The experimental uncertainties are a set of bounds on the shock speed measurements which could be fit with a polynomial or similar, discretised, and used as inputs to a LASTA 2.0 simulation. However, as with the original shock speed profile, the user could make several justifiably different choices about the shock detection instrumentation, method of determining shock arrival, and trajectory fit that will lead to different results.

Rather than prescribing a single approach to the user, uncertainty in the experimental shock speed is accounted for via a perturbation analysis in LASTA 2.0. Two LASTA 2.0 simulations are performed, one with the nominal shock trajectory and another with the nominal trajectory perturbed at every time point by a fixed velocity, 100 $\mathrm{m\,s^{-1}}$ by default. The allows the Jacobian of the primitive variables with respect to the shock speed to be evaluated and then used to produce bounds on the solution. The Jacobian is calculated as:

$$J_{q,V_s} = \frac{\Delta q}{\Delta V_s} \tag{3.39}$$

where q is the solution vector and ΔV_s is the shock speed perturbation. This approach limits the number of inputs required from the user and affords them flexibility in studying the effect of shock speed uncertainty on the solution. It is possible to perturb the solution by a fixed shock speed value here, but it does not allow perturbation of the shock speed at individual time points i.e. the approach that would be desired to directly incorporate experimental shock speed uncertainty measurements. It is possible

to achieve this, but it would require the Jacobian of the solution with respect to the shock speed at each time point. This must be calculated via finite difference and thus a simulation for every time point would be required, significantly increasing the computational cost. For this reason, direct inclusion of the experimental uncertainty was considered a subject for future work. Unless otherwise stated, a constant perturbation velocity of 100 $\mathrm{m\,s^{-1}}$ has been used. 100 $\mathrm{m\,s^{-1}}$ is chosen as the default as it reflects a typical uncertainty in shock speed at the T6 observation window.

3.3.3 Treatment of the experimental pressure profile

The second experimental input is the pressure distribution in the test slug, obtained via a wall pressure trace. Pressure sensors in impulse facilities can exhibit a number of non-ideal behaviours which should be considered when integrating them into the simulation. Firstly, they can be relatively noisy and thus a degree of smoothing or fitting is necessary. Secondly, they have a limited bandwidth and response time, in the case of PCB113s approximately 500 kHz and 2 $\mu\mathrm{s}$ respectively, so flow features with timescales less than these are not resolved. This manifests as an inherent uncertainty in the time of shock arrival. Thirdly, they respond to thermal shock which can limit the range of usable data over larger timescales. To reduce the risk of spurious experimental measurements arising from these uncertainties affecting the results the pressure data is processed before being used as a boundary condition for a LASTA 2.0 simulation.

Firstly, the portion of the pressure profile representing the test slug is segmented from the raw trace[2]. The excerpted profile must begin at the time of shock arrival and end after passage of the contact surface. Shock arrival is determined using the method described in the previous section. Secondly, a moving average fit is applied to the profile based on a window width (in seconds) specified by the user in the input file[3]. Increasing this parameter increases solution stability because the smoothness of the boundary condition increases, however this comes at the cost of potentially decreasing the fidelity of the solution as some subtle experimental features may be lost. The parameter is set to 2 $\mu\mathrm{s}$ by default. Thirdly, the pressure profile is converted from a dependence on time to a dependence on space, a requirement to match the simulation domain, by multiplying by the local velocity. Ideally an experimental measurement of the velocity would be used for this purpose, however such a measurement is often unavailable and thus the simulated

[2]The raw trace typically contains on the order of 10 ms of data of which perhaps 10–100 $\mu\mathrm{s}$ is the test slug. Thus, much of the raw trace is not required for the purposes of a LASTA 2.0 shock tube simulation.

[3]This is the parameter wi

values must be used.

It should be noted that it is possible for the shock and pressure boundary conditions to disagree. This disagreement manifests as a difference in the values specified for pressure at the first streamwise cell at the final time step (i.e. where the boundary conditions overlap). The pressure at the shock is determined from a Rankine-Hugoniot normal shock relation which can disagree with the experimentally measured value for a number of reasons, some of which have already been discussed in this section. The value predicted by the shock boundary condition is always selected in LASTA 2.0 to preserve smoothness of the shock boundary. Ideally, improved measurements of both the experimental shock speed and pressure would be available to resolve this potential discrepancy.

3.4 Numerical Validation of the Shock Tube Model with Ideal Gas

LASTA 2.0 was validated against a series of numerical simulations by Satchell et al. (2022a), as was done for LASTA 1.0 (Satchell et al., 2022b). These validation cases use an ideal gas model and thus remove the complication of thermochemistry. The results from application of LASTA 2.0 to more complex experimental trajectories are presented in Section 3.6.

3.4.1 Two-dimensional simulations

The FRamework for Overset Simulation of Shock Tubes (FROSST) is an axisymmetric, explicit, structured finite volume method for solution of the Navier-Stokes equations for ideal gas simulation of shock tube flows. The code is written using an overset formulation that allows a highly refined grid to be attached to both shock and contact discontinuity with the intention of reducing computational cost when compared to typical axisymmetric shock tube solvers. FROSST has the capability to model the effect of primary diaphragm opening, allowing for the production of non-uniform shock trajectories. FROSST has been validated against a number of historical and canonical shock tube cases and serves as the benchmark for comparison to LASTA 2.0 in the present work. FROSST is described in greater detail by Satchell et al. (2021).

3.4.2 Test cases

Satchell et al. (2022a) devised three ideal gas shock tube test cases using the FROSST code with the same final shock speed but differing initial shock speeds, thus allowing the effect of non-uniform shock speed on the test slug properties to be evaluated. The trajectories are shown in Figure 3.7, consisting of a strongly decelerating, strongly accelerating, and relatively constant shock speed case. All cases result in a shock speed of $2100\ \mathrm{m\,s^{-1}}$ at a distance $8\ \mathrm{m}$ from the primary diaphragm. Pure Argon was used as the test gas at an initial pressure and temperature of $66.7\ \mathrm{Pa}$ and $300\ \mathrm{K}$ respectively. A tube diameter of $100\ \mathrm{mm}$ was selected.

For all data presented herein the LASTA 2.0 domain was discretized into 150 points behind the shock with 5 % grid clustering toward the shock front, that is, $x(i) = x(i-1) + dx(i)$ where $dx(i) = 1.05dx(i-1)$ with $dx(1) = 0.005\ \mathrm{m}$. The supplied shock trajectory was discretized into 128 time points. Simulations were run on a workstation with an

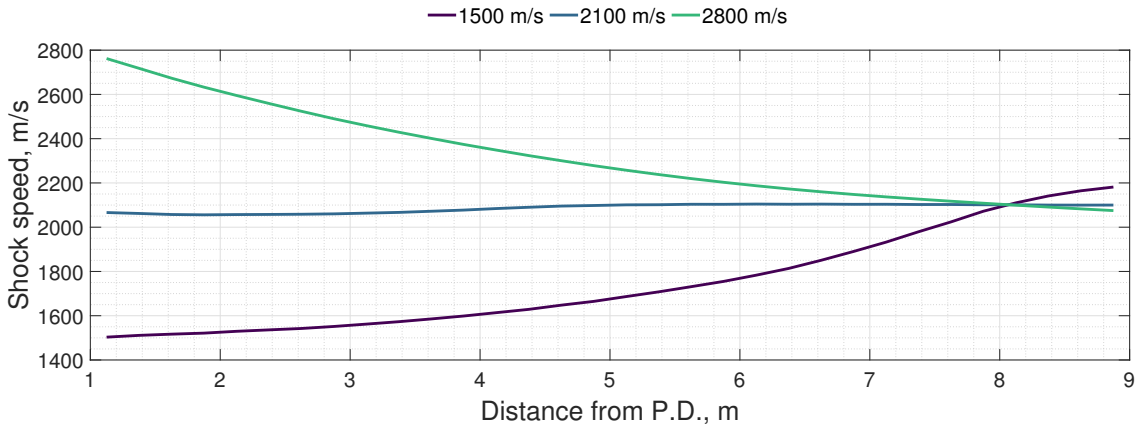

Figure 3.7: Shock speed as a function of distance from the primary diaphragm for the three test cases

Intel(R) Xeon(R) W-2265 CPU clocked at 3.50 GHz and 64.0 GB of RAM. The average run time for the simulations was 26.5 s.

For each simulation, the full shock trajectory, and the pressure profile at $9\ \mathrm{m}$ from the primary diaphragm from the FROSST test cases were used as boundary conditions. The pressure profile at any location along the length of the tube may in principle be used as the boundary condition. $9\ \mathrm{m}$ was selected so that the profiles at $8\ \mathrm{m}$, the location where the test case shock trajectories converge on $2100\ \mathrm{m\,s^{-1}}$, were within the domain of influence of but not explicitly set by the new boundary condition. This arrangement is analogous to interrogating a location slightly upstream of a pressure transducer in an experimental facility, which is ultimately the intended use case.

3.4.3 Results

LASTA 2.0 pressure and temperature profiles at various points along the shock trajectory are compared to results from LASTA 1.0 and FROSST for the same cases. Here, LASTA 2.0 is expected to improve over LASTA 1.0 in the region where sound waves emanating from the driver that are encapsulated in the pressure boundary condition overlap with the test slug. This region increases in size as the boundary condition is approached in time, beginning with improvements at the rear of the slug and ending at the boundary condition its self where the entire slug is affected. Figures 3.8 and 3.9. show pressure and temperature profiles at $8\ \mathrm{m}$, $8.5\ \mathrm{m}$, and $9\ \mathrm{m}$ from the primary diaphragm. Each of these locations are within the domain of influence of the boundary condition and thus improved agreements for pressure between FROSST and LASTA 2.0 versus LASTA 1.0 are expected for all, particularly toward the rear of the test slug.

LASTA 2.0 pressure profiles exactly match those of FROSST at $9\ \mathrm{m}$ from the diaphragm, the location of the boundary condition. LASTA 2.0 pressure profiles at $8\ \mathrm{m}$ and $8.5\ \mathrm{m}$ also show excellent agreement with FROSST where the difference is less than 1 % for all cases. LASTA 1.0 results for the $1500\ \mathrm{m\,s^{-1}}$ case differ from the other two approaches, albeit by a maximum of 3.5 % at each location. This has previously been attributed to 2D-effects, namely the arrival of a jet of driver gas and subsequent deformation of the contact discontinuity in the FROSST simulations, which are not accounted for in the 1D LASTA 1.0 simulation. Although LASTA 2.0 is also a 1D code, these pressure deviations are not apparent, a fact that can only be attributed to the inclusion of the new boundary condition.

Profiles of temperature, which are not set explicitly as a boundary condition in LASTA 2.0, agree with LASTA 1.0 and FROSST within 1% except in the decelerating case where divergence begins at 150 µs. This is due to the arrival of a cold jet of driver gas in the FROSST simulation which is not accounted for in LASTA 2.0. Contour plots of temperature in the FROSST simulations are shown in Satchell et al. (2022a), illustrating the arrival of the jet. The fact that LASTA 1.0 does not also diverge with LASTA 2.0 is an illustration of the LASTA 1.0 *pressure limiter* in effect. Rather than solving for the full Euler equations for one dimensional flow including conservation of momentum, LASTA 1.0 features a constraint on pressure that mimics the effect of momentum exchange between gas slices. This follows the observation that, even for strongly decelerating cases, pressure behind the shock tends to increase monotonically until the contact discontinuity. This manifests in LASTA 1.0 as a condition that pressure must not decrease moving upstream from the shock. This is a non-physical constraint that improves agreement between LASTA 1.0 and many shock tube test cases, but precludes application of LASTA 1.0 to test cases where upstream waves are dominant, most notably the expansion tube.

The test times predicted by LASTA 2.0 show improved agreement with FROSST compared with LASTA 1.0. Since pressure across the contact discontinuity must be equal, the FROSST temperature profiles in Figure 3.9 provide the best indication of the extent of the test slug, the sharp drop in each case corresponding to driver gas arrival. Satchell et al. (2022b) highlighted that the cause of the LASTA 1.0 test time over prediction was two fold:

1. The one dimensional nature of the method could not account for a multidimensional effect in the accelerating case, namely the jetting of driver gas into the rear 35% of the test slug leading to a decrease in test time

2. Inability to account for loss of test slug mass past the contact discontinuity

These effects are still present, but their effect is reduced in LASTA 2.0 as additional information about the contact surface state is included in the pressure boundary condition, which is in turn included in the test slug state via backwards time integration. The greatest difference is evident in the strongly accelerating case, where the LASTA 1.0 predicted test time is 15% larger than that of LASTA 2.0. This is expected, as in this case the cause of the shock acceleration is the contribution of pressure waves from the driver and thus their exclusion leads to error. It should also be noted that, because both methods are one-dimensional approximations of the test slug, the location and geometry of the contact surface can only be approximated.

LASTA 2.0 test time predictions still differ from FROSST, in some cases under predicting and some cases over predicting. This is expected, since LASTA 2.0 cannot fully account for the multidimensional nature of the contact discontinuity as a 1D method. The difference is in part due to boundary layer implementation. The Mirels model was developed under the assumption of a steady, constant shock speed, which is not the case here. Mirels' model is re-evaluated at each time point in the simulation, the physical implication being that the boundary layer instantly resizes to match the current shock speed. This is not the case in reality as the boundary layer would require time to resize and would therefore entrain a different amount of mass from the test slug, leading to a different test time. Implementation of an unsteady boundary layer solution would likely improve agreement with FROSST.

The percentage difference between LASTA 2.0 and FROSST temperature predictions at 9 m from the primary diaphragm is shown in Figure 3.10. This location was chosen for quantitative comparison as it is representative of the point where comparisons to emission spectroscopy or other thermodynamic diagnostics would be made in a real experiment. As expected, agreement with FROSST is best closest to the shock. Disagreement is largest at the rear of the shock for the accelerating and decelerating cases due to the presence of the non-uniform contact surface which has already been discussed.

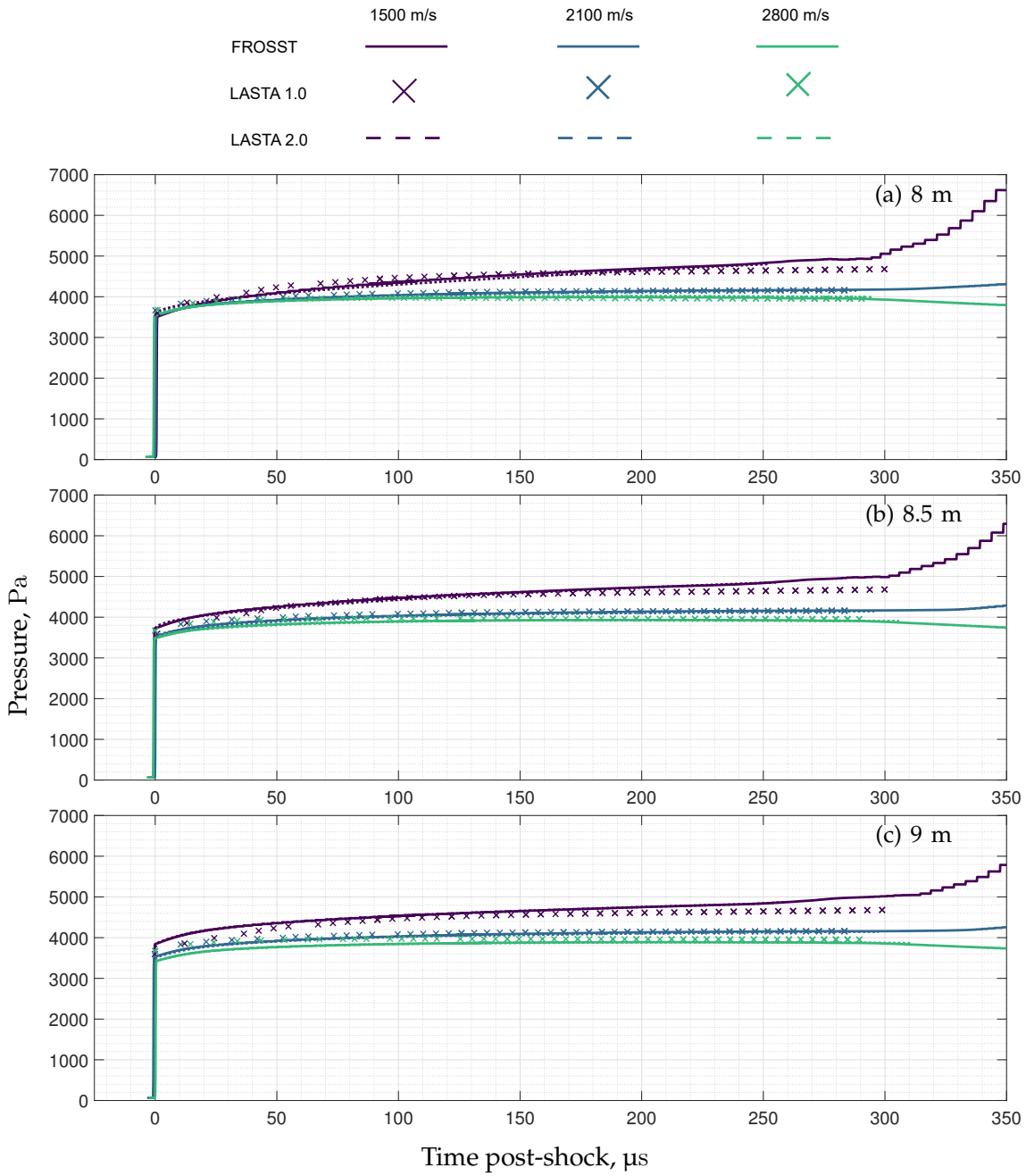

Figure 3.8: Profiles of pressure obtained a three axial locations along the shock tube from FROSST, LASTA 1.0, and LASTA 2.0

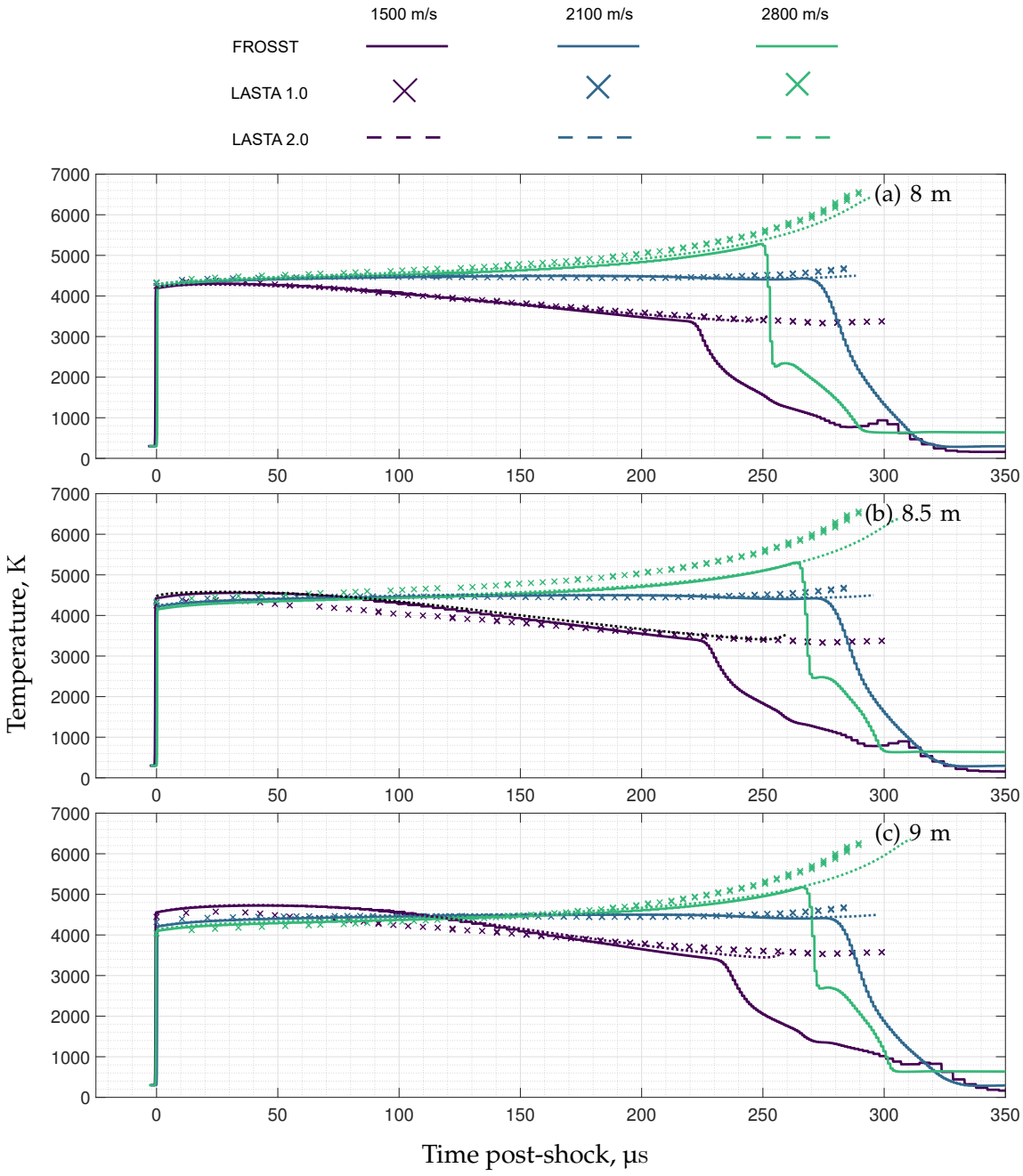

Figure 3.9: Profiles of temperature obtained a three axial locations along the shock tube from FROSST, LASTA 1.0, and LASTA 2.0

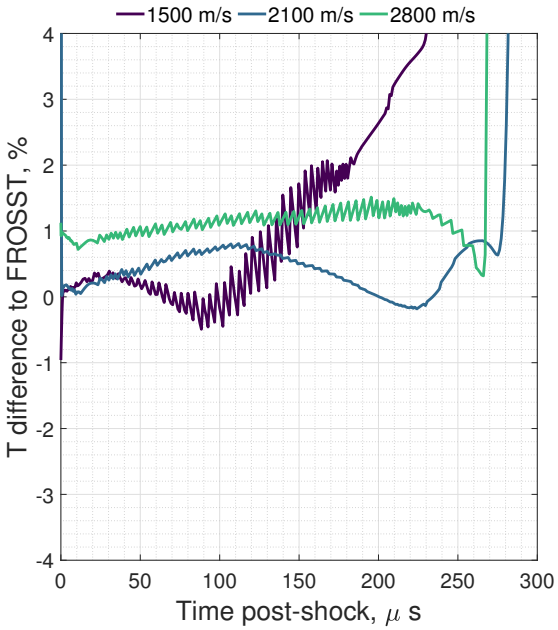

Figure 3.10: Difference between LASTA 2.0 and FROSST predictions for temperature at 9 m from the primary diaphragm

3.5 Non-Equilibrium Thermochemistry Validation

To validate the implementation of the non-equilibrium thermochemistry model, LASTA 2.0 is compared to the Non-equilibrium shock tube solver or NESS (Clarke et al., 2023a). Both NESS and LASTA 2.0 utilise an in-house thermochemistry library known as OCEAN. OCEAN provides functions to evaluate thermodynamic properties, transport properties, and reaction and relaxation rates in non-equilibrium two-temperature plasmas. The parameters of interest and their exact Jacobians with respect to a set of working variables are returned. In this section, the NESS tool and test case are briefly outlined and results are discussed.

3.5.1 NESS

NESS solves the compressible, steady Navier-Stokes equations in quasi-one dimensional form to establish the flow state behind the normal shock wave in a shock tube. NESS utilises a Park two-temperature approach to model the thermochemical relaxation behind the shock wave. NESS is the first tool to combine the solution of the viscous Navier-Stokes equations with appropriate source terms for mass loss from the core flow to the boundary layer, however, NESS is used here in its most basic form with no boundary layer source terms and initialised with the Rankine-Hugoniot post-shock properties. NESS has been validated against the POSHAX 3 code (Gollan, 2007) and a variety of experimental data (Clarke et al., 2024a), making it an appropriate choice for comparison to LASTA 2.0.

The validation case chosen is a 5.3 $\mathrm{km\,s^{-1}}$ shock in a 26.6 Pa synthetic air mixture (79 N_2 / 21 O_2 %v/v). Both codes were initialised with the Rankine-Hugoniot post-shock properties and the chemical reaction scheme of Marrone and Treanor (1963). The LASTA 2.0 simulation was run with 150 streamwise grid points compared to 4000 for the NESS simulation [4]. LASTA 2.0 was run with a constant shock speed. No boundary layer effects were included for either code.

3.5.2 Results

Results from the validation simulations are shown in Figure 3.11. Excellent agreement between the codes is generally achieved between the codes with differences closer to the

[4]LASTA 2.0 is in principle limited to a lower grid resolution that NESS because of the added computational cost of solving at many time points. Five time points were used in the simulation presented in this section.

shock due to the viscous effects modelled by NESS that are not included in LASTA 2.0.

3.5.3 Streamwise grid dependence study

A grid refinement study was performed to assess the effect of the number of post-shock cells on the non-equilibrium region. Here, the simulations settings were maintained from the previous section but the number of stream wise grid points were increased. The resulting vibrational-electronic temperature profiles and percentage difference to the highest grid density case are shown in Figure 3.12. The maximum temperature difference between the cases and the finest mesh (n = 500) was 307, 23, 7, and 3 K. This corresponds to a convergence of within 1.5% for the 200 point case, which is deemed as a satisfactory compromise between computational time and accuracy and is used as a minimum grid size for the remainder of the document.

The slug-length should be taken into consideration when determining an appropriate grid size. The LASTA 2.0 grid is built in non-dimensional units and the physical size of the grid changes depending on the slug length at a given time step. The slug-length for this refinement study was 406 mm, thus a minimum grid density of 0.5 points per mm is required[5]. In practice, the minimum grid size is dependent on the thermochemical model and grid independence should be confirmed on a case by case basis.

3.5.4 Time-wise grid dependence study

A refinement study considering the number of time steps choses was also performed. Here, it was necessary to interrogate a non-uniform shock trajectory as a uniform trajectory, such as the one used as a test case so far in this section, does not yield time dependent differences in the solution and hence does not indicate if time-wise grid independence has been achieved. A fictitious shock trajectory was devised for this purpose and is shown in Figure 3.13. The trajectory decelerates by 318 $\mathrm{m\,s^{-1}}$ over 5.1 m and follows a cubic polynomial trend. These parameters were selected as they are representative of the typical deceleration that occurs in the T6 AST [6].

For this study, a 26.6 Pa synthetic air mixture (79 N_2 / 21 O_2 %v/v) was again selected. LASTA 2.0 was initialised with Rankine-Hugoniot post-shock properties and the chemical reaction scheme of Marrone and Treanor (1963). The simulations was run with 220 streamwise grid points and the number of time-wise points was varied between 15

[5] Note that the grid spacing is not uniform and is biased toward the shock front, as discussed in Section 3.4.2

[6] See the next section for examples

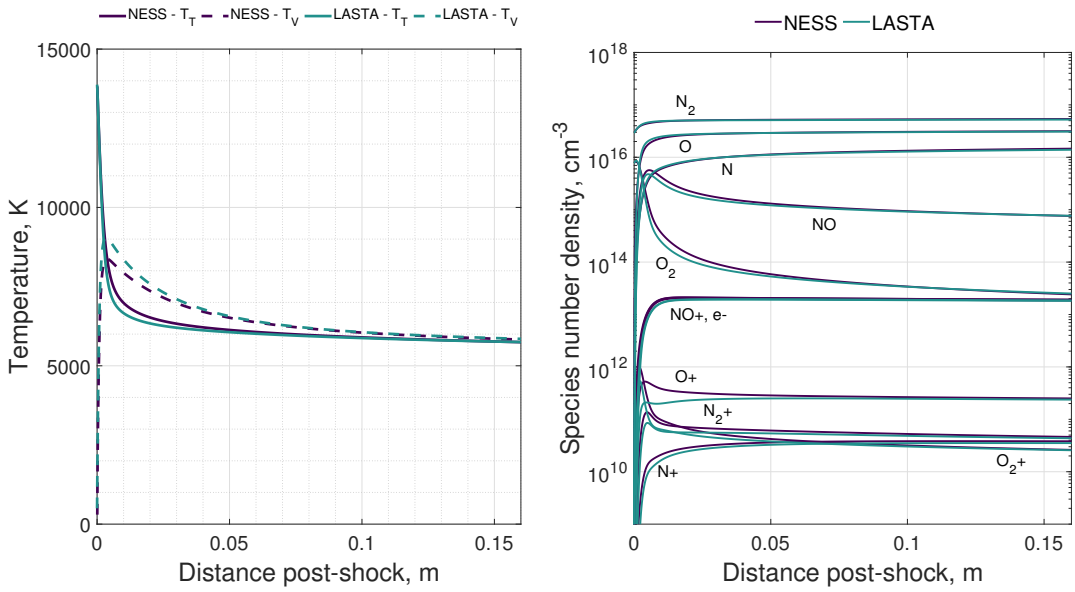

(a) Mode temperatures

(b) Species number densities

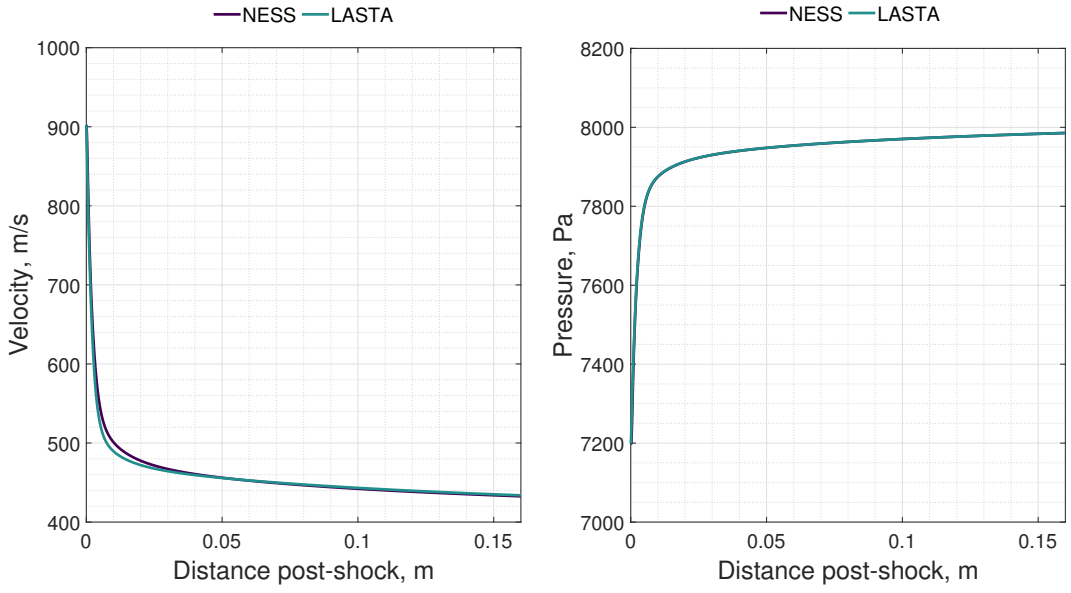

(c) Velocity

(d) Pressure

Figure 3.11: Comparison between LASTA 2.0 and NESS simulation results

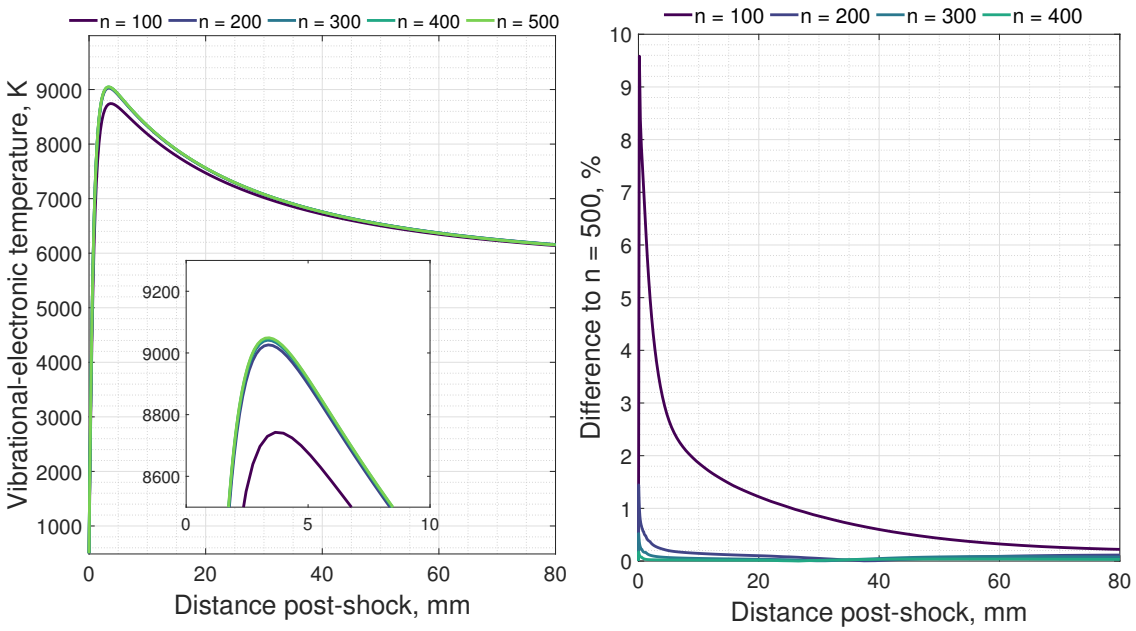

(a) T_V (b) Percentage difference in T_V

Figure 3.12: Dependence of the predicted vibrational-electronic temperature on the number of streamwise points chosen

and 95. Boundary layer effects were included in the simulations so that an assessment of the assumption of instantaneously boundary layer reshaping discussed in Section 3.2.2 could be made. It would be expected that, if this was a poor assumption, changing the number of time steps would have a large effect on the solution because the incorrect boundary layer shape had been used.

The predicted vibrational-electronic temperatures for four time-wise grid sizes (15, 30, 60, and 95) are shown in Figure 3.14a. The percentage difference between each result and the prediction for the highest grid density ($t = 95$) is shown in Figure 3.14b. The $t = 60$

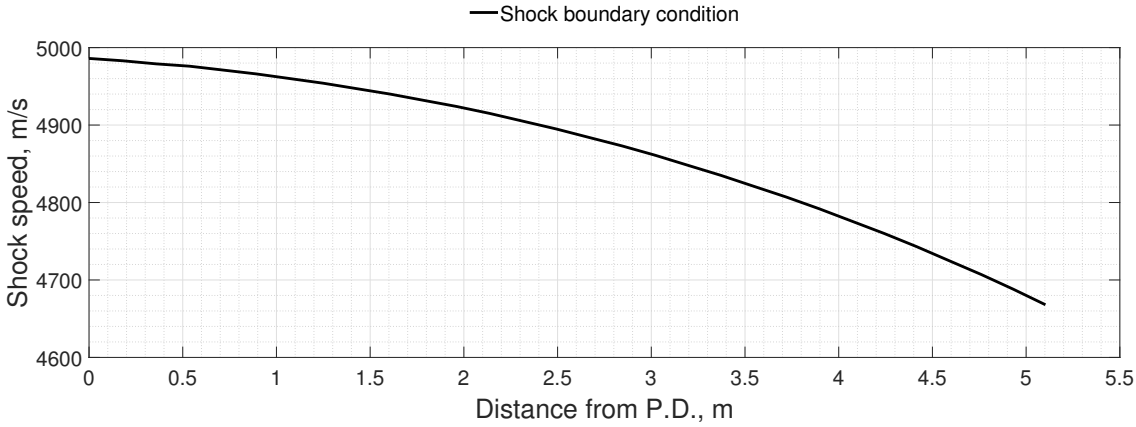

Figure 3.13: Shock speed as a function of distance from the primary diaphragm for the time-wise grid dependence study

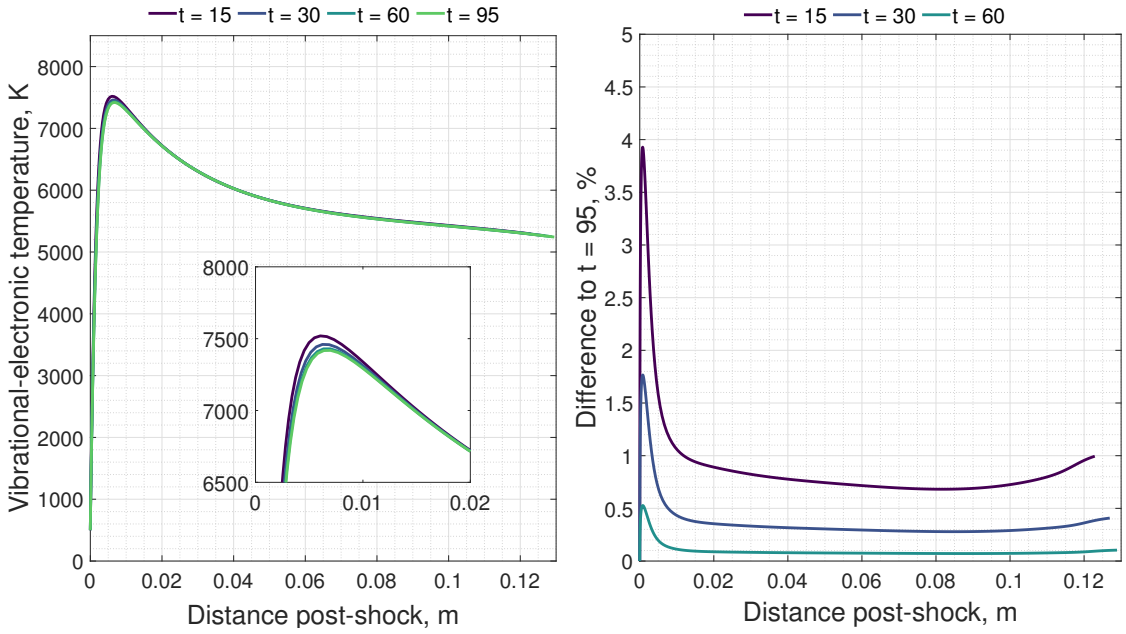

(a) T_V (b) Percentage difference in T_V

Figure 3.14: Dependence of the predicted vibrational-electronic temperature on the number of time steps chosen

and $t = 90$ cases converge to within 0.5% which is deemed acceptable for subsequent simulations. This also demonstrates that, at least for this test case, the instantaneous boundary layer reshaping assumption is acceptable.

3.6 Non-Reacting Shock Tube Application

Given the satisfactory agreement seen between FROSST and LASTA 2.0 in the previous section, LASTA 2.0 is now applied to experimental cases where more complex upstream waves are expected to be present. All experiments were performed in the T6 Stalker Tunnel and have previously been used as validation for LASTA 1.0 (Satchell et al., 2022c).

3.6.1 T6 Stalker Tunnel AST Mode

The operation of the T6 Stalker Tunnel has been discussed in detail in Chapter 5, so it is not repeated here. The experiments included here were performed in the T6 Aluminium Shock Tube (AST), shown schematically in Figure 4.3. This configuration features a conical expansion nozzle at 3.8 m from the primary diaphragm which increases the facility internal diameter from 96.3 mm to 225 mm. A larger internal diameter offers many advantages if emission spectroscopy is utilised. Further details about the AST are provided by (Collen, 2021).

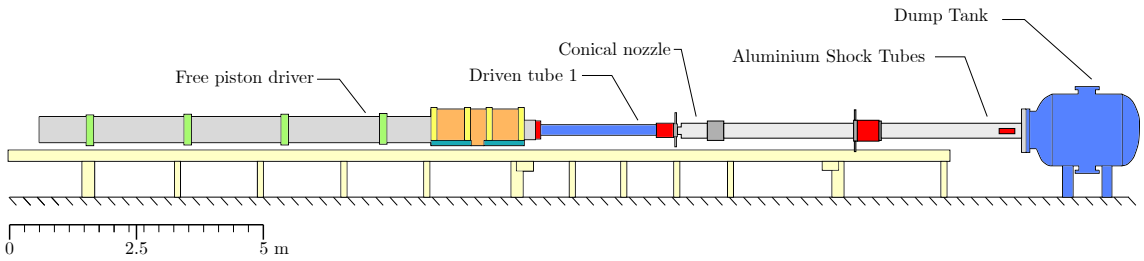

Figure 3.15: Schematic diagram of the T6 Stalker Tunnel in aluminium shock tube mode (AST)

3.6.2 Test cases

Two test cases are considered in this section. Both employed pure Argon as the test gas in an effort to minimise thermochemical effects. Equilibrium simulations of the post shock states indicate that only 0.1% of the test gas was ionized at any point. The experimental shock trajectories for the two cases are shown in Figure 3.16. Both cases feature deceleration after the conical expansion located at 3.8 m. Here, the pressure profile obtained from shock timing station 17 located at a distance 9.584 m from the primary diaphragm, is always used as the pressure boundary condition for LASTA 2.0 simulations. Both LASTA 1.0 and 2.0 simulations were initiated at the 4.31 m from the primary diaphragm so as to exclude the conical expansion section. Grid discretisation and workstation settings remained the same as those specified in Section 3.4.

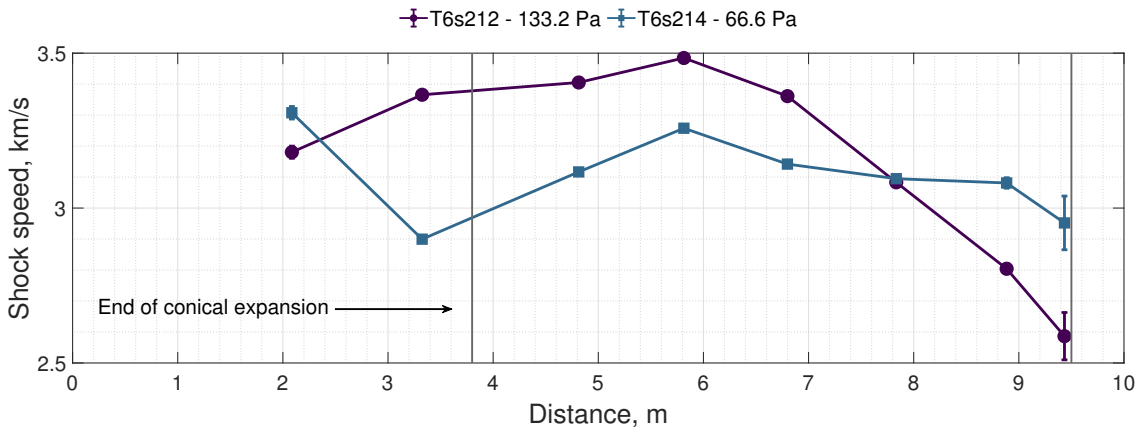

Figure 3.16: Shock speed as a function of distance from the primary diaphragm for the two experimental test cases

3.6.3 Results

Pressure profiles obtained from experiment, LASTA 1.0, and LASTA 2.0 simulations for T6s212 are shown in Figure 3.17. Results are presented at locations corresponding to the three most downstream static pressure transducers available. STS-17, STS-15, and STS-13 are the names of the pressure transducers are they are located at axial distances of 9.584 m, 9.384 m, and 8.934 m from the primary diaphragm respectively. A 200 kHz bandpass filter has been applied to all experimental data presented. This case features strong shock deceleration between 6.0 and 9.5 m which is expected to highlight the differences between LASTA 1.0 and 2.0. LASTA 1.0 generally under predicts the experimental pressure profiles at all locations. Because conservation of momentum is not strictly enforced in LASTA 1.0, gas 'slices' at the rear of the slug that have a higher post shock speed are not able to exchange their momentum for pressure with slices further ahead. This manifests as a non-physical drop in pressure toward the rear of the slug. The effect is more apparent in the experimental data than the FROSST cases in Section 3.4 as shock deceleration occurs over a much shorter distance, 3.8 m versus 7.0 m.

LASTA 2.0 generally shows improved agreement with the experimental data. The domain of influence of the pressure boundary condition is evident in Figure 3.17 as the point where LASTA 2.0 profiles depart from LASTA 1.0. This point moves further back in the slug for timing stations further upstream. This is a demonstration of the utility of reverse time integration approach for shock tubes cases with strong shock speed non-uniformity as improved information is available not only at the location of the boundary condition, but also upstream of it.

Pressure profiles obtained from experiment, LASTA 1.0, and LASTA 2.0 simulations

Table 3.1: Summary of test time predictions at the location of STS-17

Shot Number	p_1, Pa	U_s, m/s	ℓ, m	LASTA 1.0 τ, us	LASTA 2.0 τ, us
T6s212	133.2	2700 - 3500	0.826 - 0.875	520	424
T6s214	66.6	3000 - 3200	0.973 - 0.983	324	345

for T6s214 are shown in Figure 3.18. Better agreement between LASTA 1.0 and experiment is seen here because of the less extreme shock trajectory for this case. The shock speed profile is relatively flat and is therefore not expected to be a strenuous test case for the LASTA 1.0 methodology. The domain of influence of the new pressure boundary condition is again evident for this test case with LASTA 2.0 showing generally improved agreement with experimental data versus LASTA 1.0 in these regions.

Slug length predictions differ between each version of LASTA in both test cases. Although the theory of Mirels assumes a steady shock speed, it can be used here to provide upper and lower bounds for the expected slug lengths in each test case. Table 3.1 summarises the predictions of Mirels' theory over the range of shock speeds in each experimental case expected at STS-17, 9.584 m from the primary diaphragm. It should be noted that Mirels' predictions are made assuming the trajectory began at the end of conical expansion, which will lead to an under-prediction of the experimental case where the test slug will have time to grow before and during the conical expansion. Notably, the LASTA 1.0 slug length predictions are much greater than those of LASTA 2.0 for the strongly decelerating T6s212 case. The reasons for the differing predictions are similar to those discussed in Section 3.4, primarily that the one-dimensional nature of the methods cannot account for complex, multidimensional driver/test gas interactions.

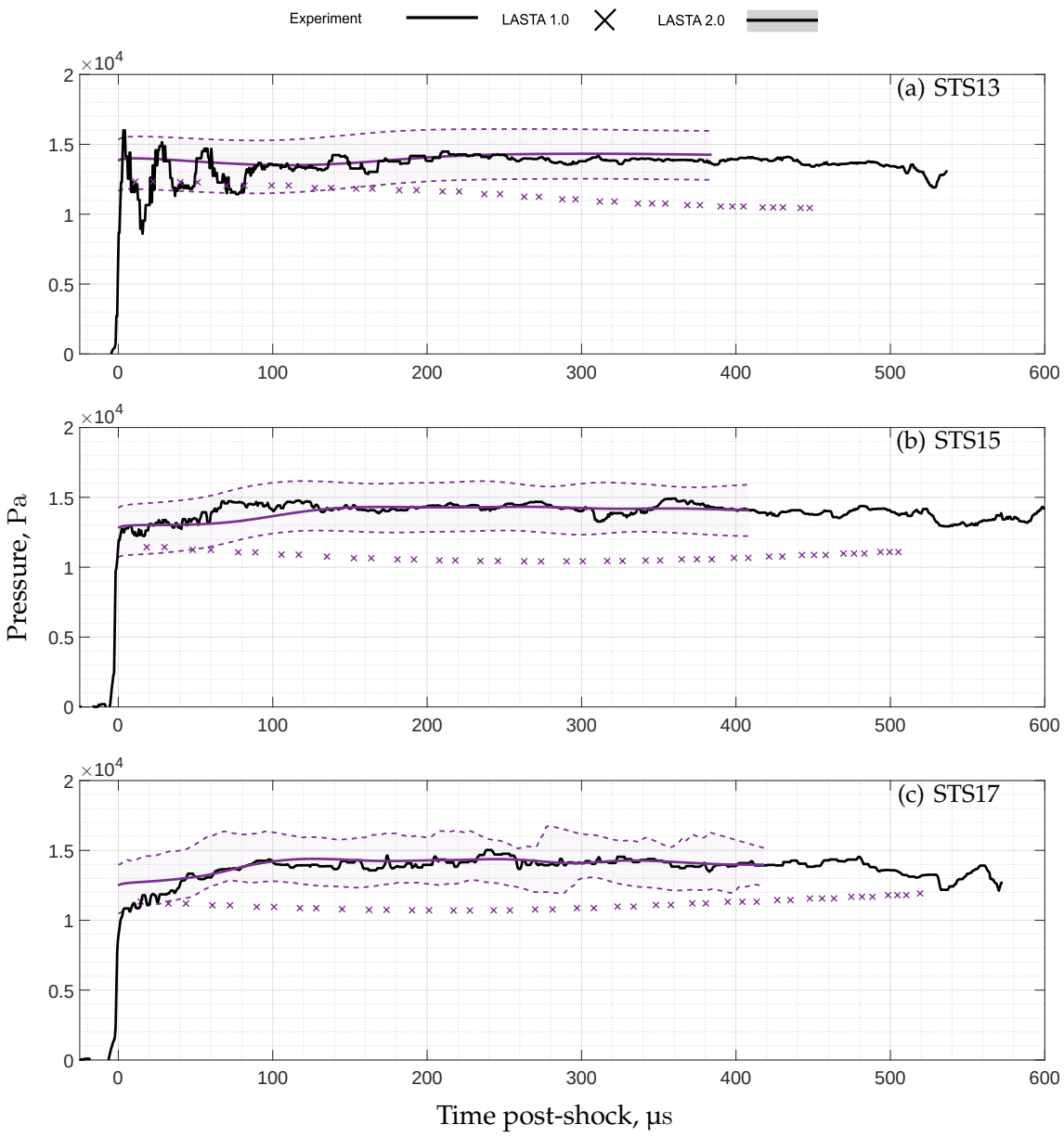

Figure 3.17: Comparisons between experimental pressure profiles and those obtained from LASTA 1.0 and LASTA 2.0 for T6s212. Dashed lines and shaded region represent $\pm 100\ \mathrm{m\,s^{-1}}$ perturbations to the shock trajectory

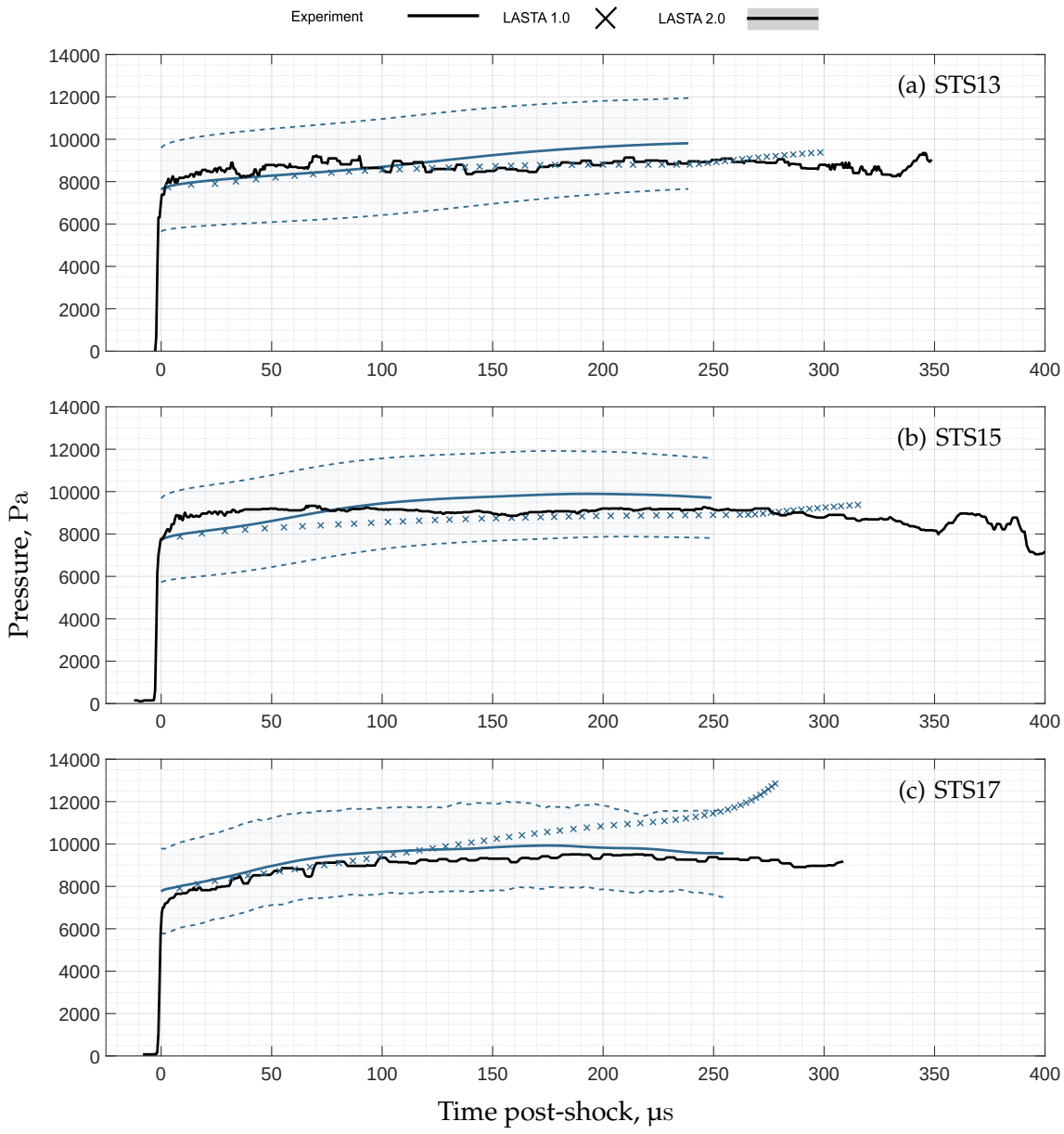

Figure 3.18: Profiles of temperature obtained a three axial locations along the shock tube from FROSST, LASTA 1.0, and LASTA 2.0 for T6s214. Dashed lines and shaded region represent $\pm 100\ \mathrm{m\,s^{-1}}$ perturbations to the shock trajectory

3.7 Summary

A novel, rigorous approach to shock tube modelling has been validated against established numerical tools and applied to several test cases. It has been demonstrated that, via a reverse time integration method, it is possible to extract valuable information about wave trains originating from the driver gas by utilizing available pressure data as a boundary condition. This method removes the need for non-physical constraints on pressure that are present in previous attempts which allows for the implementation of non-equilibrium thermochemistry and application to expansion tube flow reconstruction. Improved agreement with experimental data has been demonstrated versus the previous version of the code in the region where corrections from the new boundary condition may propagate. The tool is applied to test cases with strong non-equilibrium effects in the next chapter.

Chapter 4

The Effect of Shock Speed Variation on Non-Equilibrium Thermochemistry in Shock Tubes

Contents

4.1 Introduction

The previous chapter presented the development and validation of a new shock tube modelling methodology. In this chapter, LASTA 2.0 is used to analyse shock tube test cases with shock speed non-uniformity to assess the performance of the tool and the new features, in particular the implementation of a Park two-temperature thermochemical model. Shock tubes are an essential source of thermochemical rate data for validation

of numerical models used to design hypersonic vehicles. An improved understanding of the operation of shock tube facilities is not only valuable intrinsically, but directly translates into improved confidence in vehicle performance.

Similarity between the shock tube flow and the flight vehicle is achieved by matching the composition, velocity, and density of the gas between the two cases. Whereas the flight vehicle encounters only relatively small changes in freestream velocity over a short timescale, the speed of the shock wave in a shock tube may change significantly as it propagates from the primary diaphragm to the measurement location. This variation has been shown to lead to a strong enthalpy and temperature gradient in the final test slug, as shown in Figure 4.1. Compression effects from the growth of the boundary layer also lead to a non-linear time of flight for gas in the test slug when progressing backward from the shock. For both of these reasons, treating the test gas as if it been produced via a constant shock speed leads to error in measurements of the thermochemistry.

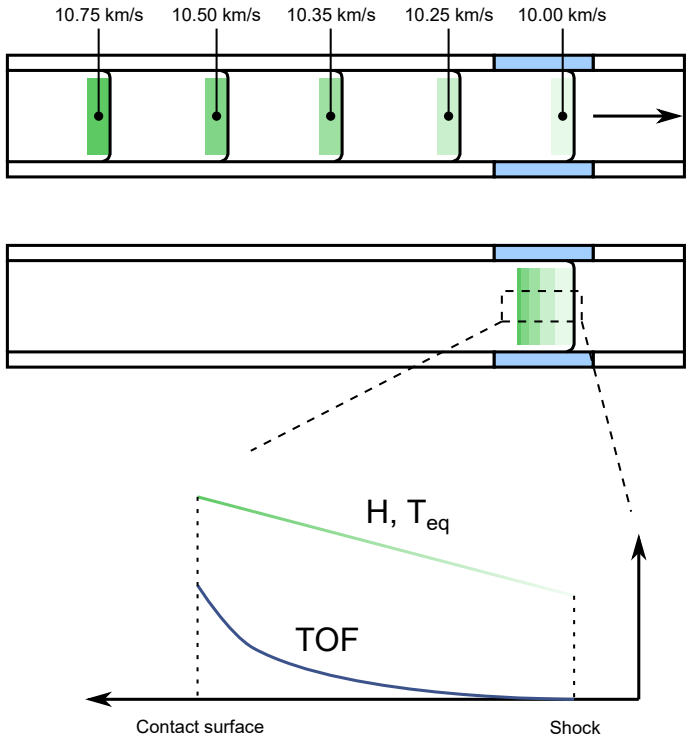

Figure 4.1: Enthalpy, temperature, and time of flight gradient in a shock tube test slug resulting from a decelerating shock trajectory, adapted from Brandis et al. (2010)

LASTA 1.0 has been used to reinterpret historical radiation data from the T6 and EAST facilities. Collen et al. (2022) purposely designed driver conditions in the T6 facility that would result in accelerating, decelerating, and flat shock trajectories in synthetic air mixtures, importantly all terminating in a similar shock speed at the measurement window. Spectrally integrated radiance measurements between 760 and 780 nm were obtained that

showed clear differences due to the shock history. Combined LASTA 1.0/NEQAIR simulations using the experimental shock trajectories were run to provide a comparison to the experimental data. The experimental shock speeds were obtained at a maximum of 11 points in the tube, corresponding to a measurement density of one every $0.82\ \mathrm{m}$. This number of measurements was insufficient to initialise the LASTA 1.0 simulation with the desired grid density and thus either a cubic spline or polynomial fit was applied to interpolate between the available data points. The LASTA 1.0 simulation provided, under an assumption of thermochemical equilibrium, the temperatures and species number densities behind the shock wave at the time of measurement which were used as an input to a radiation model.

Agreement with experimental results in the equilibrium region was generally very good, especially toward the front (shock) of the test slug. However, the equilibrium assumption precluded accurate modelling of the radiance in the non-equilibrium region. POSHAX 3 simulations of the test conditions assuming a constant shock speed were shown to bound the LASTA 1.0 equilibrium results, indicating that the equilibrium assumption was valid for modelling in that region, however a clear distinction between the non-equilibrium and equilibrium regions could not be made because neither LASTA 1.0 or POSHAX 3 could simultaneously model non-equilibrium thermochemistry and non-uniform shock trajectory effects. Predictions of the post-shock electron number density were also shown to agree within an order of magnitude. Only radiance from the oxygen 777 nm line was considered in detail in this study. Oxygen has a relatively short relaxation time and thus would be expected to agree well with equilibrium predictions, however molecular radiation from species such as NO should be more strongly influenced by non-equilibrium behaviour and thus show reduced agreement with this simulation approach.

Collen et al. (2023) applied this approach to historical data from the NASA EAST facility to determine if it was facility dependent. The tests analysed featured much larger variations in shock speed when compared to the T6 cases, 5 $\mathrm{km\,s^{-1}}$ vs 2 $\mathrm{km\,s^{-1}}$, and thus were a harsher test case for the LASTA 1.0 approach. The selected test cases were again in synthetic air and focused on the oxygen 777 nm atomic line. Agreement with the EAST data was not as close as with the T6 data, but was still an improvement over an assumption of constant shock speed. Radiance predictions toward the end of the test slug, where the influence of sound waves emanating from the driver is significant, were generally worse. In strongly accelerating cases, for example E50-32, the LASTA 1.0/NEQAIR pre-

dictions departed appreciably from the experiment toward the end of the test slug. This appears to result from an over prediction of the test slug length for this test case, potentially indicating that the implementation of and unsteady Mirels' boundary layer model is not appropriate in the presence of strong shock speed non-uniformity. Again, only the oxygen 777 nm line was analysed in detail and an equilibrium assumption limited the predictions.

There is a need to revisit this promising initial analysis of historical test conditions with a numerical model that can:

1. Simultaneously account for the effect of shock speed variation and non-equilibrium thermochemistry

2. Model the influence of pressure waves emanating from the driver

In this Chapter, the model developed in Chapter 3 is applied to several test cases analysed to demonstrate the new capabilities of the model. Full spectrum radiation predictions for synthetic air, N_2-CH_4, and H_2-He gas mixtures in the T6 and EAST facilities are compared to experiment. The original test cases analysed by Collen et al. (2022, 2023) are revisited to provide a direct comparison between LASTA 1.0 and LASTA 2.0. Finally, the effect of specific model features, such as the pressure boundary condition, is analysed in greater detail by focusing on a single test case.

4.2 Experimental Facilities

Data from two experimental facilities, the NASA EAST and the T6 Stalker Tunnel, are analysed. These facilities are selected as they utilise different driver technologies and tube geometries, allowing the effect of each of these on shock attenuation to be examined.

4.2.1 EAST

The EAST facility has been discussed extensively in many publications and also in Chapter 2, so only a brief overview is provided here. The EAST driven tube has a bore diameter of 10.16 cm and is 12.5 m in length. The facility is driven by means of an electric arc, which discharges 1.2 MJ of energy from a 40 kV capacitor bank into the gas in a buffer tube. The buffer tube typically contains hydrogen or helium and is separated from the driven tube by a thin diaphragm. This driver approach affords EAST a large performance envelope with shock speeds between 1.3 and 46 $\mathrm{km\,s^{-1}}$ possible depending on

the driven gas. Measurements of post-shock radiation in the EAST are made with up to four independent spectrographs coupled to intensified CCD cameras. The spectrographs view the test gas through slot windows in the driven tube just before the dump tank. The use of many spectrometers allows a wide spectral range to be captured for each experiment from the vacuum ultraviolet (VUV) to the near infrared (NIR). EAST has provided support for the design of many NASA planetary entry missions and thus benchmark datasets for a large number of atmospheres and speed ranges are available. These include Venus (Cruden et al., 2012), Mars (Cruden et al., 2016; Brandis et al., 2013; Cruden et al., 2018; Cruden, 2014; Tibère-Inglesse et al., 2023a), Earth (Brandis and Cruden, 2017a; Cruden and Brandis, 2020; Brandis and Cruden, 2018), Saturn, Uranus, Neptune, Jupiter (Cruden and Bogdanoff, 2017; Cruden and Tibere-Inglesse, 2024), and Titan (Bose et al., 2006; Brandis and Cruden, 2017c; Tibère-Inglesse et al., 2023b). A schematic overview of the EAST facility is shown in Figure 4.2.

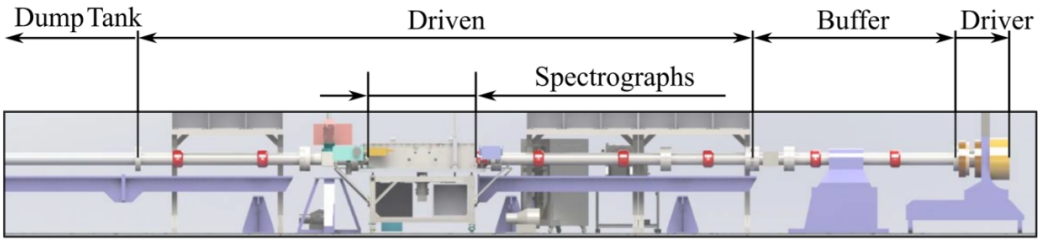

Figure 4.2: Schematic diagram of the EAST facility

4.2.2 T6 Stalker Tunnel

The T6 facility and its various operating modes is discussed at length in other parts of this document so, like EAST, only a brief overview is included here. Data from the AST mode (see Section 3.6.1) with 225 mm bore diameter and the SST mode (see Section 5.2.1) with 96.3 mm bore diameter is analysed here.

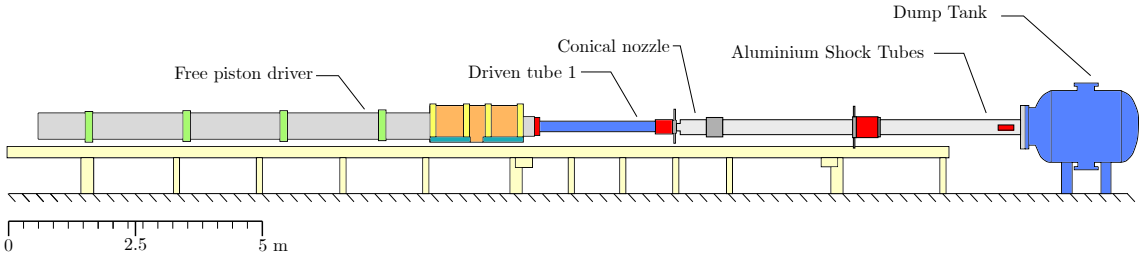

Figure 4.3: Schematic diagram of the T6 Stalker Tunnel in aluminium shock tube mode (AST)

4.3 Simulation Methodology

As discussed in the previous chapter, LASTA 2.0 provides as outputs the profiles of species number density, translational-rotational temperature, vibrational-electronic temperature, velocity, and pressure through the test slug. Data from shock tubes is usually available as a spectrally and spatially resolved image of the test slug radiance. To compare between the two results, a radiation solver is required. The coupling between NEQAIR, the radiation solver used in this work, and LASTA 2.0, is discussed in this section.

4.3.1 NEQAIR v15.2.2

The Nonequilibrium Radiative Transport and Spectra Program (NEQAIR) program, first developed by Park (Park, 1985), is a code for simulating radiative transport which is a benchmark for comparison to shock tube data. The full capabilities of the code are summarised by Cruden and Brandis (Cruden and Brandis, 2014). NEQAIR takes flow-field properties (temperature, species number densities) as inputs and outputs spectral radiation characteristics, including emission and absorption spectra along a given line of sight.

All NEQAIR simulations in this chapter were run with the recommended default settings. The state population method was set to be non-Boltzmann with a local escape flux limited method of 1.0. The shock tube mode was selected with species number densities and position imported directly from the LASTA 2.0 simulation. Boundary conditions were set with no initial radiance and blackbody at the final LOS point temperature so that incident radiant heat flux was returned. The simulation wavelength range was set depending on the feature of interest. Automatic grid spacing was selected with 10 points per line and a range of 10. No spatial scanning was performed unless otherwise stated with the results. NEQAIR was run with the NEQ_QSS_EXC_V environment variable set to 1 to include the updated non-Boltzmann behaviour which became standard in NEQAIR 15.3.

4.3.2 LASTA 2.0

LASTA 2.0 requires an experimental shock trajectory and an optional static pressure profile as boundary conditions. For all of the experiments analysed in this section, the experimental shock speeds are known at relatively few points along the facility and thus

interpolation is required to initialise the simulation with sufficient grid resolution. Either a polynomial or cubic spline fit is used here. The shock trajectories and polynomial fit types are discussed on a shot-by-shot basis in the results section. Static pressure measurements were not available for all of the test conditions analysed, the pressure boundary condition was not imposed for those cases. The simulation domain was comprised of 200 stream-wise points and 35 time points. Mirels source terms were included in all cases. The LASTA 2.0 domain was initialised with a length of 50 mm at time zero.

N_2–O_2 Air Gas Model

An 11-species gas model (e^-, N, O, N^+, O^+, N_2, NO, O_2, NO^+, ${N_2}^+$, ${O_2}^+$) was used for the synthetic air test cases. The reaction scheme is that of Park (1993). The Millikan-White approach to translational-vibrational relaxation times is utilised (Millikan and White, 1963). Detailed discussion of the kinetic models used is presented in Appendix C.

N_2–CH_4 Titan Gas Model

A 19-species gas model (e^-, N, C, H, N^+, C^+, H^+, N_2, CN, CH_4, CH_3, CH_2, CH, C_2, H_2, NH, HCN, ${N_2}^+$, CN^+) was used for the Titan entry simulations. The Gokcen (2007) reaction scheme was used.

H_2–He Giant Planet Gas Model

A 6-species gas model (e-, H, He, H+, He+, H_2) was used to model the hydrogen-helium test conditions. The reaction scheme of Leibowitz (1973) was used in the first instance and is detailed in Appendix C. Radiation predictions for H_2-He flows are known to be highly sensitive to the kinetic rates selected, in particular the hydrogen ionization rates (both heavy particle and electron impact). Carroll et al. (2024) recently examined the effect of different rates from the literature on radiation predictions for the EAST facility with a 23 species state-to-state[1] model. Importantly, this included modelling of a two-step excitation and the ionization process for H which is common in the literature. This approach is currently not possible with LASTA 2.0.

[1]Here, *state-to-state* is intended to mean a method for modelling non-equilibrium thermochemical processes where the quantum state specific behaviour of a some or all species is considered

4.4 Comparison to LASTA 1.0 via Analysis of Oxygen 777 nm Radiance

In this section, a study of radiance from the oxygen 777 nm atomic line is presented. Data from two facilities with different internal diameters, different shock trajectories, and different initial fill pressures are presented. This study is performed as it provides a direct point of comparison to previous work from Collen et al. (2023, 2022) who used LASTA 1.0. Tests in this section consist exclusively of shocks in synthetic air mixtures at low initial pressures.

4.4.1 Test Conditions

Table 4.1 includes the fill pressures (p_1), test gas compositions, shock speeds at the observation window (U_s), and estimates for the Mirels slug length (ℓ_m) at the measurement location assuming a constant shock speed equal to the final shock speed. Improved slug length estimates are provided by the numerical simulations. The slug time estimates (τ_m) are calculated using the final shock speed and steady slug length estimate.

Table 4.1: Summary of test conditions analysed in this chapter

Condition	Symbol	Test Gas Composition, %v/v	p_1, Pa	U_s, km/s	ℓ_m, mm	τ_m, µsec
E50-36		79% N_2 / 21% O_2	26.6	9.02	109.6	12.1
E50-40		79% N_2 / 21% O_2	26.6	8.56	109.8	12.8
T6s164		79% N_2 / 21% O_2	13.3	9.70	156.5	16.13
T6s186		79% N_2 / 21% O_2	66.6	7.55	236.8	31.4

Figure 4.4 shows the experimental shock speed measurements and fit trajectories used in the LASTA 1.0 and 2.0 simulations. For the EAST cases, although the primary diaphragm is located at 0 m, shock trajectory data is only available beginning at 3.74 m. This is not expected to affect the numerical results as it is likely that, as seen in previous work, the test gas that is processed close to the primary diaphragm is entrained in the boundary layer and exits the test slug by the time the shock reaches the optical measurement location. The experimental shock speed appears to fluctuate significantly close to the end of the trajectory however; this effects is caused by the decreased sensor spacing at this location. The shock speeds are calculated by a finite difference method and thus a decreased sensor spacing increases uncertainty. This is a direct illustration of the need for an improved method of shock speed measurement in shock tubes, such as the microwave

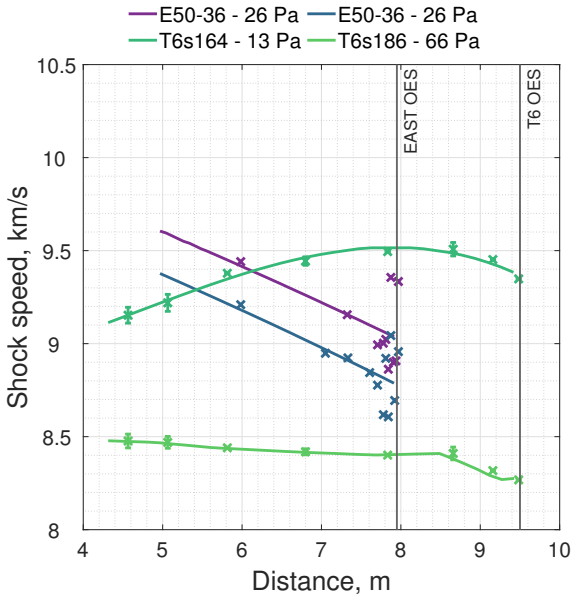

Figure 4.4: Experimentally measured shock speeds and fitted polynomial for E50-40

sensor of Dufrene et al. (2015).

The T6 experiments were run in AST mode where the tube diameter is 225 mm. One accelerating and one decelerating trajectory were selected. The location of the T6 OES system is further downstream than the EAST system with respect to the primary diaphragm and this is indicated in Figure 4.4.

Pressure data was available for the T6 cases, but not the EAST cases. The pressure sensors installed during the EAST 50 test series had a decay time that was long enough to allow them to be used for shock timing, but too short to allow them to be used for an accurate pressure measurement during the test time. Analysis of this test series is valuable as it provides an opportunity to compare directly against LASTA 1.0 predictions made by Collen et al. (2022). The pressure boundary conditions imposed on the T6 simulations are shown in Figure 4.5.

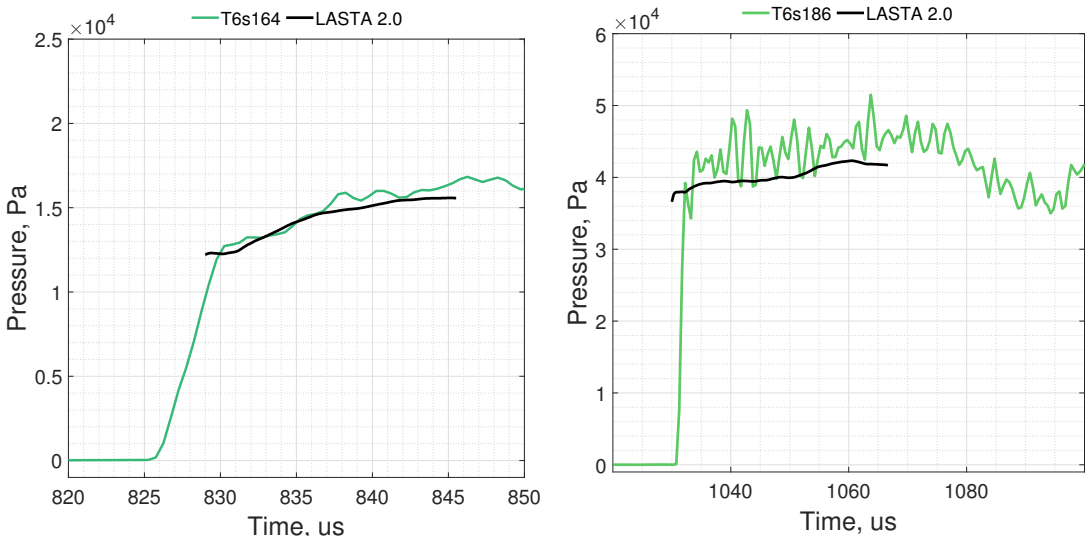

(a) T6s164 (b) T6s186

Figure 4.5: Experimental pressure boundary conditions for the T6 simulations

4.4.2 Oxygen 777 nm Radiance Predictions

EAST Experiments: E50-36 & E50-40

Figure 4.6 shows radiance profiles integrated between 760 nm - 800 nm for E50-36. The experimental measurement, LASTA 1.0, and LASTA 2.0 predictions are shown. The LASTA 1.0 results have been extracted directly from Collen et al. (2023) where identical NEQAIR settings to those described in Section 4.3.1 were used. There is good agreement between the three in the equilibrium region. The increasing radiance in the equilibrium region when moving toward to rear of the test slug reflects decelerating shock trajectory, as gas further toward the rear of the slug was shocked at a higher speed and thus equilibrates to a higher temperature.

Figure 4.7 shows the mode temperature and oxygen number density profiles predicted for this test case[2]. These metrics are included as the oxygen 3p-3s transition is primarily responsible for the radiation observed in the 760 nm - 800 nm region and the radiance of a particular atomic transition is proportional to the population of the excited state[3]. As expected, both temperatures and the O+ number density increase when moving toward the rear of the test slug due to the decelerating shock trajectory, the combination of these factors is responsible for the increase in radiance.

The CEA equilibrium predictions for a 9.02 $\mathrm{km\,s^{-1}}$ are included in both plots, corresponding to the final point in the shock trajectory. The temperatures and O number density are reasonably well predicted by the equilibrium assumption, however the O^+ number density is under-predicted by a factor of approximately 2. By considering the inset plot, this appears to be because the O^+ concentration does not have time to fully relax to the equilibrium value before it is influenced by waves from the higher temperature gas further back in the slug.

The non-equilibrium peak radiance is under-predicted by LASTA 2.0 when convolved with the experimental SRF. There are a number of reasons why this might be the case. First is the assumption of Rankine-Hugoniot post-shock properties. Clarke et al. (2023a) have shown that inclusion of viscous terms to model the effect of shock thickness lead to appreciably different (lower or higher) post-shock temperatures immediately post-shock than those predicted by the Rankine-Hugoniot assumption. Both radiance and reaction rates, in particular the ionization rate of oxygen atoms, are directly proportional to tem-

[2]These parameters have not been spatially convolved, only the radiance profile is convolved in this section unless otherwise stated

[3]It should be noted that the 11 species model does not capture the state populations of individual species but this is modelled by the non-Boltzmann local escape factor approach in NEQAIR

perature and thus LASTA 2.0 predictions may differ from experiment. Another reason for the difference could be the thermochemical model chosen, in particular the choice of the $\hat{c}_1$ parameter. Kim and Jo (2021) demonstrate that use of a constant value for $\hat{c}_1$ may not be appropriate, rather some dependence on temperature should be considered. It could also be that the reaction rates themselves require modification, which has been suggested by many authors. Finally, the 11-species model cannot account for any of the state-specific processes occurring and is inherently an engineering approximation.

Figure 4.15 shows a comparison between the experimental and LASTA 2.0-NEQAIR predicted radiance profiles for E50-40. Good agreement between LASTA and experiment is seen in the equilibrium and is consistent with the findings of Collen et al. (2023), which are also co-plotted. As seen in Chapter 3, the LASTA 1.0 and LASTA 2.0 predictions deviate toward to end of the test slug.

Figures 4.8a and 4.8b show the LASTA 2.0 predicted profiles of temperature and atomic oxygen number density for E50-40. The OCEAN equilibrium temperature predictions for the initial and final shock speeds are also included in Figure 4.8a. As might be expected, the temperature at immediately after the non-equilibrium temperature is close to the final shock speed equilibrium temperature with a gradual increase toward the initial shock speed equilibrium temperature moving backward through the test slug.

The OCEAN predicted equilibrium number densities for O and O^+ are shown in Figure 4.8b. The equilibrium assumption predicts O number density well and bounds the LASTA 2.0 predicted O^+ number density. The increase in radiance seen in Figure 4.15 is driven by the increase in O^+ beginning at 70 mm post-shock, which is in turn driven by the electron impact ionization reactions in the Park model[4].

The slug length is over-predicted for both EAST test cases analysed due to the exclusion of the pressure boundary condition. Exclusion of the pressure boundary condition effectively neglects the influence of upstream wave processes which in this case, appear to have caused compression of the test slug. Availability of reliable pressure data at the measurement window would significantly improve the performance of LASTA 2.0 for these test cases.

[4]The last three reaction mechanisms shown in Appendix C.1

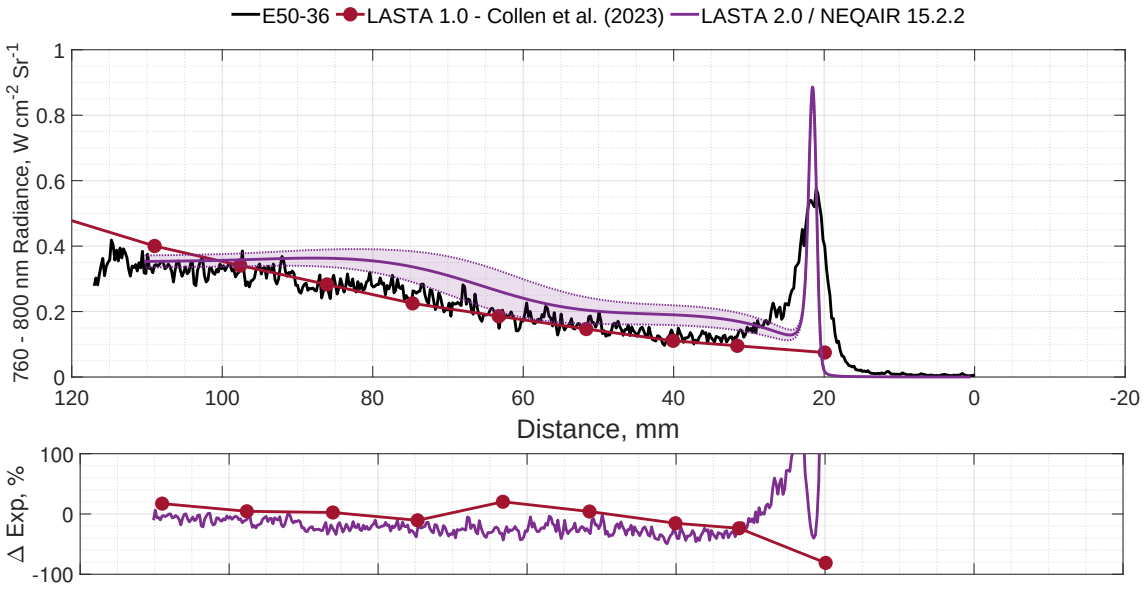

Figure 4.6: Integrated 760 nm - 800 nm radiance profiles for shot E50-36 and percentage difference to experiment. Dashed lines and shaded region represent $\pm 100\ \mathrm{m\,s^{-1}}$ perturbations to the shock trajectory

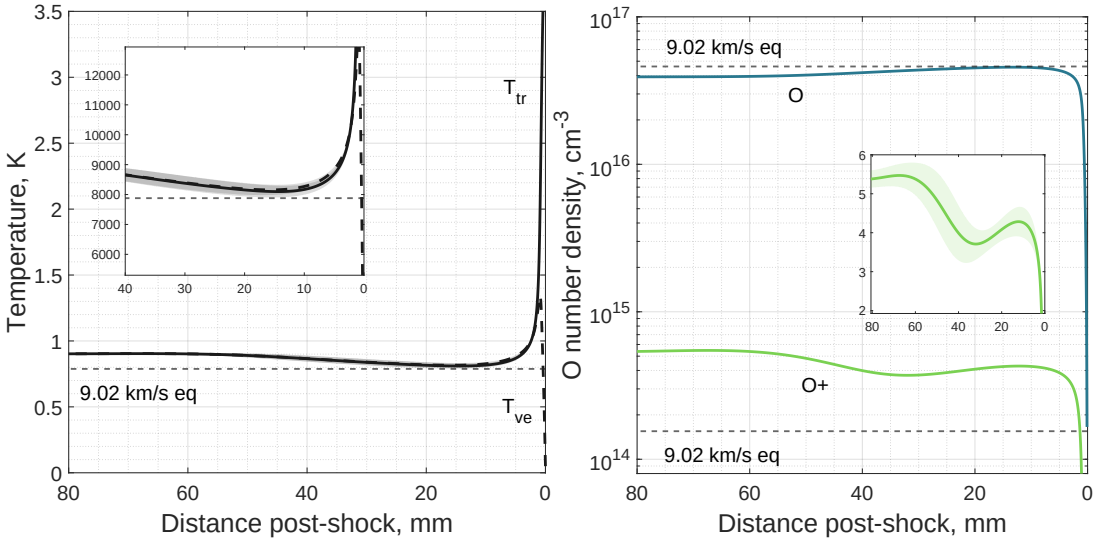

(a) Temperatures

(b) Oxygen number density

Figure 4.7: Temperature and number density profiles predicted by LASTA 2.0 for E50-36. Dashed lines and shaded region represent $\pm 100\ \mathrm{m\,s^{-1}}$ perturbations to the shock trajectory

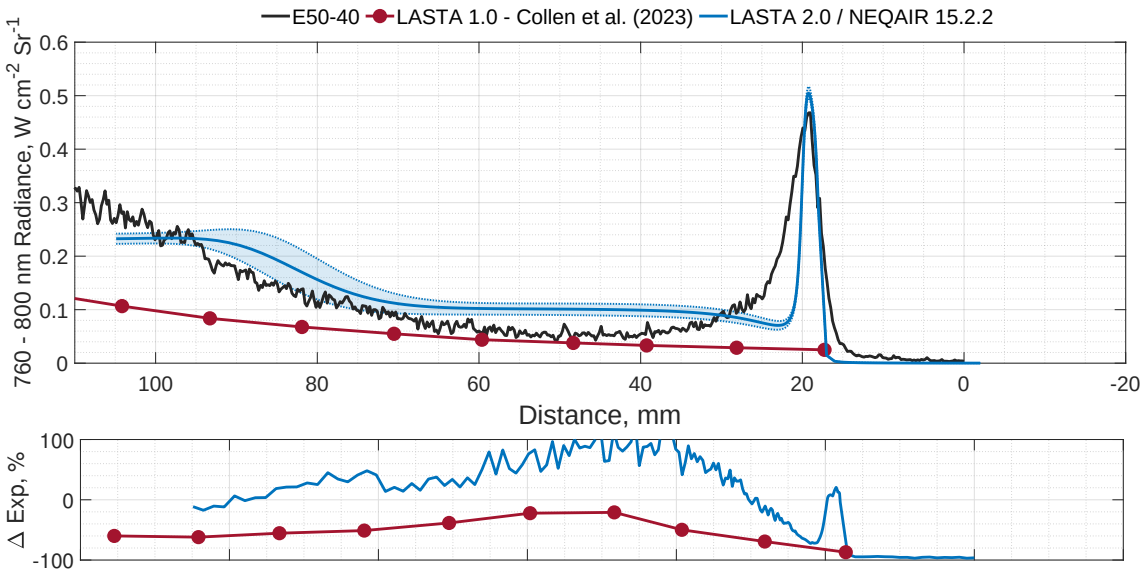

Figure 4.8: Integrated 760 nm - 800 nm radiance profiles for shot E50-40 and percentage difference to experiment. Dashed lines and shaded region represent $\pm 100\ \mathrm{m\,s^{-1}}$ perturbations to the shock trajectory

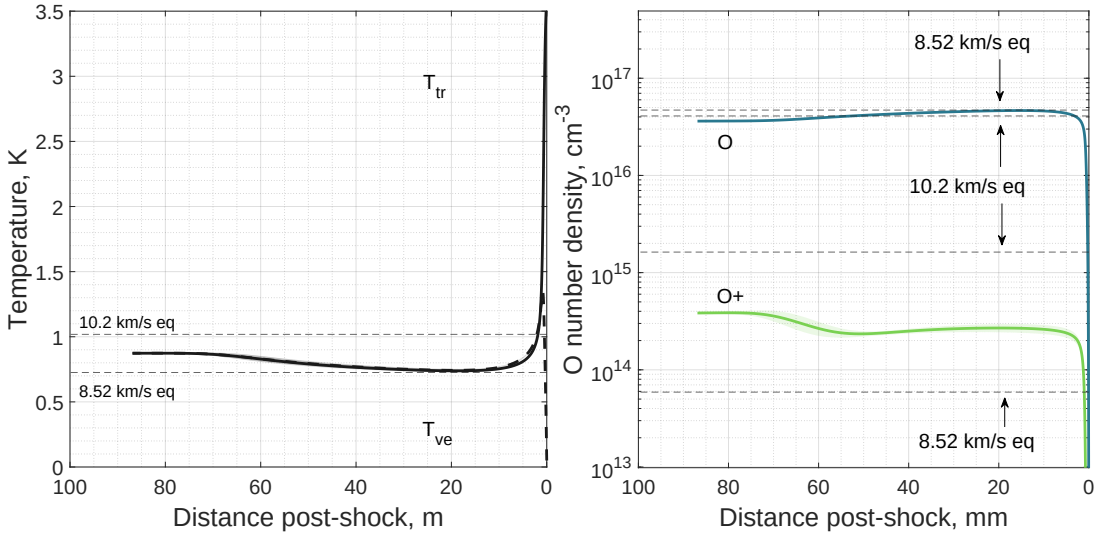

(a) Temperatures

(b) Oxygen number density

Figure 4.9: Temperature and number density profiles predicted by LASTA 2.0 for E50-40. Dashed lines and shaded region represent $\pm 100\ \mathrm{m\,s^{-1}}$ perturbations to the shock trajectory

T6 Experiments: T6s164 & T6s186

The integrated 760 - 800 nm radiance profiles are shown for the experiment, LASTA 1.0[5], and LASTA 2.0. Following the method of Brandis and Cruden (2017b), the LASTA 2.0 result is convolved with a 5 mm rectangular and 5 mm triangular blurring function to account for the motion of the shock during the camera gating and for the off-axis position of the non-equilibrium peak. This method was also used by Collen et al. (2022). LASTA 2.0 results with a constant shock speed are also shown as a demonstration.

There is again good agreement between the three methods in the equilibrium region. The difference between LASTA 1.0 and 2.0 in the equilibrium region is attributed to differences in the fitted shock trajectory. The sensitivity of radiance from the oxygen 777 nm line to temperature, and hence shock speed, is relatively high in this regime. As in the EAST test cases, the radiance in the non-equilibrium region is also under-predicted. The reasons for this presented in the previous section and also applicable to this case.

The temperature and oxygen number density profiles for T6s164 are shown in Figure 4.11. A gentle decrease in temperature toward the rear of the test slug is evident due to the accelerating shock trajectory. The effect is less pronounced than for the EAST cases because the magnitude of the change in shock speed is smaller, approximately + 600 $\mathrm{m\,s^{-1}}$ versus - 2 $\mathrm{km\,s^{-1}}$. This is also reflected in the oxygen number density profiles.

The radiance predictions and experimental measurements for this case are shown in Figure 4.12. There is again good qualitative agreement between the three methods. LASTA 2.0 radiance predictions are 46% greater than LASTA 1.0 at 27 mm post-shock which decreases to 17% by 90 mm. This difference is again likely due to slight differences in the selected shock trajectory and the high sensitivity of oxygen 777 nm radiance to temperature in this regime.

The temperature and number density profiles are shown in Figure 4.13. Relaxation to equilibrium occurs more quickly in this test case because of the increased fill pressure. Both the O number density and temperature predictions agree well with the 7.55 $\mathrm{km\,s^{-1}}$ equilibrium predictions, with the O^+ number density slightly over predicted.

[5]Obtained from Collen et al. (2022), rather than Collen et al. (2023) as for previous cases

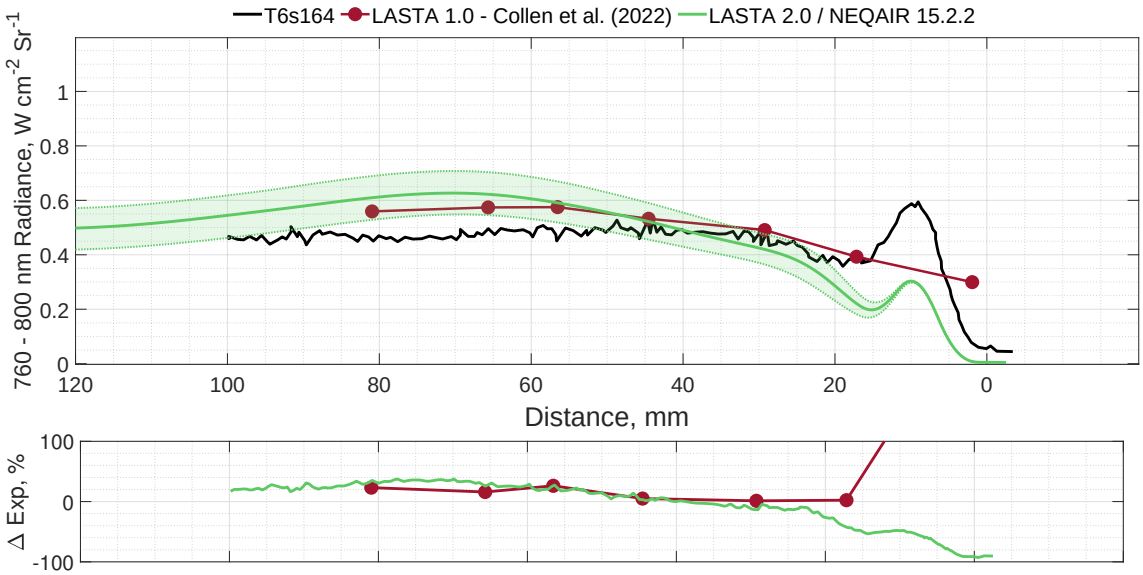

Figure 4.10: Integrated 760 nm - 800 nm radiance profiles for shot T6s164 and percentage difference to experiment. Dashed lines and shaded region represent $\pm 100\ \mathrm{m\,s^{-1}}$ perturbations to the shock trajectory

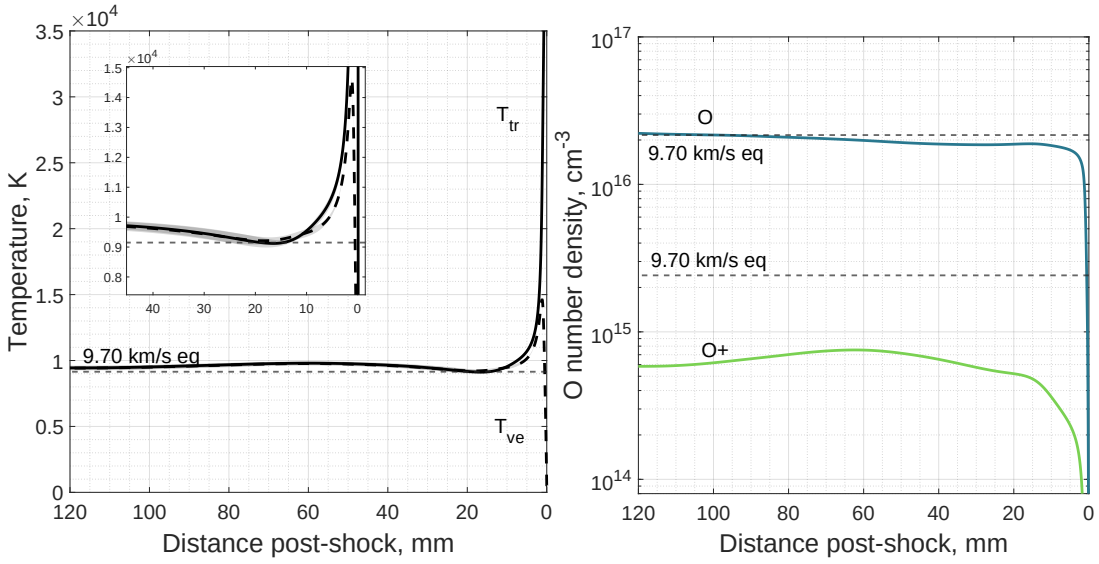

(a) Temperatures

(b) Oxygen number density

Figure 4.11: Temperature and number density profiles predicted by LASTA 2.0 for T6s164. Dashed lines and shaded region represent $\pm 100\ \mathrm{m\,s^{-1}}$ perturbations to the shock trajectory

Figure 4.12: Integrated 760 nm - 800 nm radiance profiles for shot T6s186. Dashed lines and shaded region represent $\pm 100\ \mathrm{m\,s^{-1}}$ perturbations to the shock trajectory

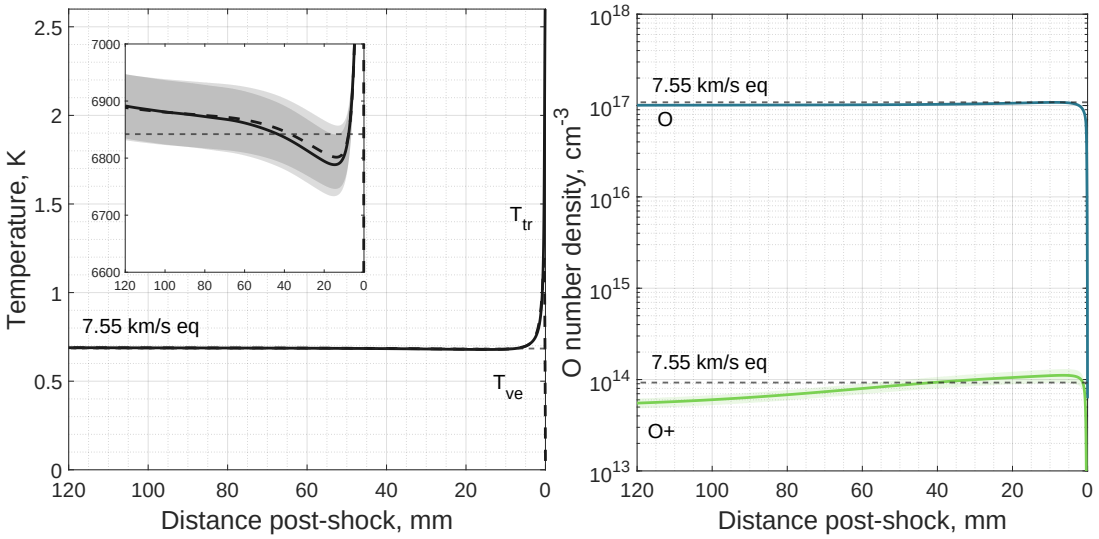

(a) Temperatures

(b) Oxygen number density

Figure 4.13: Temperature and number density profiles predicted by LASTA 2.0 for T6s186. Dashed lines and shaded region represent $\pm 100\ \mathrm{m\,s^{-1}}$ perturbations to the shock trajectory

4.5 Full Spectrum Radiation Predictions for Shock Tube Experiments in Various Gas Mixtures

The capabilities of LASTA 2.0 to simulate a wide variety of test conditions are demonstrated in this section. Several gas mixtures and reaction schemes are used which a representative of a number of planetary entry trajectories including Lunar return, Titan entry, and Giant Planet entry. Radiation predictions over the full experimental dataset are provided for each case. Unless otherwise stated, the *final shock speed* quoted for each test case refers to the velocity obtained from the polynomial/spline fit at the centre of the OES field of view.

4.5.1 N_2–O_2: Lunar Return

This section focuses on a test case in the EAST facility, originally for determination of the radiation expected for a Lunar return mission such as Artemis (Cruden, 2012). Test E50-40 was run in the 4 inch (101.6 mm) EAST driven tube with a fill pressure of 0.2 torr (26.6 Pa) and a composition of 79 N_2-21 O_2 %v/v. The final shock speed was determined to be 8.56 $\mathrm{km\,s^{-1}}$.

The experimentally measured shock speeds and fitted polynomial for this test case are shown in Figure 4.14. This test case decelerates by nearly 2 $\mathrm{km\,s^{-1}}$ from the first experimentally measured shock speed to the measurement window, making it an interesting LASTA 2.0 test case. No pressure data was available, so the pressure boundary condition imposed was $\frac{\partial p}{\partial t} = 0$.

The full-spectrum radiance profiles for this test case are shown in Figure 4.15. The wavelength regions chosen reflect the spectral ranges of the four spectrometers used for the experiment. The regions are labelled VUV, Blue, Red, and IR with exact wavelength ranges shown. The LASTA 2.0 radiance prediction has been convolved with the spatial resolution function (SRF) provided with the EAST test series 50 dataset. The spatial resolution function is comprised of three components as described by Cruden (2014). The first is to account for smearing of the experimental results due to the finite resolution of the camera CCD, which can be measured experimentally. The second component is smearing due to the geometry of the optics. If the optical arrangement is telescopic, as in this case, photons originating from different axial locations along the centreline of the shock tube must travel different distances to reach the camera sensor and will thus appear smeared. Finally, there is a smearing of the image due to the gating time of the camera. The SRF is

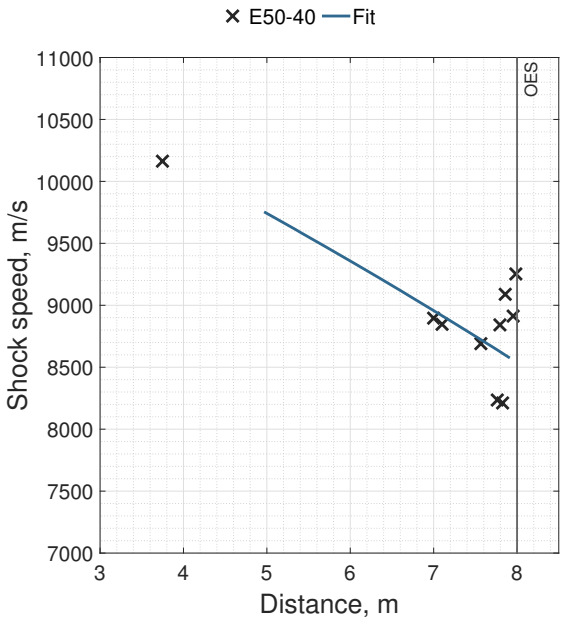

Figure 4.14: Experimentally measured shock speeds and fitted polynomial for E50-40

different for each spectral range.

Qualitatively, agreement with the experimental predictions is good. LASTA 2.0 predicts an increase in radiance towards the end of the test slug in all spectral ranges, which is due to the decelerating shock trajectory. The timing of this post-shock rise is slightly delayed when compared to the experiment, suggesting that use of the shock boundary condition alone is not sufficient to capture all fluid processes taking place in this case. Despite this, the magnitude of radiance in the radiance in the red and IR regions of the spectrum is well captured in both the equilibrium and non-equilibrium regions.

The magnitude of radiance in the VUV and blue regions of the spectrum is generally under-predicted. No carbon was included in the LASTA 2.0 simulation, which may explain the under-prediction in the blue region. C readily reacts with N to form CN which radiates around in the 380 nm region even in small concentrations. Other features in the blue region include radiation from molecular nitrogen which can be affected by the choice of state population method in NEQAIR (Cruden and Brandis, 2019). Radiation in the VUV region is dominated by the 174 nm atomic nitrogen line, which is not quantitatively replicated by the LASTA 2.0-NEQAIR approach.

The radiation predictions for the non-equilibrium region generally differ from the experiment. Tuning of reaction and relaxation parameters to match this particular test case outside the scope of the present work. However, LASTA 2.0 provides a platform to carry out this *tuning* with significantly improved confidence given that the fluid mechanics of the shock tube are accurately modelled.

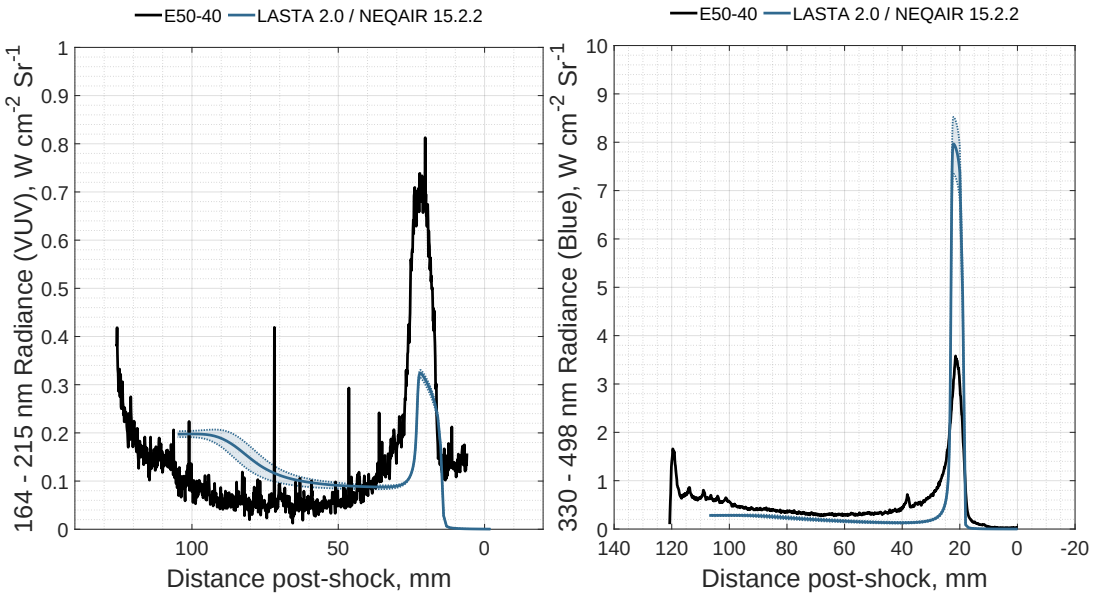

(a) VUV: 164 - 215 nm

(b) Blue: 330 - 498 nm

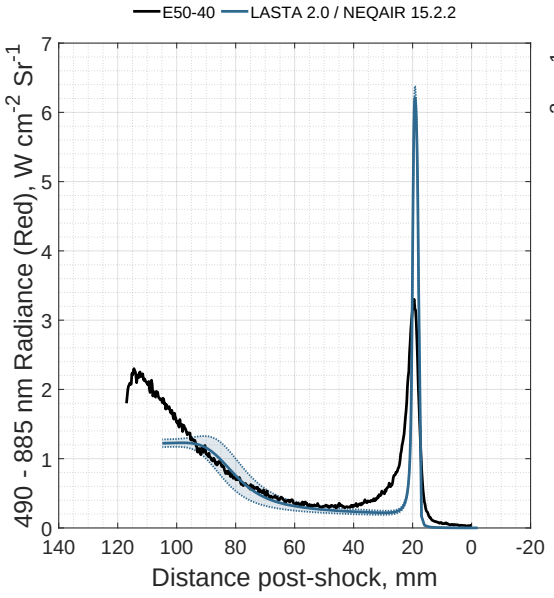

(c) Red: 490 - 885 nm

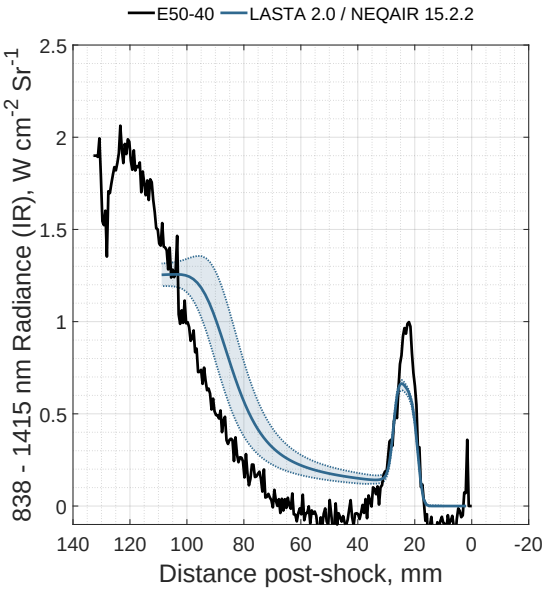

(d) IR: 838 - 1415 nm

Figure 4.15: Radiance predictions for E50-40. Dashed lines and shaded region represent $\pm 100\ \mathrm{m\,s^{-1}}$ perturbations to the shock trajectory

4.5.2 N_2–CH_4: Titan Entry

In this section, a recent test case from the EAST facility representative of a possible Titan entry is analysed. E65-16 was run in the 4 inch (101.6 mm) EAST driven tube and is discussed in detail by Tibère-Inglesse et al. (2023b). The aim of this test series was to quantify the level of radiation that might be encountered by the back shell of the Dragonfly entry module, which is expected to be a driving design parameter. The test slug in this case was found to be nearly entirely in nonequilibrium, making it an interesting test case of the new LASTA 2.0 features. The fill pressure was 0.21 torr (27 Pa) with a composition of 97.8 N_2-2.2 CH_4 %v/v. The Gokcen (2007) reaction scheme is used.

The experimentally measured shock speeds and fitted polynomial used in the simulation are shown in Figure 4.16. The simulation is initialised at 4 m from the primary diaphragm to simplify the shock boundary condition. The trajectory is mildly decelerating and decreases from approximately 6 $\mathrm{km\,s^{-1}}$ to 5.4 $\mathrm{km\,s^{-1}}$ by the measurement window. No pressure boundary condition was included for this simulation.

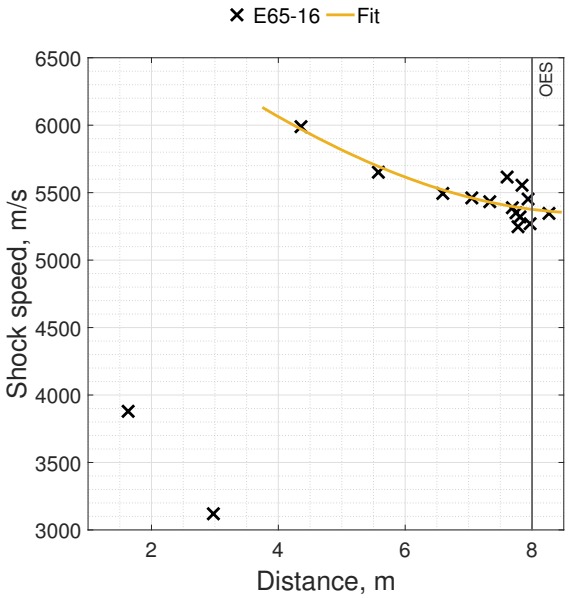

Figure 4.16: Experimentally measured shock speeds and fitted polynomial for E65-16

The radiance profiles for the experiment and LASTA 2.0 are shown in Figure 4.17. Results are presented for the four spectral ranges available.

The temperature and CN number density profiles predicted by LASTA 2.0 and NESS are shown in Figure 4.18, highlighting the strengths and weaknesses of the two approaches. NESS temperature profiles are different closer to the shock due to the inclusion of viscous effects and modelling of the shock structure, whereas LASTA 2.0 is initialised

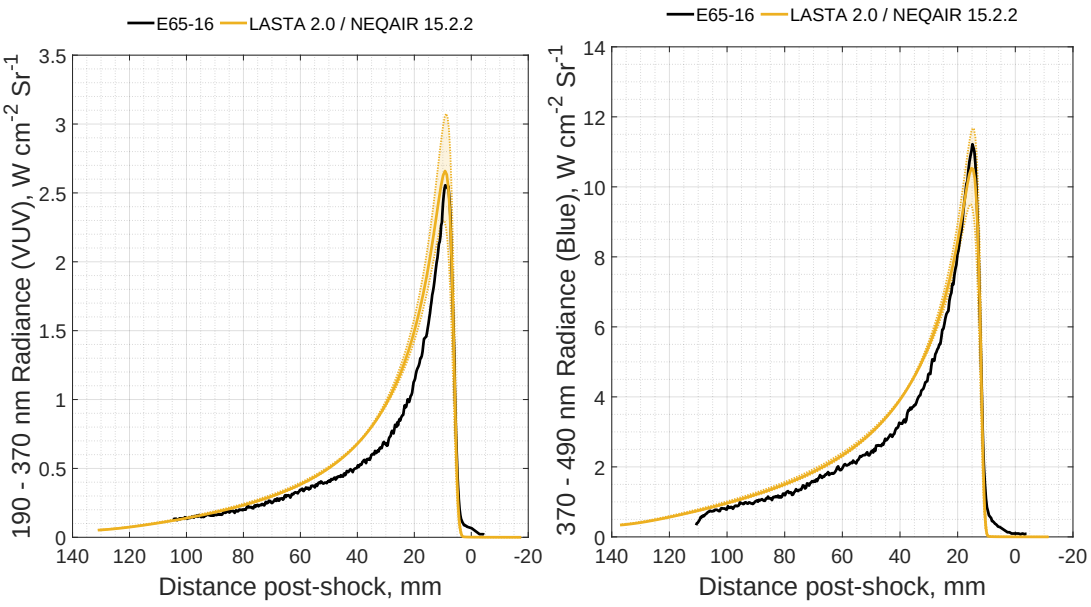

(a) VUV: 190 - 370 nm

(b) Blue: 370 - 490 nm

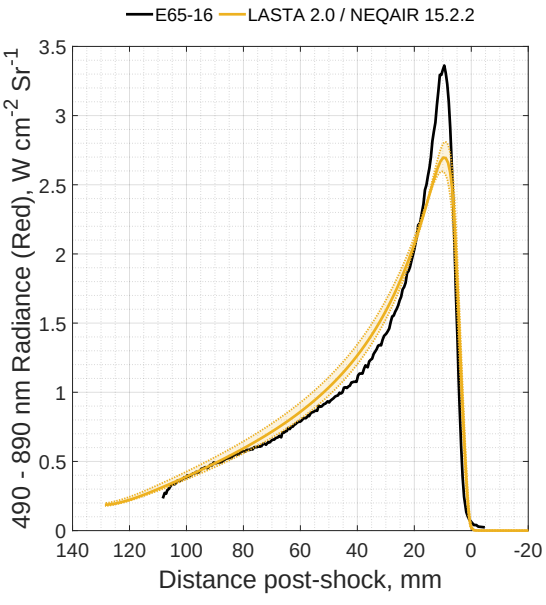

(c) Red: 490 - 890 nm

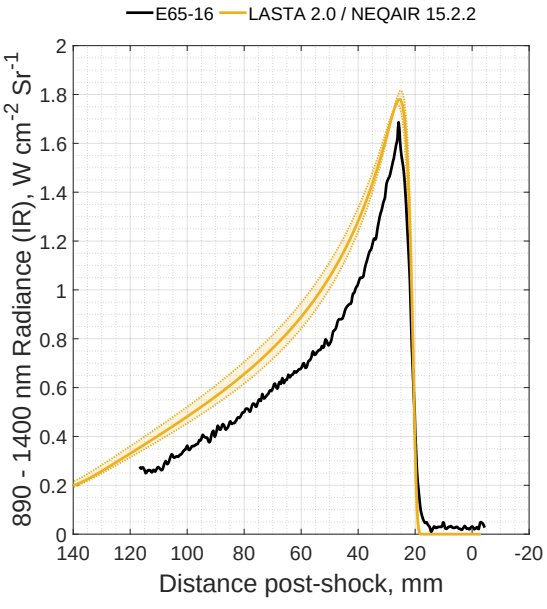

(d) IR: 890 - 1400 nm

Figure 4.17: Radiance predictions for E65-16. Dashed lines and shaded region represent $\pm 100\ \mathrm{m\,s^{-1}}$ perturbations to the shock trajectory

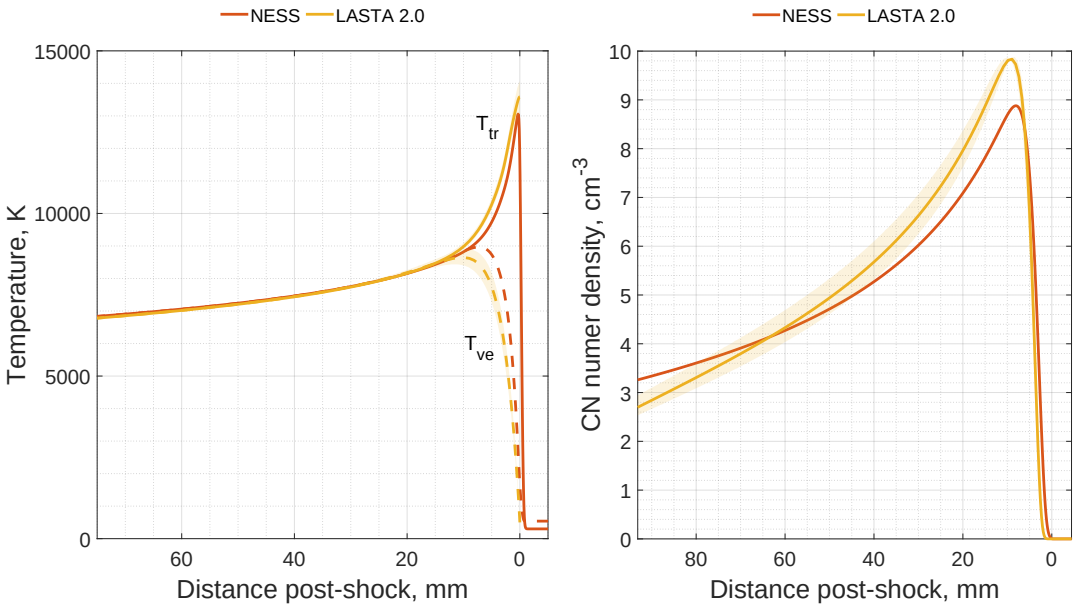

(a) Temperatures

(b) CN number density

Figure 4.18: Temperature and number density profiles predicted by LASTA 2.0 for E65-16 for $\hat{c}_1 = 0.35$

from the Rankine-Hugoniot value. This difference resolves to within 100 K by 70 mm post-shock, meaning this is likely not the cause of the difference in radiance predictions seen in Figure 4.17. The CN number density predicted by LASTA 2.0 decreases below NESS at 65 mm post-shock, reflecting the inclusion of shock history effects. CN number density decreases with increasing shock speed between the 5.7 - 6.0 $\mathrm{km\,s^{-1}}$ range. This is also the likely cause of the difference in radiance predictions as the emission spectrum is dominated by CN features. This is quantified in Figure 4.19 which shows the percentage difference between NESS and LASTA 2.0 predictions for CN number density profiles.

Tibère-Inglesse et al. (2023b) attributed the differences between simulated and experimental radiance to shortcomings in the NEQAIR non-Boltzmann modelling of CN. This conclusion is supported by the findings in this section, however differences toward the rear of the test slug are also due to CN overpopulation caused by the assumption of constant shock speed. Future studies aiming to improve CN non-Boltzmann modelling or N_2–CH_4 reaction rates should ideally include non-uniform shock trajectory effects based on the findings in this section, for example by using LASTA 2.0 or a similar program as the underlying fluid mechanics model for the shock tube.

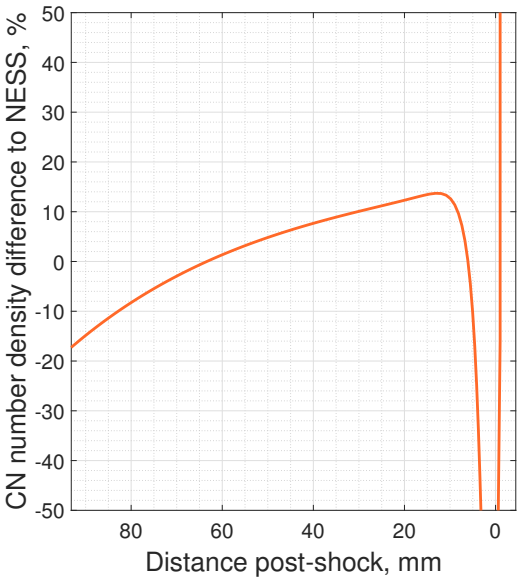

Figure 4.19: Difference between LASTA 2.0 and NESS predictions for CN number density

4.5.3 H_2–He: Giant Planet Entry

This experiment was performed in the T6 steel shock tube mode (see Section 5.2.1) with a secondary driver. The purpose of the experiment was to study radiation from the H-α and H-β lines in a mixture relevant to Giant Planet entry. The fill conditions were 28.0 Pa of 10 H_2-90 He %v/v. The shock speed at the measurement window was 14.1 $\mathrm{km\,s^{-1}}$.

The shock trajectory for this test case is shown in Figure 4.20. The shock speed measurements in the secondary driver are shown in grey to indicate that they were not used as inputs to the LASTA 2.0 simulation. The shock trajectory for this test case was relatively flat with shock speed measurements in the last 3 m of the tube within $\pm$ 200 $\mathrm{m\,s^{-1}}$, however this case still serves as a test of the thermochemical model.

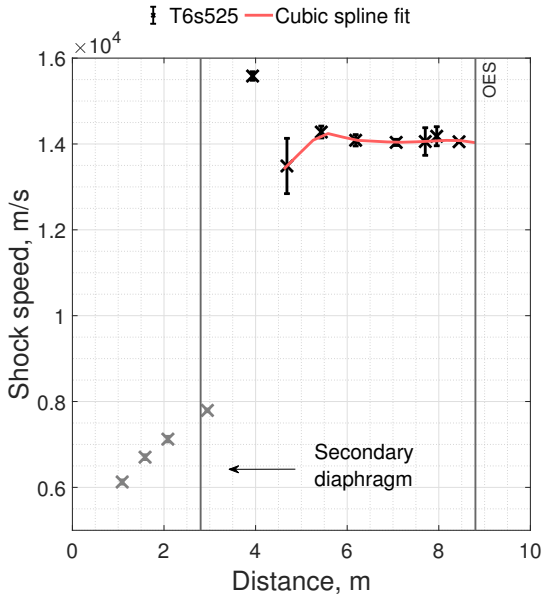

Figure 4.20: Experimentally measured shock speeds and fitted polynomial for T6s525

The radiance predictions for this experiment are shown in Figure 4.21. Only the H-α lines is presented as this was the only feature of interest in the experimental spectrum. The initial post-shock feature appears to be well captured, however the second rise seen in the experiment is not. The second experimental feature has been observed by other authors (Cruden and Bogdanoff, 2017) and is attributed to a slow ionization rate in the shock layer. It should be noted that this second feature is likely not the equilibrium region which is not reached in the experiment due to the short test slug.

Differences between the LASTA 2.0 predictions and experimental results are largely attributed to incomplete modelling of the hydrogen ionization process. Carroll et al. (2024) collates several rates for hydrogen ionization from the literature, highlighting that

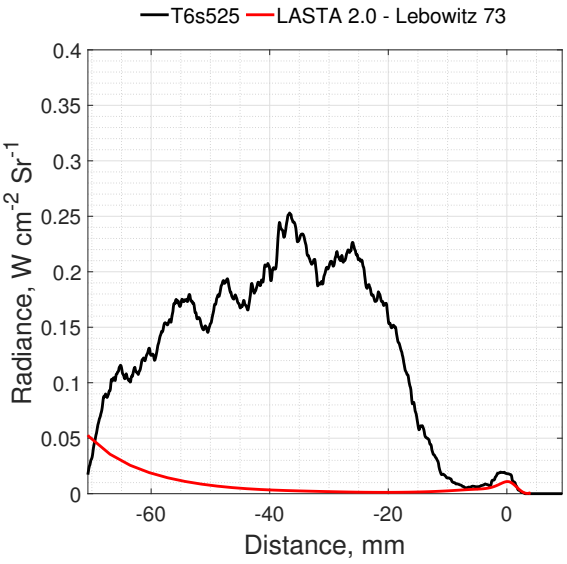

Figure 4.21: H-α: 654 – 658 nm

the rate of ionization is strongly state-dependent between 5000 K - 20,000 K. For example, the ionization rate for the $n = 1 \rightarrow 2$ transition varies between $10^{15} - 10^{17}\ \mathrm{cm^3\,mol^{-1}\,s^{-1}}$ whereas the $n = 1 \rightarrow 3$ transition varies between $10^{3} - 10^{13}\ \mathrm{cm^3\,mol^{-1}\,s^{-1}}$. Presently, the LASTA 2.0 thermochemistry model does not allow for modelling of state-specific thermochemical behaviour and thus, error is expected. This is likely the reason for the direct increase toward the equilibrium radiance rather than the two stage process seen in the experiment and in the literature.

The LASTA 2.0 predicted temperature and species number density profiles in the test slug are shown in Figure 4.22. The profiles qualitatively agree with observations of Leibowitz (1973) for a 15.5 $\mathrm{km\,s^{-1}}$ shock in a 20/80 H_2-He test case. Thermal equilibrium is not achieved within the test slug which is consistent with the findings of Cruden and Bogdanoff (2017) where equilibrium is not reached for several centimetres behind the shock.

Although agreement with the experiment here is not as satisfying as for the N_2–O_2 and N_2–CH_4 mixtures, this is attributed primarily to limitations of the thermochemical model rather than the LASTA 2.0 approach. LASTA 2.0 provides a platform for hydrogen ionization kinetics in shock tubes to be studied in isolation from the non-ideal fluid mechanics effects, which was demonstrated here.

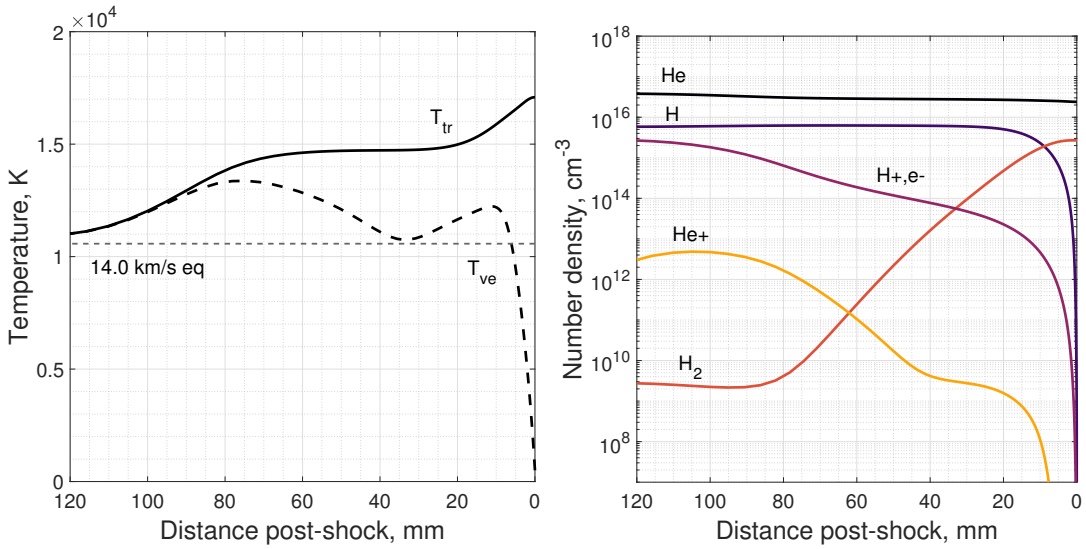

(a) Temperatures

(b) Species number density

Figure 4.22: Temperature and number density profiles predicted by LASTA 2.0 for T6s525 for $\hat{c}_1 = 0.5$

4.6 Analysis of a Test Campaign

In this section, some time is dedicated to demonstrating the intended *real-world* use case of LASTA 2.0 which is namely, rapid post-processing of shock tube experiments to quantify the effect of non-uniformities on the test case. Several additional cases from the E65 test campaign have been analysed which vary in fill pressure and shock speed. The test conditions selected are shown in Figure 4.23. E65 is an ideal test series to analyse with LASTA 2.0 because there is likely to be chemical non-equilibrium present as well as mild shock deceleration.

Table 4.2 summarises the solution time for these cases. All cases in this section were run on a 2022 MacBook Air with an M2 chip in a Docker / Linux environment. The solution time includes two runs for each case so that the uncertainty bounds can be produced by finite difference. The solution time does not included the time required to run NEQAIR 15.2.2. Assuming that this sample is representative, it would take approximately 14.3 hours of simulation time to analyse all 58 shots from this EAST test series.

Comparison between LASTA 2.0 / NEQAIR 15.2.2 simulations and experiment are shown in Appendix D.

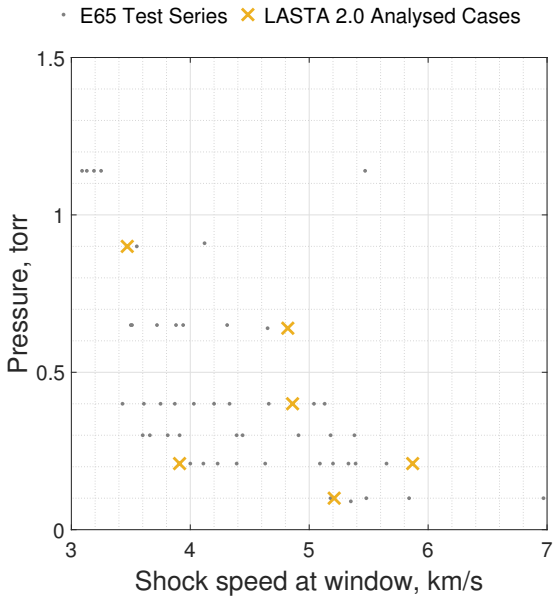

Figure 4.23: Test conditions analysed in this section from the E65 test campaign

Table 4.2: Summary of test conditions analysed from the E65 test series

Case	Pressure, Pa	Final shock speed, km/s	Solution time, minutes
E65-5	0.10	5.21	30.0
E65-10	0.21	3.91	9.24
E65-16	0.21	5.39	10.4
E65-35	0.40	4.86	23.0
E65-45	0.64	4.82	7.80
E65-49	0.90	3.47	8.30

4.7 Summary

The new features of the LASTA 2.0 code have been demonstrated by applying the method to several historical test cases. Full spectrum radiance predictions were compared to results from experiments in N_2–O_2, N_2–CH_4, and H_2–He mixtures. Radiation predictions for the N_2–O_2 and N_2–CH_4 showed excellent agreement with the experimental measurements in the equilibrium region for all wavelength ranges examined, demonstrating again the effect of non-uniform shock trajectory. Predictions for the N_2–CH_4 case, when coupled with the updated QSS modelling in NEQAIR, are particularly good, showing closer agreement with the experiment than any other numerical shock tube model analysed.

Comparisons between experiment, LASTA 1.0, and LASTA 2.0 predictions of oxygen 777 nm radiance were also shown. LASTA 2.0 provided improved predictions of the experiment in every case when compared to LASTA 1.0. Agreement with the T6 cases was

generally better than the EAST cases due to the inclusion of the final pressure boundary condition which essentially amounts to modelling of upstream wave processes. Although the non-equilibrium peak was not modelled reliably, this was not the aim of this study. The purpose was to demonstrate the suitability of LASTA 2.0 for use as a platform to evaluate thermochemical models, which was achieved.

The results presented in this chapter establish LASTA 2.0 as a state-of-the-art shock tube modelling method with a unique capability to simultaneously model non-equilibrium and non-uniform shock trajectory effects.

Chapter 5

Radiance Measurements Through Unsteady Expansion Waves

Contents

5.1 Introduction

The proceeding chapters established a numerical tool with improved capability to model the non-ideal hydrodynamic processes in a shock tube. Attention is now turned in this chapter to the case of an expansion tube. Comparatively few sources of validation data are available for expanding flows, increasing the value of and need for new studies. In this experimental chapter, the radiation emanating from the unsteadily expanding test gas in an expansion tube is characterised so that it may later be used to validate the LASTA 2.0 model.

Measurements of radiation in an expanding flow context are of direct relevance to vehicle design. Flow over an entry vehicle is a complicated interplay between different aerothermodynamic and fluid mechanics processes, as shown in Figure 5.1. Along a typ-

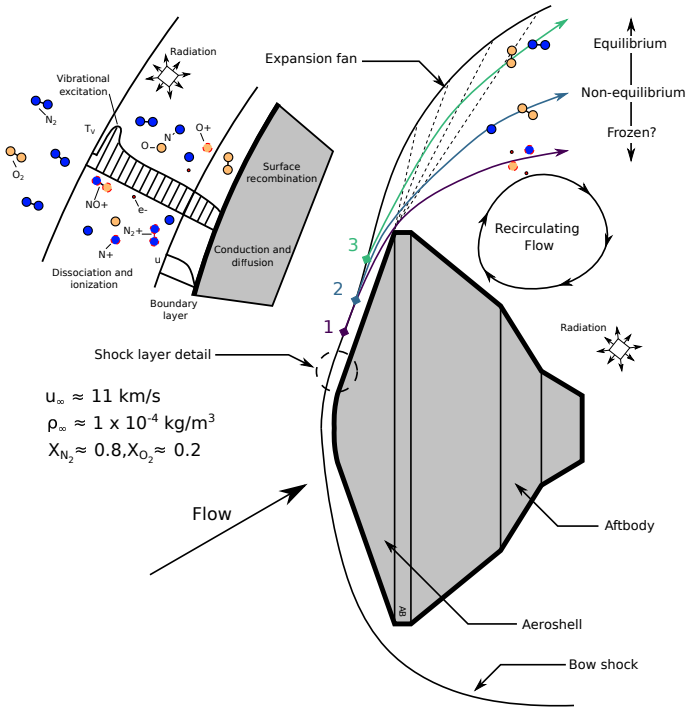

Figure 5.1: Phenomenology of a hypersonic shock layer, partly reproduced from Potter (2011)

ical streamline, the flow is first compressed by the bow shock wave, decelerated, and heated. Depending on the freestream conditions, the bow shock strength may be sufficient to first dissociate molecules and then ionise atoms in the flow which can affect the bulk gas properties. These species may then interact further with ablation products that can behave as a catalyst for one or more of the reactions occurring.

Before entering the wake region, the gas undergoes a rapid expansion to low pressure and temperature around the edge of the forebody. The speed of the expansion process can lead to a state of non-equilibrium in the wake region because there is not sufficient time for particles to collide, exchange energy, and reach equilibrium. The gas continues to emit radiation while in the wake which must be accounted for during the vehicle design phase. It is desirable to minimise the TPS thickness on the back-shell to maintain vehicle stability and facilitate design requirements such as radio-transparent materials for communication during cruise. These factors, combined with the potentially complex thermochemical state of the gas in the wake, drive uncertainty in the required backshell TPS thickness and motivate further study of expanding flow phenomena.

Despite the evident importance of expanding flows in the context of hypersonic flight, there is a lack of an established experimental test bed for study of the phenomenon. The expansion tube, discussed at length in Chapter 2, leverages a similar expansion process to produce hyper-velocity test flow. The aim of this chapter is to begin to answer the

question: can an improved understanding of the expanding flow in an expansion tube be used to produce analogues to flight?

In this chapter, the use of several radiometer probes to study radiance emanating from the unsteady expansion wave in an expansion tube is reported. Firstly, the experimental setup is presented, with a particular focus on the development of the wall-mounted radiometer probes. Next, a validation study of the radiometer probes in a shock tube is presented, where the radiometer traces are compared to results obtained from optical emission spectroscopy. Finally, results obtained from radiometers located downstream of the secondary diaphragm are presented with the aim of characterising the thermochemical state of the expanding test gas.

5.2 Methodology

5.2.1 T6 Stalker Tunnel

T6 is a multi-mode hypersonic wind tunnel. A complete overview of T6 can be found in Collen et al. (2021). The free-piston driver, which generates pressures on the order of 50 MPa during a shot, may be coupled to a range of downstream components to allow operation of the facility as either a shock tube (ST), expansion tube or expansion tunnel (ExT), or reflected shock tunnel (RST). T6 offers the only expansion tube capability in Europe with test times between 20 and 150 μs. During an experiment, a piston weighing either 36 or 90 kg is accelerated to speeds of approximately 300 $\mathrm{m\,s^{-1}}$ by high pressure air known as the reservoir gas. The gas in the volume between the piston and the primary diaphragm, typically low pressure helium, is poly-tropically compressed to the diaphragm rupture condition by the piston motion. In the present work stainless steel diaphragms are used with a rupture pressure of 46.2 MPa and temperature of 5000 K, corresponding to a volumetric compression ratio of 60:1 for a 35 kPa initial driver fill pressure. This high pressure, high temperature driver gas unsteadily expands into *Driven Tube 1* (shown in Figures 5.2 and 5.3), forming the shock wave that is studied at the end of the facility. Static pressure in the driven tubes is measured by between 9 and 17 PCB113 piezoelectric pressure transducers depending on the mode of operation. Shock speed is inferred by measuring the difference in arrival time between the transducers.

Shock Tube Mode

T6 in steel shock tube mode (SST) consists of a 9 m length, 96.3 mm internal diameter barrel connected to the driver and feeding in to the dump tank, as shown in Figure 5.2. The shock tube section features 17 axial locations where instrumentation may be installed, some of which are replicated on the opposite side of the tube. The primary purpose of SST mode is to facilitate the study of shock layer radiation at high velocities. This is achieved by imaging the post-shock region through a set of 190 x 10 mm windows in the tube wall at the far end of the facility.

Figure 5.2 shows a distance-time plot of the typical wave processes occurring in the tube during a test. Initially, the test gas (matching the density and composition of the flight condition of interest) resides in the region denoted *Driven Tube 2*. The piston motion leads to rupture of the primary diaphragm and in turn drives a strong shock wave through the test gas. The region of useful test gas, denoted τ, grows until it reaches a

maximum value limited by the boundary layer growth (Mirels, 1963). The maximum achievable shock speed can be increased via the use of a secondary driver (Gildfind et al., 2015) which has been utilised in the present work. A secondary diaphragm, in this case Mylar of 10 µm thickness, is installed between *Driven Tube 1* and *Driven Tube 2*. *Driven Tube 1* is then filled with low pressure helium ($\approx 1\mathrm{kPa}$) and *Driven Tube 2* with the test gas. By carefully selecting the secondary driver gas fill condition it can be arranged that the shock processed secondary driver gas has a higher temperature and sound speed than could have been achieved in the expanded driver gas and therefore a stronger shock is driven through the test gas. Use of this technique increased the maximum shock speed in this work by approximately 4 $\mathrm{km\,s^{-1}}$.

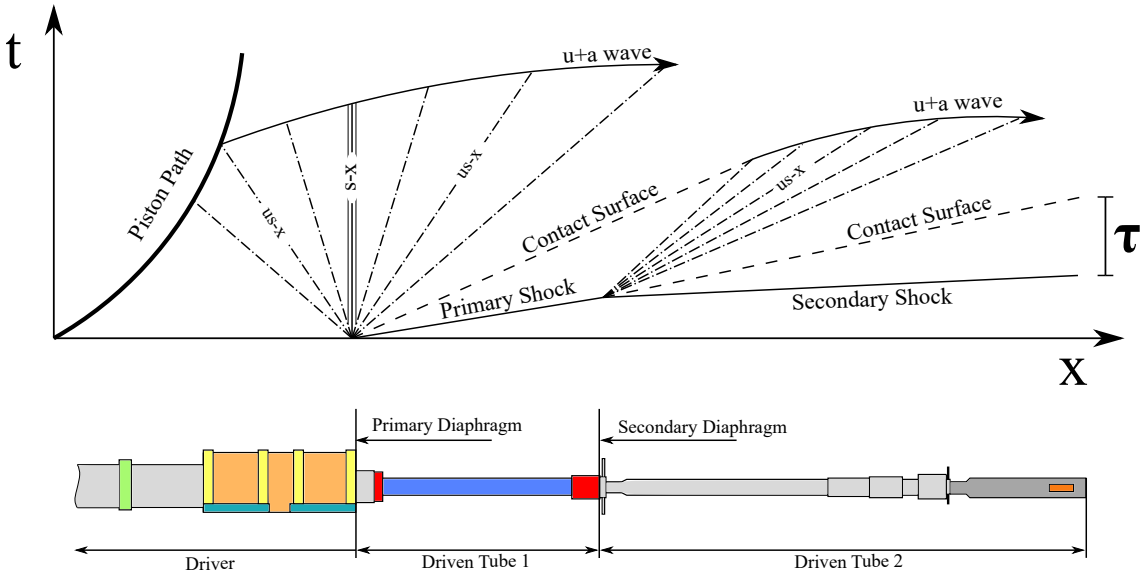

Figure 5.2: Position-time diagram of wave processes in T6 shock tube mode, adapted from (Collen et al., 2021)

Expansion Tube Mode

T6 is shown in expansion tube (ExT mode) in Figure 5.3. The arrangement is physically identical to a shock tube with a secondary driver, but the test gas originates from *Driven Tube 1* rather than *Driven Tube 2*. Figure 5.3 shows a distance-time plot of the wave processes occurring during an expansion tube test. The test gas is initially located in the region denoted *Driven Tube 1*. The remainder of the working section, denoted *Driven Tube 2*, initially contains very low density gas, typically lab air. The shock is generated in exactly the same fashion as the shock tube case, however when the shock reaches the secondary diaphragm it ruptures, allowing the high-pressure, shock heated test gas to unsteadily expand into the acceleration tube, resulting in an increase in total enthalpy

without significant dissociation of the test gas. In this way the expansion tube is functionally identical to the shock tube and the only difference is in what is considered the test gas. The expansion tube may be coupled with an expansion nozzle at the acceleration tube outlet to further expand the test gas, this arrangement is known as an expansion *tunnel*. Further details about the T6 expansion tunnel mode are available in Steer et al. (2024b).

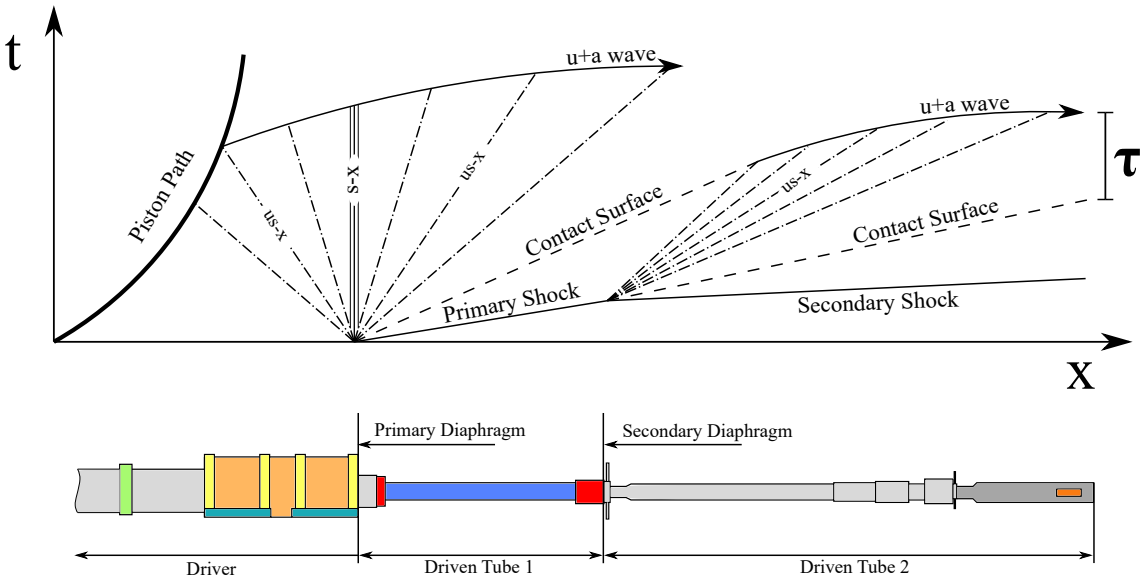

Figure 5.3: Position-time diagram of wave processes in T6 expansion tube mode, adapted from (Collen et al., 2021)

5.2.2 Observations of the Unsteady Expansion

Obtaining measurements of flow properties at many different spatial locations or observation stations in the expansion tube allows for all three chemistry regimes to be accessed (frozen, non-equilibrium, and equilibrium) and thus lends significant versatility to the experimental setup. Development of a radiometer that could be installed in place of T6 shock timing stations would allow measurement at up to 17 spatial locations and allow the flow chemistry in the unsteady expansion to be resolved with high fidelity. Such an experimental setup is shown schematically in Figure 5.4. The lines of sight of each measurement are indicated, showing that they each provide access to the test gas at different degrees of expansion. Achieving this is the primary goal of this chapter.

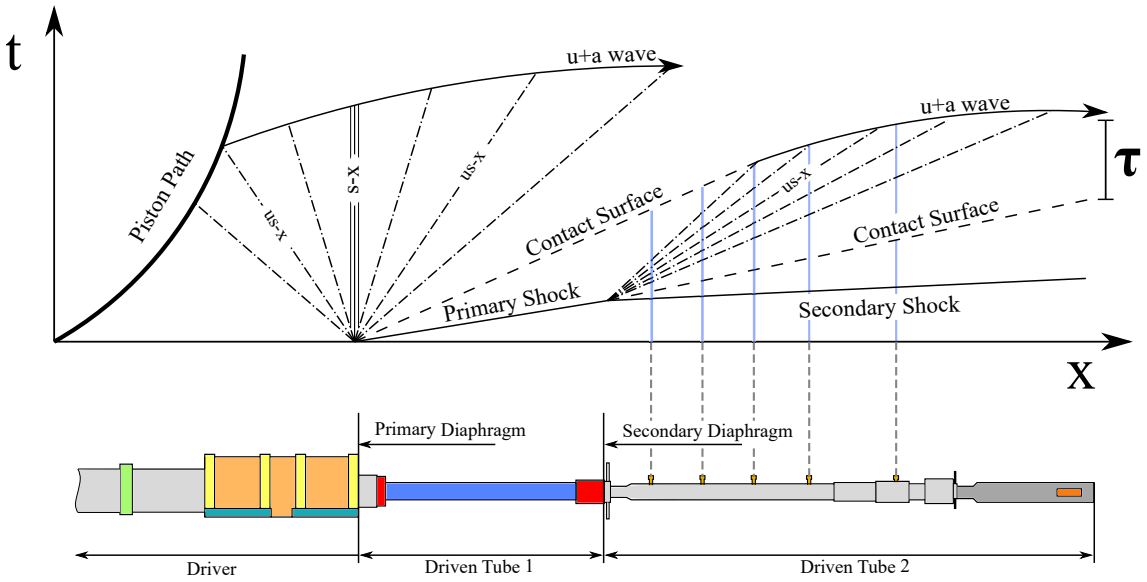

Figure 5.4: Lines of sight through the unsteady expansion permitted by installation of optical measurement devices at several locations downstream of the secondary diaphragm in the T6 expansion tube

5.2.3 Wall-Mounted Radiometer Probes

Geometry

A schematic overview of the probe used in the present work is shown in Figure 5.5. A line of sight between the radiating test gas and sensor is permitted by a $2\ \mathrm{mm}$ diameter CaF_2 window at the tunnel wall. A $1\ \mathrm{mm}$ limiting aperture behind the window restricts the system field of view, thus determining the spatial resolution. The incident light is filtered by a bandpass filter of wavelength corresponding to the spectral feature of interest before being amplified by a Hamamatsu H10721-20 photomultiplier. The inner faces of the brass backing nut that interfaces with the tube wall were coated in a black paint with absorbance of > 99 % to minimise measurement of spurious reflected light. A graduated, adjustable iris was installed to provide fine control of the system field of view. Because the aperture at the wall was the limiting one, the iris served more to reduce capture of spurious reflected and diffracted light. A neutral density filter was used in some early tests to reduce the risk of damage to the photomultiplier, although this was later removed and was not used for any of the experimental cases presented herein.

Accurate knowledge of the field of view of the radiometers is important for determination of the level of 'spatial smearing' in the results. Spatial smearing refers to the blurring or spreading of an image due to imperfections in an optical system. In this case, if the field of view of the radiometer is too large it may not be able to resolve the post-

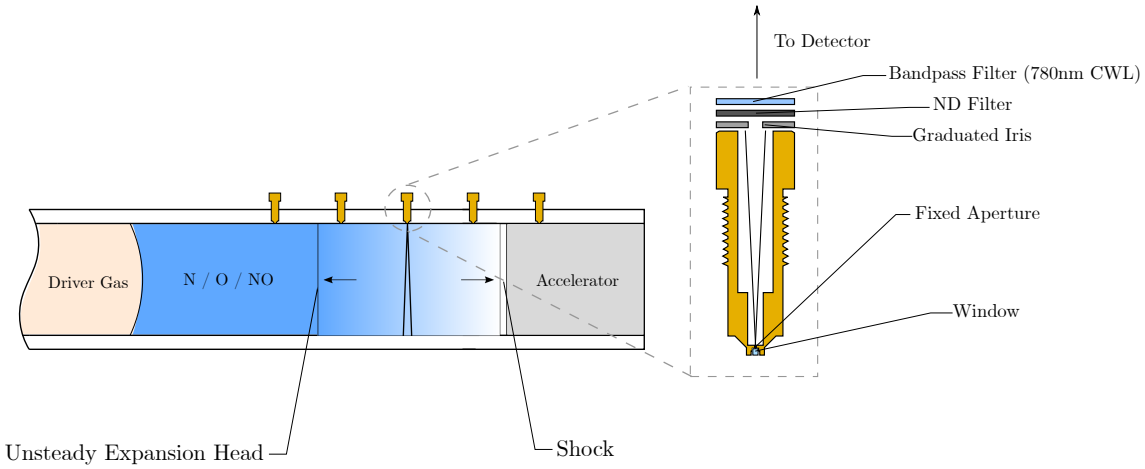

Figure 5.5: Schematic diagram of the T6 radiometers as used to view the unsteady expansion in an expansion tube

Table 5.1: Field of view of the radiometer probes calculated from their ideal geometries.

Timing Station	Mean FOV ⌀, mm	Max FOV ⌀, mm
STS01 – STS07	3.23	5.46
STS08	3.13	5.26
STS09	2.92	4.84
STS10 – STS11	3.18	5.36
STS12 – STS17	3.08	5.16

shock radiation with sufficient temporal resolution to make meaningful comparisons to optical emission spectroscopy measurements. Here, the field of view of the radiometers is estimated based on their geometries as defined in technical drawings to assess the extent to which spatial smearing may influence the final measurements.

The geometries for each backing nut are slightly different because of the varying thickness of the tube wall and thus the fields of view are different. The field of view is a function of the distance from the window because the field of view of the radiometers is conical. This is illustrated in Figure 5.6, where the field of view on the tunnel far wall is a function of the distance between the limiting aperture and the PMT sensor face, defined as d. Table 5.1 shows a summary of the field of view of the radiometer probes used at each timing station based on the ideal (i.e. as drawn) geometries. An average value, corresponding to the diameter of the field of view at the centre of the tunnel, and a maximum value, the diameter of the field of view on the opposite side, are presented.

Calibration

A Bentham SRS8 Integrating Sphere was used to provide a light source of known intensity for calibration of the radiometers. The radiometers were positioned with the exterior

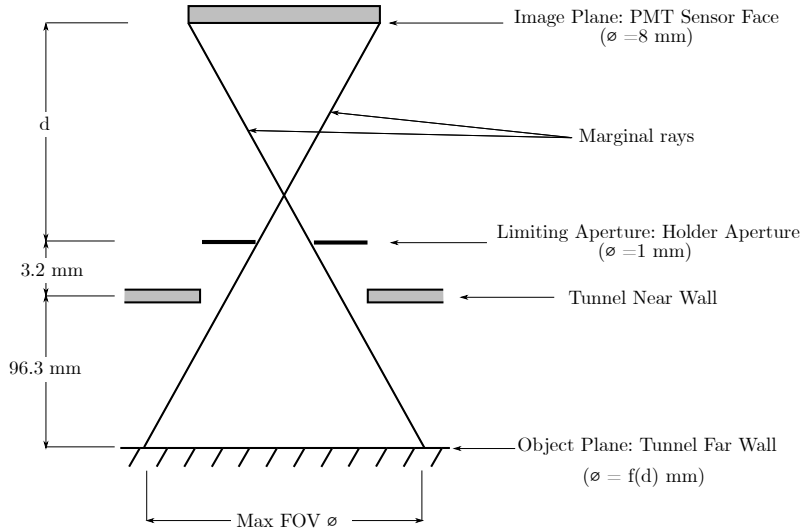

Figure 5.6: Ray tracing diagram used to define the field of view characteristics of the radiometers in this chapter. The maximum field of view diameter is given by the relation: $\varnothing = \frac{348.25}{d} - 0.5$

face of the window aligned with the outlet plane of the integrating sphere. Measurements of the output voltage were made over a period of 10 s with the integrating sphere powered on. A measurement was also made with the integrating sphere off to quantify the level of background light. The difference between the average of these two measurements was used for calibration. The output spectral radiance of the integrating sphere and the spectrally resolved transmittance of the bandpass filter are known and thus the product of these two yields a curve of spectral radiance seen by the radiometer during the calibration. An example of these curves for the 780 nm bandpass filter is shown in Figure 5.7, where Figure 5.7a is the manufacturer supplied transmittance curve, and Figure 5.7b is the transmittance curve multiplied by the known output of the integrating sphere. Integrating under the curve in Figure 5.7b yields the calibration radiance, providing the voltage response of the radiometer to a given radiance which can finally be used for conversion of the experimental voltage to radiance. Use of this calibration method assumes that the sensitivity of the photo-cathode is uniform across the spectral range of the bandpass filter i.e. the voltage response to the broad-spectrum calibration radiance is equal to the response to a narrow-band atomic emission of equivalent total radiance. This method also assumes that the voltage response of the photo-cathode is linear. Such a calibration was performed for every radiometer before every experiment after cleaning of the windows with acetone.

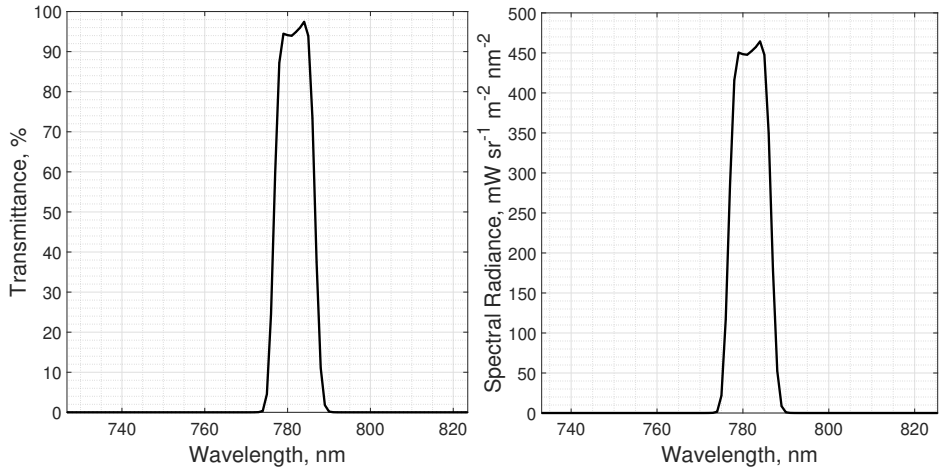

(a) Transmittance (b) Spectral radiance

Figure 5.7: Calibration curves for the 780 nm bandpass filter

Data Acquisition

The Hamamatsu H10721-20 photomultipliers are current output devices that produce a maximum safe current of 100µA. The output current is dependent on the radiance exposed to the photosensor and the voltage difference between the anode and cathode, known as the control voltage. The output could be measured as a voltage by introducing a terminating resistor of known resistance between the photomultiplier output and the recording device. Consideration was given to the relationship between resistance (Ω), circuit capacitance (C) and circuit response time (τ), $\tau = \Omega \times C$, when selecting the terminating resistance. The load capacitance of the H10721-20 series is quoted as 14 pF which corresponds to a circuit response time of 1.4 ns for a 1000 Ω terminating resistance. The output bandwidth noticeably decreased with terminating resistances larger than 500 Ω, but it found that a 50 Ω was produced a satisfactory signal-to-noise ratio in the output. The circuit control voltage was maximised (set to 1.0 V) to minimise non-linear behaviour of the photomultiplier when measuring near the maximum output current. Traces from the photomultipliers were recorded on a 4824A series PicoScope. The signals were sampled at 80 MHz.

5.2.4 Optical Emission Spectroscopy

The calibration and post-processing techniques used for the OES system have been described in detail by Collen et al. (2021) and Glenn et al. (2022). A schematic diagram of the experimental setup used is shown in Figure 5.8. Emissions from the radiating shock layer are recorded via a PI Isoplane-320 Spectrograph coupled to an Andor iStar sCMOS.

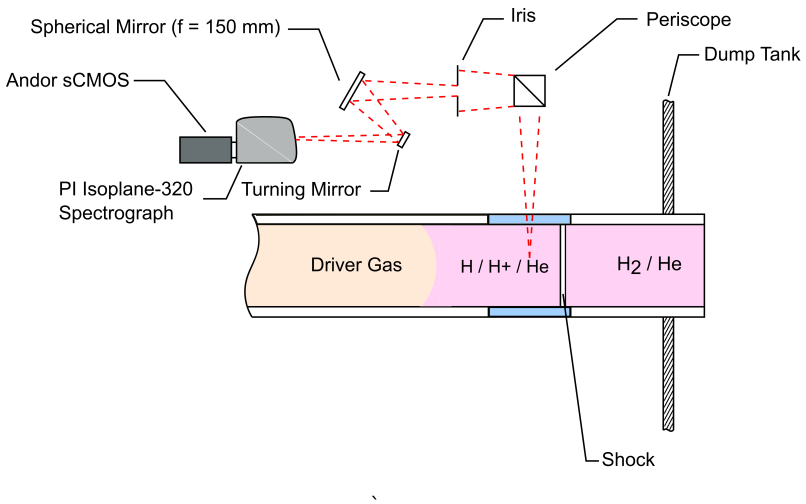

Figure 5.8: Schematic diagram of the optical emission spectroscopy setup used in shock tube mode, reproduced from Collen et al. (2021)

The measurement window used on both sides of the facility was UV grade fused silica from Crystran Ltd. Before each test a spatial, intensity, and wavelength calibration of optical setup were performed. Spatial calibration of the spectrometer was achieved with the aid of a custom alignment plate. The plate was designed to attach to the opposite side of the tube and features holes aligned with the centreline of the tunnel with a positional tolerance of 0.05 mm. By lighting the back side of this plate with a diffuse light source, the holes were clearly visible in the sCMOS view as near points. These points were then used as reference to set the desired field of view of the spectrometer via fine adjustment of optical mirrors. Intensity calibration of the spectrometer was achieved via the use of an integrated light source. The model used was a Bentham SRS8 Integrating Sphere. During the calibration process, the integrated light source was fixed to the opposite side of the tube and positioned in the line of sight of the spectrometer. A series of images were then collected using the *accumulate* feature on the Andor camera, each image having the same exposure time and gain settings as the test exposure. The same process was then completed with the integrated light source turned off which provided a reference background image. Wavelength calibration was completed using a Princeton Instruments IntelliCal Hg and Ne/Ar arc lamp.

For all experiments presented here, the spectrometer was operated with a grating with 150 grooves per millimetre, blazed at 500 nm. The spectrometer was centred on 550 nm, allowing both the H-α and H-β emission lines to be resolved. The Andor camera was triggered using a micro-controller based delay generator. A gating time of 55 ns was selected for all experiments, in which time the shock moved a maximum distance of 1 mm.

5.3 Validation of Radiometer Probe Measurements

Experiments with both the radiometer probes and conventional optical emission spectroscopy were performed with the aim of confirming that the radiometer measurements were accurate. These tests were all performed in shock tube mode to remove the complexity of the unsteady expansion. Results from these tests are presented in this section.

5.3.1 Arrangement

Figure 5.9 shows the arrangement of the facility for the validation study. Three radiometers were installed on the underside of the tube in positions opposite pressure transducers. The radiometers were located underneath the observation window so that they would image the test slug at the same time as the OES setup. The exact location of the shock at the time of imaging by the OES system is dependent on the shock trajectory in each individual experiment thus there will always be slight differences between the OES profile and the radiometer measurements as they are measuring the slug at slightly different times in its history. However, this effect is expected to be minimal for the results presented here.

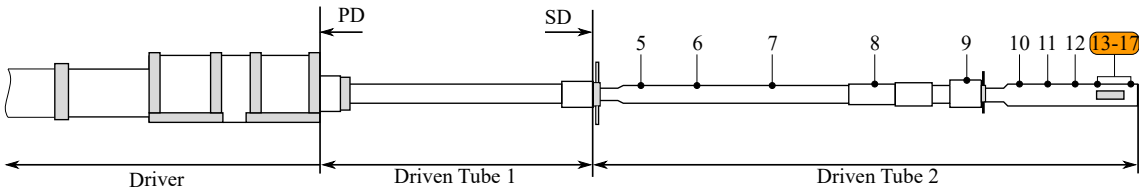

Figure 5.9: Arrangement of the radiometers for the shock tube validation tests

5.3.2 Tested Conditions

The conditions used for validation of the radiometer probes are summarised in Table 5.2. All tests utilised a pure helium secondary driver to increase the maximum achievable shock speed in the hydrogen/helium test gas. Hydrogen/helium mixtures were selected for the validation tests because, when excited, they produce an emission spectrum consisting only of the hydrogen series[1]. Such a spectrum is an ideal use case for the bandpass radiometer setup because a single spectral line may be targeted without interference from other spectral features. The H-α (656 nm) line was targeted in all validation cases with a bandpass filter of 660 nm CWL with 10 nm FWHM[2].

[1] Assuming that He does not radiate, which is typically true unless the temperature is extremely high
[2] Thorlabs FBH660-10

Table 5.2: Summary of conditions tested in shock tube mode.

Condition	Symbol	Test Gas Composition, %v/v	psd_1, Pa	p_1, Pa	U_{s1}, km/s	U_{s2}, km/s	ℓ_m, mm	ℓ_m, µ sec
A	●	40 % H_2 / 60 % He	2060	19.9	8.80	17.3	44.4	2.57
B	■	10 % H_2 / 90 % He	10000	20.0	8.20	15.2	36.0	2.37
C	◆	10 % H_2 / 90 % He	10000	28.0	7.90	14.1	53.0	3.76

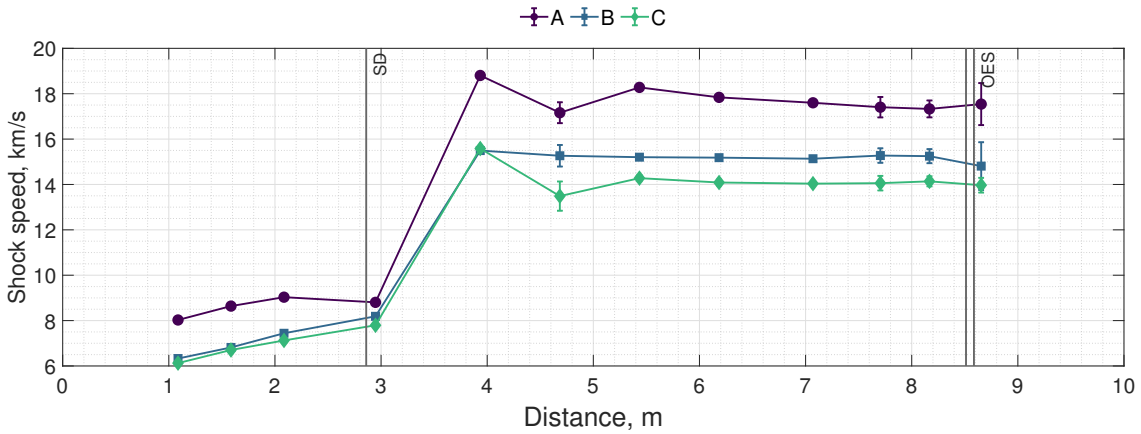

Figure 5.10: Shock trajectories achieved in the PMT validation tests. Legend entries refer to the conditions described in Table 5.2.

A profile of shock speed for each experimental case is shown in Figure 5.10. Here, distance is measured from the primary diaphragm downstream face. A large jump in shock speed occurs when the thin, Mylar diaphragm is ruptured and the secondary driver gas unsteadily expands into the volume containing the test gas. The optical emission spectroscopy field of view is located at a distance of 8.55 m from the primary diaphragm and is indicated in Figure 5.10. Mild shock attenuation is evident in each of the trajectories after the secondary diaphragm, with the greatest variation occurring in Condition A where the shock decelerates by approximately 2 $\mathrm{km\,s^{-1}}$.

5.3.3 Comparison to Optical Emission Spectroscopy

Figure 5.11 shows a comparison between the radiometer probes and integrated radiance obtained from the OES setup for conditions A, B, and C respectively. A conversion from time to space is necessary to create these plots as the OES produces a single spatially resolved image and the radiometers produce many temporally resolved points. Here, the radiometer results are converted to the spatial domain by multiplying by the Rankine-Hugoniot post-shock velocity corresponding to the experimental shock speed. This method assumes constant post-shock velocity which is an approximation as, in real-

ity, the post-shock velocity is governed by the shock history and boundary layer growth (Clarke et al., 2023b). The traces have been positioned such that 0 corresponds to the location of the shock front with flow from left to right. The location of the shock is deduced by corroborating knowledge of the shock trajectories with the trigger times and locations of the radiometers and OES system.

The OES image is spatially and spectrally resolved and so to obtain a radiance measurement that is comparable to the radiometers the results must be integrated with respect to wavelength over the region of interest, in the case across the width of the H–α line.

The radiometer results compare favourably to the OES results in all cases, indicating that the intensity calibration methodology for the radiometers is sound. The level of spatial smearing appears similar and confirms that the value estimated in Section 5.2.3 is accurate. The radiometer records are quantitatively similar despite the fact that the radiometers are situated at different points in the shock tube. This reflects the fact that the shock speeds are relatively constant over the region where the radiometers are located.

Figure 5.11 highlights that the radiometers offer an improved axial field of view when compared to the OES as they sample data throughout the entire experiment, albeit over a limited spectral range, and are not limited by the geometry of the rectangular window. Figure 5.11.a is particularly interesting because the radiometers record an increase in radiance beyond the view of the OES and after the end of the Mirels steady test time. Given that Mirels' analysis was originally developed for air at lower speeds, it could be that it is not appropriate for use in hydrogen/helium mixtures are high shock speeds Alternatively, it could be that the thermochemistry develops further in the portion of test gas that is entrained in the boundary layer.

5.3.4 Comparison to Pressure Measurements

Figure 5.12 shows a representative comparison between a radiometer and a pressure transducer located at the same point in the tube, in this case for condition C. The pressure transducer trace was recorded on a high-frequency (1 GHz) oscilloscope to provide improved temporal resolution when compared to the facility data acquisition system and thus, a useful comparison to the radiometer. The radiometer also demonstrates the usable test time, something that cannot be deduced from pressure measurements alone.

The radiometer outputs were consistently observed to rise slightly before the pressure transducers. This may be occurring for a number of reasons. The pressure transducers

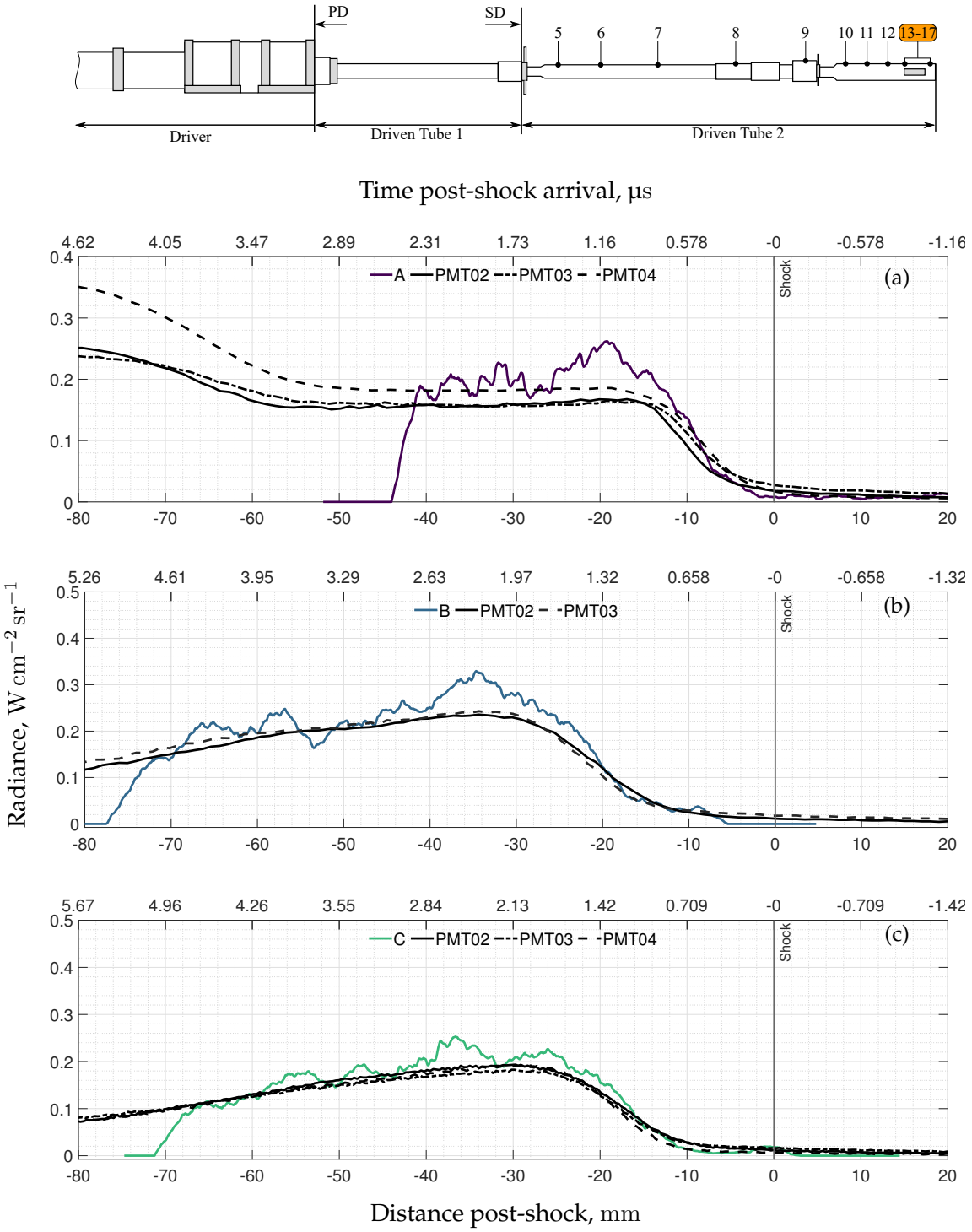

Figure 5.11: Comparison between the optical emission spectroscopy system and the radiometers for test conditions in Table 5.2. OES traces have been spectrally integrated between 655 nm and 665 nm.

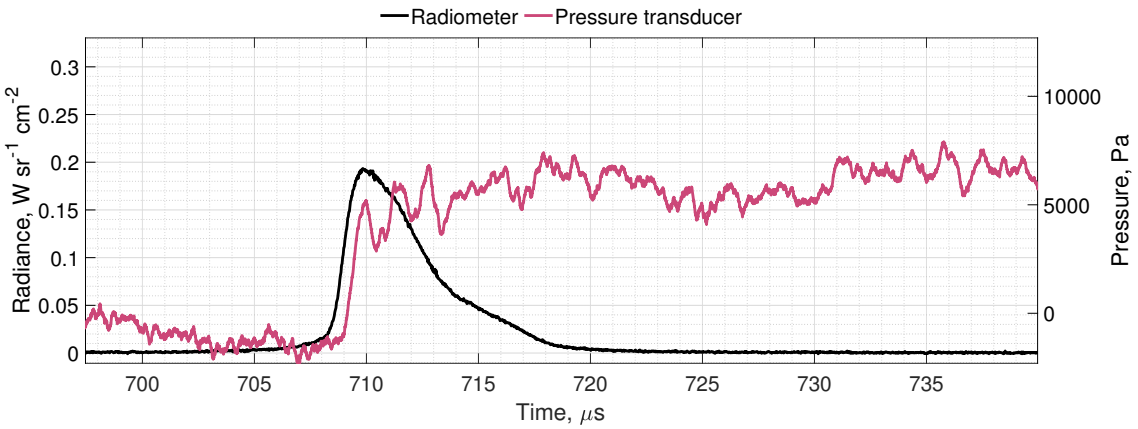

Figure 5.12: Comparison between simultaneous pressure and 660 nm radiance measurements made at STS15 for condition C

have slightly longer rise times than the photomultipliers, but not long enough that this could be the sole reason for the offset. The manufacturer quoted rise times for the radiometers and pressure transducers are 0.57 ns and ≤ 1.0 µs respectively.

The spatial smearing at the far wall calculated for the photomultiplier in this case is 5.16 mm (see Table 5.1), compared with a diameter of 5.54 mm for the head of the pressure sensor. All else being equal, this suggests that the pressure sensor would detect shock arrival before the radiometer. However, the pressure transducer signal will continue to increase as the shock crosses the head, leading to a delay.

Brandis et al. (2017) have identified precursor radiation, that is, radiation that precedes the shock front, in high velocity tests in the NASA EAST facility. Pre-shock excitation has been observed in hydrogen-helium shock tube tests by Cruden and Bogdanoff (2017) for a 25 $\mathrm{km\,s^{-1}}$ shock in an 85%-15% H_2-He mixture. Given that this test case is expected to produce a similar frozen temperature (on the order 20,000 K), the effect may also be present here.

The radiometer field of view includes the entire tunnel cross section and thus if any shock curvature were present, it would manifest as an earlier rise in the radiometer data. De Boer (1963) provide analytical estimates for the degree of shock curvature occurring in shock tubes. Evaluating these equations for condition C leads to a predicted shock curvature of 6 mm i.e. the axial distance between the shock front at the centreline and the shock front at the edge of the boundary layer. This corresponds to a difference in arrival time of 0.425 µs which agrees well with the observation.

5.4 Radiance Measurements Through Unsteady Expansion Waves

The radiometer probes are now used to interrogate the unsteady expansion region in an expansion tube given that they have proven satisfactory in their agreement with OES measurements in the shock tube. Conditions developed for two test gas mixtures, 79 % N_2 / 21 % O_2 and 10 % H_2 / 90 % He, are presented. These test conditions are representative of Earth and Gas Giant entry respectively. For each test gas, the arrangement of the facility and radiometer probes is first presented. Next, the test conditions and pressure measurements are presented. Finally, integrated radiance measurements made with the radiometers are shown and compared to predictions resulting from equilibrium analysis of the test conditions.

5.4.1 Test Time in an Expansion Tube

An analysis of the expected behaviour of the unsteady expansion process is desirable to interpret the experimental results. Note that this discussion is repeated from Chapter 2 as it is centrally relevant here. Paull and Stalker (1992) provide a complete summary of the factors limiting test time in an expansion tube which is paraphrased here. At high-enthalpy expansion tube test conditions, the test time is limited either by the downstream edge of the unsteady expansion or the reflection of the upstream edge of the expansion off the driver-test gas interface. This essentially amounts to whether the second $u + a$ wave shown in Figure 5.3 reaches the test point before or after the unsteady expansion. In the first case, assuming constant shock speed, the test time can be calculated with:

$$\tau = \frac{x_A a_7}{u_7(u_7 - a_7)} \tag{5.1}$$

Where x_A is the length of the acceleration tube, u_7 is the unsteadily expanded test gas velocity in the lab reference frame, and a_7 is the unsteadily expanded test gas speed of sound. In the second case, the test time is dependent on the time taken for the reflected expansion wave to emerge from the expansion. This time is given by:

$$t_1 = t_0 \left(\frac{a_7}{a_2} \right)^{\frac{\gamma+1}{2(1-\gamma)}} \tag{5.2}$$

Here, the subscript 2 represents the shocked (but not expanded) test gas state and γ is assumed to be the quiescent value. The parameter t_0 represents the time between rupture of the secondary diaphragm and arrival of the unsteady expansion at the driver/test gas contact surface. This value can be estimated by calculating the Mirels slug length of

Table 5.3: Axial locations of radiometers, where the primary diaphragm downstream face is the datum

	PD	SD	STS05	STS06	STS07	STS09
Position, m	0.0	2.86	3.56	4.31	5.06	6.56

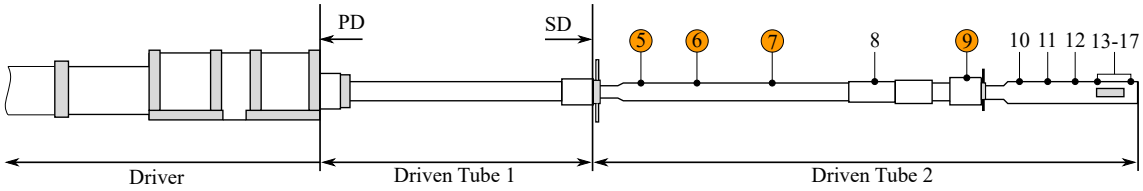

Figure 5.13: Arrangement 1

the test slug at the point of secondary diaphragm rupture and then assuming that the contact surface moves with constant velocity, u_2, after diaphragm rupture. All values required for calculation of these test times may be obtained from a simple state to state equilibrium solver. These equations have been solved to provide the test-time estimates in the following sections.

5.4.2 Synthetic Air Radiance Measurements

Arrangement

The facility shock timing stations were instrumented with four radiometer probes and piezoelectric pressure transducers for the experiments presented in this section. The radiometers were wall-mounted. A 780 ± 5 nm bandpass filter[3] targeting the oxygen 777 nm triplet with transmittance properties shown in Figure 5.7a was used for all synthetic air tests with no neutral density filter in series. The locations of the radiometers in the tube are highlighted as in Figure 5.13. All non-highlighted locations were instrumented with pressure transducers. For clarity, these figures are reproduced later in the document wherever data is presented. Table 5.3 shows the axial locations of the secondary diaphragm and radiometers where the primary diaphragm downstream face is the datum.

Tested Conditions

A summary of the expanding air conditions tested is provided in Table 5.4. The shock tube and acceleration tube fill pressures, p_1 and p_5 respectively, were recorded by facility pressure transducers immediately prior to the test. Here, the accelerator gas was always

[3]Thorlabs FBH780-10

Table 5.4: Summary of tested conditions. Values derived using the PITOT code assuming thermochemical equilibrium

Condition	Symbol	Test Gas Composition, %v/v	p_1, Pa	p_5, Pa	U_{s1}, km/s	$U_{s2/\infty}$, km/s	p_2, kPa	p_7, kPa
A	●	79 % N_2 / 21 % O_2	640	1.10	7.79	15.48	421.7	2.8
B	■	79 % N_2 / 21 % O_2	592	5.13	7.79	13.86	421.7	10.3
C	◆	79 % N_2 / 21 % O_2	601	10.00	7.79	13.31	421.7	18.4

laboratory air. The primary shock speed, $U_{s,1}$, is taken at the location immediately before the secondary diaphragm. The secondary shock speed, $U_{s,2}$, is taken as the average of the final three measurement locations in the acceleration tube. The full shock history for each experiment is shown in Figure 5.14. The post-shock pressure and fully expanded test gas pressure, p_2 and p_7 respectively, have been calculated using the PITOT state-to-state solver assuming thermochemical equilibrium and constant shock speed (James et al., 2018). Other state properties that may be referred to in the text but are not included in Table 5.4 have also been calculated using this method. The PITOT tool offers the user the option of expanding the gas at state 2 to either the experimentally measured shock speed or to the pressure of the shocked accelerator gas, the latter option was used here as the acceleration tube fill pressures are high enough that the accelerator gas should not be neglected. The T6 *high* driver condition was used in all cases. The secondary diaphragm material was always 10 μm Mylar.

Figure 5.14 shows the shock speeds for the test conditions discussed in this section. The location of the secondary diaphragm station, denoted *SD*, and the locations of the radiometer probes are also provided. The radiometer traces were used in tandem with the pressure traces to determine shock arrival. James et al. (2021) employed a similar approach to detect shock arrival in the X2 expansion tunnel but instead used a wall mounted fibre optic connected to a photodiode. A nearly identical shock trajectory is achieved in the shock tube between the cases before the profiles diverge after rupture of the secondary diaphragm and the characteristic expansion to the higher secondary shock speed. The calculated shock speeds reflect the average based on time of arrival and distance between adjacent stations. It appears that the acceleration from primary to secondary shock speed takes places over a relatively large distance (3 - 5 m), however this is because the shock speed across the secondary diaphragm is calculated using one sensor in the shock tube and one sensor in the accelerator tube which skews the value

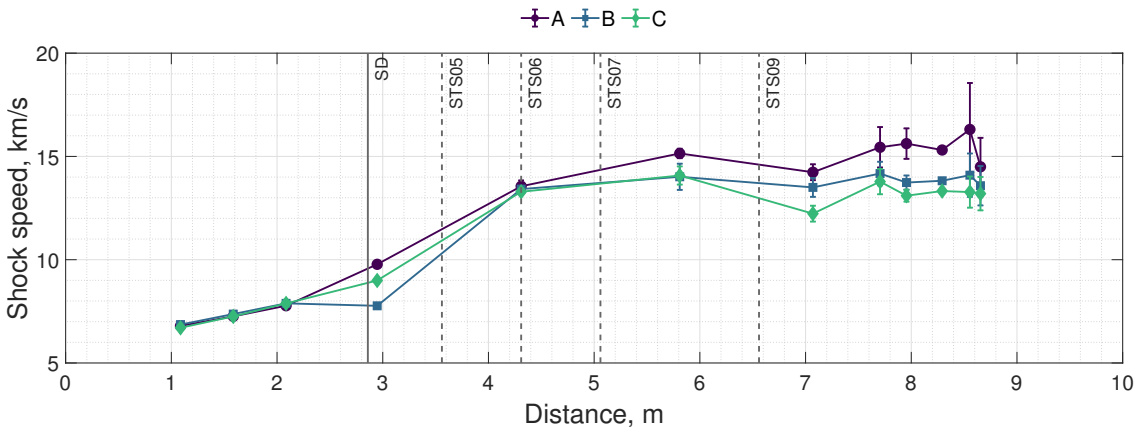

Figure 5.14: Shock trajectories for the expanding synthetic air experiments

Table 5.5: Mirels' slug lengths for the test gas and accelerator gas for each test condition. These are evaluated at the instant of secondary diaphragm rupture and at the end of the acceleration tube.

Condition	Shock Tube		Acceleration Tube	
	ℓ_m, mm	t, µs	ℓ_m, mm	t, µs
A	161	20.7	15.0	0.999
B	159	20.5	44.9	3.24
C	160	20.6	78.5	5.90

lower. Higher resolution measurements of the shock trajectory immediately after secondary diaphragm rupture are desirable but would require a specialised technique such as the microwave shock speed detector of Dufrene et al. (2015).

Table 5.5 shows the predicted Mirels' slug lengths for each test case. The values in the *Shock Tube* columns refer to the length of the test slug at the instant of secondary diaphragm rupture and the values in the *Acceleration Tube* columns refer to the length of the accelerator gas slug when the secondary shock reaches the final shock timing station approximately 7 m from the secondary diaphragm. The slug times refer to the time taken for the entire slug to pass a point if travelling at constant shock speed. Because the accelerator gas essentially behaves as a low pressure shock tube driven by the unsteadily expanding test gas, it is reasonable to apply Mirels' theory, neglecting possible deviations from the theory due to the low acceleration tube fill pressure which are discussed later.

Figure 5.15 shows static pressure traces obtained at STS10 for conditions A, B, and C. The initial peak corresponds to arrival of the secondary shock which is followed in all cases by a quasi-steady period of 20-50 µs, which is the fully expanded test gas. The expanded test gas pressures predicted using the PITOT code are shown with horizontal dashed lines. These values generally agree well with the experimental results, indicating

that the quasi-steady period observed in the experiment is the test time. The rise in pressure is in each case is the arrival of the downstream end of the unsteady expansion. In all cases the noise level increases significantly around 100 µs, potentially indicating the arrival of the reflected $u + a$ wave. This region is typically considered to be analytically indeterminate because of the complexity of the unsteady, reflected wave processes.

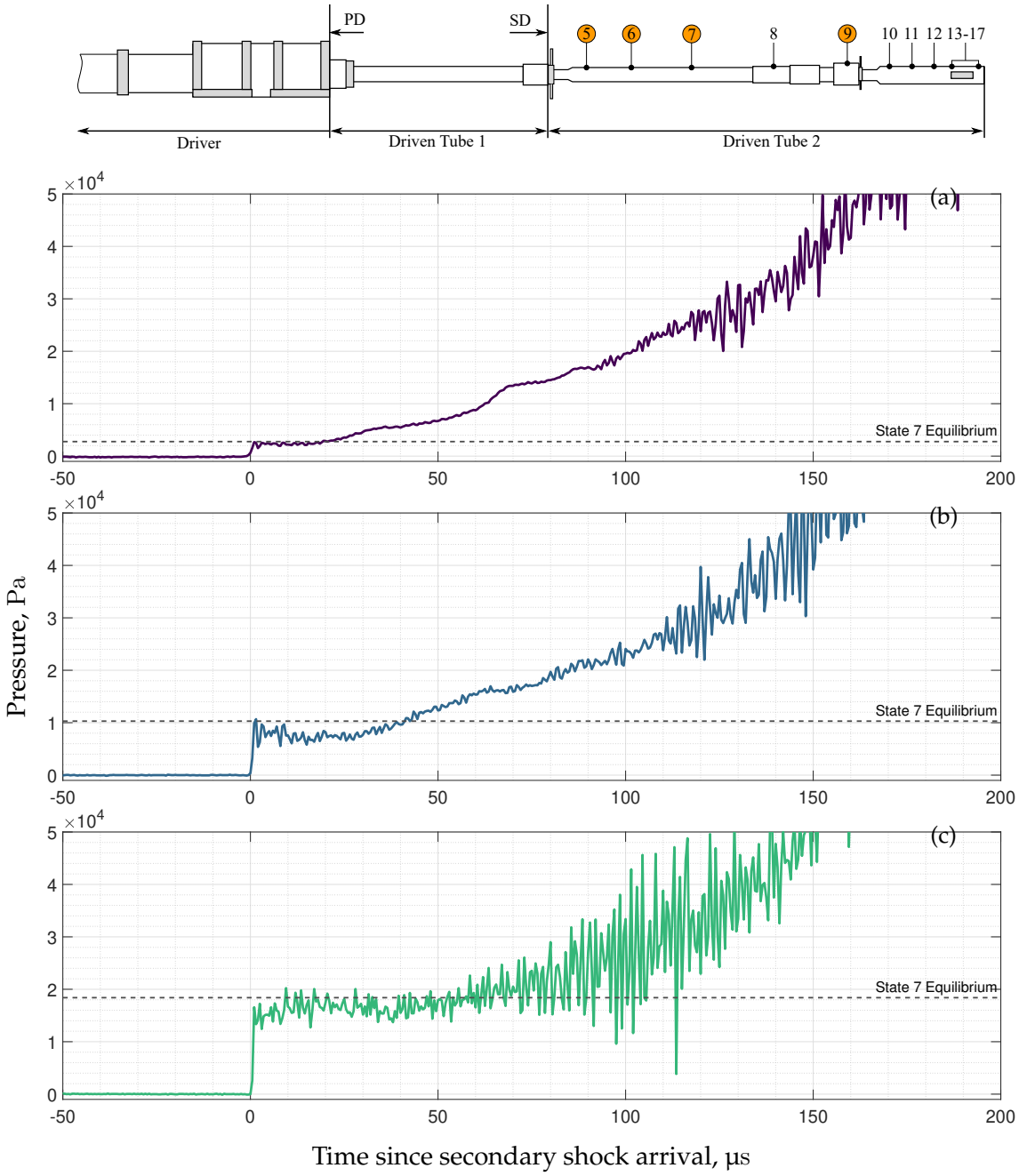

Figure 5.15: Static pressures recorded at STS10 for each of the test conditions described in Table 5.4

The analysis discussed in Section 5.4.1 can be applied to these test cases to provide estimates for the steady test time. Figures 5.16 shows distance time representations of the

wave processes in the experiments where 0 m is the location of the primary diaphragm. Here, the solid lines represent the primary shock waves. The location of the driver-test gas and test-accelerator gas contact surfaces (dashed lines) have been calculated using a steady Mirels prediction. The coloured line represents the reflected unsteady expansion wave. By taking a cross section at the location of each radiometer, an estimate of the test time may be obtained. Here, in all cases, the analysis suggests that the test time is always limited by the reflected unsteady expansion wave. This is consistent with the observations of static pressure in Figure 5.15 which show the arrival of significantly increased noise around 100 µs.

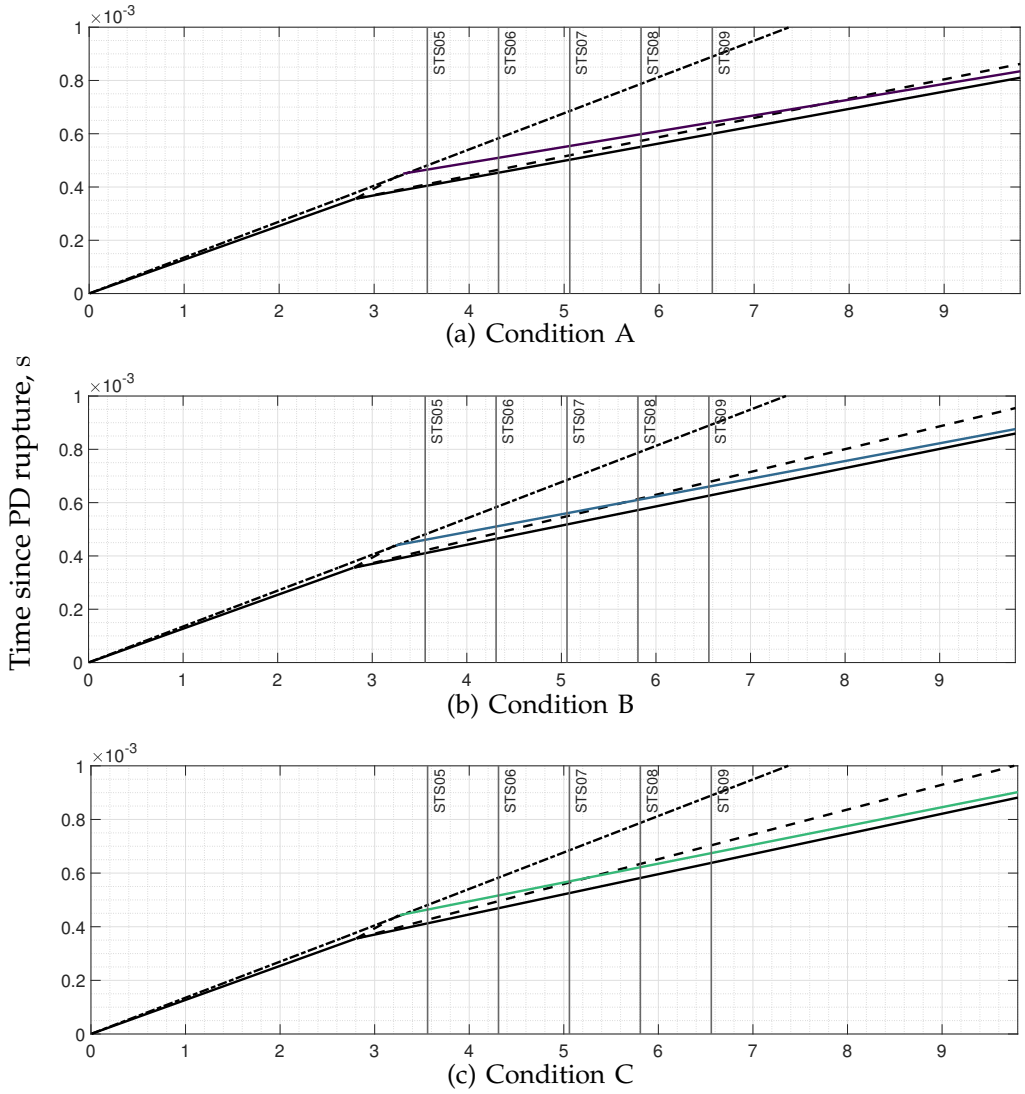

Figure 5.16: Test time predictions for the expanding air test conditions. Solid black lines represent the primary and secondary shocks, dashed lines represent the contact surfaces. The coloured line represents the reflected $u + a$ wave.

The wave diagram predictions suggest that the reflected unsteady expansion wave should reach the secondary shock and affect the entire test slug by STS09 in each case, however this is not observed in the experimental data where a steady test time and unsteady expansion is clear at STS10. This discrepancy is likely due to the inability of a constant shock speed, equilibrium model to account for the complex wave processes taking place in the expansion tube.

Radiometer Measurements

Figures 5.17, 5.18, and 5.19 show time-resolved measurements of radiance obtained from four radiometers located in the acceleration tube. The test conditions shown were designed to match as nearly as possible the shocked test gas state at the instant of secondary diaphragm rupture. The effects of varying unsteady expansion strength on the test gas radiance may then be studied by changing the acceleration tube pressures as show in Table 5.4.

The traces in every case are characterised by an initial peak, which is the accelerator gas. A steady Mirels analysis of the accelerator gas predicts a slug length on the order of microseconds for all conditions, which is generally shorter than the width of the initial peak. This discrepancy is particularly extreme for condition C, where the width of the initial peak is approximately 20 µs compared with a steady Mirels prediction of 5.9 µs. The behaviour after the initial is dependent on the location of the radiometer and the accelerator gas pressure, but typically includes a rise and fall in radiance due to the passage of the unsteady expansion wave system.

The apparent deviation from Mirels' theory could be attributed to several effects. Firstly, it is not clear if Mirels' theory is valid for very low pressure test conditions. In extreme cases, expansion tubes are susceptible to the phenomenon of *test gas necking*. Gildfind et al. (2018a) provide a complete description of this process. Gas from the accelerator slug tends to be swept past the test/accelerator gas contact surface and into the boundary layer, leading to a highly three-dimensional, ill-defined boundary between accelerator and test gas. It is likely that this is occurring here and smearing the accelerator gas slug. Secondly, it is possible that the radiometer is recording increased radiance from the thermochemically frozen portion of the expanded test gas. The test gas and accelerator gas both contain O_2 and thus the radiometers cannot be used to distinguish between the two with the present arrangement. Additionally, the higher pressure accelerator gas conditions appear to have two distinct peaks in the radiometer trace closest

to the secondary diaphragm. It could be the initial part of the expanded test gas slug or could be radiation from the secondary diaphragm material that is convected downstream with the test gas after rupture. The Mylar diaphragm, $(C_{10}H_8O)_n$, is comprised in part of oxygen and thus may radiate in the region of interest. Thirdly, non-negligible reflected shocks have been shown to form at the secondary diaphragm in expansion tubes, leading to higher temperatures in the test gas closest to the diaphragm at the instant of rupture (Neely and Morgan, 1994; Bakos and Morgan, 1994). Although the secondary diaphragms used here are relatively thin (10 µm) and thus a relatively weak reflected shock would be expected (Furukawa et al., 2007), it is possible that this phenomenon is contributing the width of the initial peak. This also makes it difficult to estimate the thermochemical state of the gas and provided an upper bound on the possible test gas radiance.

In the case where $p_5 = 1.10$ Pa, the radiometer closest to the secondary diaphragm records a reduced radiance before increasing again after 20 µs. This steady time agrees well with the observation in Figure 5.15, indicating that the reduction in radiance occurs when the expanded test gas passes through the radiometer field of view. This gas has been rapidly expanded from its state in the shock tube to a low pressure which causes the radiance to decrease. The gas further upstream from the secondary shock has expanded less when compared to the gas downstream and thus it is hotter and radiates more strongly. Radiometers further downstream image the test slug at times later in its history when the unsteady expansion wave has propagated through and thus cooled more of the test gas which is evident in the successively lower radiances measured.

For the $p_5 = 5.13$ Pa case similar trends are evident. The width of the initial peak is relatively larger which reflects the longer accelerator gas slug length due to the increased acceleration tube fill pressure. In both this and the $p_5 = 10.0$ Pa case the radiometer closest to the secondary diaphragm records a much wider than expected (i.e. greater than the accelerator gas slug length) initial peak. The radiance level behind the shock reaches a relatively steady state earlier than in the $p_5 = 1.10$ case.

Predictions of the thermochemical state and composition for the shocked test gas (2), the shocked accelerator gas (6), and the expanded test gas (7) are provided in Table 5.6. Here, the PITOT code is used with the average experimental shock speeds and the results are used to run Nonequilibrium Radiative Transport and Spectra Program (NEQAIR) simulations. In all NEQAIR simulations presented here the state population method was set to be non-Boltzmann. The geometry was set to be a tangent slab of 96.3 mm

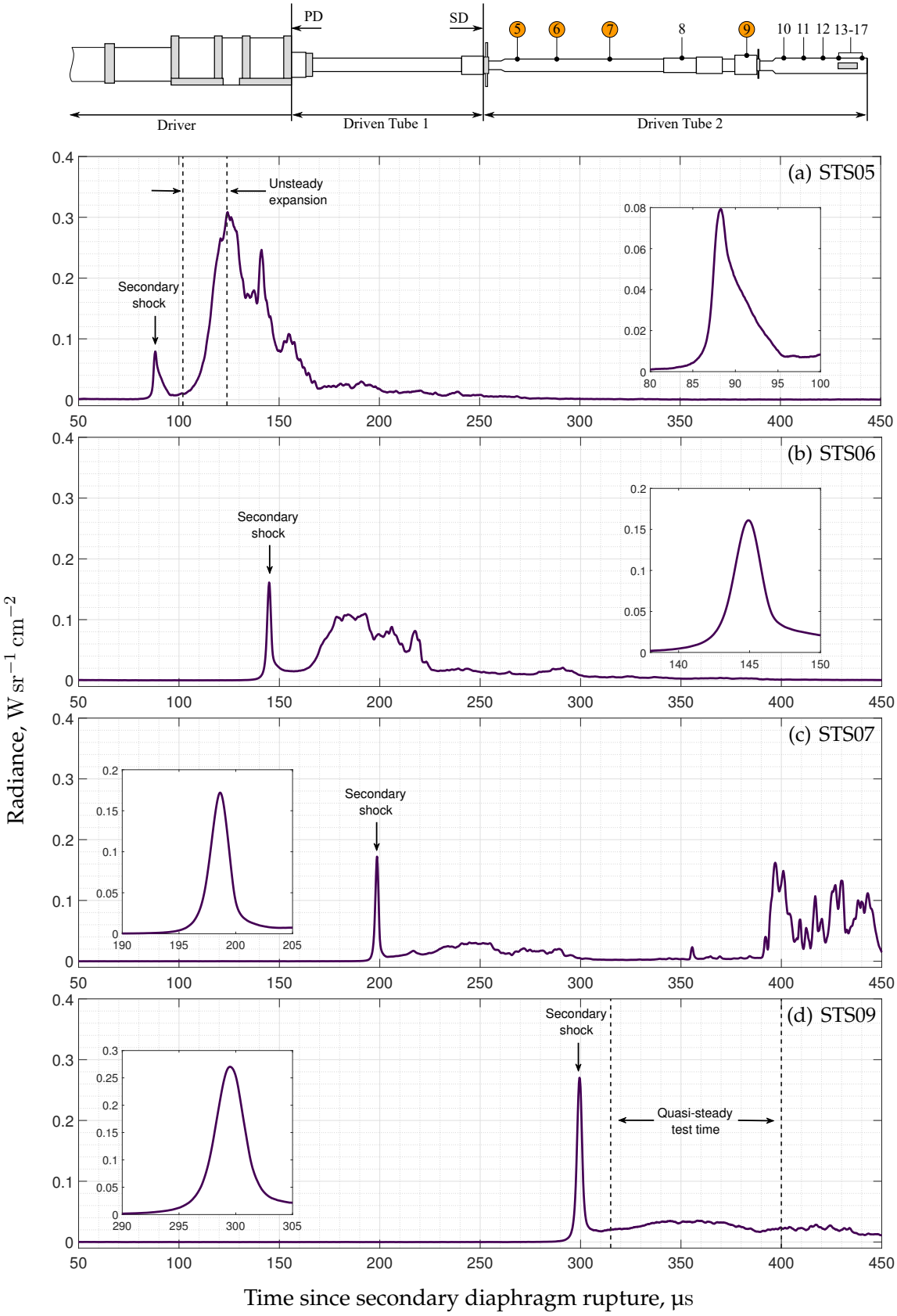

Figure 5.17: Oxygen 777 nm radiance recorded by the radiometer probes for condition A at different distances from the secondary diaphragm.

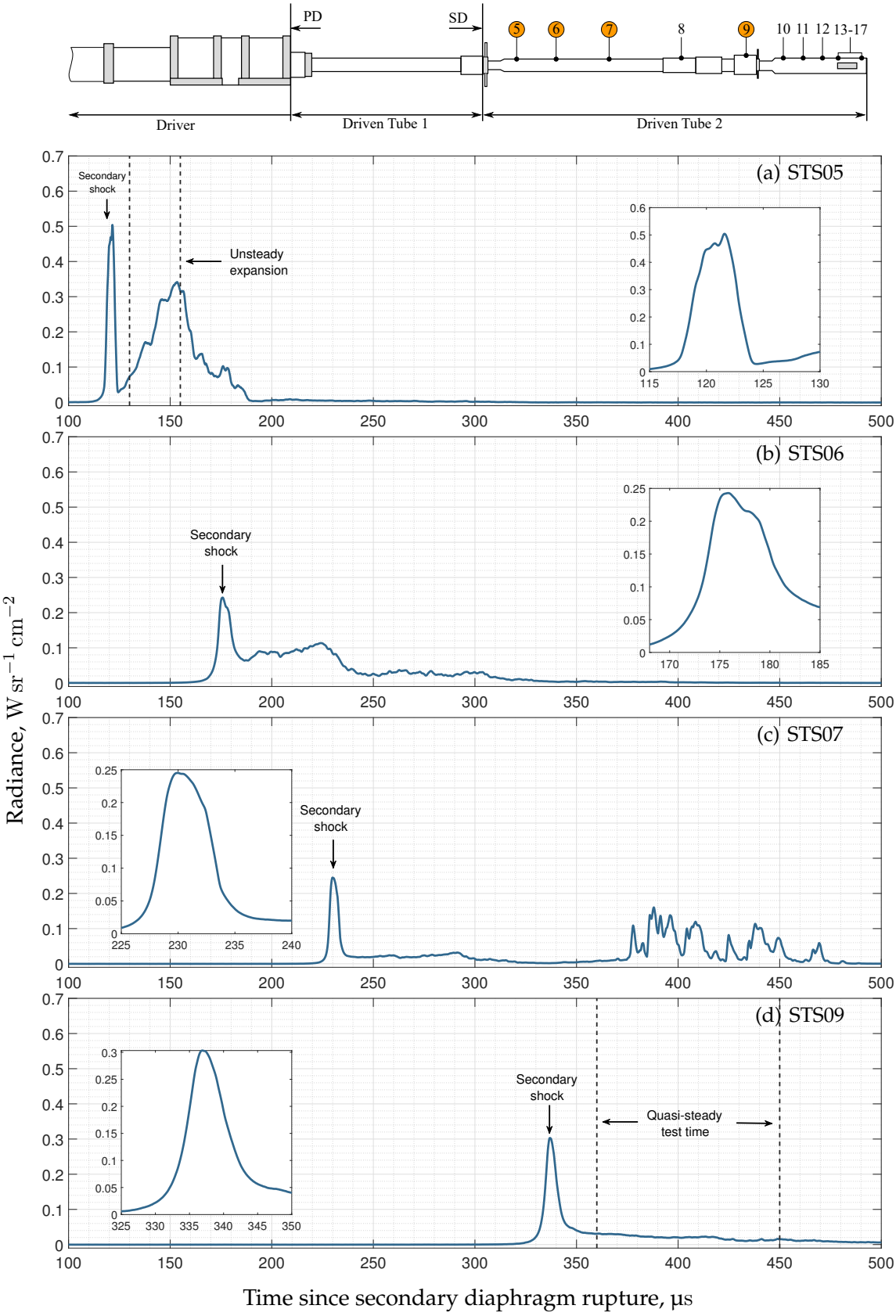

Figure 5.18: Oxygen 777 nm radiance recorded by the radiometer probes for condition B at different distances from the secondary diaphragm.

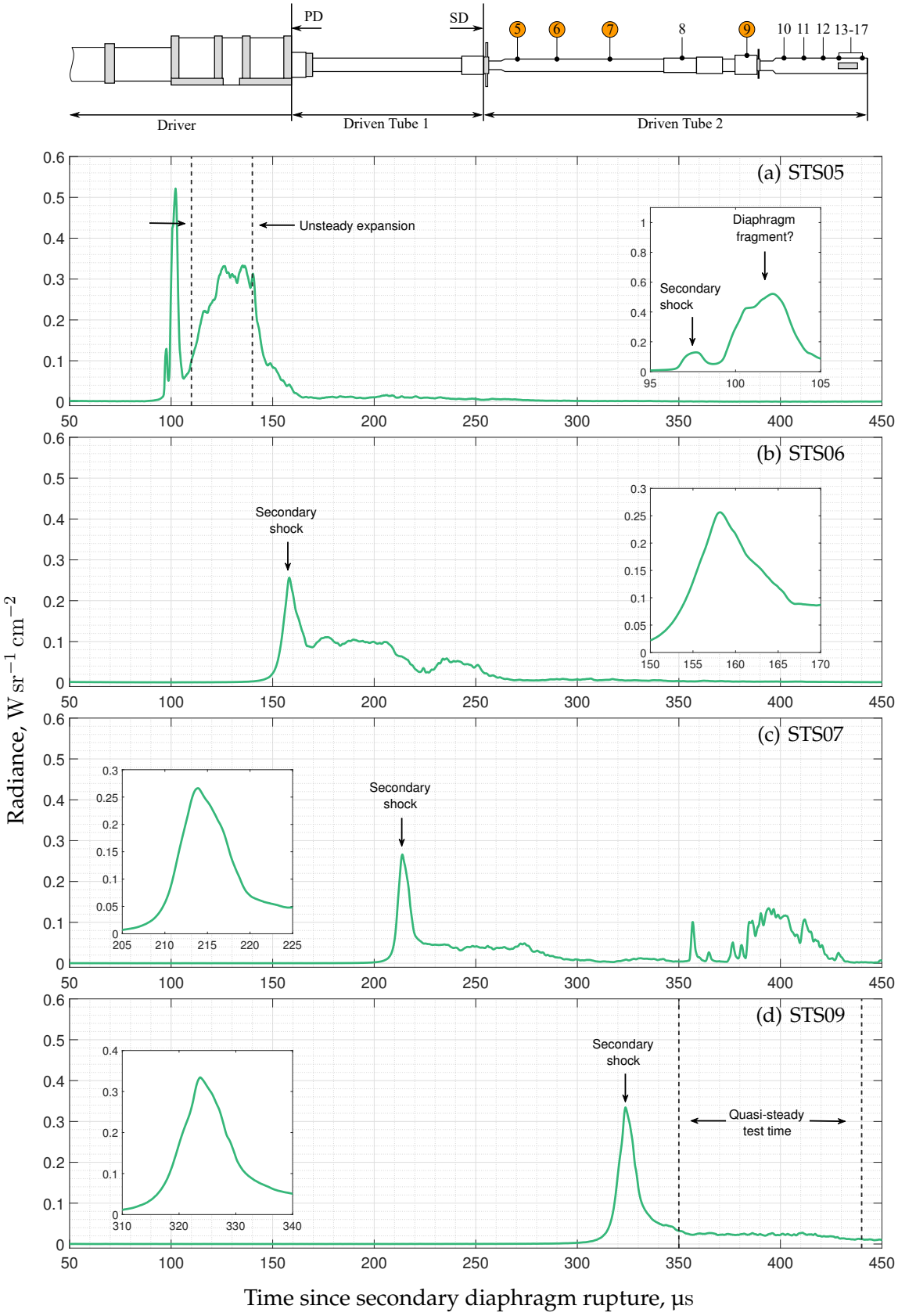

Figure 5.19: Oxygen 777 nm radiance recorded by the radiometer probes for condition C at different distances from the secondary diaphragm.

Table 5.6: Predictions of equilibrium properties for states 2, 6, and 7 for conditions A, B, and C. State 2 is assumed to be shared between the conditions.

State	2	A6	A7	B6	B7	C6	C7
State variables							
p, Pa	396,100	2,770	2,770	10,253	10,253	18,414	18,414
T, K	7,884	12,204	5,285	12,322	5822	12437	6077
ρ, kg/m^3	0.110	2.53e-4	1.32e-03	1.07e-3	4.21e-03	2.01e-3	7.09e-03
Species mole fractions							
e-	1.17e-3	3.83e-1	0	2.88e-1	0	2.52e-1	0
N_2	1.89e-1	4.41e-7	0.445	5.12e-6	0.375	1.17e-5	0.347
O_2	5.32e-5	1.43e-9	2.6e-05	1.39e-8	2.97e-05	3.11e-8	3.2e-05
N	5.58e-1	1.71e-1	0.251	3.18e-1	0.335	3.77e-1	0.37
O	2.46e-1	6.21e-2	0.302	1.03e-1	0.287	1.18e-1	0.281
NO	3.33e-3	4.24e-8	0.0019	4.55e-7	0.0022	1.03e-6	0.0024
N_2+	5.35e-5	8.95e-7	0	4.40e-6	2.16e-06	7.62e-6	3.81e-06
O_2+	6.02e-7	1.23e-8	0	4.90e-8	0	8.01e-8	0
N+	4.43e-4	3.15e-1	2.30e-06	2.42e-1	1.20e-05	2.12e-1	2.25e-05
O+	1.59e-4	6.74e-2	4.28e-06	4.62e-2	1.31e-05	3.90e-2	2.02e-05
NO+	5.22e-4	1.02e-6	1.5e-04	4.36e-6	2.40e-04	7.06e-6	2.83e-04
NEQAIR equilibrium radiance							
Radiance	0.68	0.23	7.6e-6	1.1	1.9e-4	2.0	7.4e-4

width, equal to the T6 internal diameter. The NEQAIR output was then multiplied with the transmittance function for the bandpass filter, the area under this result being the radiance shown in Table 5.6.

The PITOT/NEQAIR state 7 predicted radiance is close to zero for all test conditions, however a value of at least 0.01 $\mathrm{W\,sr^{-1}\,cm^{-2}}$ is measured in all cases in the expanded test gas. PITOT was shown to be in good agreement with the experimentally measured state 7 pressure, however it appears that the predicted temperatures and species fractions are incorrect in these cases. This could be caused by the formation of a strong reflected shock at the secondary diaphragm, causing the test gas to reach a higher temperature before entering the unsteady expansion. Additionally, an equilibrium assumption can be a poor approximation of the unsteady, non-equilibrium processes taking place in an expansion tube, which will lead to error when compared with experiment.

In all test cases, the radiance measured after the accelerator gas appears to reach a maximum value just before the noise level in the pressure traces increases. This suggests that this is when the reflected $u + a$ wave arrives, further expanding the test gas and thus decreasing the temperature and radiance. After this point, the radiance remains above zero for 50-100 µs. This radiance may originate from test gas entrained in the boundary

layer across the driver/test-gas interface.

The radiometer located at shock timing station 7 consistently records disturbances after passage of the unsteady expansion that are not seen by other radiometers. This corresponds to the time that noise level seen in the pressure traces rises significantly and is thus believed to be a mechanical disturbance, rather than an optical phenomenon.

To summarise, the features evident in the radiometer traces are broadly consistent with those expected in an expansion tube and good agreement with corresponding pressure measurements is seen. Absolute radiance levels measured for the oxygen 777 nm atomic line do not agree with PITOT/NEQAIR equilibrium simulations, however this is not unexpected as this simulation approach does not account for many of the complexities inherent in expansion tube operation previously discussed. The radiometer measurements indicate that effects such as thermochemical freezing, non-ideal secondary diaphragm rupture, complex boundary layer growth, and upstream wave processes are playing a significant role in determination of the freestream conditions and thus further study is necessary.

Repeatability

Repeat runs of condition A are presented in this section in order to provide an indication of the variation in radiance observed on a shot-to-shot basis. Table 5.7 shows the fill conditions and average shock speeds achieved. The fill pressures p_1 and p_5 were as close as possible given the T6 fill infrastructure available at the time[4]. It should be noted that for these cases the secondary diaphragm was located downstream of STS09, rather than STS05 as for the previously shown test cases. The position of the diaphragm is clearly shown in Figure 5.22.

Table 5.7: Summary of condition A repeats. Values derived using the PITOT code assuming thermochemical equilibrium. U_{s1} and $U_{s2/\infty}$ have been calculated using the last three and four measurements in the shock and acceleration tube respectively

Condition	Symbol	Test Gas Composition, %v/v	p_1, Pa	p_5, Pa	U_{s1}, km/s	$U_{s2/\infty}$, km/s
T6s533 (A)	●	79 % N_2 / 21 % O_2	537	0.958	8.51	13.8
T6s534 (A)	●	79 % N_2 / 21 % O_2	525	1.01	8.41	13.9

The shock trajectories observed for the two repeat cases are shown in Figure 5.20. The shock speeds achieved in the shock tube for T6s534 were lower by 1.2% and higher in the

[4]I.e. No mass flow controller available

acceleration tube by 0.72% on average. Shock speed measurements in the acceleration tube agree within uncertainty despite the large variation due to the smaller spacing of shock timing stations.

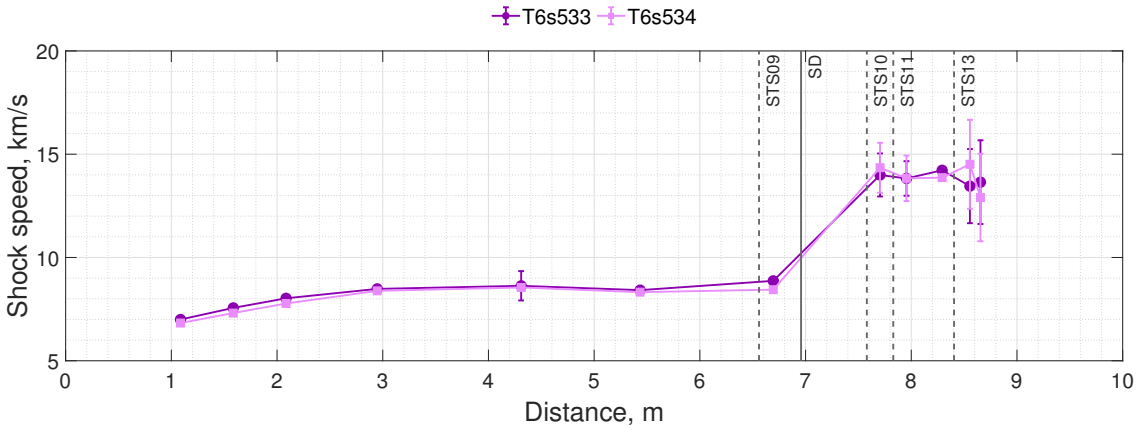

Figure 5.20: Shock trajectories for repeats of condition A

Figure 5.21 shows the pressures measured at the final common pressure transducer in the shock tube, STS08, and the first common pressure transducer in the acceleration tube, STS11. These traces, particularly those at STS11, highlight that the wave processes taking place in the acceleration tube are qualitatively different despite these test cases being nominal repeats of one another with matching driver conditions, fill pressures, sensors, diaphragms, etc. This is again a demonstration of the need for modelling of impulse facility experiments on a test-to-test basis.

Finally, the Oxygen 777 nm radiance measured by two radiometers positioned in STS11 and STS13 for these test cases is shown in Figure 5.22. Only two radiometer traces are shown since these were the positions shared between these test cases, other were positioned further downstream. Again, it is evident that different wave processes take place in the experiments. Possible reasons for this behaviour have been outlined in detail earlier in the thesis.

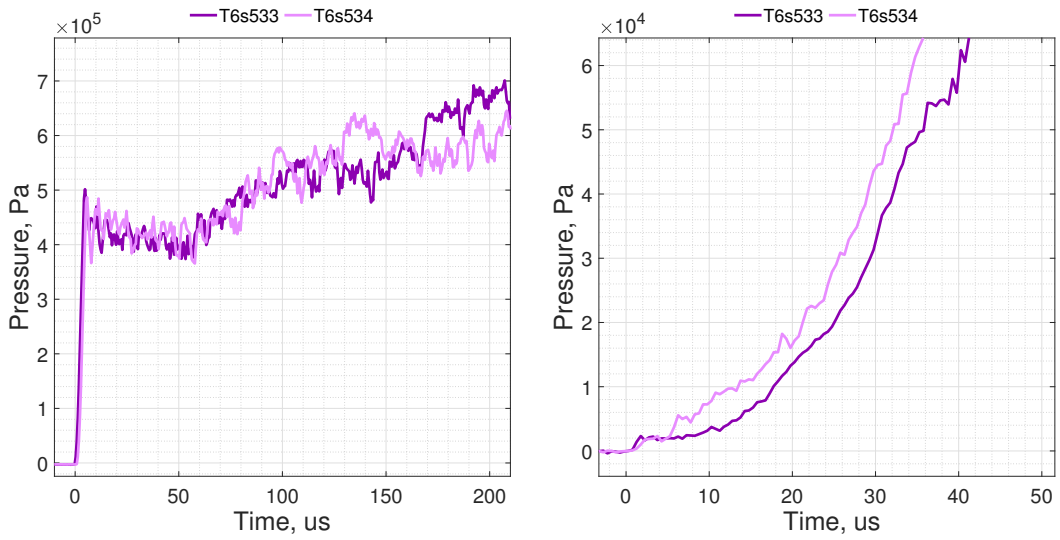

(a) STS08 (b) STS11

Figure 5.21: Pressure measurements at the final common shock timing station in the shock tube and first shock timing station in the acceleration tube for the condition repeats

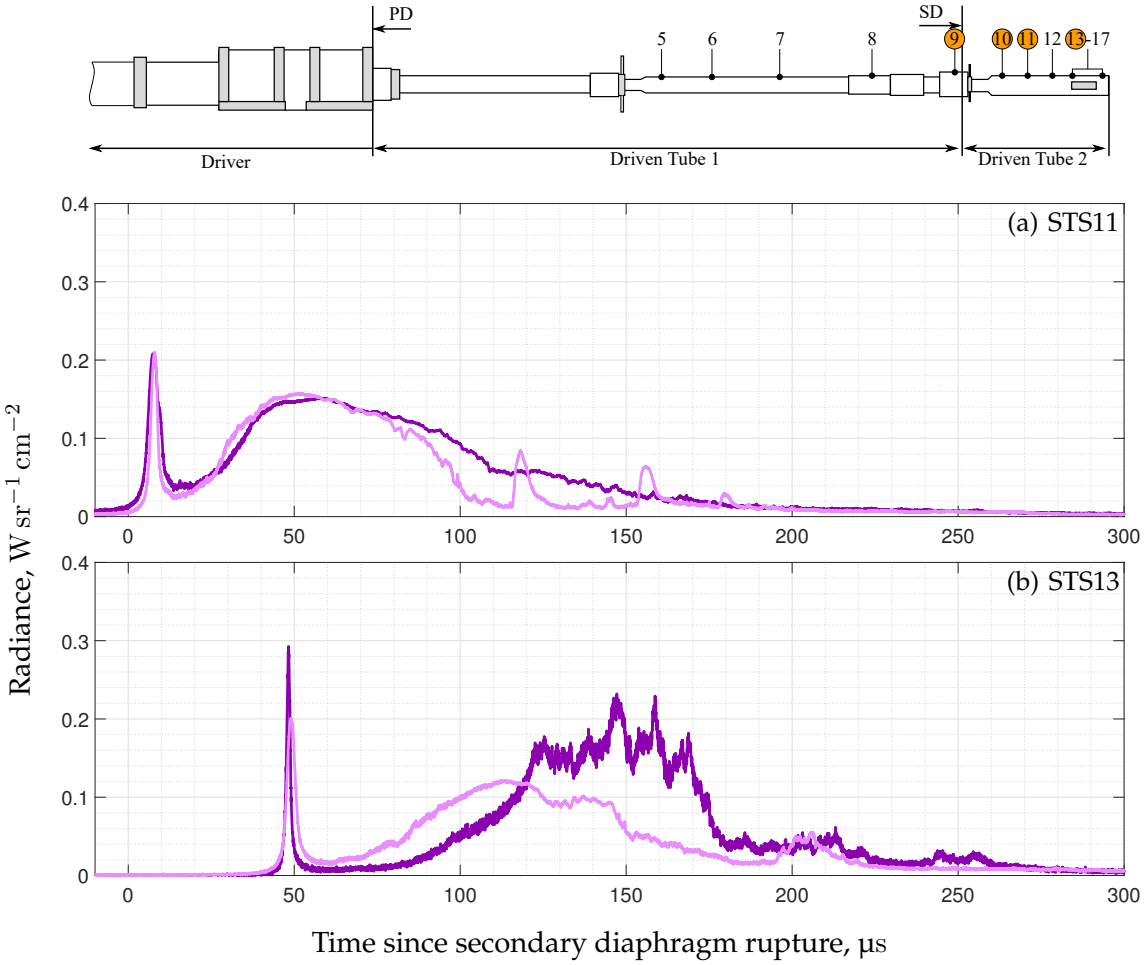

Figure 5.22: Oxygen 777 nm radiance recorded by the radiometer probes for repeats of condition A at different distances from the secondary diaphragm.

5.4.3 H_2-He Radiance Measurements

The measurements of H-α radiance are presented in this section. Two arrangements were used here in an effort to maximise the achievable temperature, and thus radiance of the test gas. These are outlined first, followed by discussion of the test conditions and finally presentation of the radiance.

Arrangement

The first physical arrangement used was identical to the one described in the previous section. 660 nm bandpass filters were installed in all radiometers to target the 656 nm H-α line. A third diaphragm was included for later experiments, allowing the expansion tube to be operated with a secondary driver in the hopes of increasing the post-shock temperature and radiance. James et al. (2020) have used a similar approach achieve flight equivalent velocities in excess of 22.2 $\mathrm{km\,s^{-1}}$. A 660 $\pm$ 5 nm bandpass filter targeting the H-α line was used for all H_2-He tests with no neutral density filter in series.

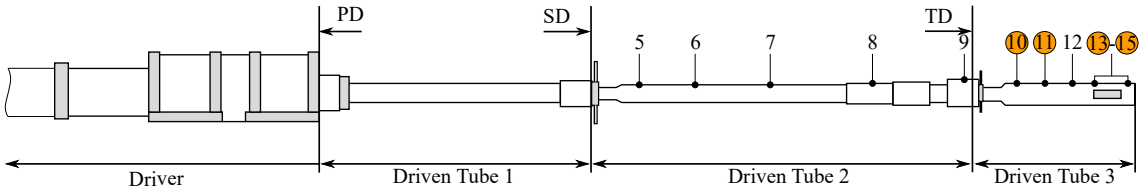

Figure 5.23: Arrangement of the radiometers for the case with the tertiary diaphragm

Tested Conditions

Table 5.8 shows the details of the tested H_2-He conditions. A mixture fraction of 10% H_2 / 90% He was used in an effort to increase the achievable temperature in the post-shock gas and thus radiance. The equilibrium temperature achieved for this mixture is estimated by CEA to be 4706 K, compared with 2800 K for the same shock speed and initial pressure in a 85% H_2 / 15% He mixture. The properties presented in Table 5.8 were again derived using the PITOT code. For test condition E, the secondary and tertiary diaphragms were made from 10 $\mu\mathrm{m}$ Mylar sheet, while the primary diaphragm was kept as 2 $\times$ 0.4 mm stainless steel corresponding to the T6 *high* driver condition.

Figure 5.24 shows the experimental shock trajectory for test condition D. As discussed in Section 5.4.2, the rise in shock speed after the secondary diaphragm appears gradual because of the point-to-point calculation method. A relatively constant shock speed is observed toward the end of the tube. Three distinct plateaus are evident for condition E,

Table 5.8: Summary of tested conditions. Values derived using the PITOT code assuming thermochemical equilibrium

Condition	Symbol	Test Gas Composition, %v/v	p_{sd}, Pa	p_1, Pa	p_5, Pa	U_{s1}, km/s	$U_{s2/\infty}$, km/s	p_2, kPa	p_7, kPa
D		10 % H_2 / 90 % He	-	2135	1.10	8.8	16.6	211	3.2
E		85 % H_2 / 15 % He	19,938	2,246	0.48	9.02	18.2	241.5	2.70

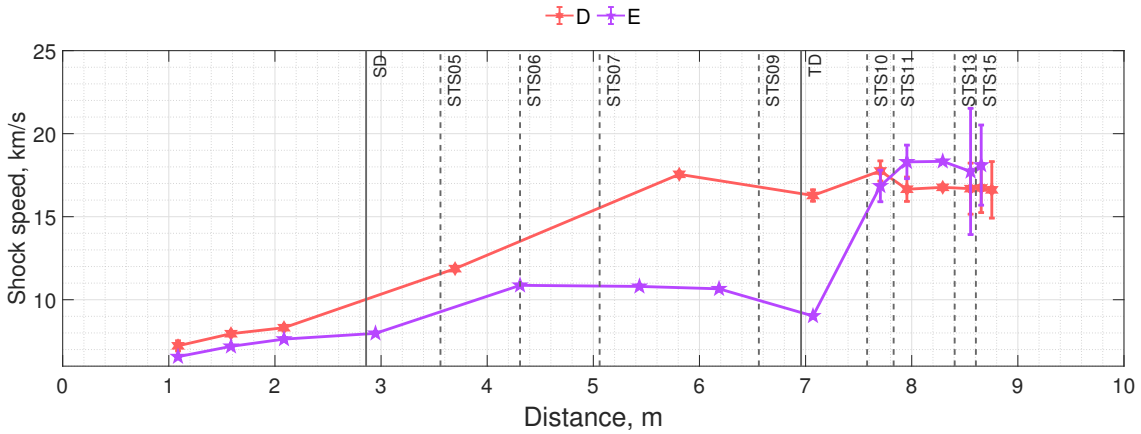

Figure 5.24: Shock trajectory for test condition D

each corresponding to one of the driven tubes. Strong shock attenuation occurs toward the end of the second driven tube, nearly nullifying the added performance provided by inclusion of a secondary driver. The shock accelerates from 7.97 $\mathrm{km\,s^{-1}}$ at the end of driven tube 1 to a speed of 10.87 $\mathrm{km\,s^{-1}}$ in driven tube 2, before decelerating to 9.02 $\mathrm{km\,s^{-1}}$ just before the tertiary diaphragm. This arrangement appears to provide minimal if any improvement over the conventional double diaphragm arrangement in the previous section.

Figure 5.25 shows static pressure recorded at STS10 for condition D. The fully-expanded test gas state (state 7) predicted by PITOT is also shown, which is in reasonable agreement with the experimental data. A period of steady pressure persists for approximately 30 µs after arrival of the secondary shock and before arrival of the downstream edge of the unsteady expansion. A longer steady test period is expected for condition D when compared with conditions A-C because of the higher shock tube fill pressure and hence longer Mirels slug length. As with the synthetic air test conditions, a large disturbance arrives at the end of the unsteady expansion which is likely the arrival of the reflected $u + a$ wave.

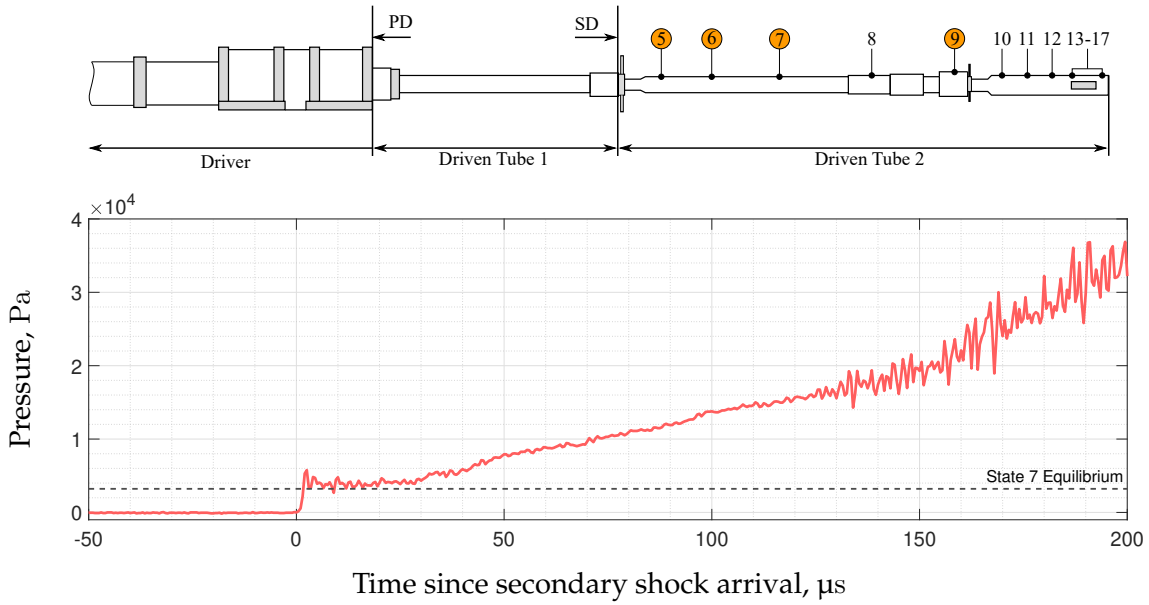

Figure 5.25: Static pressure recorded at STS10

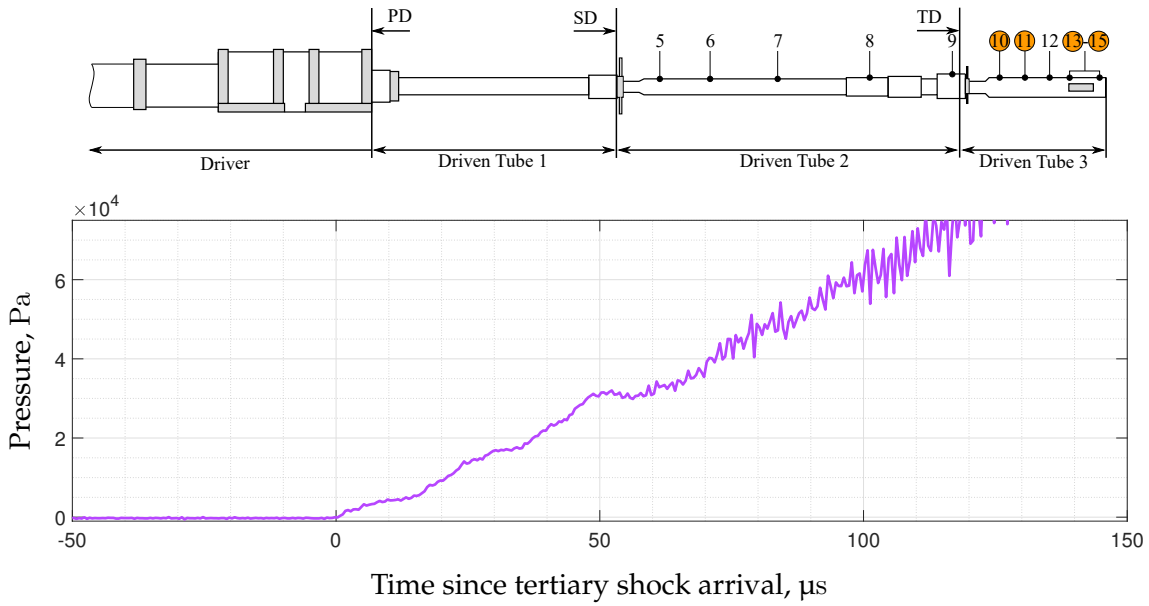

Figure 5.26: Static pressure recorded at STS15

Radiometer Measurements

Figure 5.27 shows records from the radiometers for condition D. As with the synthetic air cases, the initial peak for each radiometer is radiance from the accelerator gas. Despite the usage of a 660 nm bandpass filter which should not transmit oxygen atomic radiation, the accelerator gas peak is still visible. This likely originates from trace contamination of H_2O in the lab air accelerator gas.

NEQAIR predicts negligible ($< 1 \times 10^{-5}\ \mathrm{W\,sr^{-1}\,cm^{-2}}$) integrated radiance for the H-α line for both the post-shock state (2) and the fully expanded test gas state (7). This is consistent with experimental observations of state 7, however it does not explain the presence of the rise after the steady test time where the test gas radiance should also be close to zero. Many of the non-ideal effects present in expansion tubes have been discussed in Section 5.4.2 which may contribute here, particularly the reflected shock formed at the secondary diaphragm. It could also be that impurities in the tube, such as carbon products, are contributing to the radiation seen post-shock.

Figure 5.28 shows the radiance observed for test condition E. Radiance emitted in the region where the expanded test gas is expected is negligible which is consistent with NEQAIR predictions. Radiance through the unsteady expansion is of a lower magnitude than that seen in condition D despite the slightly higher shock speed achieved in the test gas (9.02 $\mathrm{k\,m/s}$ vs 8.8 $\mathrm{km\,s^{-1}}$). This is a reflection of the lower post-shock temperature that can be achieved in H_2-He mixtures with higher hydrogen fractions.

5.5 Summary

Integrated measurements of the oxygen 777 nm and hydrogen 656 nm atomic lines have been made through unsteady expansion waves in the T6 Stalker tunnel. The measurements were made with wall-mounted radiometer probes that were validated against conventional optical emission spectroscopy. Good agreement was seen with the OES system for the H-α line both in terms of absolute radiance and spatial resolution. Radiance measurements through the unsteady expansion wave indicate a test time that is in agreement with that deduced from wall mounted pressure transducers. Absolute radiance measurements made during the test time are higher than those predicted by equilibrium, state-to-state analysis, indicating the need for improved modelling tools for expansion tube flows. These measurements constitute a novel dataset for expanding flows where historically relatively few experimental measurements are available. The work in this sec-

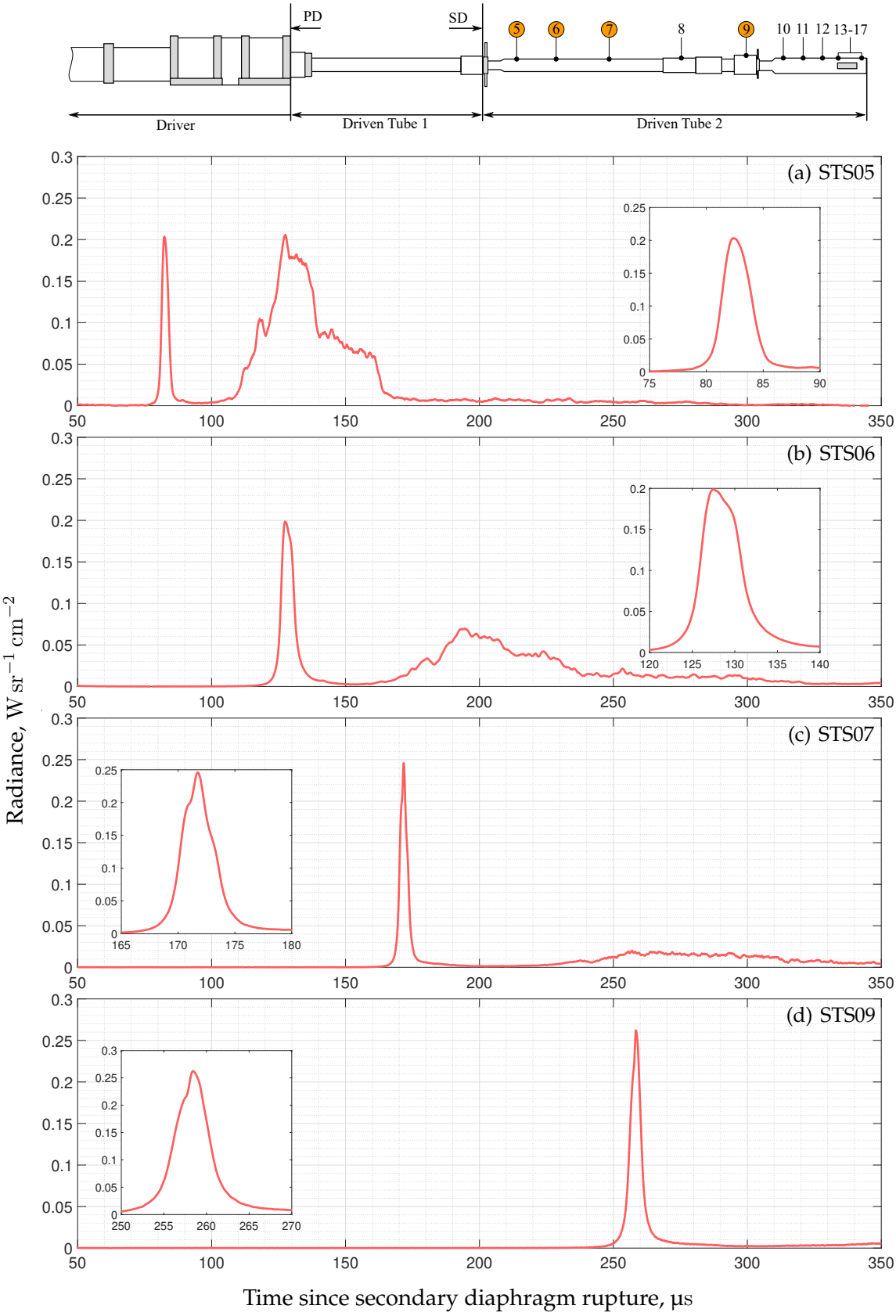

Figure 5.27: Hydrogen 656 nm radiance recorded by the radiometer probes for different distances from the secondary diaphragm.

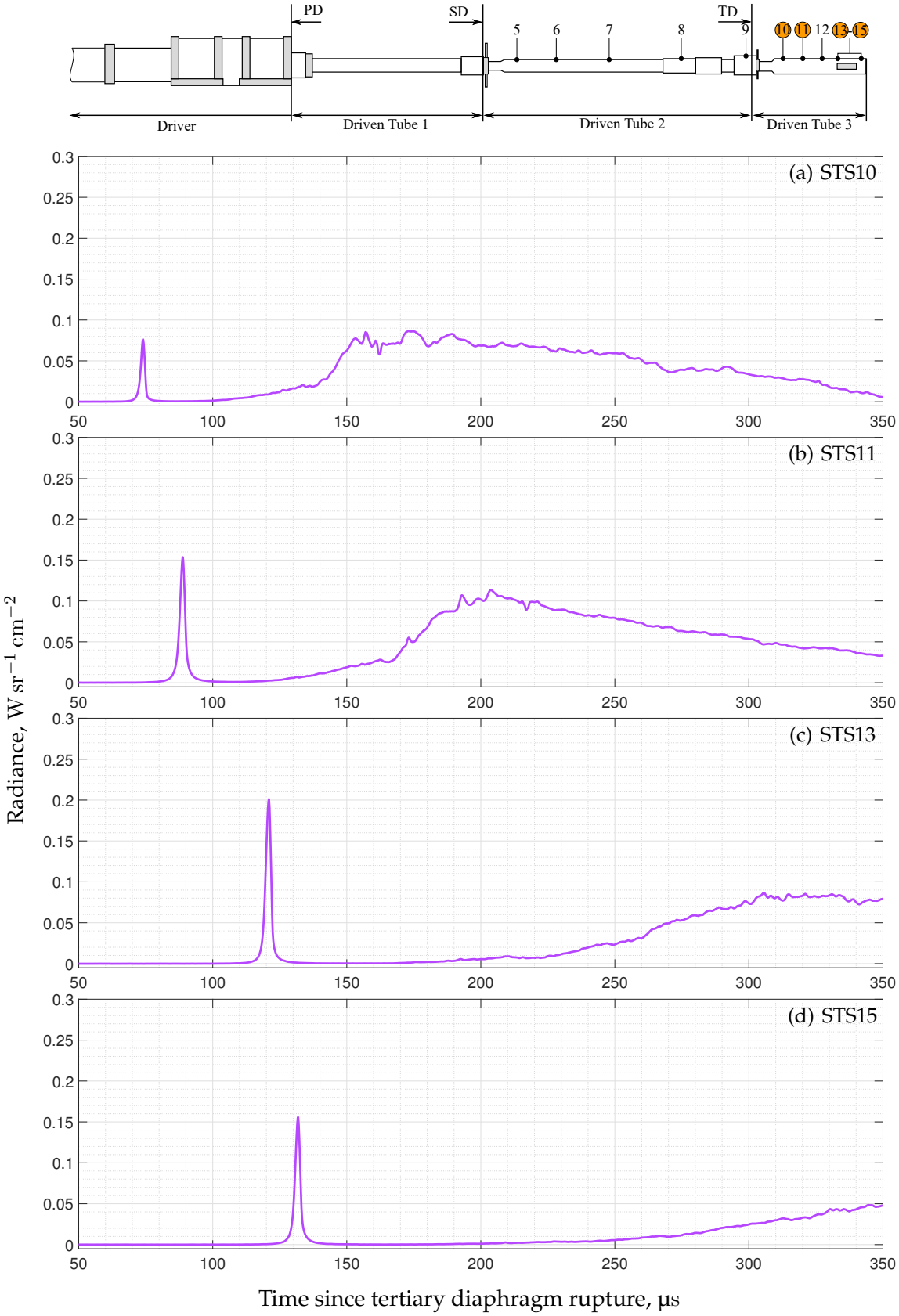

Figure 5.28: Hydrogen 656 nm radiance recorded for test condition E

tion serves as a platform for validation of the LASTA 2.0 expansion tube model, which is outlined in the next chapter.

Chapter 6

Modelling the Expansion Tube with LASTA 2.0

Contents

6.1 Introduction

Now that an experimental validation dataset for radiance through the unsteady expansion has been produced, LASTA 2.0 can be adapted to allow simulation of an expansion tube and thus achieve the final stated objective of the thesis.

The changes to LASTA 2.0 required to simulate the expansion tube are discussed first. Next, in a similar way to Chapter 3, LASTA 2.0 is verified against a viscous, two-dimensional simulation of expansion tube with ideal gas. To verify the thermochemical model, LASTA 2.0 is again paired with NEQAIR 15.2.2 and used to simulate a test case

This chapter contains FROSST simulations performed by Matthew Satchell

from Chapter 5. The results are compared to the experimental radiometer measurements. Finally, a Titan entry test case from the X3 expansion tunnel facility is simulated and the quasi-steady test time analysed.

6.2 Methodology

Changes to the LASTA 2.0 methodology are required to model the low pressure acceleration tube. These include modifications to the domain, the boundary conditions, and the boundary layer model. The changes are presented in this section.

6.2.1 Domain

It is possible, in principle, to model the entire expansion tube in a single LASTA 2.0 domain by changing the fill pressure used to calculate the shock boundary condition after the secondary diaphragm to reflect the lower acceleration tube fill pressure. However, because of the reverse time integration update methodology for the $u + a$ characteristic, waves are able to cross the location of the secondary diaphragm before rupture should have occurred, effectively meaning simultaneous rupture of the primary and secondary diaphragms. To avoid this it is necessary to split the simulation domain in two.

The two-domain approach is shown in Figure 6.1. The first domain encompasses only the shock tube with the purpose of establishing the gas state at the instant of secondary diaphragm rupture. Here, the model is used exactly as has been described so far. The second domain encompasses the acceleration tube but the final time step from the shock tube simulation becomes a new boundary condition at $t = 0$. The final pressure in the second domain is again constrained by an experimental measurement of pressure.

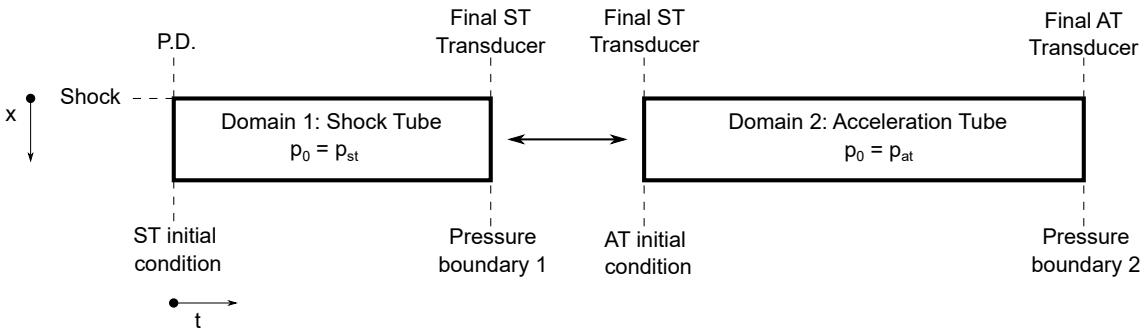

Figure 6.1: Simulation domain for the expanding flow cases

This approach can have some limitations when applied to an experiment. Because the end of the shock tube domain is used as the inlet to the acceleration tube, the approach

essentially assumes that the secondary diaphragm is located at the final pressure transducer in the shock tube. This is of course not correct, however given that no pressure information is typically available at the secondary diaphragm, it is the closest approximation possible. For example in T6, the final shock tube transducer is 0.3 m from the secondary diaphragm and this part of the tube is effectively neglected with this approach.

There is also no explicit modelling of the secondary diaphragm opening or reflected shock formation as the secondary diaphragm is modelled as a Sod diaphragm i.e. it opens instantaneously and is massless. This limitation is deemed to be acceptable for test cases with thin secondary diaphragms (thickness on the order 10 $\mu\mathrm{m}$) as discussed in the previous chapter. Many models for diaphragm rupture have been presented in the literature that could be considered in for implementation in the future, some of which are detailed in Section 2.2.2.

6.2.2 Boundary layer model

Boundary layer development in an expansion tube is a poorly understood phenomenon and no comprehensive analytical model exists in the literature. Consider Figure 6.2, which shows a schematic diagram of boundary layer development in an expansion tube. The boundary layer properties in the accelerator gas may be determined using the Mirels approach (as it behaves essentially as a low pressure shock tube), however the boundary layer development in the expanded test gas is more complex. The increase in density from accelerator to test gas violates the local similarity assumption for the Mirels model. In practice this means that use of the same Mirels model for the accelerator and test gas will greatly over-predict the mass removal from the test gas slug as the boundary layer state is predicted assuming the accelerator gas properties describe the entire flow field. More specifically, there is a large difference between the shape factor β in the accelerator gas and the test gas.

Figure 6.3 shows the large variation in Mirels' model over varying fill pressures. These curves have been generated for a 6 $\mathrm{km\,s^{-1}}$ shock in pure argon with a tube radius of 100 mm. Figure 6.3a shows the maximum slug length for varying fill pressure and Figure 6.3b shows the radial velocity profile versus non-dimensionalised distance behind the shock. In a typical expansion tube test, the fill pressure difference between the shock and acceleration tubes will be between 1 - 2 orders of magnitude[1]. Across this range the radial velocity profiles differ by at least an order of magnitude, meaning that if

[1] In an expansion tube, the shock tube fill pressure is typically on the order of kPa and the acceleration tube on the order < 10 Pa

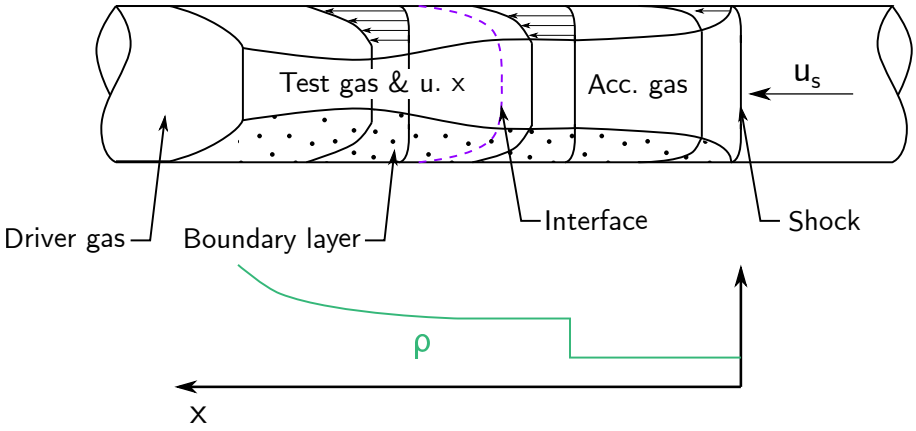

Figure 6.2: Boundary layer development in an expansion tube, adapted from McGilvray (2008)

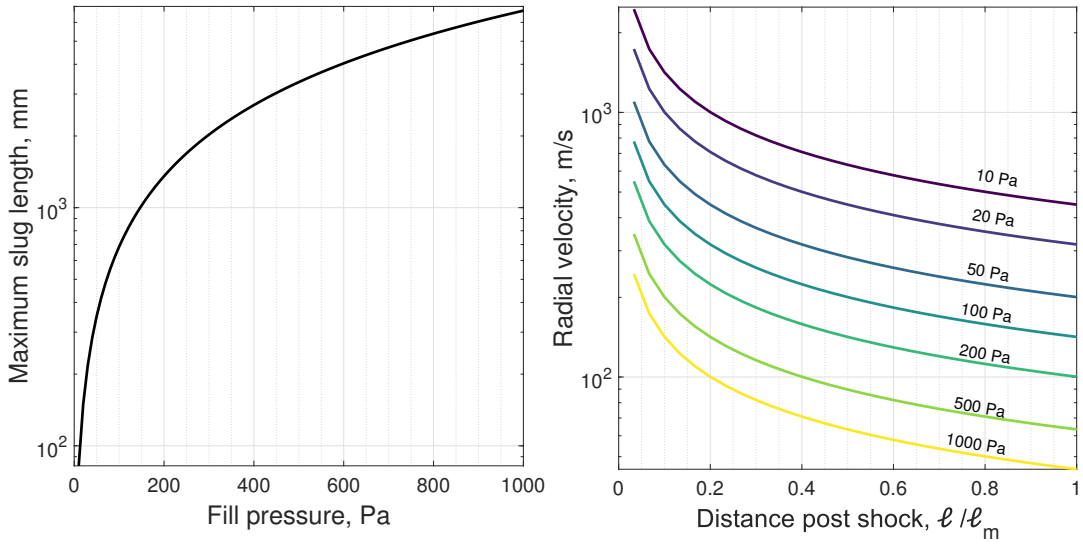

(a) Slug length

(b) Radial velocity profile

Figure 6.3: Mirels effects as a function of fill pressure

the lower acceleration tube radial velocity profile is used in the test gas then there will be significant error.

It is also possible that, as discussed in the previous chapter, the nature of the boundary in the acceleration tube is highly two-dimensional. *Necking* of the test gas may occur causing significant mixing between the accelerator and test gas at the contact surface which is a phenomenon that cannot be fully accounted for with one-dimensional boundary layer assumption.

The approach taken here is to apply separate radial velocity profiles to the test and accelerator gas. A typical Mirels boundary layer profile is applied in LASTA 2.0 until the temperature in the core flow decreases below a set value. Then, the radial velocity profile is decreased exponentially, approaching zero after the contact discontinuity. This

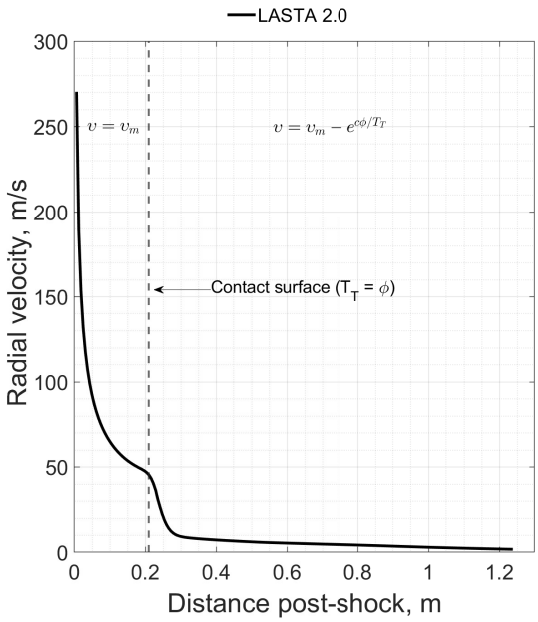

Figure 6.4: Example of the radial velocity profile imposed when modelling an expansion tube

amounts to an assumption of minimal boundary layer effects in the test gas.

In practice, it is necessary to have a continuous, differentiable function that describes the radial velocity profile to obtain a solution via the Newton method. To achieve this, a temperature threshold (ϕ) for the boundary layer model is set with the profile of radial velocity obeying the following when less than the threshold:

$$T_T > \phi : v = v_m \tag{6.1}$$

$$T_T < \phi : v = v_m - e^{\frac{c\phi}{T_T}} \tag{6.2}$$

Where v is the radial velocity, v_m is the radial velocity calculated assuming a Mirels boundary layer profile with properties determined by the accelerator gas, and T_T is the local translational-rotational temperature. The temperature threshold is selected on a test-to-test basis and defines the accelerator / test gas boundary for the purposes of the boundary layer model. An example of the resulting radial velocity profile is shown in Figure 6.4.

6.3 Numerical Verification of the Expansion Tube Model

The LASTA 2.0 expansion tube implementation is compared to a FROSST simulation of an ideal gas to provide confidence in the simulation approach and boundary layer model. The simulation setup is first discussed, followed by a comparison of the results in the acceleration tube.

6.3.1 Simulation Setup

The shock trajectory for the FROSST case analysed here is shown in Figure 6.5. In the FROSST simulation the secondary diaphragm was located 2.83 m from the primary diaphragm and was modelled with a 1 $\mu\mathrm{s}$ holding time. The shock tube contained 1000 Pa of pure argon and the acceleration tube contained 60 Pa of pure argon, both at initial temperatures of 300 K.

The final LASTA 2.0 grid consisted of 300 streamwise points and 50 time points in the shock tube and 300 streamwise points and 347 time points in the acceleration tube. In contrast to previous simulations, the grid was not clustered toward the shock. This was done to improve resolution through the unsteady expansion which was the feature of interest. The final pressure boundary condition in the acceleration tube was located at the point of comparison to FROSST, in this case at 5 m from the primary diaphragm[2]. The workstation was maintained from previous simulations with a solution time of 15 minutes. For the boundary layer model $c = 0.02$ and $\phi = 11000$.

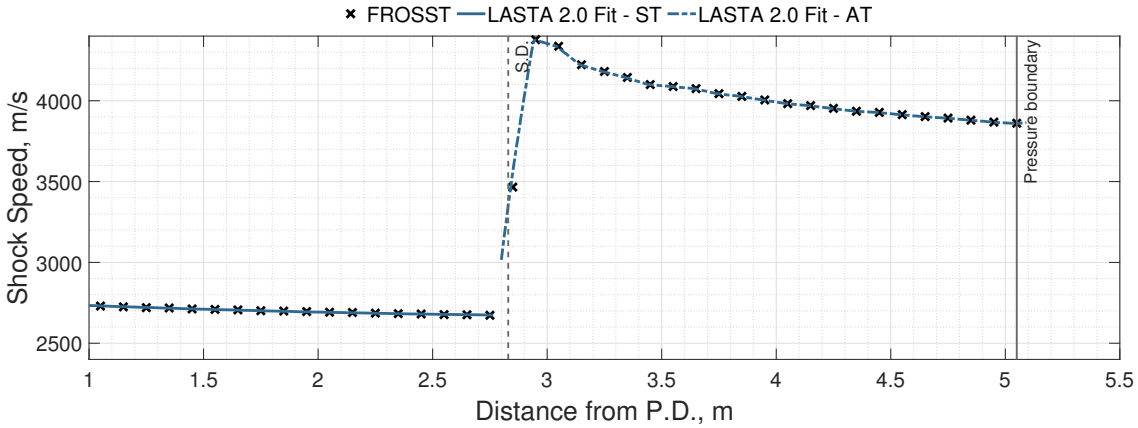

Figure 6.5: Shock speed as a function of distance from the primary diaphragm for the argon verification case

PITOT simulations are included in this section and were run using the *experimental* mode. The final shock speed in the shock tube (2676 $\mathrm{m\,s^{-1}}$) and the shock speed at 5 m

[2]The pressure profile used is shown in Figure 6.6a

from the secondary diaphragm (3850 $\mathrm{m\,s^{-1}}$) were used as inputs. The *flow-behind-shock* configuration option was selected, meaning that the test gas is expanded until the its velocity equals the accelerator gas post-shock velocity or $u_6 = u_7$.

6.3.2 Results

Table 6.1 shows the test time averaged properties for the FROSST, LASTA 2.0, and PITOT 3 simulations. The bounds on the FROSST and LASTA 2.0 results indicate the variation in properties throughout the test time, which is determined to be between 0.34 and 0.7 m. There is generally good agreement between the three methods for all properties, with LASTA 2.0 and FROSST agreeing within 5%. It is interesting that LASTA 2.0 over-predicts the temperature whereas PITOT under-predicts, suggesting under and over expansion of the test gas respectively.

Table 6.1: Average test slug predictions for the argon verification case. The test time was deemed to be between 0.34 and 0.7 m

	FROSST	LASTA 2.0	PITOT 3
ρ, $\mathrm{kg\,m^{-3}}$	$1.91 \pm 0.09 \times 10^{-2}$	$1.91 \pm 0.003 \times 10^{-2}$	1.88×10^{-2}
u, $\mathrm{m\,s^{-1}}$	3540 ± 10	3554 ± 26	3512
p, Pa	12549 ± 432	12549 ± 432	12056
T, K	3232 ± 12.1	3204 ± 37	3085

The spatial results for the simulations at $5\mathrm{m}$ from the primary diaphragm are shown in more detail in Figure 6.6. The distinction between the test gas and accelerator gas is clear in the temperature and density results as a sharp decrease or increase respectively. The unsteady expansion arrives at 0.8 m post-shock, signified by the sharp increase in pressure.

The advantage of LASTA 2.0 is clear here as an unsteady prediction for the test time is made rather than a constant value. This is particularly important even in this simple test case as the properties vary appreciably over the test time, the density varying by nearly 20% for example. There is generally good agreement between FROSST and LASTA 2.0 for all of the properties. Unsurprisingly, the LASTA 2.0 and FROSST pressures are identical as this is used as a boundary condition in the LASTA 2.0 simulation. Predictions for the accelerator gas slug are nearly identical which is expected given that the acceleration tube behaves essentially as a low pressure shock tube.

Figure 6.7 provides a quantitative comparison between the properties predicted by LASTA 2.0 and FROSST. A large difference in the temperature and density profiles at

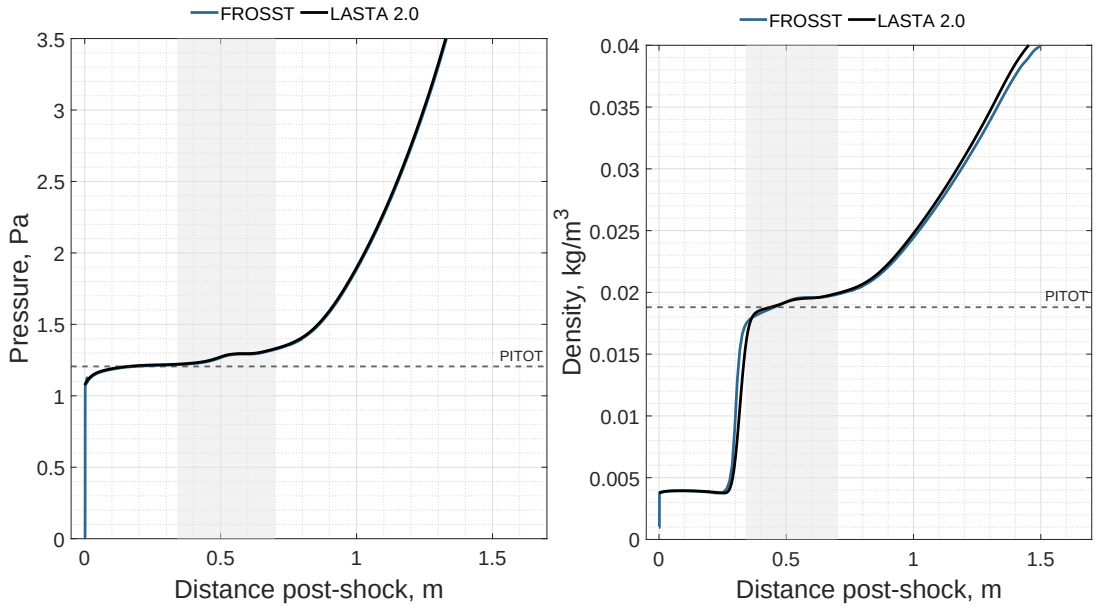

(a) Pressure

(b) Density

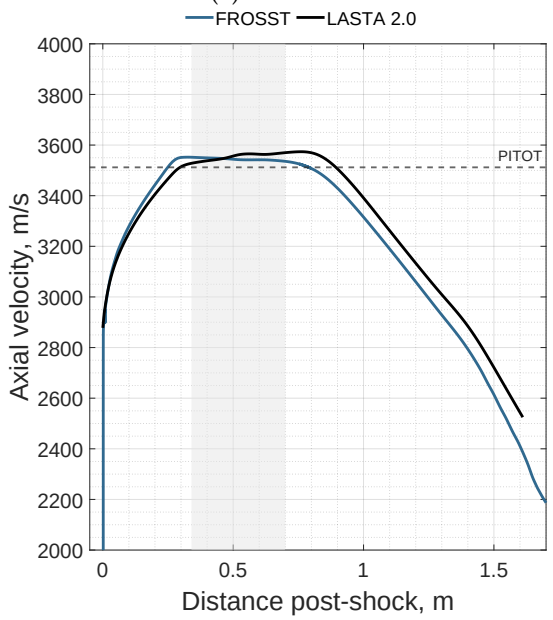

(c) Axial velocity

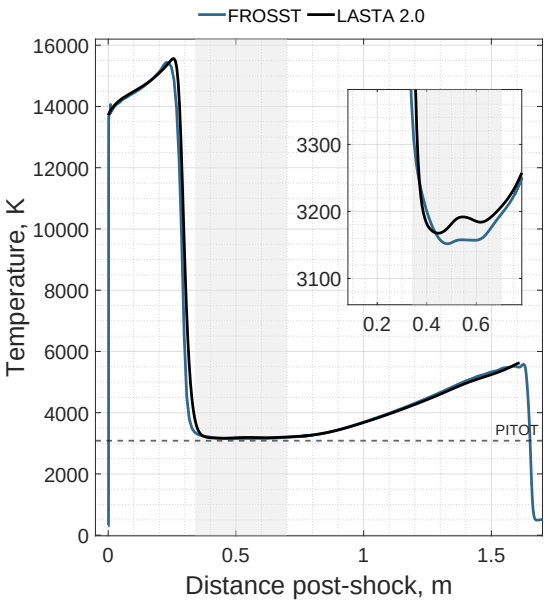

(d) Temperature

Figure 6.6: Properties for the uniform shock tube velocity case at 5 m from the primary diaphragm. The test time is deemed to be between 0.34 and 0.7 m and is shown by the vertical lines

$0.3\ \mathrm{m}$ post-shock occurs because LASTA 2.0 and FROSST predict the test/accelerator gas interface to be in slightly different locations. This was also observed in Chapter 3 and was in that case due to the non-uniform, two-dimensional nature of the contact surface. Given that the secondary shock is decelerating throughout the trajectory, this could also be the case here. However, LASTA 2.0 prediction fall within $\pm 1.4\%$ for all properties during the test time if this slight offset is neglected, showing that the approach taken to modelling the expansion tube with LASTA 2.0 is sound.

Overall, the results in this section demonstrate that it is appropriate to use LASTA 2.0 for expansion tube modelling. Although there is a slight offset between the FROSST and LASTA 2.0 results in the region of expanded test gas, this could be addressed with an improved model of the boundary layer development through the unsteady expansion.

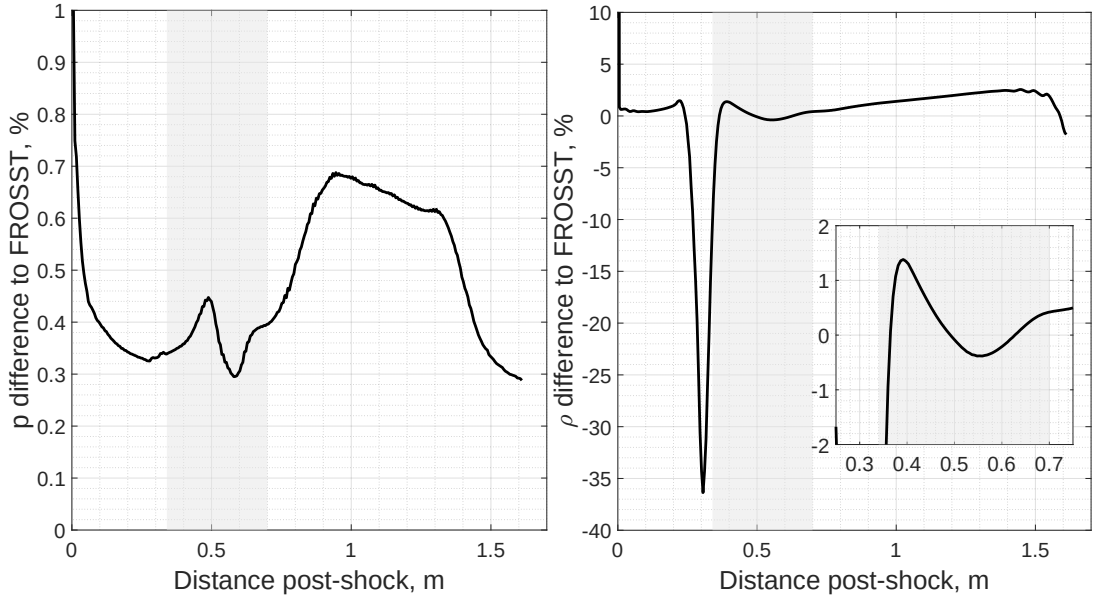

(a) Pressure

(b) Density

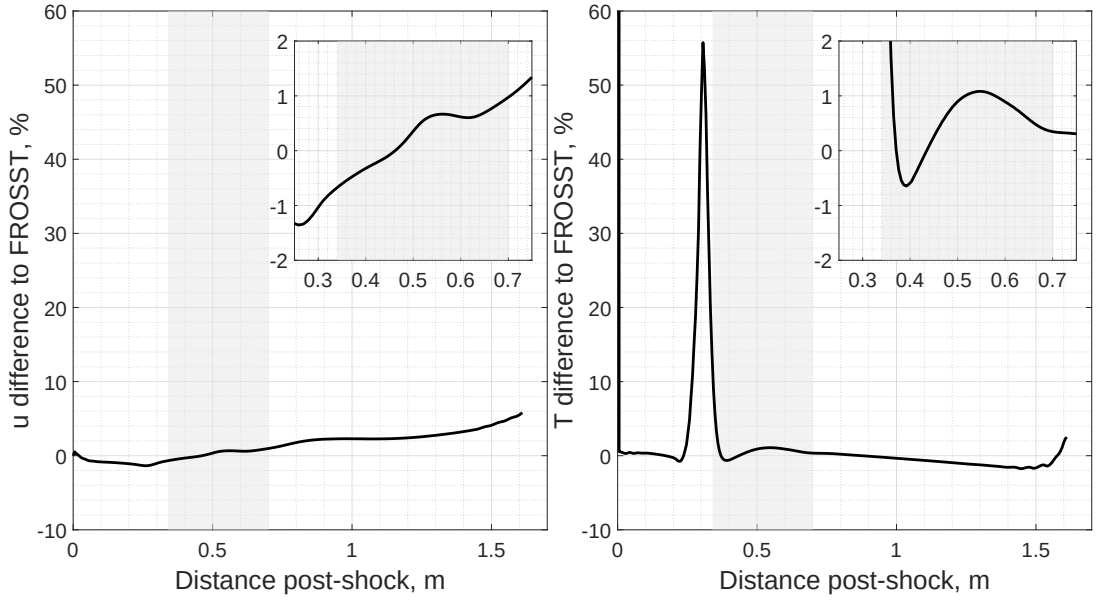

(c) Axial velocity

(d) Temperature

Figure 6.7: Difference in properties predicted by FROSST and LASTA at 5 m from the primary diaphragm. The test time is deemed to be between 0.34 and 0.7 m and is shown by the shaded region

6.4 Application to a Synthetic Air Experiment (Condition C from Chapter 5)

Given the satisfactory predictive power of LASTA 2.0 for the expansion tube established in the previous section, it is now applied to a case with thermochemical effects. In this section LASTA 2.0 is applied to a test case presented in Chapter 5 with the aim of modelling the radiance measured by the radiometer probes. Results from simulation of the shock tube are presented. Then, results from simulation of the acceleration tube are shown, including predictions for radiance at the location of the radiometer probes.

6.4.1 Simulation Setup

Condition C from Chapter 5 is chosen for analysis. This case featured fill pressures of 601 Pa and 10 Pa of synthetic air in the shock and acceleration tubes respectively. The final shock speeds in the shock and acceleration tubes were 7.79 $\mathrm{km\,s^{-1}}$ and 13.31 $\mathrm{km\,s^{-1}}$.

The simulation domain is shown schematically in Figure 6.8. The first simulation beings at the primary diaphragm and ends at shock timing station 4, highlighted in red. Shock timing station 4 was instrumented with a static pressure transducer for all cases presented so this was used as the final boundary condition. The second simulation, using the final state of the previous simulation as the initial condition, begins at the location of the secondary diaphragm and ends at shock timing station 10 (shown in blue) which was again populated with a static pressure transducer and used as a boundary condition. The timing stations highlighted in gold were populated with radiometers as discussed in the previous chapter.

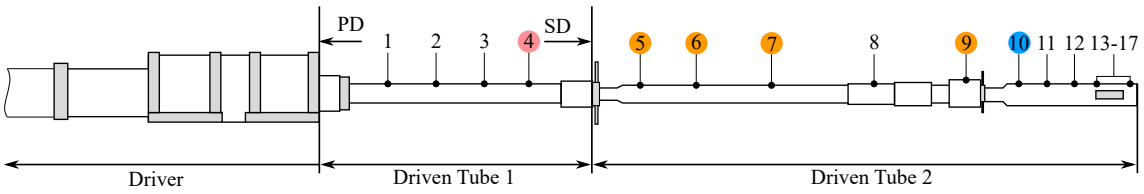

Figure 6.8: Timing stations used in LASTA 2.0 analysis of Condition C

The grid in the shock tube consisted of 200 equispaced streamwise points and 35 time points. The grid in the acceleration tube consisted of 200 equispaced streamwise points and 84 time points. A two-temperature, 11-species air gas model was used with the Park (1993) reaction rates and relaxation constants. The shock boundary in the acceleration tube was set using an equilibrium condition. This was done in an effort to simplify the problem as detailed non-equilibrium modelling of the accelerator gas was not the pur-

pose of the simulation. The region of interest is the expanded test gas behind the accelerator gas which should be modelled correctly provided that the rear of the accelerator gas slug is well approximated. For the synthetic air conditions analysed in Chapter 4 at similar speeds and pressures, equilibrium is reached within 20 mm of the shock, indicating that this is a reasonable assumption for this test case as the accelerator gas slug length is predicted to be 78.5 mm as shown in Table 5.5. Note that the initial condition (final shock tube state) was fully non-equilibrium and thermochemical source terms were included in the acceleration tube simulation. The final pressure boundary conditions used for the shock and acceleration tube simulations are shown in Figures 6.10a and 6.11a respectively. The settings for the boundary layer model were maintained from the previous section i.e. $c = 0.02$ and $\phi = 11000$. NEQAIR settings were maintained from Section 4.3.1.

PITOT simulations in this section were again run using the experimental mode. Here, the final values in both the shock tube and acceleration tube were used, 7.9 $\mathrm{km\,s^{-1}}$ and 13.3 $\mathrm{km\,s^{-1}}$ respectively with the $u_6 = u_7$ and $u_7 = u_{s,2}$ options.

The shock trajectory and fitted curves for condition C are shown in Figure 6.9. The shock trajectory in Driven Tube 1 is mildly accelerating with an increase over the measurement range of approximately 31 %. The trajectory in Driven Tube 2 is relatively flat after 4 m from the primary diaphragm, with variation of approximately ± 8 %.

The shock trajectory fit in the acceleration tube was applied using a high order polynomial, however it is likely not an accurate description of the shock behaviour close to the secondary diaphragm due to the low density of shock timing stations between 3 and 4 m. The secondary shock likely accelerated to approximately 13 $\mathrm{km\,s^{-1}}$ soon after secondary diaphragm rupture [3]. The behaviour of the shock in this region is of particular interest as it governs the rate of the unsteady expansion and in turn the ultimate test slug properties. Unfortunately, without improved shock speed measurements LASTA 2.0 will be limited in its accuracy here.

[3] The experimental shock speed measurement just after the secondary diaphragm is somewhat misleading as it was calculated using one timing station from the shock tube and one from the acceleration tube

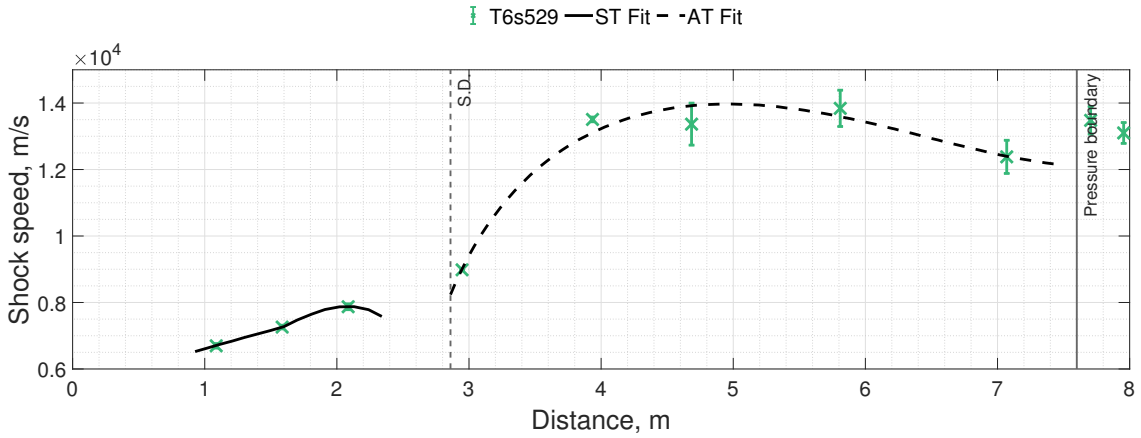

Figure 6.9: Shock trajectory for the synthetic air case, Condition C

6.4.2 Shock Tube Simulation Results

Figure 6.10 shows LASTA 2.0 predictions for the test gas at STS04 or the end of the shock tube. The shaded region indicates perturbations of $\pm$ 100 $\mathrm{m\,s^{-1}}$ to the shock trajectory. The temperature profiles demonstrate that thermal equilibrium is reached essentially immediately in the test slug, with the decreasing profile reflect the accelerating shock trajectory in the shock tube.

The importance of the final slug length should be noted. Since the shock trajectory is only available after 1 m from the diaphragm and end at 2.1 m, the final slug length is sensitive to the choice of initial slug length. The final slug length in the shock tube was found to have a large effect on the ultimate slug length in the acceleration tube for similar reasons to those discussed in Section 5.4.1. Again, this reflects the need for improved measurements of the experimental shock speed.

Using Mirels' theory with constant shock speed equal to the average shock speed in the shock tube, a test slug length at the location of the secondary diaphragm can be predicted, in this case 0.163 m. To produce a test slug of a similar length to that with LASTA 2.0 and the available (truncated) shock trajectory, an initial slug length of 0.1 m was chosen for this simulation in contrast to all previous simulations which have used 0.05 m as the initial value. This is equivalent to an assumption of constant shock speed from the primary diaphragm to the first available shock timing station. The effect of this assumption is most evident in Figure 6.10b, where the species mole fractions are approximately constant after 10 $\mu\mathrm{s}$ due to the constant shock trajectory. Failure to make this change results in an unrealistically short test time in the acceleration tube. Better estimates of test slug length at diaphragm rupture could potentially be obtained with full facility, axisymmetric simulations.

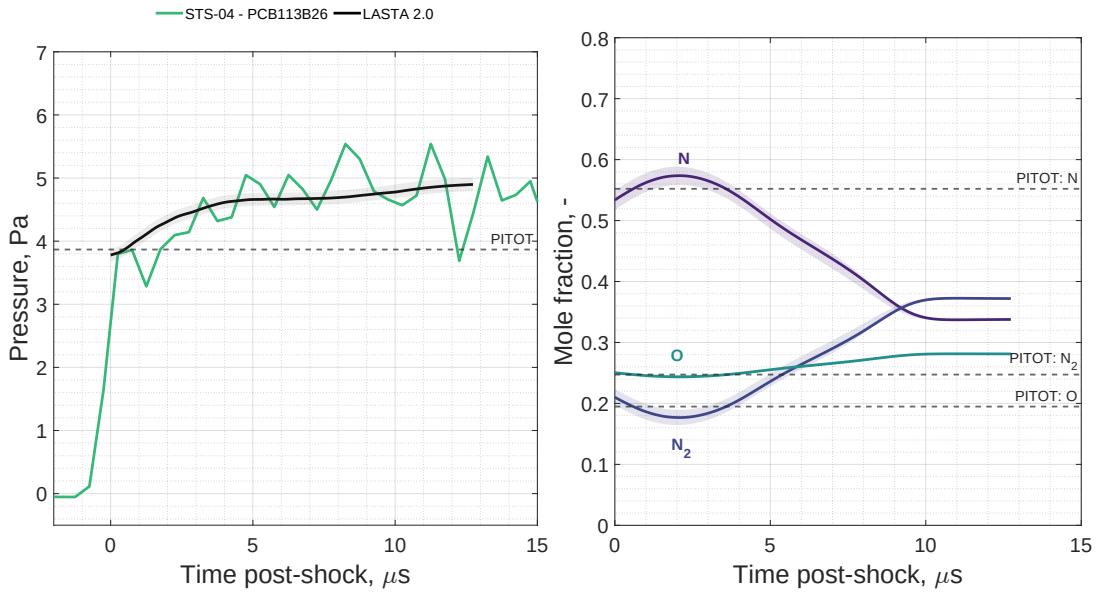

(a) Pressure

(b) Species

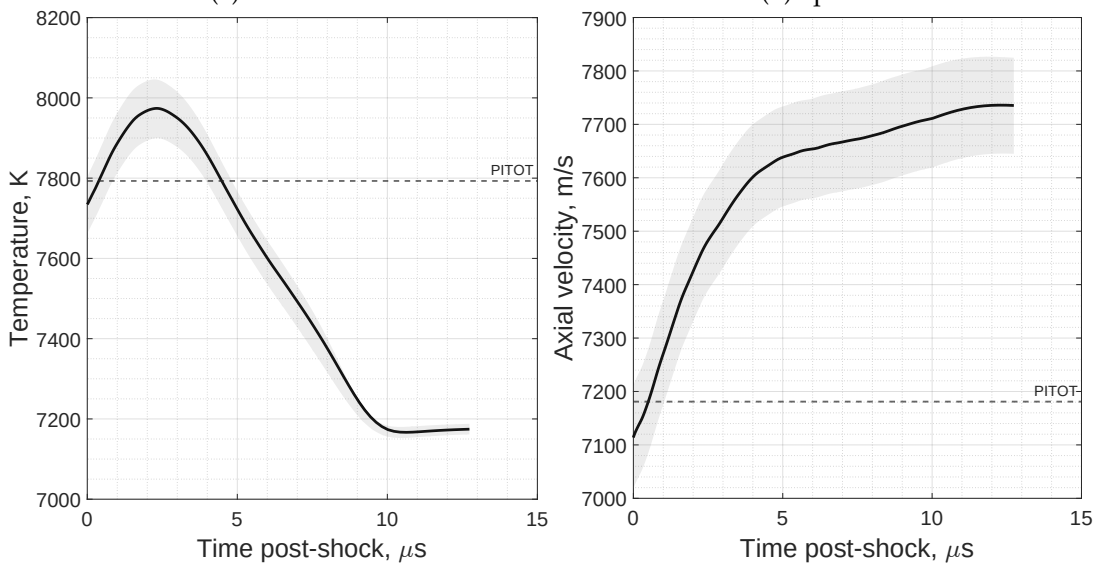

(c) Axial velocity

(d) Temperature

Figure 6.10: Properties at the end of the shock tube for the LASTA 2.0 simulation of Condition C (T6s529). Shaded regions represent perturbations of $\pm$ 100 $\mathrm{m\,s^{-1}}$ to the nominal shock trajectory

6.4.3 Acceleration Tube Simulation Results

The properties of the test gas at the final simulation time (i.e. the location of STS10) are discussed in this section. A detailed comparison between LASTA 2.0 and PITOT at the end of the acceleration tube is shown in Figure 6.11. Generally, LASTA 2.0 predictions are non-uniform, demonstrating that, at least for this case, the test time is *quasi*-steady rather than steady.

Inspection of Figure 6.11d indicates that the accelerator gas slug ends at approximately 10 µs as evidenced by the sharp drop in temperature. Similarly, inspection of Figures 6.11a and 6.11b indicates that the unsteady expansion arrives at approximately 70 µs as it is accompanied by an increase in noise in the experimental pressure measurement and a rapid change in the species mole fractions. The resulting useful test time for this condition is then approximately 60 µs.

A summary of the average properties predicted by LASTA 2.0 for this test time is provided in Table 6.2. PITOT3 predictions are also shown, with both results for both options for test gas expansion.

Table 6.2: Average test slug predictions for T6 Condition C. The test time was deemed to be between 10 and 70 µs

	LASTA 2.0	PITOT3 ($u_7 = u_6$)	PITOT3 ($u_7 = u_{s,2}$)
ρ, $\mathrm{kg\,m^{-3}}$	$6.80 \pm 0.17 \times 10^{-3}$	7.17×10^{-3}	3.55×10^{-3}
u, $\mathrm{m\,s^{-1}}$	13065 ± 1169	12189	13300
p, Pa	18538 ± 4313	18379	8346
T, K	6171 ± 280	6046	5702

There are several qualitative features of interest in Figure 6.11. Firstly, the temperatures predicted by LASTA 2.0 are in equilibrium within the uncertainty predicted by $\pm$ 100 $\mathrm{m\,s^{-1}}$ perturbations to the shock trajectory i.e. no thermochemical freezing occurs. Secondly, LASTA 2.0 predicts more N_2 dissociation than PITOT3. Finally, certain properties vary less than others during the test time, for example the species mole fractions vary by 3.3% on average whereas the axial velocity varies by 8.9 %. Unfortunately, since no direct experimental measurements of any properties other than the static pressure are available, no quantitative statements can be made about merits of LASTA 2.0 v.s. PITOT3[4] based on Figure 6.11. Comparisons to measurements made with the radiometers can provide further insight, this is discussed in the next section.

[4] Aside from the fact that the LASTA 2.0 static pressure matches experiment by design

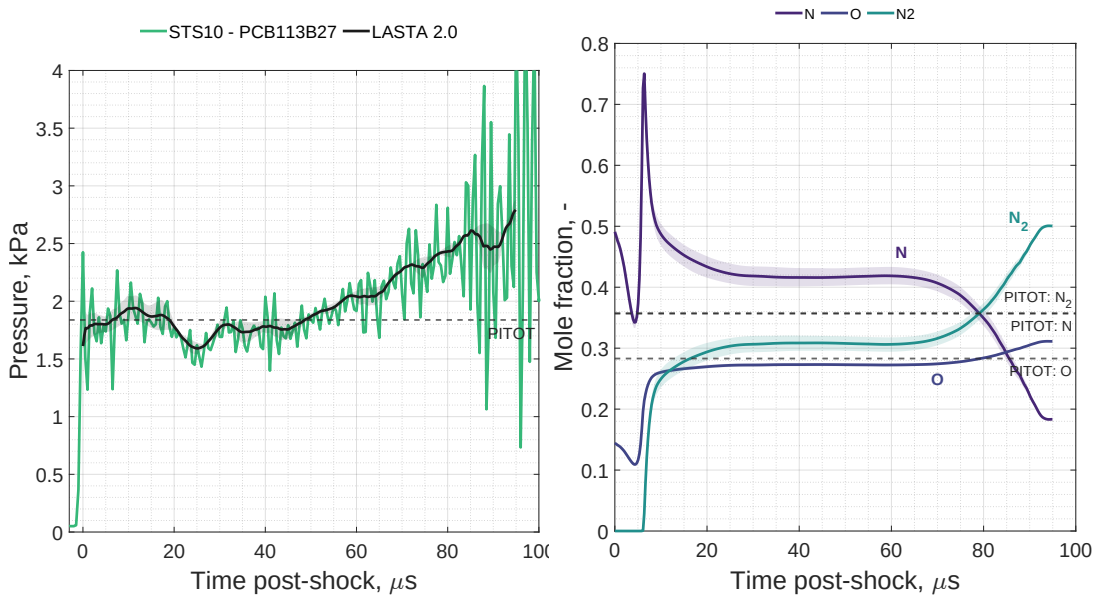

(a) Pressure

(b) Species

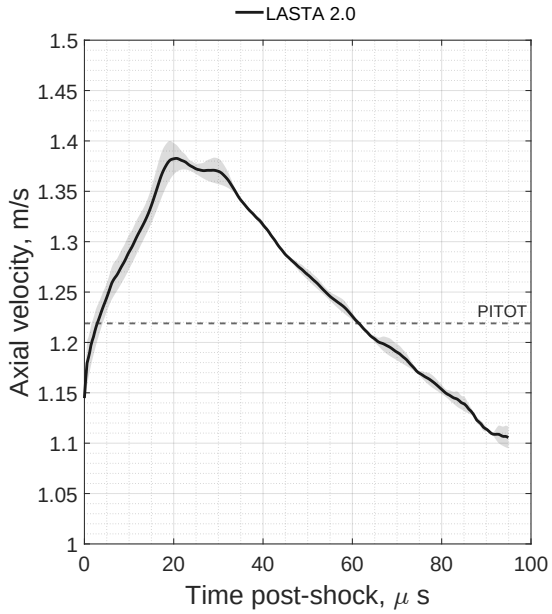

(c) Axial velocity

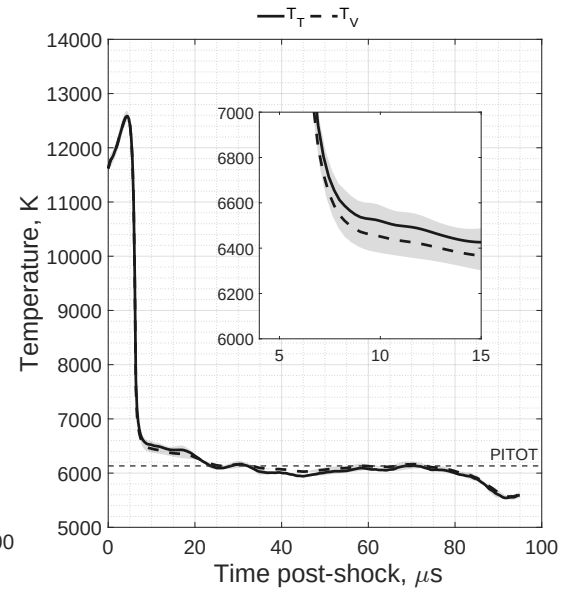

(d) Temperature

Figure 6.11: Properties at the end of the acceleration tube for the LASTA 2.0 simulation of Condition C (T6s529). PITOT results are for the $u_6 = u_7$ case. Shaded regions represent perturbations of $\pm$ 100 $\mathrm{m\,s^{-1}}$ to the nominal shock trajectory

Oxygen 777 nm Radiance Predictions

Coupled LASTA 2.0 / NEQAIR 15.2. radiance predictions are compared to the radiometer measurements in Chapter 5 in this section. The results are shown in Figure 6.12.

Predictions for the radiance in the accelerator gas are consistently higher than in the experiment[5]. This is primarily caused by the choice of an equilibrium boundary condition in the acceleration tube. The secondary shock was likely still coalescing to some extent when it was observed by the radiometers, giving rise to a strongly two-dimensional accelerator gas slug as has been discussed at length previously in this thesis. This means that modelling the thermochemistry as if it had fully proceeded to equilibrium was not correct. However, given that the accelerator gas is not the object of study here, this approximation is deemed acceptable.

The radiance predictions in the unsteady expansion tend to decrease for timing stations further from the secondary diaphragm which agrees with the experimental observations. Radiometers consistently recorded higher radiance in the immediate post-shock region than the LASTA 2.0 prediction. The general under-prediction of radiance by the simulations might be attributed to reflected shock formation at the secondary diaphragm. Linear interpolation of the experimental observations for Mylar diaphragm opening times made by Furukawa et al. (2007) suggest that a 10 µm diaphragm such as the one used here would have an opening time of 12 µs. It would be expected that the gas closest to the secondary diaphragm at the instant of rupture and thus closest to the secondary shock after the expansion is most likely to be affected by such a shock and hence have its temperature raised. Again, this is difficult to determine without additional experimental information.

Radiance predictions for the test gas agree well with the experiment at STS05. The test slug was predicted to end just before 130 µs after secondary diaphragm rupture, however the experimental radiance did not reduce immediately as would be expected if this were the case. Instead, the experimental radiance remained constant for a further 20 µs before reducing. It could be that the LASTA 2.0 slug length prediction was simply incorrect, in which case that would likely be due to assumptions made about the boundary layer model. Alternatively, it could be that some of the test gas was entrained in the boundary layer, forming a complex, two-dimensional contact surface between driver and test gas. This effect was observed in Chapter 3 and had a clear effect on the LASTA 2.0 slug length prediction when compared to FROSST.

[5]The vertical axis in Figure 6.12 has been deliberately truncated to provide an improved view of the object of study, the expanded test gas

A less satisfying agreement between simulation and experiment was seen for STS06 and STS07. The simulations predict negligible radiance at the accelerator/test-gas interface, however this was not observed in the experiment. This could be evidence of reflected shock formation at the secondary diaphragm, as it would be expected that such a flow feature would lead to an elevated temperature, and therefore radiance, at the start of the test slug.

Radiance predictions at STS09 were qualitatively similar to the experiment, but as was seen in Chapter 5 for the equilibrium analysis, were lower than the experimental values. LASTA 2.0 predicted a mean radiance of 0.004 $\mathrm{W\,cm^{-1}\,sr^{-2}}$ compared to the mean experimental value of 0.02 $\mathrm{W\,cm^{-1}\,sr^{-2}}$. This would suggest that at least one of the pressure, temperature, and oxygen number density are under-predicted by LASTA 2.0 (because of the thermochemical model), or that the experimental value is spuriously high, possibly due to measurement of contaminant species radiating in the same region. Diagnosis of the true reason possibly requires additional experimental measurements, ideally using a technique such as TDLAS or similar that does not rely on emission and hence comparisons can be made to LASTA 2.0 without coupling to a radiation model.

The temperature and mole fraction profiles predicted by LASTA 2.0 at the location of each radiometer are shown in Figures 6.13 6.14 respectively. It can be seen that despite the expansion process that has occurred, the test slug was predicted to be in thermal, but not chemical equilibrium for the majority of the test time. Interestingly, some decoupling or freezing of the temperatures was seen closer to the accelerator/test gas which subsides by STS09.

To summarise, the results in this section demonstrated that LASTA 2.0 makes greatly improved predictions about the radiance through the unsteady expansion and by extension, the test slug properties in an expansion tube than the conventional constant shock speed equilibrium method (PITOT).

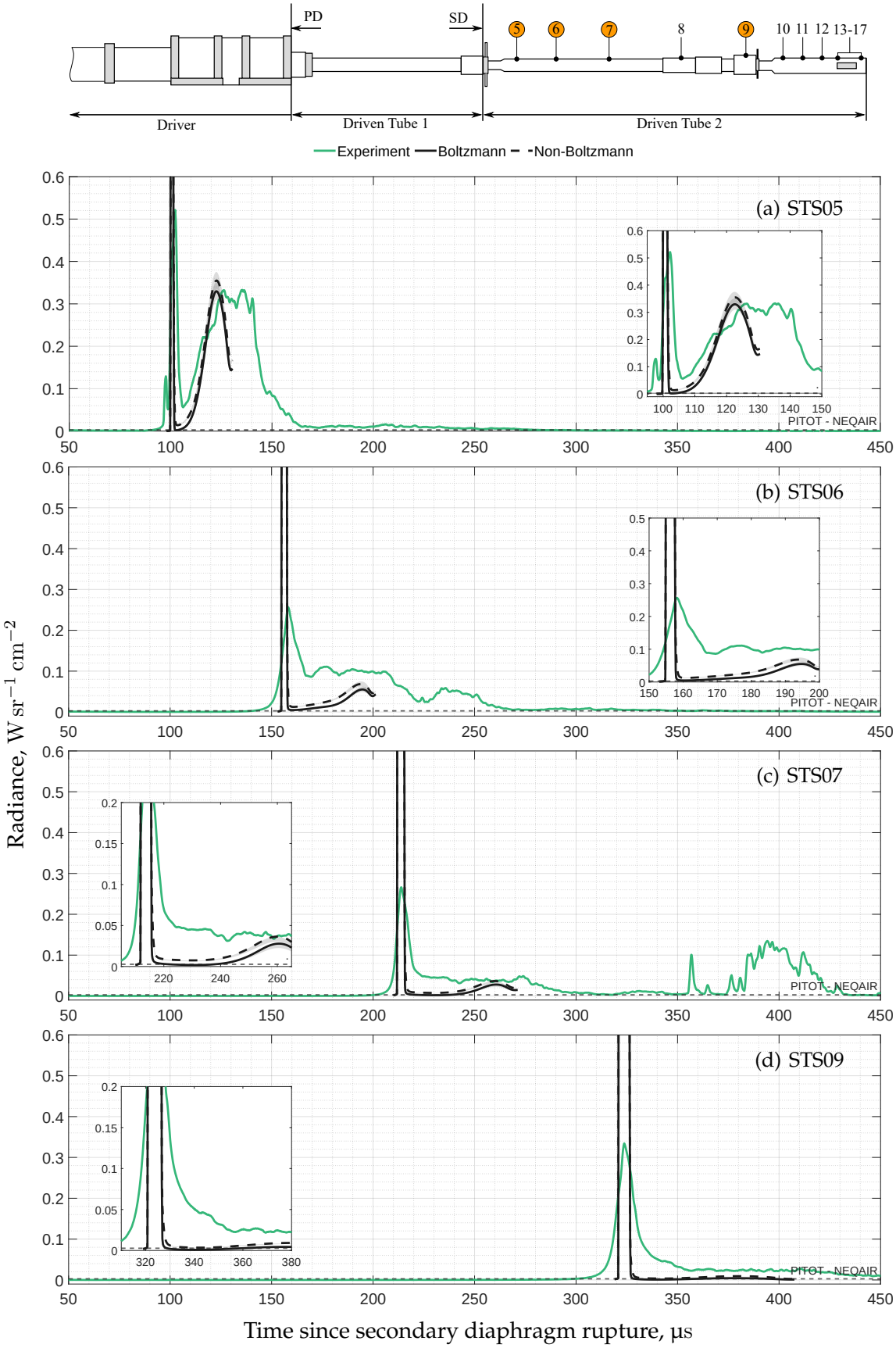

Figure 6.12: Oxygen 777 nm radiance recorded by the radiometer probes for condition C at different distances from the secondary diaphragm compared to LASTA 2.0 / NEQAIR 15.2.2 predictions. Shaded regions represent perturbations of $\pm$ 100 $\mathrm{m\,s^{-1}}$ to the nominal shock trajectory

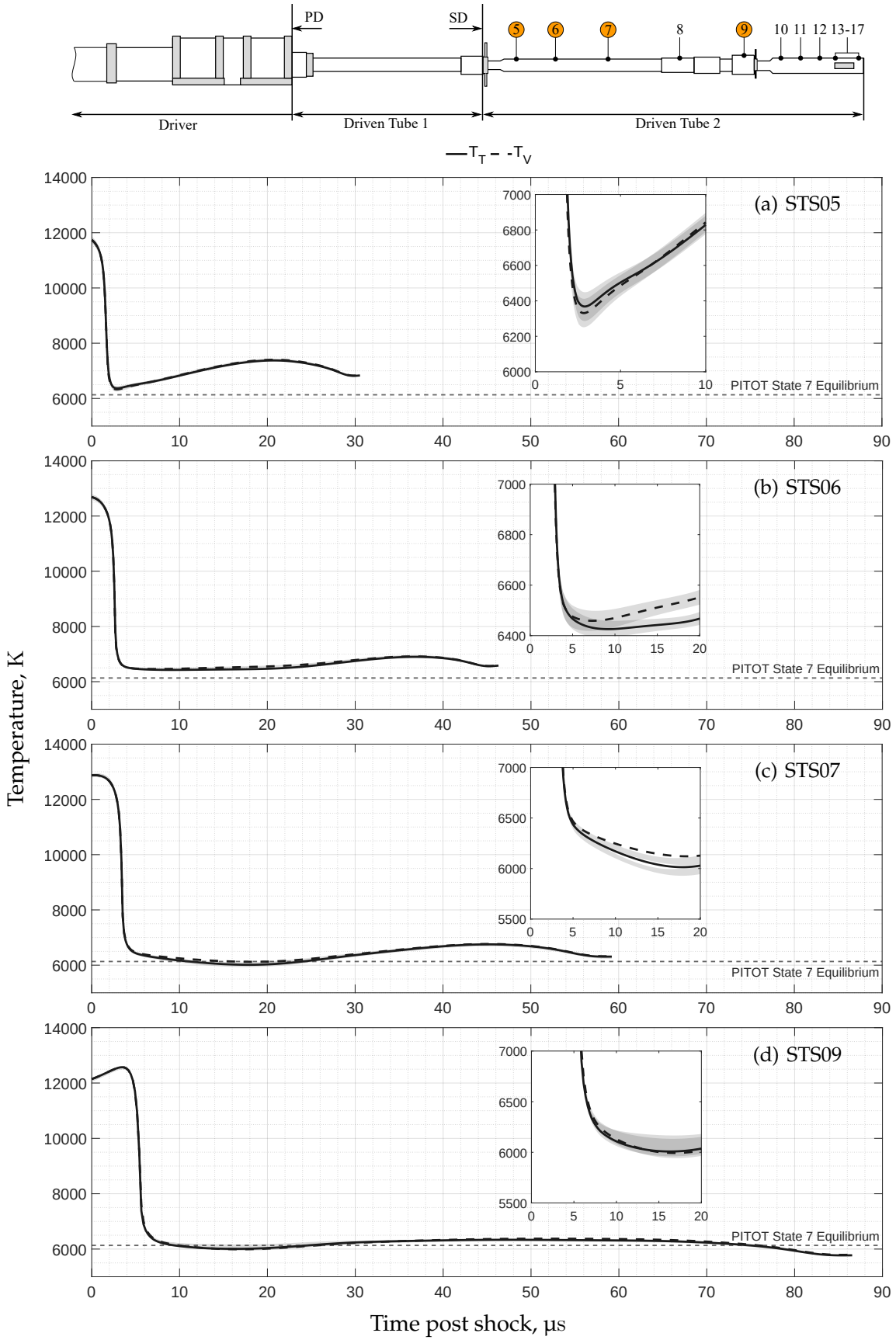

Figure 6.13: Temperature profiles predicted by LASTA 2.0 for condition C. Shaded regions represent perturbations of $\pm$ 100 $\mathrm{m\,s^{-1}}$ to the nominal shock trajectory

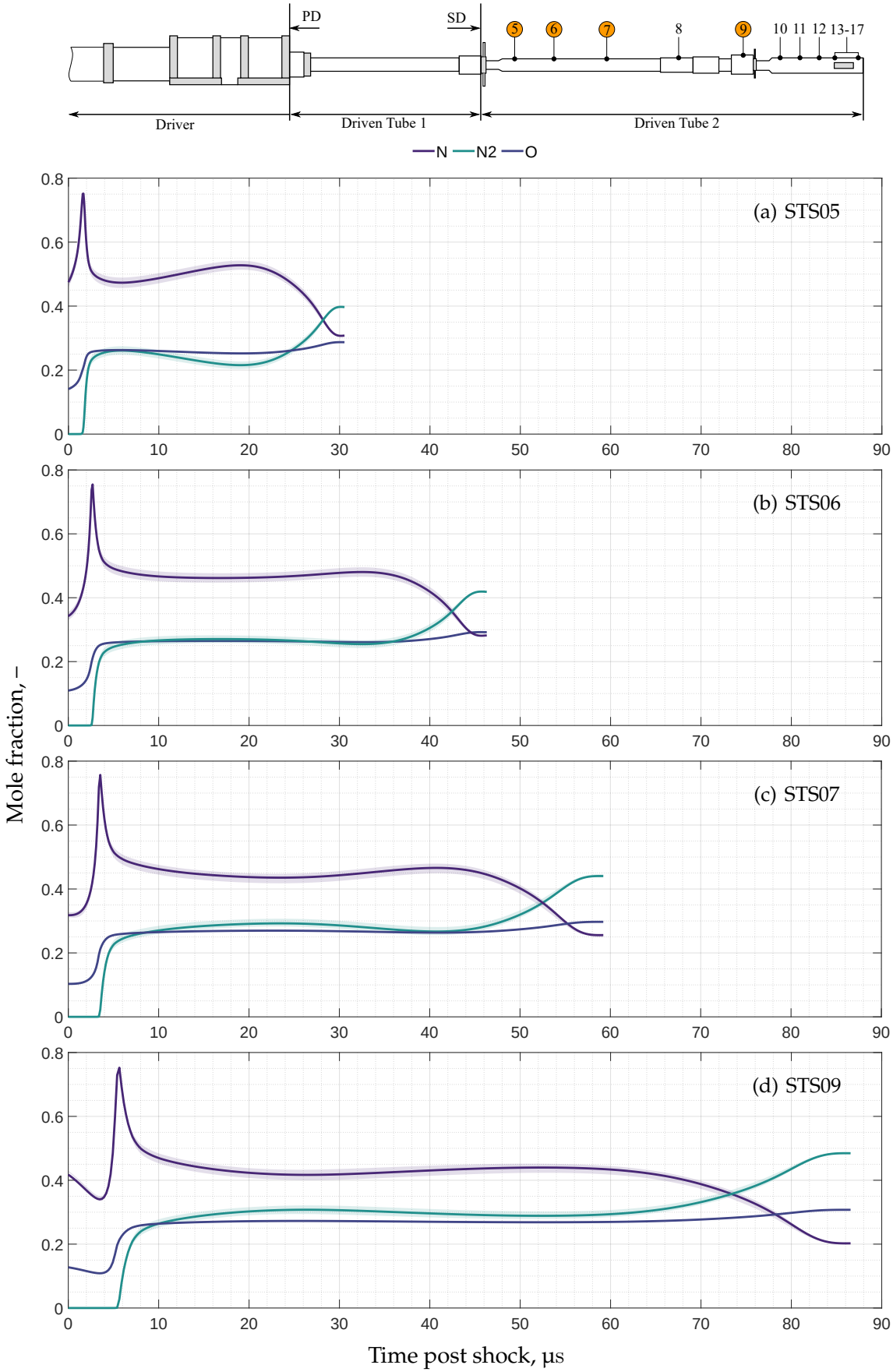

Figure 6.14: Mole fractions predicted by LASTA 2.0 for condition C. Shaded regions represent perturbations of $\pm$ 100 $\mathrm{m\,s^{-1}}$ to the nominal shock trajectory

6.5 Application to a Titan Entry Experiment

A Titan entry expansion tube case is analysed in this section. Titan gas is selected as mixtures containing heavier species typically have longer relaxation time constants and are thus more susceptible to thermochemical freezing. Such cases are ideal for study with LASTA 2.0, as the apparent reaction rates will inherently be effected by the flow process in the facility. LASTA 2.0 can therefore be used as a platform to tune these rates whilst accounting for variations in the experimental conditions.

6.5.1 The X3 Expansion Tunnel

The X3 expansion tunnel is shown schematically in Figure 6.15. X3 was discussed in Chapter 2, so only a few key features are repeated here. The X3 driven tube diameter (at the time of the experiment in question) was 182.6 mm, nearly double the T6 diameter. X3 is also longer than T6, providing an opportunity for the thermochemical relaxation to be studied over a larger length and time scale. At the time of the experiment, no expansion nozzle was installed, meaning that the facility operated as an expansion tube with an outlet at 35 m from the primary diaphragm.

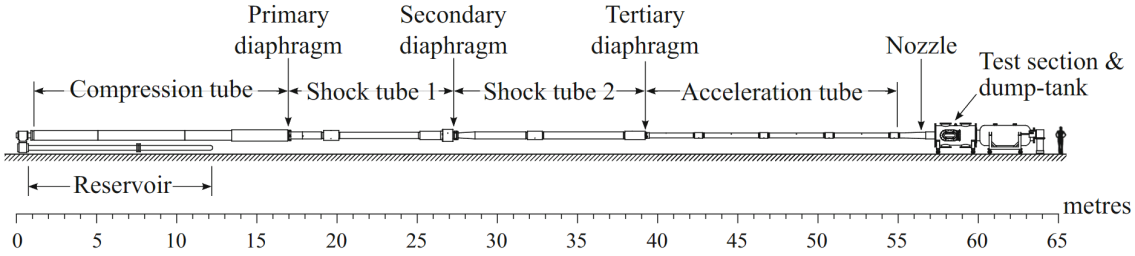

Figure 6.15: Schematic diagram of the X3 expansion tunnel facility, reproduced from Gildfind et al. (2018b)

6.5.2 Simulation Setup

The test case chosen is from the thesis of Capra (2007). The shock tube was filled with 2 kPa of 95% N_2 – 5 % CH_4 and the acceleration tube with 3 Pa of laboratory air[6].

The grid in the shock tube consisted of 300 equispaced streamwise points and 84 time points, as did the grid in the acceleration tube. A two-temperature, 19-species gas model was used with the Gokcen (2007) reaction and relaxation rates. The accelerator gas was

[6]It should be noted that the shot details provided with the X3s273 dataset record that the acceleration tube pressure was 5 Pa. Using this value in combination with the experimental shock speeds would give an equilibrium post-shock pressure of 1600 Pa in the acceleration tube which disagrees with all wall static pressure measurements. Hence, it was deemed likely that the true fill pressure was 3 Pa

modelled as pure nitrogen with the shock boundary set using an equilibrium condition. The shock tube boundary was also set with an equilibrium boundary condition as it was found that the gas in the shock tube reached an equilibrium state within 10 mm of the shock. The boundary layer in the acceleration tube was modelled with $c = 0.02$ and $\phi = 5000$.

The shock trajectory and fitted profiles are shown in Figure 6.16. Unfortunately, only two transducers in the shock tube produced usable time-of-arrival measurements for this test case, resulting in a single shock speed for the shock tube. The shock trajectory in the shock tube was then assumed to be constant as shown which was deemed acceptable given that simulation of this test case was intended to demonstrate the thermochemical freezing effect. No pressure information was available at the end of the shock tube and so the $\frac{\partial w}{\partial t} = 0$ condition was imposed at the final time. Pressure information was available at the end f the acceleration tube however, and this was imposed as a boundary condition for the second simulation.

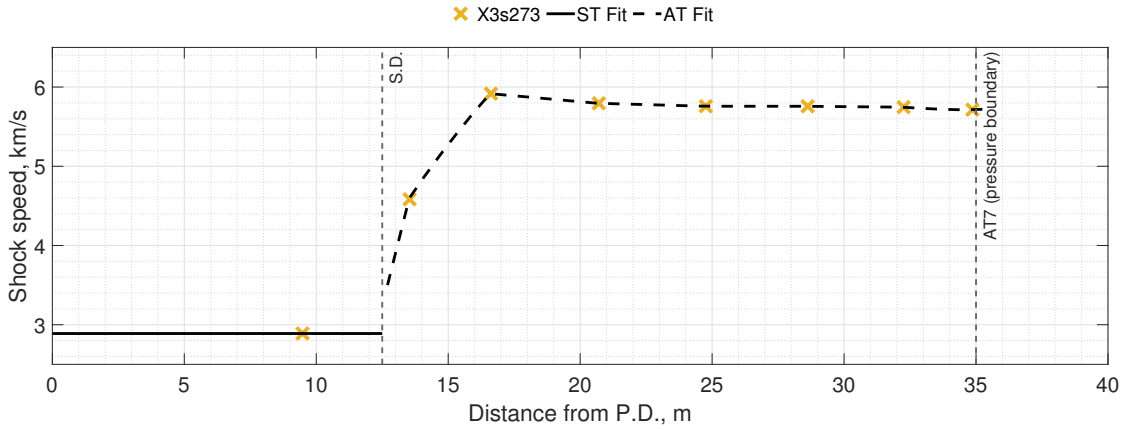

Figure 6.16: Shock trajectory for the X3 Titan case

6.5.3 Shock Tube Simulation Results

The test slug properties at the instant of secondary diaphragm rupture predicted by LASTA 2.0 and PITOT are shown in Figure 6.17. As expected, PITOT and LASTA 2.0 results are similar in this region because of the assumptions made about the shock speed profile i.e. constant. It is interesting to note that the slug length of 600 $\mu\mathrm{s}$ is much greater than in previous cases, reflecting the larger tube diameter. It should also be noted that the N_2 in the shock tube has not dissociated significantly, whereas the CH_4 has almost completely dissociated to form H_2.

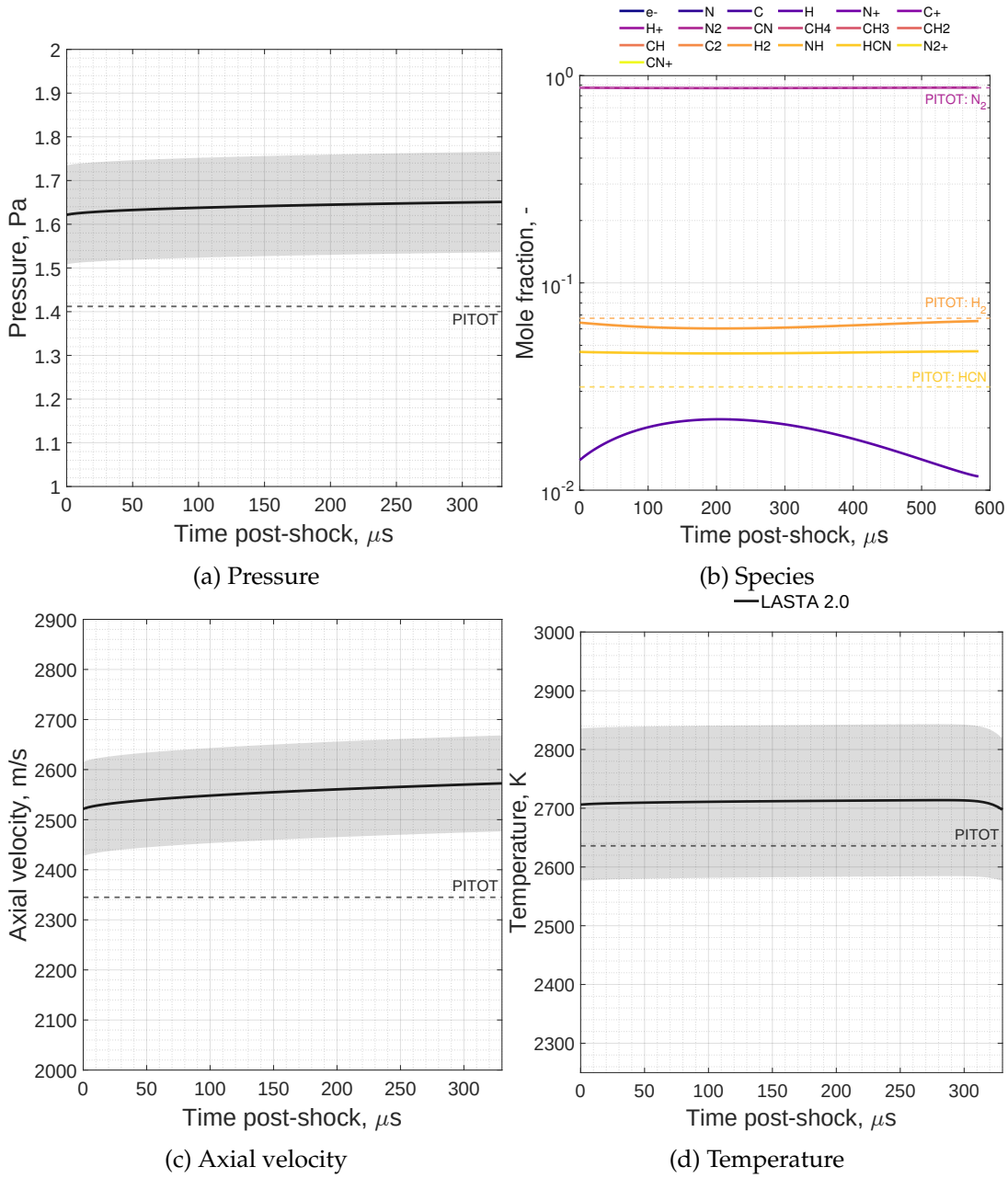

(a) Pressure

(b) Species

(c) Axial velocity

(d) Temperature

Figure 6.17: Test slug properties at the end of the shock tube for the Titan entry test case(X3s273).

6.5.4 Acceleration Tube Simulation Results

The properties of the test gas at the final simulation time (i.e. the location of at7) are discussed in this section. A detailed comparison between LASTA 2.0 and PITOT at the end of the acceleration tube is shown in Figure 6.18.

Inspection of Figure 6.18d suggests that the accelerator gas slug ended at approximately 100 µs post-shock given the sharp decrease in temperature. Similarly, the unsteady expansion likely arrived at approximately 700 µs, given the rapid change in the experimental static pressure. This suggests that the useful test time was approximately 600 µs for this condition.

The average test slug predictions for LASTA 2.0 and PITOT3 based on this test time have been summarised in Table 6.3.

Table 6.3: Average test slug predictions for X3s273

	LASTA 2.0	PITOT3 ($u_7 = u_6$)	PITOT3 ($u_7 = u_{s,2}$)
ρ, $\mathrm{kg\,m^{-3}}$	$2.4 \pm 0.03 \times 10^{-3}$	1.72×10^{-3}	1.71×10^{-3}
u, $\mathrm{m\,s^{-1}}$	6021 ± 854	5760	5720
p, Pa	1006 ± 105	885	881
T_T, K	1511 ± 667	994	993
T_V, K	1683 ± 536	994	993

The reason for the discrepancy is clear in Figure 6.18, which shows the temporally resolved results. LASTA 2.0 predicts strong freezing of the vibrational-electronic mode throughout the entire test time. The difference between the two-temperatures reaches a maximum value before they trend toward equilibrium, behaviour that is consistent with the *breakaway and subsequent rise* described by Holbeche (1964a).

Despite the presence of strong thermal non-equilibrium, the test slug appears to close to a state of chemical equilibrium as shown in Figure 6.18b. The species mole fractions predicted by LASTA 2.0 and PITOT3 are similar which suggests that either relatively few chemical reactions take place through the expansion. Again, it is difficult to say conclusively if LASTA 2.0 are an improvement without direct measurements of the test slug composition, temperatures, etc.

To provide an estimate of how the LASTA 2.0 approach affects properties that can be measured experimentally, the Pitot pressure and stagnation point heat transfer are examined in Figure 6.19. The traces indicated PP3 and PP4 are Pitot probes located at different distances from the centreline, but both in the core flow as described by Capra (2007). It should be noted that the experimental Pitot rake was located in the test section which

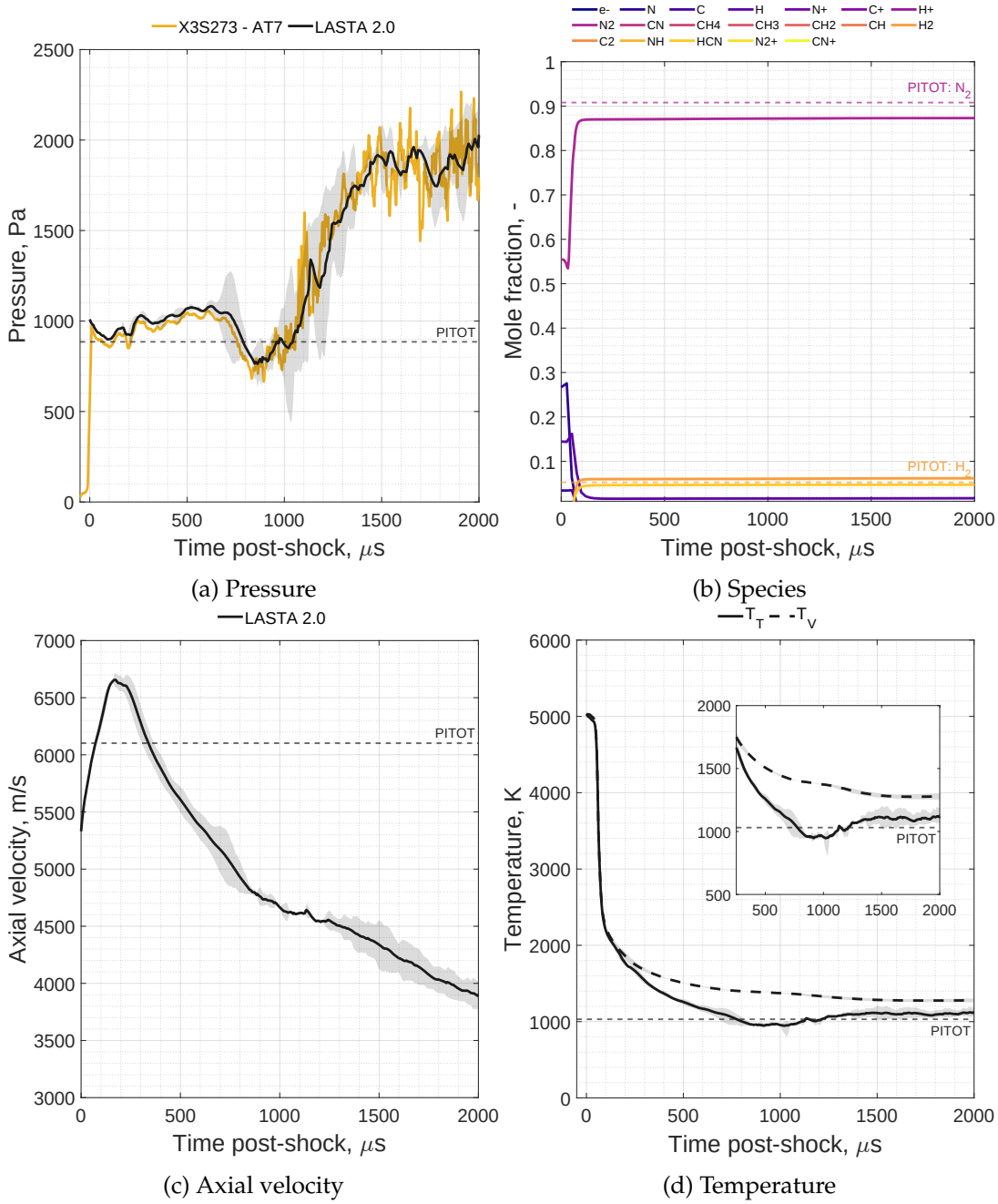

(a) Pressure

(b) Species

(c) Axial velocity

(d) Temperature

Figure 6.18: Test slug properties for the Titan entry case (X3s273). Shaded regions represent perturbations of $\pm$ 100 $\mathrm{m\,s^{-1}}$ to the nominal shock trajectory. The test time was deemed to be between 100 and 700 µs

is further downstream of the end of the LASTA 2.0 simulation. Despite this, LASTA 2.0 compares well with the experiment during the test time.

The stagnation point heat transfer is presented solely with the intention of demonstrating the differences between LASTA 2.0 and PITOT. The heat transfer was calculated using the Sutton and Graves Jr (1971) method assuming a nose radius of 22.6 mm, the same size as the model used by Capra (2007). Clearly, significant differences result between the two methods with LASTA 2.0 peaking 75% above the PITOT value. LASTA 2.0 suggests that the heat transfer during the steady test time is highly non-uniform, again demonstrating the importance of test-to-test modelling of expansion tubes.

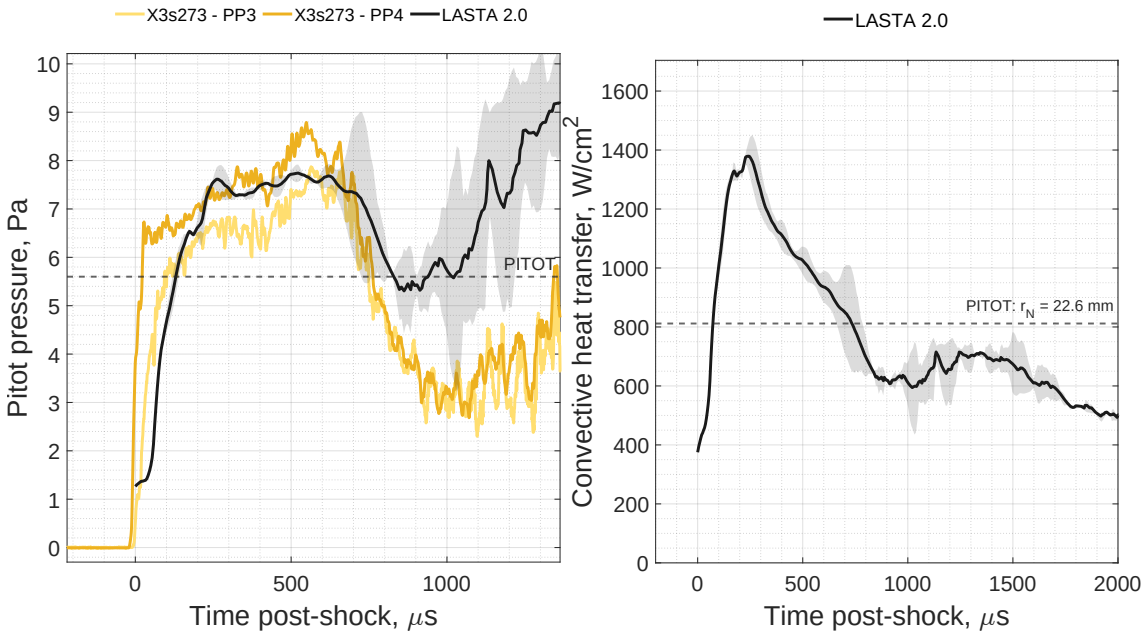

(a) Pitot pressure

(b) Heat transfer

Figure 6.19: Predicted Pitot pressure and stagnation point convective heat transfer at the end of the acceleration tube. Shaded regions represent perturbations of $\pm$ 100 $\mathrm{m\,s^{-1}}$ to the nominal shock trajectory

6.6 Summary

In this chapter, the application of LASTA 2.0 to simulation of the expansion tube has been demonstrated. Comparisons to a two-dimensional, axisymmetric, viscous simulation of an expansion tube using argon as the test and accelerator gas agreed during the test time within 1%, demonstrating the capability of LASTA 2.0 to model fundamental expanding flow processes. The need for an analytical expansion tube boundary layer model was also demonstrated as LASTA 2.0 test time predictions could be improved to closer match FROSST by tuning the boundary layer treatment.

Application of LASTA 2.0 to modelling of a synthetic air test case from Chapter 5 showed good agreement with radiometer measurements of the oxygen 777 nm line, especially when compared to conventional constant shock speed, equilibrium, state-to-state analysis. Predictions of test slug properties for the quasi-steady test time were highly non-uniform, demonstrating the effect of including non-equilibrium thermochemical and non-uniform shock speed effects. Significant thermochemical freezing was also observed in the Titan entry case, demonstrating the need to include non-equilibrium effects when estimating the expansion tube freestream state.

The work in this section shows that LASTA 2.0 can provide meaningful predictions of the test slug properties for an expansion tube even in the presence of strong thermochemical non-equilibrium and establishes LASTA 2.0 as a state-of-the-art tool for modelling of expansion tube flows.

Chapter 7

Conclusion

Contents

The primary aim of this thesis was to develop an improved capability to simulate radiation in expansion and in doing so, provide improved estimates of the freestream properties. In Chapter 1 this aim was subdivided into four objectives: development of a non-equilibrium, Lagrangian shock and expansion tube numerical method, application of the method to historical shock tube experiments, produce a validation radiance dataset for the unsteady expansion, and simulate the dataset using the new method.

This chapter concludes the thesis, provides a summary of the major findings, and compares the outcomes to the originally stated objectives. It is shown that, in general, these objectives were achieved and that this thesis constitutes a significant, original contribution to the wider literature.

7.1 Conclusions and Contributions

The major conclusions of each chapter are summarised in this section as they relate to the original aims of the thesis.

7.1.1 LASTA 2.0: A Novel Shock and Expansion Tube Method

Chapter 2 highlighted the many non-ideal processes that occur in impulse facilities, specifically the shock tube and expansion tube. These result in a non-uniform shock trajectory that strongly affects the test slug properties, an effect that had been accounted for by recent numerical models. These models could not capture thermochemical non-equilibrium effects, strong driver wave processes, or be applied to the expansion tube, leaving a clear gap in the literature.

Chapter 3 detailed the development and validation of a new method for numerical modelling of shock and expansion tubes. The method simultaneously accounts for the effects of shock speed variation, driver wave processes, and thermochemical non-equilibrium. The method was validated against existing tools, FROSST and NESS, to demonstrate the fluid mechanics and thermochemistry modelling respectively. To the author's knowledge, there is no other numerical tool in the literature with an equivalent capability.

7.1.2 Application of the New Method to Shock Tube Cases in the Literature

The new method was applied to historical test cases in the EAST and T6 facilities where shock speed non-uniformity was previously found to be responsible for large changes in post-shock radiance. Inclusion of non-equilibrium thermochemistry was, as expected, shown to improve agreement with the experiment in the non-equilibrium region when compared to previous equilibrium models. Increased agreement with the experiment was also seen in the equilibrium region which is attributed to the new pressure boundary condition.

The inclusion of non-equilibrium thermochemistry allowed application of LASTA 2.0 to new test cases that were previously not accessible. These were cases where the test slug largely does not equilibrate, notably Titan entry relevant gas mixtures. Improved agreement was seen at the rear of the test slug for a mildly decelerating EAST Titan test case when compared with other state of the art non-equilibrium modelling approaches such as DPLR and NESS. This was attributed to reduced CN number density due to

shock deceleration. These results establish the LASTA 2.0 method as a state-of-the-art shock tube modelling tool with a unique capability.

7.1.3 A Novel Unsteady Expansion Radiance Dataset

Relatively few sources are available in the literature for the *unsteady* expansion process and a need for a new dataset was identified. In Chapter 5, a series of spectrally integrated radiometer probes were developed featuring photomultipliers to provide a high signal-to-noise ratio for measurement of the weak radiative emission in the expansion. The radiometers had a spatial resolution of approximately 5 mm and a temporal resolution on the order of nanoseconds. The radiometer measurements were calibrated and validated against optical emission spectroscopy measurements made in a shock tube.

The emission of the oxygen 777 nm and hydrogen 656 nm atomic lines were measured at several locations in the acceleration tube of the T6 expansion tube. The qualitative features were consistent with observations of the wall static pressure, indicating that both the unsteady expansion and quasi-steady test time were captured by the probes. Radiance predictions based on a 0D, equilibrium state-to-state model of the expansion tube were consistently lower than the probe measurements, highlighting the need for an improved expansion tube model.

The data presented in this Chapter 5 demonstrate the feasibility of using wall-mounted, intensified optics to interrogate the unsteady expansion. The measurements constitute one of the only validation datasets in the world for the *unsteady* expansion.

7.1.4 Simulation of Radiation in the Unsteady Expansion

In Chapter 6, two LASTA 2.0 domains were coupled to simulate the shock and acceleration tubes in an expansion tube. The boundary conditions in the acceleration tube simulation were modified such that the final state of the shock tube simulation could be used as a fixed initial boundary condition in the acceleration tube, thereby modelling the secondary diaphragm as massless with instantaneous opening.

Simulation of three non-reacting, FROSST argon test cases revealed the importance of capturing the reflected shock as LASTA 2.0 predictions deviated from FROSST results when this wave arrived. Application of a coupled LASTA2.0–NEQAIR approach to modelling radiometer data from Chapter 5 showed greatly improved agreement when compared to a state-to-state equilibrium, constant shock speed approach. Modelling of a Titan entry condition in the X3 facility demonstrated the importance of including non-

equilibrium effects when modelling the freestream of an expansion tube. These results establish LASTA 2.0 as a state-of-the-art expansion tube solver.

7.2 Recommendations for Future Work

7.2.1 Further Research

Application of LASTA 2.0 to More Test Cases

The primary purpose of LASTA 2.0 is to, as much as possible, decouple the fluid mechanics of shock tubes from the underlying thermochemical processes to be studied. Use of LASTA 2.0 to simulate a wide range of historical shock tube cases where non-equilibrium effects have been dominant is now possible. Examples of such cases include Titan entry studies (Tibère-Inglesse et al., 2023b), Giant planet entry studies (Cruden and Bogdanoff, 2017), Mars entry studies (Cruden et al., 2012), and low pressure shock tube experiments in general. It is recommended that these cases are revisited and LASTA 2.0 is used as a tool to tune thermochemical rates, thus removing the need for assumptions about the particle time of flight that were previously required.

This thesis has included the application of the LASTA 2.0 tool to a single expansion tube test case, however there is significant scope to revisit past test cases where uncertainty in the freestream conditions has been highlighted as an issue. Cases of particular interest are those that are *slow-reacting* such as Titan or Mars atmospheres (Gu, 2018). Here, the influence of thermochemical freezing may be expected to have a larger effect on the test flow.

Expand the Capabilities of LASTA 2.0

The version of LASTA 2.0 developed as part of this thesis is an improvement over the previous iteration. In this spirit, there are many more avenues for development in the code that should be considered in the future. Firstly, the inclusion of diffusion terms to capture the shock structure should be considered. The code is presently initialised with Rankine-Hugoniot post-shock conditions which is a simplified assumption as shown by Clarke et al. (2023a). Secondly, the treatment of the secondary diaphragm should be improved when modelling an expansion tube. The secondary diaphragm opening has been shown to create a strong reflected shock that can change the test slug properties and modelling this explicitly is an important aspect of of accurate expansion tube modelling. Thirdly, a capability to model an expansion nozzle at the end of the domain would allow the full expansion tunnel to be modelled and significantly increase the applicability of the code. This implementation would likely be similar to the Mirels boundary layer model as it is simply an area change. Finally, improved boundary layer modelling for expansion

tube cases is required. The applicability of Mirels' theory in an expansion tube is unclear and direct measurements of the boundary layer growth are desirable.

Interrogate the Unsteady Expansion with Other Experimental Techniques

Measurements of the radiance emanating from flow undergoing an unsteady expansion flow process were made successfully in Chapter 5 using a radiometer probe. Whilst these measurements were useful for the test conditions chosen, they may not be informative for a broader range of test conditions as the freestream flow must radiate strongly to produce a measurements with acceptable signal to noise ratio. They are also limited in the information they provide as a they are not spectrally resolved. Other experimental methods of interrogating the unsteady expansion should be explored such as:

1. Streak photography
2. Laser absorption spectroscopy (TDLAS and CARS)
3. Intensified high speed spectroscopy

Absorption measurements are particularly desirable because they do not rely on radiation from the test flow and thus can be used at lower temperatures that are typical of expansion tubes. Absorption measurements also have the advantage allowing direct measurement of the population of a particular species or excited state which removes the need for an interstitial radiation model (such as NEQAIR) to link simulations to experiment.

7.2.2 Facility Improvements

Improve Quality of Shock / Expansion Tube Experiments

Experiments in impulse facilities are conducted for many reasons. As the fidelity of numerical models increases, the determination of reaction rate coefficients is increasingly becoming the primary objective. It is the author's belief that uncertainty in experimental measurements made in impulse facilities now limits progress toward an improved understanding of high temperature gas dynamics for hypersonic applications. General improvements in the standard and measurement quality of impulse facilities are greatly desirable. Specifically:

1. Shock speed measurement: The speed of the shock is not measured with sufficient resolution and is usually measured with only one technique (i.e. finite difference

based on time of arrival). LASTA 2.0 relies on curves fits of shock speeds from pressure transducer time of arrival measurements to determine the post-shock properties. Whilst this approach is workable, LASTA 2.0 can only be as good as the experimental measurements and therefore if there is uncertainty in the experimental shock speed measurement, there must also be uncertainty in the LASTA 2.0 results. Recently, several authors have built upon the initial work of Dufrene et al. (2015) to produce cheap and reliable microwave reflectometers for high resolution measurement of shock speed in shock tubes and expansion tubes (Straede et al., 2024; Kurosaka and Shimamura, 2024). These designs now have the advantage of operating *off-centreline* so that they are not exposed to the test flow and do not impede other experiments that may be taking place in the test section. It is strongly recommended that such a system be implemented in all impulse facilities as soon as possible.

2. Test gas composition: The composition of the test gas is not known with sufficient accuracy - samples of the test gas are not taken and analysed on a test by test basis and trace contaminants can be neglected

3. Condition design: Efforts to designed test conditions with relatively uniform shock trajectories and thus minimum interference from non-ideal wave patterns are not undertaken

4. Complexity: Experiments often target highly complex gas mixtures at velocities where many physical phenomena take place simultaneously (i.e. dissociation, ionization, vibrational excitation and relxation, radiation). The focus should shift as much as possible toward isolation of single chemical reactions or processes, for example fundamental study of H_2 or N_2 dissociation at low velocity, so that reaction rates can be determined with the lowest possible uncertainty

5. Reliance on radiation modelling: The majority of experimental data for study of shock layer radiation is, understandably, emission spectroscopy data. Unfortunately, this means that direct comparison to numerical models is not possible and an interstitial radiation model, such as NEQAIR, is required. Such a radiation model will inevitably have its own sources of uncertainty and thus it cannot be said with certainty that improvements made in the fluid model are actually improvements if errors are present in the radiation model. Direct measurements of species number density and temperature made via other techniques should be incorporated as a

standard part of impulse facility testing

T6 Driver Upgrades

Despite the commissioning of major upgrades to the facility, T6 is not able to reproduce the full range of test conditions that are relevant for Ice Giant aerocapture and Saturn entry missions. T6 currently operates at a fraction of its rated maximum driver pressure and thus there is significant scope to further improve the facilities performance envelope to potentially include these missions. The design of a lightweight piston, as done by Gildfind et al. (2011) for the X3 facility, could allow these conditions to be achieve whilst maintaining the piston *soft-landing* and this is recommended. The addition of a dedicated secondary driver barrel for the expansion tube mode is also recommended. Initial testing with a secondary driver in expansion tube mode showed a modest improvement in shock speed for a given test condition, however the relatively short length of the current first T6 driven tube appears to set a limit on the maximum achievable shock speed as highlighted by Collen (2021). An additional driven tube could alleviate this constraint whilst also improving the achievable test time.

References

Allison, G. (2023). Britain in £1bn push for hypersonic missile strike capability.

Anderson Jr., J. D. (2006). *Hypersonic and High-Temperature Gas Dynamics, Second Edition*. American Institute of Aeronautics and Astronautics, Reston ,VA.

Andrianatos, A., Gildfind, D., and Morgan, R. (2015). *A Study of Radiation Scaling of High Enthalpy Flows in Expansion Tubes*. PhD thesis, University of Queensland.

Appleton, P. (1966). Calculations of the Structure of Unsteady Rarefaction Waves in Oxygen/Argon Mixtures, Allowing for Vibrational Relaxation. Technical C.P. No. 720, Ministry of Aviation.

Bakos, R. J. and Morgan, R. G. (1994). Chemical recombination in an expansion tube. *AIAA Journal*, 32(6):1316–1319.

Bayon, S. (2019). CDF Study Report - Ice Giants. Technical CDF-187(C), European Space Agency.

Beck, W. H. and Mackie, J. C. (1978). Application of the shock tube unsteady expansion wave technique to the study of chemical reactions. *Journal of Physics D: Applied Physics*, 11(9):1249–1262.

Bensassi, K. and Brandis, A. M. (2019). Time Accurate Simulation of Nonequilibrium Flow inside the NASA Ames Electric Arc Shock Tube. In *AIAA Scitech 2019 Forum*, San Diego, California. American Institute of Aeronautics and Astronautics.

Birch, B., Zander, F., Buttsworth, D., Noller, L., and Payne, A. (2022). Hayabusa2 Capsule Reentry: Visible and Near-IR Emission Spectroscopy from the Australian Airborne Observation. In *AIAA AVIATION 2022 Forum*, Chicago, IL & Virtual. American Institute of Aeronautics and Astronautics.

Bolles, D. (2024a). Dragonfly - NASA Science.

Bolles, D. (2024b). OSIRIS-REx - NASA Science.

Bose, D., Wright, M. J., Bogdanoff, D. W., Raiche, G. A., and Allen, G. A. (2006). Modeling and Experimental Assessment of CN Radiation Behind a Strong Shock Wave. *Journal of Thermophysics and Heat Transfer*, 20(2):220–230.

Bostrom, N. (2019). The Vulnerable World Hypothesis. *Global Policy*, 10(4):455–476.

Bowman, A. (2023). Humans to Mars - NASA.

Bowman, A. (2024). Artemis - NASA. Section: Artemis.

Bowman, R. M. (1966). *Investigation of Shock Front Topography in Shock Tubes*. PhD thesis, California Institute of Technology.

Brandis, A. (2009a). *Experimental Study and Modelling of Non-equilibrium Radiation During Titan and Martian Entry*. PhD thesis, University of Queensland.

Brandis, A., Cruden, B., Prabhu, D., Bose, D., McGilvray, M., Morgan, R., and Morgan, R. (2010). Analysis of Air Radiation Measurements Obtained in the EAST and X2 Shock-tube Facilities. In *10th AIAA/ASME Joint Thermophysics and Heat Transfer Conference*, Chicago, Illinois. American Institute of Aeronautics and Astronautics.

Brandis, A., Johnston, C., Cruden, B., and Prabhu, D. (2017). Equilibrium radiative heating from 9.5 to 15.5 km/s for earth atmospheric entry. *Journal of Thermophysics and Heat Transfer*, 31(1):178–192. Publisher: American Institute of Aeronautics and Astronautics.

Brandis, A., Johnston, C., Panesi, M., Cruden, B., Prabhu, D., and Bose, D. (2013). Investigation of Nonequilibrium Radiation for Mars Entry. In *51st AIAA Aerospace Sciences Meeting including the New Horizons Forum and Aerospace Exposition*, Grapevine (Dallas/Ft. Worth Region), Texas. American Institute of Aeronautics and Astronautics.

Brandis, A. M. (2009b). Analysis of shock tube equilibrium radiation for Earth re-entry applications. In *Annual Research Briefs 2009*, page 83.

Brandis, A. M. and Cruden, B. A. (2017a). Benchmark Shock Tube Experiments of Radiative Heating Relevant to Earth Re-entry. In *55th AIAA Aerospace Sciences Meeting*, Grapevine, Texas. American Institute of Aeronautics and Astronautics.

Brandis, A. M. and Cruden, B. A. (2017b). Benchmark Shock Tube Experiments of Radiative Heating Relevant to Earth Re-entry. In *55th AIAA Aerospace Sciences Meeting*, Grapevine, Texas. American Institute of Aeronautics and Astronautics.

Brandis, A. M. and Cruden, B. A. (2017c). Titan Atmospheric Entry Radiative Heating. In *47th AIAA Thermophysics Conference*, Denver, Colorado. American Institute of Aeronautics and Astronautics.

Brandis, A. M. and Cruden, B. A. (2018). Shock Tube Radiation Measurements in Nitrogen. In *2018 Joint Thermophysics and Heat Transfer Conference*, Atlanta, Georgia. American Institute of Aeronautics and Astronautics.

Brandis, A. M., Saunders, D. A., Johnston, C. O., Cruden, B. A., and White, T. R. (2020). Radiative Heating on the After-Body of Martian Entry Vehicles. *Journal of Thermophysics and Heat Transfer*, 34(1):66–77.

Bray, K. N. C. (1968). Vibrational relaxation of anharmonic oscillator molecules: Relaxation under isothermal conditions. *Journal of Physics B: Atomic and Molecular Physics*, 1(4):705–717.

Candler, G. V., Johnson, H. B., Nompelis, I., Gidzak, V. M., Subbareddy, P. K., and Barnhardt, M. (2015). Development of the US3D Code for Advanced Compressible and Reacting Flow Simulations. In *53rd AIAA Aerospace Sciences Meeting*, Kissimmee, Florida. American Institute of Aeronautics and Astronautics.

Capra, B. R. (2007). *Aerothermodynamic simulation of subscale models of the FIRE II and Titan Explorer vehicles in expansion tubes*. PhD thesis, University of Queensland.

Capra, B. R. and Morgan, R. G. (2012). Radiative and Total Heat Transfer Measurements to a Titan Explorer Model. *Journal of Spacecraft and Rockets*, 49(1):12–23.

Capra, B. R. and Morgan, R. G. (2013). Total Heat Transfer Measurements on a Flight Investigation of Reentry Environment Model. *Journal of Spacecraft and Rockets*, 50(3):494–503.

Carroll, A. T., Blanquart, G., Brandis, A. M., and Cruden, B. A. (2024). State-Specific Kinetic Modeling for Predictions of Radiative Heating in H2/He Entry Flows. In *AIAA SciTech Forum*.

Chandel, D., Brandis, A., and Candler, G. V. (2019). Full facility shock frame simulations of the electric arc shock tube. In *AIAA SciTech forum & exposition (SciTech 2019)*. Number: ARC-E-DAA-TN57169.

Chandel, D., Nompelis, I., and Candler, G. V. (2018). Computations of High Enthalpy Shock-waves in Electric Arc Shock-Tube (EAST) at NASA Ames. In *2018 AIAA Aerospace Sciences Meeting*, Kissimmee, Florida. American Institute of Aeronautics and Astronautics.

Clarke, J., Brody, S., Steer, J., McGilvray, M., and Di Mare, L. (2024a). Quasi-one-dimensional non-equilibrium method for shock tube and stagnation line flows. *Physics of Fluids*, 36(9):096140.

Clarke, J., Collen, P. L., McGilvray, M., and Di Mare, L. (2023a). Numerical Simulation of a Shock Tube in Thermochemical Non-Equilibrium. In *AIAA SciTech 2023 Forum*, National Harbor, MD & Online. American Institute of Aeronautics and Astronautics.

Clarke, J., Di Mare, L., and McGilvray, M. (2023b). Spatial Transformations for Reacting Gas Shock Tube Experiments. *AIAA Journal*, pages 1–10.

Clarke, J., Glenn, A. B., McGilvray, M., and Luca, D. M. (2024b). Numerical Simulations of Carbon Contaminants in T6 Shock Tube Tests. In *AIAA SCITECH 2024 Forum*, Orlando, FL. American Institute of Aeronautics and Astronautics.

Cleaver, J. W. and Crow, I. G. (1973). Vibrational relaxation of oxygen in an unsteady expansion wave. *The Journal of Chemical Physics*, 59(4):1592–1598.

Collen, P., Doherty, L., and McGilvray, M. (2019). Measurements of radiating hypervelocity air shock layers in the T6 Free-Piston Driven Shock Tube. In *International conference on flight vehicles, aerothermodynamics and re-entry missions and engineering (FAR 2019)*. ESA Conference Bureau.

Collen, P., Doherty, L. J., Subiah, D., Sopek, T., Gildfind, D., Penty, R., Gollan, R., and Morgan, R. (2021). Development and Commissioning of the T6 Stalker Tunnel. *Experiments in Fluids*, page 41.

Collen, P. L. (2021). *Development of a high-enthalpy ground test facility for shock-layer radiation*. PhD Thesis, University of Oxford.

Collen, P. L., Di Mare, L., McGilvray, M., and Satchell, M. (2023). Analysis of Shock Deceleration Effects in the NASA Electric Arc Shock Tube. *Journal of Thermophysics and Heat Transfer*, 37(2):503–512.

Collen, P. L., Satchell, M., Di Mare, L., and McGilvray, M. (2022). The influence of shock speed variation on radiation and thermochemistry experiments in shock tubes. *Journal of Fluid Mechanics*, 948:A51.

Connor, L. N. (1967). Calculation of the centered one-dimensional unsteady expansion of a reacting gas mixture subject to vibrational and chemical nonequilibrium. Technical, National Aeronautics and Space Administration.

Cooper, D. M. and Borucki, W. J. (1973). Measurements of hydrogen-helium radiation at shock-layer temperatures appropriate for jupiter entry. *Journal of Quantitative Spectroscopy and Radiative Transfer*, 13(10):1047–IN3.

Cruden, B., Martinez, R., Grinstead, J., and Olejniczak, J. (2009). Simultaneous Vacuum-Ultraviolet Through Near-IR Absolute Radiation Measurement with Spatiotemporal Resolution in An Electric Arc Shock Tube. In *41st AIAA Thermophysics Conference*, San Antonio, Texas. American Institute of Aeronautics and Astronautics.

Cruden, B. A. (2012). Electron Density Measurement in Reentry Shocks for Lunar Return. *Journal of Thermophysics and Heat Transfer*, 26(2):222–230.

Cruden, B. A. (2014). Absolute Radiation Measurements in Earth and Mars Entry Conditions. Technical STO-AVT-218-VKI, National Aeronautics and Space Administration.

Cruden, B. A. and Bogdanoff, D. W. (2017). Shock Radiation Tests for Saturn and Uranus Entry Probes. *Journal of Spacecraft and Rockets*, 54(6):1246–1257.

Cruden, B. A. and Brandis, A. M. (2014). Updates to the NEQAIR radiation solver. *Radiation in High Temperature Gases*. Publisher: European Space Agency St. Andrews, UK.

Cruden, B. A. and Brandis, A. M. (2019). Analysis of Shockwave Radiation Data in Nitrogen. In *AIAA Aviation 2019 Forum*, Dallas, Texas. American Institute of Aeronautics and Astronautics.

Cruden, B. A. and Brandis, A. M. (2020). Measurement of Radiative Nonequilibrium for Air Shocks Between 7 and 9 km/s. *Journal of Thermophysics and Heat Transfer*, 34(1):154–180.

Cruden, B. A., Brandis, A. M., and MacDonald, M. E. (2018). Characterization of CO Thermochemistry in Incident Shockwaves. In *2018 Joint Thermophysics and Heat Transfer Conference*, Atlanta, Georgia. American Institute of Aeronautics and Astronautics.

Cruden, B. A., Brandis, A. M., White, T. R., Mahzari, M., and Bose, D. (2016). Radiative Heating During Mars Science Laboratory Entry: Simulation, Ground Test, and Flight. *Journal of Thermophysics and Heat Transfer*, 30(3):642–650.

Cruden, B. A., Prabhu, D., and Martinez, R. (2012). Absolute Radiation Measurement in Venus and Mars Entry Conditions. *Journal of Spacecraft and Rockets*, 49(6):1069–1079.

Cruden, B. A., Tang, C. Y., Olejniczak, J., Amar, A. J., and Tanno, H. (2021). Characterization of Radiative Heating Anomaly in High Enthalpy Shock Tunnels. In *AIAA Scitech 2021 Forum*, VIRTUAL EVENT. American Institute of Aeronautics and Astronautics.

Cruden, B. A. and Tibere-Inglesse, A. (2024). Impact of Trace CH4 on Shock Layer Radiation in Outer Planet Entry. In *AIAA SciTech 2024 Forum*.

Crumpton, T. J. (2024). Analysis of Mars Entry Shock Wave Radiance in the T6 Stalker Hypersonic Wind Tunnel. In *AIAA SCITECH 2024 Forum*, Orlando, FL. American Institute of Aeronautics and Astronautics.

Davey, M. G. and Litster, J. (2006). *A Hypersonic Nozzle for the X3 Expansion Tube*. PhD thesis, University of Queensland.

De Boer, P. C. T. (1963). Curvature of Shock Fronts in Shock Tubes. *The Physics of Fluids*, 6(7):962–971.

De Crombrugghe, G. (2017). *On binary scaling and ground-to-flight extrapolation in high-enthalpy facilities*. PhD Thesis, The University of Queensland.

Dean, T., Blair, T. R., Roberts, M., Limbach, C., and Bowersox, R. D. (2022). On the Initial Characterization of a Large-Scale Hypervelocity Expansion Tunnel. In *AIAA SCITECH 2022 Forum*, San Diego, CA & Virtual. American Institute of Aeronautics and Astronautics.

Dean, T. S., Pehrson, J. C., Bowersox, R. D. W., and Dogariu, A. (2024). Expansion Tunnel Freestream Characterization Using Ultrafast Diagnostics. In *AIAA SciTech 2024 Forum*.

Dufrene, A. T., Holden, M. S., and Ringuette, M. J. (2015). Microwave Shock-Speed Diagnostic Development and Analysis of Expansion Tunnel Viscous Effects. *AIAA Journal*, 53(3):573–587.

Eberhart, J. (1967). When the SST is too slow... *Science News*, 91(22):528–529. Publisher: [Society for Science & the Public, Wiley].

Erb, A. J., West, T. K., and Johnston, C. O. (2020). Investigation of Galileo Probe Entry Heating with Coupled Radiation and Ablation. *Journal of Spacecraft and Rockets*, 57(4):692–706.

ESA (2024). ExoMars.

Furukawa, T., Aochi, T., and Sasoh, A. (2007). Expansion Tube Operation with Thin Secondary Diaphragm. *AIAA Journal*, 45(1):214–217.

Gibbons, N. N., Damm, K. A., Jacobs, P. A., and Gollan, R. J. (2023). Eilmer: an Open-Source Multi-Physics Hypersonic Flow Solver. *Computer Physics Communications*, 282:108551. arXiv:2206.01386 [cs].

Gildfind, D. E., Jacobs, P. A., Morgan, R. G., Chan, W. Y. K., and Gollan, R. J. (2018a). Scramjet test flow reconstruction for a large-scale expansion tube, Part 1: quasi-one-dimensional modelling. *Shock Waves*, 28(4):877–897.

Gildfind, D. E., Jacobs, P. A., Morgan, R. G., Chan, W. Y. K., and Gollan, R. J. (2018b). Scramjet test flow reconstruction for a large-scale expansion tube, Part 2: axisymmetric CFD analysis. *Shock Waves*, 28(4):899–918.

Gildfind, D. E., James, C. M., Toniato, P., and Morgan, R. G. (2015). Performance considerations for expansion tube operation with a shock-heated secondary driver. *Journal of Fluid Mechanics*, 777:364–407.

Gildfind, D. E., Morgan, R. G., McGilvray, M., Jacobs, P. A., Stalker, R. J., and Eichmann, T. N. (2011). Free-piston driver optimisation for simulation of high Mach number scramjet flow conditions. *Shock Waves*, 21(6):559–572.

Glenn, A. B., Collen, P. L., and McGilvray, M. (2022). Experimental Non-Equilibrium Radiation Measurements for Low-Earth Orbit Return. In *AIAA SCITECH 2022 Forum*, San Diego, CA & Virtual. American Institute of Aeronautics and Astronautics.

Gnoffo, A., Gupta, N., and Shinn, L. (1989). Conservation Equations and Physical Models for Hypersonic Air Flows in Thermal and Chemical Non-equilibrium. Technical NASA-TP-2867, National Aeronautics and Space Administration.

Gnoffo, P. A. (1999). Planetary-entry gas dynamics. *Annual Review of Fluid Mechanics*, 31(1):459–494. Publisher: Annual Reviews 4139 El Camino Way, PO Box 10139, Palo Alto, CA 94303-0139, USA.

Gokcen, T. (2007). N2-CH4-Ar Chemical Kinetic Model for Simulations of Atmospheric Entry to Titan. *Journal of Thermophysics and Heat Transfer*, 21(1):9–18. Publisher: American Institute of Aeronautics and Astronautics (AIAA).

Gollan, R. (2007). POSHAX: Computing post-shock thermochemically relaxing flow behind a steady normal shock. *Division of Mechanical Engineering Report*, 9.

Gollan, R. (2008). *Computational modelling of high-temperature gas effects with application to hypersonic flows*. PhD thesis, University of Queensland.

Gollan, R. and Jacobs, P. (2013). About the formulation, verification and validation of the hypersonic flow solver Eilmer. *International Journal for Numerical Methods in Fluids*, 73(1):19–57.

Goulard, R. (1961). The coupling of radiation and convection in detached shock layers. *Journal of Quantitative Spectroscopy and Radiative Transfer*, 1(3-4):249–257.

Grigat, F., Löhle, S., Eberhart, M., Meindl, A., Poloni, E., Ravichandran, R., Zuber, C., and Fasoulas, S. (2023). Spallation of Carbon Ablators in Arcjet Facility Experiments. *Journal of Thermophysics and Heat Transfer*, 37(2):341–352.

Gu, S. (2018). *Mars entry afterbody radiative heating: an experimental study of nonequilibrium CO2 expanding flow*. PhD Thesis, The University of Queensland.

Gu, S., Hao, J., Wang, Q., and Wen, C.-Y. (2023). Influence of thermochemical nonequilibrium on expansion tube air test conditions: A numerical study. *Physics of Fluids*, 35(3):036106.

Hartunian, R. A. (1961). Shock Curvature due to Boundary-Layer Effects in a Shock Tube. *The Physics of Fluids*, 4(9):1059–1063.

Henshall, B. D. (1956). The Use of Multiple Diaphragms in Shock Tubes. Technical C.P. No. 291, Ministry of Supply.

Hertzfeld, H. R. (2002). Measuring the economic returns from successful NASA life sciences technology transfers. *The Journal of Technology Transfer*, 27(4):311–320. Publisher: Springer.

Higgins, C. E. (2005). *Aerothermodynamics of the Gas Giants*. PhD thesis, University of Queensland.

Holbeche, T. (1964a). Spectrum-line-reversal temperature measurements through unsteady rarefaction waves in vibrationally-relaxing oxygen. Technical report, Royal Aircraft Establishment Farnborough.

Holbeche, T. (1964b). A theoretical and experimental investigation of temperature variation behind attenuating shock waves. *Proceedings of the Royal Society of London. Series A. Mathematical and Physical Sciences*, 279(1376):111–128.

Holden, M. S. (2015). Experimental Research and Analysis in Supersonic and Hypervelocity Flows in the LENS Shock Tunnels and Expansion Tunnel. In *20th AIAA International Space Planes and Hypersonic Systems and Technologies Conference*, Glasgow, Scotland. American Institute of Aeronautics and Astronautics.

Hollis, B., Striepe, S., Wright, M., Bose, D., Sutton, K., and Takashima, N. (2005). Prediction of the Aerothermodynamic Environment of the Huygens Probe. In *38th AIAA Thermophysics Conference*, Toronto, Ontario, Canada. American Institute of Aeronautics and Astronautics.

Hurle, I. R., Russo, A. L., and Hall, J. G. (1964). Spectroscopic Studies of Vibrational Nonequilibrium in Supersonic Nozzle Flows. *The Journal of Chemical Physics*, 40(8):2076–2089.

Hwang, H., Bose, D., Wright, H., White, T. R., Schoenenberger, M., Santos, J., Karlgaard, C. D., Kuhl, C., Oishi, T., and Trombetta, D. (2016). Mars 2020 Entry, Descent, and Landing Instrumentation (MEDLI2). In *46th AIAA Thermophysics Conference*, Washington, D.C. American Institute of Aeronautics and Astronautics.

Inger, G. R., Higgins, C., and Morgan, R. (2003). Generalized Nonequilibrium Binary Scaling for Shock Standoff on Hypersonic Blunt Bodies. *Journal of Thermophysics and Heat Transfer*, 17(1):126–128.

Jacobs, P., Gollan, R., Potter, D., Zander, F., Gildfind, D., Blyton, P., Chan, W., and Doherty, L. (2014). Estimation of high-enthalpy flow conditions for simple shock and expansion processes using the ESTCj program and library. Technical 2014-01-25, University of Queensland. Publisher: Citeseer.

Jacobs, P. A. (1994). Quasi-one-dimensional modeling of a free-piston shock tunnel. *AIAA Journal*, 32(1):137–145.

Jacobs, P. A. (1998). Shock tube modelling with L1d. Research 13/98, University of Queensland.

James, C. (2018). *Radiation from simulated atmospheric entry into the gas giants*. PhD Thesis, The University of Queensland.

James, C. M. (2019). Using a simplified Canny edge detector to detect shock arrival in expansion tubes and shock tunnels. Publisher: Research Publishing Services.

James, C. M., Cox, D., Komonen, A., Barltrop, L., Wikner, D. R., and McIntyre, T. J. (2021). Detecting shock arrival in expansion tubes and shock tunnels using high-frequency photodiodes. *Shock Waves*, 31(4):399–411.

James, C. M., Gildfind, D., Morgan, R. G., Lewis, S., and Mcintyre, T. (2017). Experimentally Simulating Gas Giant Entry in an Expansion Tube. In *21st AIAA International Space Planes and Hypersonics Technologies Conference*, Xiamen, China. American Institute of Aeronautics and Astronautics.

James, C. M., Gildfind, D. E., Lewis, S. W., Morgan, R. G., and Zander, F. (2018). Implementation of a state-to-state analytical framework for the calculation of expansion tube flow properties. *Shock Waves*, 28(2):349–377.

James, C. M., Gildfind, D. E., Morgan, R. G., Lewis, S. W., and McIntyre, T. J. (2020). Experimentally Simulating Giant Planet Entry in an Expansion Tube. *Journal of Spacecraft and Rockets*, 57(4):656–671.

Jewell, J. S., Parziale, N. J., Leyva, I. A., and Shepherd, J. E. (2017). Effects of Shock-Tube Cleanliness on Hypersonic Boundary Layer Transition at High Enthalpy. *AIAA Journal*, 55(1):332–338.

Johnston, C., Brandis, A., and Sutton, K. (2012). Shock Layer Radiation Modeling and Uncertainty for Mars Entry. In *43rd AIAA Thermophysics Conference*, New Orleans, Louisiana. American Institute of Aeronautics and Astronautics.

Johnston, C. O. (2015). Features of Afterbody Radiative Heating for Earth Entry. *Journal of Spacecraft and Rockets*.

Just, T. and Roth, P. (1971). Measurements of CO Relaxation in an Unsteady Expansion Wave. *The Journal of Chemical Physics*, 55(5):2395–2399.

Kelly, R. (2020). *Spectral analysis of atomic argon radiation in an expanding hypersonic flow*. PhD Thesis, The University of Queensland.

Kim, J. G. and Jo, S. M. (2021). Modification of chemical-kinetic parameters for 11-air species in re-entry flows. *International Journal of Heat and Mass Transfer*, 169:120950.

Kotov, D. V., Yee, H., Panesi, M., Prabhu, D. K., and Wray, A. A. (2014). Computational challenges for simulations related to the NASA electric arc shock tube (EAST) experiments. *Journal of Computational Physics*, 269:215–233.

Kurosaka, Y. and Shimamura, K. (2024). Microwave radar diagnostics of piston motion in a free-piston-driven expansion tube. *Shock Waves*.

Landau, L. and Teller, E. (1936). Zur theorie der schalldispersion. *Physikalische Zeitschrift der Sowjetunion*, 10(1):34–43.

Lani, A., Quintino, T., Kimpe, D., Deconinck, H., Vandewalle, S., and Poedts, S. (2005). The COOLFluiD framework: design solutions for high performance object oriented scientific computing software. In *Computational science–ICCS 2005: 5th international conference, atlanta, GA, USA, may 22-25, 2005. Proceedings, part I 5*, pages 279–286. Springer.

Leader, J., Steer, J., Collen, P., and McGilvray, M. (2022). Measurement of aeroheating of satellite components at true flight total enthalpies. Publisher: European Space Agency.

Leibowitz, L. P. (1973). Measurements of the structure of an ionizing shock wave in a hydrogen-helium mixture. *Physics of Fluids*, 16(1):59.

Leibowitz, M. G. and Austin, J. M. (2019). Hypervelocity Measurements of Mid-Wave Infrared CO2 Radiation Impinging on Blunt Bodies. In *AIAA Scitech 2019 Forum*, San Diego, California. American Institute of Aeronautics and Astronautics.

Leyland, P., McIntyre, T. J., Morgan, R., Jacobs, P., Zander, F., Sheikh, U., Eichmann, T., Joshi, O., Duffa, G., Potter, D., Banerji, N., Mora-Monteros, J., and Marguet, V. (2013). Radiation-Ablation Coupling for Capsule Reentry Heating via Simulation and Expansion Tube Investigations. In *5th European Conference for Aeronautics and Space Sciences (EUCASS)*.

Liu, Y. (2021). *Non-equilibrium radiation in simulated giant planet entries*. PhD thesis, University of Queensland.

Loehle, S., Hermann, T. A., Zander, F., Fulge, H., and Marynowski, T. (2014). Ablation Radiation Coupling Investigation in Earth Re-entry Using Plasma Wind Tunnel Experiments. In *11th AIAA/ASME Joint Thermophysics and Heat Transfer Conference*, Atlanta, GA. American Institute of Aeronautics and Astronautics.

Loehle, S., Meindl, A., Poloni, E., Steer, J., Sopek, T., McGilvray, M., and Walpot, L. (2022). Experimental Simulation of Gas Giant Entry in the PWK1 Arcjet Facility including CH4. In *AIAA SCITECH 2022 Forum*, San Diego, CA & Virtual. American Institute of Aeronautics and Astronautics.

Lu, F. K. (2002). *Advanced hypersonic test facilities*, volume 198. AIAA.

Lu, N., Andrianatos, A., James, C. M., Jacobs, C., and McIntyre, T. (2022). Ultrahigh-Speed Emission Spectroscopy for Flow Analysis in Laboratory Environments. In *AIAA AVIATION 2022 Forum*, Chicago, IL & Virtual. American Institute of Aeronautics and Astronautics.

Macmillan, J. (2020). Scott Morrison evokes World War II as Australia unveils larger, more lethal defence strategy. *ABC News*.

Marrone, P. V. and Treanor, C. E. (1963). Chemical relaxation with preferential dissociation from excited vibrational levels. *The Physics of Fluids*, 6(9):1215–1221. Publisher: AIP Publishing.

McBride, B. J. (1996). *Computer program for calculation of complex chemical equilibrium compositions and applications*, volume 2. NASA Lewis Research Center.

McGilvray, M. (2008). *Scramjet testing at high enthalpies in expansion tube facilities*. PhD thesis, University of Queensland.

McGilvray, M., Austin, J. M., Sharma, M., Jacobs, P. A., and Morgan, R. G. (2009). Diagnostic modelling of an expansion tube operating condition. *Shock Waves*, 19(1):59–66.

McGilvray, M., Collen, P., Doherty, L., Steer, J., Leader, J., Glenn, A., and Hambidge, C. (2022). The Oxford T6 Stalker tunnel: performance, upgrades and new modes of operation. Publisher: European Space Agency.

McGilvray, M., Dann, A. G., and Jacobs, P. A. (2013). Modelling the complete operation of a free-piston shock tunnel for a low enthalpy condition. *Shock Waves*, 23(4):399–406.

McGilvray, M., McIntyre, T. J., Glenn, A., and Morgan, R. G. (2024). Shock-Tube Measurements of Radiation for Titan Atmospheric Entry. *Journal of Thermophysics and Heat Transfer*, pages 1–8.

McGuire, S. D., Tibère-Inglesse, A. C., Mariotto, P. B., Cruden, B. A., and Laux, C. O. (2020). Measurements and modeling of CO 4th positive (A–X) radiation. *Journal of Quantitative Spectroscopy and Radiative Transfer*, 245:106855.

McLaren, T. I. and Appleton, J. P. (1970). Vibrational Relaxation Measurements of Carbon Monoxide in a Shock-Tube Expansion Wave. *The Journal of Chemical Physics*, page 9.

Menard, W. A. (1971). A higher performance electric-arc-driven shock tube. *AIAA Journal*, 9(10):2096–2098.

Merlin, P. (2009). Design and Development of the Blackbird: Challenges and Lessons Learned. In *47th AIAA Aerospace Sciences Meeting including The New Horizons Forum and Aerospace Exposition*, Orlando, Florida. American Institute of Aeronautics and Astronautics.

Miller, C. and Jones, J. (1984). Development and performance of the NASA Langley Research Center expansion tube/tunnel, a hypersonic-hypervelocity real-gas facility. In *Shock Tubes and Waves*, Sydney.

Miller, C. G. (1978). Operational Experience in the Langley Expansion Tube with Various Test Gases. *AIAA Journal*, 16(3):195–196.

Miller, V. A., Gamba, M., Mungal, M. G., and Hanson, R. K. (2014). Secondary Diaphragm Thickness Effects and Improved Pressure Measurements in an Expansion Tube. *AIAA Journal*, 52(2):451–456.

Miller III, C. G. (1975). Shock shapes on blunt bodies in hypersonic-hypervelocity helium, air, and CO2 flows, and calibration results in Langley 6-inch expansion tube. Technical report, National Aeronautics and Space Administration.

Millikan, R. C. and White, D. R. (1963). Systematics of Vibrational Relaxation. *The Journal of Chemical Physics*, 39(12):3209–3213.

Milos, F. S., Chen, Y.-K., Squire, T. H., and Brewer, R. A. (1999). Analysis of Galileo Probe Heatshield Ablation and Temperature Data. *Journal of Spacecraft and Rockets*, 36(3):298–306.

Mirels, H. (1961). Laminar boundary layer behind a strong shock moving into air. Technical report, National Aeronautics and Space Administration.

Mirels, H. (1963). Test Time in Low-Pressure Shock Tubes. *Physics of Fluids*, 6(9):1201.

Mirels, H. (1966). Flow Nonuniformity in Shock Tubes Operating at Maximum Test Times. *Physics of Fluids*, 9(10):1907.

Morgan, R. (2000). Development of X3, a superorbital expansion tube. In *38th Aerospace Sciences Meeting and Exhibit*, Reno,NV,U.S.A. American Institute of Aeronautics and Astronautics.

Morgan, R. (2001). Free piston-Driven expansion tubes. In *Handbook of Shock Waves*, volume 1, pages 603–622. Academic Press, 1 edition. Publisher: Academic Press.

Morgan, R. and Gildfind, D. (2013). Shock tube simulation of low Mach number blast waves. In *International symposium on shock waves*, pages 83–88. Springer.

Morgan, R., McIntyre, T., Buttsworth, D., Jacobs, P., Potter, D., Brandis, A., Gollan, R., Jacobs, C., Capra, B., McGilvary, M., and Eichmann, T. (2008). Impulse Facilities for the Simulation of Hypersonic Radiating Flows. In *38th Fluid Dynamics Conference and Exhibit*, Seattle, Washington. American Institute of Aeronautics and Astronautics.

Morgan, R. and Stalker, R. (1992). Double diaphragm driven free piston expansion tube. In *Shock waves; proceedings of the 18th international symposium*, volume 2, pages 1031–1038.

Morgan, R. G. (1997). A review of the use of expansion tubes for creating superorbital flows. In *35th Aerospace Sciences Meeting & Exhibit*.

NASA (2024). DAVINCI Homepage - Probe and Flyby Mission To Venus Atmosphere NASA Goddard.

Nasser, A. E. and Cleaver, J. W. (1977). Vibrational relaxation of carbon monoxide in an unsteady expansion wave. *Acta Astronautica*, 4(3-4):357–373.

Neely, A. and Morgan, R. (1994). The superorbital expansion tube concept, experiment and analysis. *The Aeronautical Journal*, 98(973):97–105. Publisher: Cambridge University Press.

NIST (2022). Experimental vibrational frequencies.

Nompelis, I., Candler, G., Holden, M., and Wadhams, T. (2004). Numerical Simulation of High-Enthalpy Experiments in the LENS X Expansion Tube Facility. In *42nd AIAA Aerospace Sciences Meeting and Exhibit*, Reno, Nevada. American Institute of Aeronautics and Astronautics.

Parcero, K., Allen, G., Witkowski, A., McKee, S., and Torres, L. (2022). Planetary Entry Mission Vehicles Quick Reference Guide Version 4.0.

Park, C. (1985). Nonequilibrium air radiation (Nequair) program: User's manual. Technical report, National Aeronautics and Space Administration.

Park, C. (1989). Assessment of two-temperature kinetic model for ionizing air. *Journal of thermophysics and heat transfer*, 3(3):233–244.

Park, C. (1993). Review of chemical-kinetic problems of future NASA missions. I - Earth entries. *Journal of Thermophysics and Heat Transfer*, 7(3):385–398.

Paull, A., Stalker, R., and Stringer, I. (1988). Experiments on an expansion tube with a free piston driver. In *15th Aerodynamic Testing Conference*, page 2018.

Paull, A. and Stalker, R. J. (1992). Test flow disturbances in an expansion tube. *Journal of Fluid Mechanics*, 245(-1):493.

Petersen, E. L. and Hanson, R. K. (2001). Nonideal effects behind reflected shock waves in a high-pressure shock tube. *Shock Waves*, 10(6):405–420. Publisher: Springer.

Potter, D. F. (2011). *Modelling of radiating shock layers for atmospheric entry at Earth and Mars*. PhD thesis, University of Queensland.

Ravichandran, R., Leiser, D., Zander, F., Löhle, S., Matlovič, P., Tóth, J., and Ferrière, L. (2021). High frame rate emission spectroscopy for ablation tests in plasma wind tunnel. *Review of Scientific Instruments*, 92(3):033101.

Resler, E. and Bloxsom, D. (1952). Very high Mach number flows by unsteady flow principles. *Cornell University Graduate School of Aeronautical Engineering, Limited Distribution Monograph*.

Reuters (2023). Aukus deal 'the biggest single investment in Australia's defence capability in history' – video. *the Guardian*.

Roberts, G., Morgan, R., and Stalker, R. (1995). *Influence of secondary diaphragm on flow quality in expansion tubes*. Springer.

Rond, C., Boubert, P., Félio, J.-M., and Chikhaoui, A. (2007). Radiation Measurements in a Shock Tube for Titan Mixtures. *Journal of Thermophysics and Heat Transfer*, 21(3):638–646.

Rothkopf, E. M. and Low, W. (1974). Diaphragm opening process in shock tubes. *The Physics of Fluids*, 17(6):1169–1173.

Satchell, M., Collen, P., McGilvray, M., and Di Mare, L. (2021). Numerical Simulation of Shock Tubes Using Shock Tracking in an Overset Formulation. *AIAA Journal*, 59(6):2102–2112.

Satchell, M., Di Mare, L., and McGilvray, M. (2022a). Flow Nonuniformities Behind Accelerating and Decelerating Shock Waves in Shock Tubes. *AIAA Journal*, 60(3):1537–1548.

Satchell, M., Glenn, A., Collen, P., Penty-Geraets, R., McGilvray, M., and Di Mare, L. (2022b). Analytical method of evaluating nonuniformities in shock tube flows: Application. *AIAA Journal*, 60(2):669–676. Publisher: American Institute of Aeronautics and Astronautics.

Satchell, M., McGilvray, M., and Di Mare, L. (2022c). Analytical method of evaluating nonuniformities in shock tube flows: Theory and development. *AIAA Journal*, 60(2):654–668. Publisher: American Institute of Aeronautics and Astronautics.

Schwartz, T., Girard, J., Finch, P. M., Yu, W., Lawson, J. M., Strand, C. L., Austin, J. M., Hornung, H. G., and Hanson, R. K. (2021). Characterization of the Caltech Hypervelocity Expansion Tube via Tunable Diode Laser Absorption Spectroscopy. In *AIAA Propulsion and Energy 2021 Forum*, VIRTUAL EVENT. American Institute of Aeronautics and Astronautics.

Scott, M., Morgan, R., and Jacobs, P. (2005). A New Single Stage Driver for the X2 Expansion Tube. In *43rd AIAA Aerospace Sciences Meeting and Exhibit*, Reno, Nevada. American Institute of Aeronautics and Astronautics.

Scott, M. P. (2006). *Development and Modelling of Expansion Tubes*. PhD thesis, University of Queensland.

Sharma Priyadarshini, M., Munafò, A., Brandis, A. M., Cruden, B. A., and Panesi, M. (2018). One-dimensional modeling methodology for shock tubes: Application to the EAST facility. In *2018 Joint Thermophysics and Heat Transfer Conference*, Atlanta, Georgia. American Institute of Aeronautics and Astronautics.

Sopek, T., Glenn, A., Clarke, J., Di Mare, L., Collen, P., and McGilvray, M. (2024). Radiative Heat Transfer Measurements of Titan Atmospheric Entry in a Shock Tube. *Journal of Thermophysics and Heat Transfer*, pages 1–23.

SpaceX (2024). Starship.

Spence, D. (1961). Unsteady shock propagation in a relaxing gas. *Proceedings of the Royal Society of London. Series A. Mathematical and Physical Sciences*, 264(1317):221–234. Publisher: The Royal Society London.

Stalker, R. and Plumb, D. (1968). Diaphragm-type shock tube for high shock speeds. *Nature*, 218(5143):789–790. Publisher: Nature Publishing Group UK London.

Stalker, R. J. (1972). Development of a hypervelocity wind tunnel. *The Aeronautical Journal*, 76(738):374–384.

Steer, J., Clarke, J., Collen, P., McGilvray, M., and Di Mare, L. (2025a). Characteristic numerical method for shock tube flows with non-equilibrium thermochemistry and non-uniform shock speed. *Physics of Fluids*.

Steer, J., Clarke, J., Collen, P., Satchell, M., McGilvray, M., and Di Mare, L. (2025b). Characteristic numerical method for expansion tube flows. *Physics of Fluids*.

Steer, J., Clarke, J., Collen, P. L., Satchell, M., Di Mare, L., and McGilvray, M. (2025c). Effect of Non-Uniform Shock Speed on Expansion Tube Flows. In *AIAA SCITECH 2025 forum*, page 2159.

Steer, J., Clarke, J., McGilvray, M., and Luca, D. M. (2024a). LASTA 2.0: Validation of a reverse time integration method. In *AIAA SCITECH 2024 forum*, page 0447.

Steer, J., Collen, P., Glenn, A., Hambidge, C., Doherty, L. J., McGilvray, M., Sopek, T., Loehle, S., and Walpot, L. (2024b). Commissioning of Upgrades to T6 to Study Giant Planet Entry. *Journal of Spacecraft and Rockets*.

Steer, J., Collen, P., and McGilvray, M. (2024c). Radiance Measurements Through Unsteady Expansion Waves in Relaxing Air and H_2 -He Mixtures. In *AIAA AVIATION*

FORUM AND ASCEND 2024, Las Vegas, Nevada. American Institute of Aeronautics and Astronautics.

Steer, J., Collen, P., and McGilvray, M. (2025d). Radiance measurements of thermochemically relaxing N2-O2 and H2-He mixtures through unsteady expansion waves. *Journal of Thermophysics and Heat Transfer*.

Steer, J., Collen, P. L., Glenn, A. B., Hambidge, C., Doherty, L. J., McGilvray, M., Loehle, S., and Walpot, L. (2023a). Shock radiation tests for ice giant entry probes including CH4 in the T6 free-piston driven wind tunnel. In *AIAA SCITECH 2023 forum*, page 1729.

Steer, J., Collen, P. L., Glenn, A. B., Sopek, T., Hambidge, C., Doherty, L. J., McGilvray, M., Loehle, S., and Walpot, L. (2023b). Experimental study of a galileo sub-scale model at ice giant entry conditions in the T6 free-piston driven wind tunnel. In *AIAA SCITECH 2023 forum*, page 1339.

Straede, H. G., Jenkinson, I., Van Den Herik, T., and James, C. M. (2024). Implementation of Microwave Interferometry for Continuous Shock Speed Measurement in Shock and Expansion Tubes. In *AIAA SCITECH 2024 Forum*, Orlando, FL. American Institute of Aeronautics and Astronautics.

Sutton, K. and Graves Jr, R. A. (1971). A general stagnation-point convective heating equation for arbitrary gas mixtures. Technical report, National Aeronautics and Space Administration.

Takayanagi, H. and Fujita, K. (2013). Infrared Radiation Measurement behind Shock Wave in Mars Simulant Gas for Aerocapture Missions. In *44th AIAA Thermophysics Conference*, San Diego, CA. American Institute of Aeronautics and Astronautics.

Takayanagi, H., Fujita, K., Ishida, H., Yamada, K., and Abe, T. (2014). Radiation intensity measurement in VUV wavelength region behind strong shock wave for future sample return missions. In *11th AIAA/ASME Joint Thermophysics and Heat Transfer Conference*, Atlanta, GA. American Institute of Aeronautics and Astronautics.

Thorne, A., Litzén, U., and Johansson, S. (1999). *Spectrophysics: principles and applications*. Springer Science & Business Media.

Tibere-Inglesse, A. C., West, T. K., Jelloian, C. C., Minesi, N. Q., Spearrin, R. M., Clarke, J., Di Mare, L., McGilvray, M., and Cruden, B. A. (2024). Reconstruction of Mars 2020

Backshell Radiative Heating via Infrared Emission Spectroscopy of $CO_2/N_2/Ar$ Shockwaves. *Journal of Thermophysics and Heat Transfer*, pages 1–17.

Tibère-Inglesse, A. C., Bensassi, K., Brandis, A. M., and Cruden, B. A. (2022). Shock tube radiation measurement in expanding air flows. In *AIAA SCITECH 2022 forum*, page 0117.

Tibère-Inglesse, A. C., Cruden, B. A., Jelloian, C., and Spearrin, R. M. (2023a). Examination of Mars2020 shock-layer conditions via infrared emission spectroscopy of CO2. In *AIAA SCITECH 2023 Forum*, National Harbor, MD & Online. American Institute of Aeronautics and Astronautics.

Tibère-Inglesse, A. C., Johnston, C. O., Brandis, A. M., and Cruden, B. A. (2023b). Dragonfly backshell radiation measurements in the EAST facility. In *AIAA AVIATION 2023 Forum*, San Diego, CA and Online. American Institute of Aeronautics and Astronautics.

Toniato, P., Gildfind, D. E., Jacobs, P. A., and Morgan, R. G. (2020). Expansion tube nozzle design using a parallel simplex algorithm. *Shock Waves*, 30(2):185–199.

Trimpi, R. L. (1962). A preliminary theoretical study of the expansion tube, a new device for producing high-enthalpy short-duration hypersonic gas flows/ by Robert L. Trimpi. Technical R-133, National Aeronautics and Space Administration.

UKSA (2024). Executive summary: Expanding frontiers.

USNI, U. N. I. (2024). Report to Congress on Hypersonic Weapons.

Vincenti, W. G., Kruger Jr, C. H., and Teichmann, T. (1966). *Introduction to physical gas dynamics*. American Institute of Physics.

Wegener, M., Sutcliffe, M., and Morgan, R. (2000). Optical study of a light diaphragm rupture process in an expansion tube. *Shock Waves*, 10(3):167–178.

Wei, H., Morgan, R. G., Mcintyre, T., Brandis, A. M., and Johnston, C. O. (2017). Experimental and Numerical Investigation of Air Radiation in Superorbital Expanding Flow. In *47th AIAA Thermophysics Conference*, Denver, Colorado. American Institute of Aeronautics and Astronautics.

Weilmuenster, K. J. (1974). An experimental investigation of wall boundary layer transition Reynolds numbers in an expansion tube. Technical report, National Aeronautics and Space Administration.

West, T. K., Johnston, C. O., and Hosder, S. (2017). Uncertainty and Sensitivity Analysis of Afterbody Radiative Heating Predictions for Earth Entry. *Journal of Thermophysics and Heat Transfer*, 31(2):294–306.

White, D. R. (1958). Influence of diaphragm opening time on shock-tube flows. *Journal of Fluid Mechanics*, 4(6):585–599.

White, T. R., Mahzari, M., Bose, D., and Santos, J. A. (2013). Post-flight Analysis of Mars Science Laboratory's Entry Aerothermal Environment and Thermal Protection System Response. In *44th AIAA Thermophysics Conference*, San Diego, CA. American Institute of Aeronautics and Astronautics.

Yamada, G., Suzuki, T., Takayanagi, H., and Fujita, K. (2011). Development of Shock Tube for Ground Testing Reentry Aerothermodynamics. *The Japan Society for Aeronautical and Space Sciences*, 54(183).

Yamada, G., Takayanagi, H., Suzuki, T., and Fujita, K. (2012). Shock Layer Radiation Analysis using a Hypervelocity Shock Tube (HVST). *TRANSACTIONS OF THE JAPAN SOCIETY FOR AERONAUTICAL AND SPACE SCIENCES*, 55(1):37–43.

Appendices

Appendix A

LASTA 2.0 Guide

Contents

This Appendix includes a brief guide for usage of LASTA 2.0 in shock tube mode and a summary of the input files and run details for all LASTA 2.0 test cases presented in the thesis. It is hoped that this provides future users of the software with a platform to reproduce the results shared so far.

A.1 Quick Start Guide for LASTA 2.0

The source code for LAgrangian Shock Tube Analysis (LASTA) 2.0, affectionately known as SLug Interaction Model for Expansion tubes (SLIME), is contained in this repository. The information in this file is intended to allow the user to quickly install, compile, and run a LASTA 2.0 shock tube test case.

Dependencies

- The OCEAN thermochemistry library. OCEAN should be installed and compiled at OCEANPATH. OCEANPATH should point to the folder containing the OCEAN software, in my case `OCEANPATH = /home/joesteer/ocean/`
- BLAS & LAPACK linear algebra libraries. The specific installation commands for these depends on your system, for an Ubuntu distribution: `apt-get install`

`libblas-dev liblapack-dev`

- gfortran & g++, compilers for the Fortran and C++ code respectively. Ubuntu: `apt get install gfortran g++`
- OpenMPI, parallel computing. Ubuntu: `apt install openmpi`. This is primarily used to invert Jacobian matrices in parallel, which requires a larger stack. Ensure to increase the parallel stack size before running LASTA 2.0 or you will be met with a segmentation fault. In console: `export OMP_STACKSIZE=2G`

Compilation

LASTA 2.0 is compiled simply with:

1. `cd src`
2. `make`

This produces the `a.out` executable file. `make clean` is available to remove all object files. This command should also be used when any changes are made to the OCEAN library to ensure that they are reflected in LASTA 2.0.

Usage

LASTA 2.0 is executed from the command line using:

- `./a.out -flag inputfile.inp`

This must of course be executed in the `src` folder, where the executable was compiled. The flags correspond to the following options:

- `-i` : initialise the shock tube problem
- `-ie`: initialise the expansion tube problem
- `-r` : run and solve the shock tube problem
- `-re`: run and solve the expansion tube problem
- `-v` : write the results to a readable file (shared)

Input files should be located: `../in/your-input-file.inp`. I suggest running the `default.inp` shock tube example to verify that you have installed the code correctly. An example input file for a test case used in this thesis is shown below:

E65-57 Example Input File

```
c ... ------------------------------------------------------------
c ... Simulation details
c ... ------------------------------------------------------------

c ... name of the simulation

name = "E65-57"

c ... save
c     overwrite name.dat with results of this simulation

save = 1

c ... ------------------------------------------------------------
c ... Driven gas properties
c ... ------------------------------------------------------------

c ... the fill conditions in the shock tube

p0 = 533.2
t0 = 300

c ... the composition of the fill gas

elem = 'E N C H'
spec = 'e- N C H N+ C+ H+ N2 CN CH4 CH3 CH2 CH C2 H2 NH HCN N2+ CN+'

c ... the mole fractions of each species in the fill gas

fr =   '0.0 0.0 0.0 0.0 0.0 0.0 0.0 0.978 0.0 0.0222 0.0
 //  0.0 0.0 0.0 0.0 0.0 0.0 0.0 0.0'

c ... non-equilibrium thermochemistry

chmf=     "../in/thermo/gokcen04/chemkin_titan.dat"
rcnf=     '../in/thermo/gokcen04/reactions_gokcen04.dat'
cond=     '../in/thermo/gokcen04/cond_titan.dat'
mw_file=  '../in/thermo/gokcen04/mw_millikan_titan.dat'
```

```
cs_file=  '../in/thermo/gokcen04/cs_titan.dat'
mst_file= '../in/thermo/gokcen04/tbr_gokcen04.dat'
diss_file='../in/thermo/gokcen04/diss_zero.dat'
ion_file= '../in/thermo/gokcen04/ion_zero.dat'
apb_file= '../in/thermo/gokcen04/e_neu_cs_titan.dat'

c ... type of gas model
c     ideal: initialised with rh, no source terms
c     eq: initialised with eq, source terms
c     non-eq: initialised with rh, source terms

ns = non-eq

c ... species specific heats (to initialise the program only)

cpi = 1.6
cvi = 1.0

c ... viscosity
c     select from the following options to specify viscous behaviour
c     1. none       : no mirels boundary layer source terms
c     2. sutherland : use sutherland's law defaults in suth.inp

visc = "sutherland"

c ... sutherland constants

mu0=  1.716e-5
tmu0= 273.d0
smu = 111.d0

c ... Mirels model constants
c     exponent of the cm constant
cm = 0.48

c ... ---------------------------------------------------------------
c ... Facility properties
c ... ---------------------------------------------------------------

```

```
c ... wall temperature

tw = 300

c ... tube radius

rd = 0.05058d0


c ... ---------------------------------------------------------------
c ... Grid details
c ... ---------------------------------------------------------------

c ... the number of streamwise grid points

m = 80

c ... CFL number based on max eigenvalue (dictates the number of time points)

sgm = 1500.d0

c ... initial slug length estimate

li = 0.05d0

c ... dx in radii

dx0= 0.001d0
dxm= 0.015d0

c ... grid clustering strength

clu = 1.1

c ... ---------------------------------------------------------------
c ... Shock trajectory boundary condition
c ... ---------------------------------------------------------------

c ... the file containing t-x information
```

```
117
118 fss = '../in/E65/E65-57-xt.dat'
119
120 c ... type of curve fit
121 c     1. polynomial
122 c     2. c-spline (suggested)
123
124 fit = 1
125
126 c ... order of polynomial fit if selected
127
128 degree = 2
129
130 c ... ---------------------------------------------------------------
131 c ... Final pressure boundary condition
132 c ... ---------------------------------------------------------------
133
134 c ... the file containing pressure v.s. time information
135
136 fpp = '../in/T6s492-pp.txt'
137
138 c ... type of data
139 c     1. spatial pressure profile (in m)
140 c     2. temporal profile (in s)
141 c     3. constant (use value from shock trajectory)
142 c     4. not enforced (dw/dt = 0)
143
144 type = 4
145
146 c ... ---------------------------------------------------------------
147 c ... Solution controls
148 c ... ---------------------------------------------------------------
149
150 c ... iterations, relaxation
151 c     rmin: minimum or initial relaxation factor
152 c     rmax: maximum or final relaxation faction
153 c     rdel: increase the relaxtion factor by this factor every iteration
154 c     nito: number of iterations for the main or outer (o) loop
155 c     niti: number of iterations for the jacobian inversion or inner (i) loop
```

```
c     nits: number of iterations to invert the Schur complement (s)

rmin = 0.01
rmax = 0.99
rdel = 1.1

nito = 50
niti = 3
nits = 200

c ... solution approach parameters
c     sini: begin this speed below the nominal shock speed
c     nsim: approach the nominal simulation with this many interstitial simulations

sini = 100
nsim = 2

c ... ------------------------------------------------------------
c ... Post-processing
c ... ------------------------------------------------------------

c ... write full solution to inv.dat

full = 1

c ... x-locations to write (distance from initial x in fss)

xloc = "8.00"
```

A.2 Input Files Used in the Thesis

The table below summarises the input files, dates, and LASTA 2.0 GitHub versions used to run each of the test cases presented in the thesis. The input files (also for NEQAIR) are available on request. Minor differences between versions are related to quality of life improvements and bug fixes; the main program remains unchanged.

Test Case	Figure(s)	Input File Name	LASTA 2.0 Version
FROSST Validation Accelerating	3.7, 3.8, 3.9	frosst-valid-accel	2025-04-07 89ea982
FROSST Validation Uniform	3.7, 3.8, 3.9	frosst-valid-uniform	2025-04-07 89ea982
FROSST Validation Decelerating	3.7, 3.8, 3.9	frosst-valid-decel	2025-04-07 89ea982
NESS Validation 5.3 $\mathrm{km\,s^{-1}}$	3.11, 3.12a 3.14	ness-validation-c	2025-04-07 89ea982
Time-wise grid dependence study	3.13, 3.14	ness-validation	2025-04-07 89ea982
T6s212	3.16, 3.17	T6s212	2025-04-07 89ea982
T6s214	3.16, 3.18	T6s214	2025-04-07 89ea982
E50-40	4.14, 4.15, 4.4, 4.9	E50-40	2025-04-07 89ea982
E65-16	4.16, 4.17	E65-16	2025-04-15 37fddd3
E65-35	D.1	E65-35	2025-04-15 37fddd3
E65-45	D.2	E65-45	2025-04-15 37fddd3
E65-5	D.3	E65-5	2025-04-15 37fddd3
E65-49	D.4	E65-49	2025-04-15 37fddd3
E65-10	D.5	E65-10	2025-04-15 37fddd3
T6s525	4.20, 4.21, 4.22	T6s525	2025-04-07 89ea982
E50-36	4.4, 4.7	E50-36	2025-04-07 89ea982
T6s164	4.4, 4.5,4.11	T6s164	2025-04-25 1368a38
T6s186	4.4, 4.5,4.13	T6s186	2025-04-07 89ea982
FROSST Validation Expansion Tube	6.5,6.4, 6.6	frosst-valid-st, frosst-valid-at	2025-05-16 78ed3ea
T6s529	6.9, 6.10, 6.11, 6.12, 6.13, 6.14	T6s529-st, T6s529-at	2025-05-16 78ed3ea
x3s273	6.16, 6.17, 6.18, 6.19	x3s273-st, x3s273-at	2025-05-16 78ed3ea

Appendix B

Derivation of Governing Equations for the Two-Temperature Plasma

Contents

B.1 Perfect gas

B.1.1 General Euler equations

The one dimensional Euler equations are:

$$\frac{\partial \rho}{\partial t} + \frac{\partial (\rho u)}{\partial x} = 0 \tag{B.1}$$

$$\frac{\partial (\rho u)}{\partial t} + \frac{\partial (\rho u u + p)}{\partial x} = 0 \tag{B.2}$$

$$\frac{\partial (\rho E)}{\partial t} + \frac{\partial (\rho u E + u p)}{\partial x} = 0 \tag{B.3}$$

E is given by:

$$E = e + \frac{1}{2} u^2 \tag{B.4}$$

Where E is the total energy, e is the specific internal energy, and u is the one-dimensional

velocity. The equations are closed with an equation of state, in the ideal case:

$$p = \rho e(\gamma - 1) \tag{B.5}$$

This is the *conservative* form of the Euler equations, which can be written in matrix form as:

$$U_t + [F(U)]_x = 0 \tag{B.6}$$

with

$$U = \begin{bmatrix} \rho \\ \rho u \\ \rho E \end{bmatrix} \quad F(U) = \begin{bmatrix} \rho u \\ \rho u u + p \\ \rho u E + up \end{bmatrix} \tag{B.7}$$

A more convenient way to express these equations is in *primitive form*, where each equation describes a *primitive variable*: ρ, u, p. To transform from one form to another, linear row operations are necessary. The *conservative* form of the Euler equations can be represented by the following matrix system:

$$\begin{array}{ccc|ccc|c} \frac{\partial \rho}{\partial t} & \frac{\partial u}{\partial t} & \frac{\partial p}{\partial t} & \frac{\partial \rho}{\partial x} & \frac{\partial u}{\partial x} & \frac{\partial p}{\partial x} & \\ \hline 1 & 0 & 0 & u & \rho & 0 & 0 \\ u & \rho & 0 & u^2 & 2\rho u & 1 & 0 \\ E & \rho u & 0 & uE & \gamma/(\gamma-1)p + 3/2\rho u^2 & u & -\rho(\partial e/\partial t) - \rho u(\partial e/\partial x) \end{array}$$

Where the entries of the matrix correspond to the coefficients of the partial derivatives in the governing equations. If e is expressed in terms of the primitive variables, the derivatives are:

$$\frac{\partial e}{\partial t} = \frac{1}{(\gamma - 1)\rho^2}\left(\frac{\partial p}{\partial t}\rho - \frac{\partial \rho}{\partial t}p\right) \tag{B.8}$$

$$\frac{\partial e}{\partial x} = \frac{1}{(\gamma - 1)\rho^2}\left(\frac{\partial p}{\partial x}\rho - \frac{\partial \rho}{\partial x}p\right) \tag{B.9}$$

For completeness, E is simply:

$$E = \frac{p}{\rho(\gamma - 1)} + \frac{1}{2}u^2 \tag{B.10}$$

The system of equations then becomes:

$$\left[\begin{array}{ccc|ccc|c} \frac{\partial\rho}{\partial t} & \frac{\partial u}{\partial t} & \frac{\partial p}{\partial t} & \frac{\partial\rho}{\partial x} & \frac{\partial u}{\partial x} & \frac{\partial p}{\partial x} & \\ 1 & 0 & 0 & u & \rho & 0 & 0 \\ u & \rho & 0 & u^2 & 2\rho u & 1 & 0 \\ E-p/(\gamma-1)\rho & \rho u & 1/(\gamma-1) & uE-pu/(\gamma-1)\rho & \gamma/(\gamma-1)p+3/2\rho u^2 & u+u/(\gamma-1) & 0 \end{array}\right]$$

$$\left[\begin{array}{ccc|ccc|c} \frac{\partial\rho}{\partial t} & \frac{\partial u}{\partial t} & \frac{\partial p}{\partial t} & \frac{\partial\rho}{\partial x} & \frac{\partial u}{\partial x} & \frac{\partial p}{\partial x} & \\ 1 & 0 & 0 & u & \rho & 0 & 0 \\ u & \rho & 0 & u^2 & 2\rho u & 1 & 0 \\ u^2/2 & \rho u & 1/(\gamma-1) & u^3/2 & \gamma/(\gamma-1)p+3/2\rho u^2 & u+u/(\gamma-1) & 0 \end{array}\right] \quad R_2 \to R_2 - uR_1$$

$$\left[\begin{array}{ccc|ccc|c} \frac{\partial\rho}{\partial t} & \frac{\partial u}{\partial t} & \frac{\partial p}{\partial t} & \frac{\partial\rho}{\partial x} & \frac{\partial u}{\partial x} & \frac{\partial p}{\partial x} & \\ 1 & 0 & 0 & u & \rho & 0 & 0 \\ 0 & \rho & 0 & 0 & \rho u & 1 & 0 \\ u^2/2 & \rho u & 1/(\gamma-1) & u^3/2 & \gamma/(\gamma-1)p+3/2\rho u^2 & u+u/(\gamma-1) & 0 \end{array}\right] \quad R_2 \to (1/\rho)R_2$$

$$\left[\begin{array}{ccc|ccc|c} \frac{\partial\rho}{\partial t} & \frac{\partial u}{\partial t} & \frac{\partial p}{\partial t} & \frac{\partial\rho}{\partial x} & \frac{\partial u}{\partial x} & \frac{\partial p}{\partial x} & \\ 1 & 0 & 0 & u & \rho & 0 & 0 \\ 0 & 1 & 0 & 0 & u & \rho^{-1} & 0 \\ u^2/2 & \rho u & 1/(\gamma-1) & u^3/2 & \gamma/(\gamma-1)p+3/2\rho u^2 & u+u/(\gamma-1) & 0 \end{array}\right] \quad R_3 \to R_3 - (u^2/2)R_1$$

$$\left[\begin{array}{ccc|ccc|c} \frac{\partial\rho}{\partial t} & \frac{\partial u}{\partial t} & \frac{\partial p}{\partial t} & \frac{\partial\rho}{\partial x} & \frac{\partial u}{\partial x} & \frac{\partial p}{\partial x} & \\ 1 & 0 & 0 & u & \rho & 0 & 0 \\ 0 & 1 & 0 & 0 & u & \rho^{-1} & 0 \\ 0 & \rho u & 1/(\gamma-1) & 0 & \gamma/(\gamma-1)p+\rho u^2 & u+u/(\gamma-1) & 0 \end{array}\right] \quad R_3 \to (\gamma-1)R_3$$

$$\begin{array}{c} \frac{\partial \rho}{\partial t} \quad \frac{\partial u}{\partial t} \quad \frac{\partial p}{\partial t} \quad \frac{\partial \rho}{\partial x} \quad \frac{\partial u}{\partial x} \quad \frac{\partial p}{\partial x} \\ \left[\begin{array}{ccc|ccc|c} 1 & 0 & 0 & u & \rho & 0 & 0 \\ 0 & 1 & 0 & 0 & u & \rho^{-1} & 0 \\ 0 & \rho u(\gamma-1) & 1 & 0 & \gamma p + (\gamma-1)\rho u^2 & u + u(\gamma-1) & 0 \end{array}\right] \end{array} R_3 \to R_3 - \rho u(\gamma-1)R_2$$

$$\begin{array}{c} \frac{\partial \rho}{\partial t} \quad \frac{\partial u}{\partial t} \quad \frac{\partial p}{\partial t} \quad \frac{\partial \rho}{\partial x} \quad \frac{\partial u}{\partial x} \quad \frac{\partial p}{\partial x} \\ \left[\begin{array}{ccc|ccc|c} 1 & 0 & 0 & u & \rho & 0 & 0 \\ 0 & 1 & 0 & 0 & u & \rho^{-1} & 0 \\ 0 & 0 & 1 & 0 & \gamma p & u & 0 \end{array}\right] \end{array}$$

If we assume an ideal gas then:

$$p = \rho RT \tag{B.11}$$

$$\gamma p = \gamma \rho RT \tag{B.12}$$

$$\gamma p = \rho a^2 \tag{B.13}$$

Where a is the speed of sound. So the final system is:

$$\begin{array}{c} \frac{\partial \rho}{\partial t} \quad \frac{\partial u}{\partial t} \quad \frac{\partial p}{\partial t} \quad \frac{\partial \rho}{\partial x} \quad \frac{\partial u}{\partial x} \quad \frac{\partial p}{\partial x} \\ \left[\begin{array}{ccc|ccc|c} 1 & 0 & 0 & u & \rho & 0 & 0 \\ 0 & 1 & 0 & 0 & u & \rho^{-1} & 0 \\ 0 & 0 & 1 & 0 & \rho a^2 & u & 0 \end{array}\right] \end{array}$$

or

$$q_t + A(q)q_x = 0 \tag{B.14}$$

with

$$q = \begin{bmatrix} \rho \\ u \\ p \end{bmatrix} \quad A(q) = \begin{bmatrix} u & \rho & 0 \\ 0 & u & 1/\rho \\ 0 & \rho a^2 & u \end{bmatrix} \tag{B.15}$$

Ideally, the matrix $A(q)$ would be diagonal to simplify the solution. We would essen-

tially like to express the matrix in a different basis such that the solution is easy to obtain, but we can transform out of the basis once we want the actual (primitive) variables. To diagonalize the matrix, we must find the eigenvalues/eigenvectors by solving:

$$|A - \lambda I| = 0 \tag{B.16}$$

$$u \begin{vmatrix} u & 1/\rho \\ \rho a^2 & u \end{vmatrix} = 0 \tag{B.17}$$

Note that the second and third 2 x 2 determinants are 0.

$$u(u^2 - a^2) = 0 \tag{B.18}$$

$$u(u + a)(u - a) = 0 \tag{B.19}$$

Clearly u, $u + a$, and $u - a$ are all solutions of the equation and therefore eigenvalues (λ) of the system. The right and left eigenvectors of the system satisfy:

$$A\mathbf{r} = \lambda\mathbf{r},\ \mathbf{l}A = \lambda\mathbf{l} \tag{B.20}$$

Once the eigenvectors are obtained, we can build R and L which are matrices comprised of the right and left eigenvectors. These matrices have the property $LR = I = RL$ and importantly $\Lambda = LAR$ is a diagonal matrix. Now, defining $dw = Ldq$, we can write:

$$\begin{aligned} q_t + Aq_x &= 0 && \text{(B.21)} \\ Lq_t + LAq_x &= 0 && \text{(B.22)} \\ Lq_t + LAIq_x &= 0 && \text{(B.23)} \\ Lq_t + LARLq_x &= 0 && \text{(B.24)} \\ w_t + \Lambda w_x &= 0 && \text{(B.25)} \end{aligned}$$

Note that the left and right matrices of eigenvectors are:

$$L = \begin{bmatrix} 1 & 0 & -1/c^2 \\ 0 & \rho/2c & 1/2c^2 \\ 0 & -\rho/2c & 1/2c^2 \end{bmatrix} \quad R = \begin{bmatrix} 1 & 1 & 1 \\ 0 & c/\rho & -c/\rho \\ 0 & c^2 & c^2 \end{bmatrix} \tag{B.26}$$

These matrices allow us to transform the system between characteristic and primitive form. Put another way, the left matrix of eigenvectors *projects* the primitive variables on to the characteristics.

B.1.2 Lagrangian form

The governing equations can be written in Lagrangian form with a source term for boundary layer mass removal:

$$\frac{\partial}{\partial t'}\begin{bmatrix}\rho\\u\\p\end{bmatrix} = -\begin{bmatrix}u' & \rho & 0\\0 & u' & \rho^{-1}\\0 & \rho a^2 & u'\end{bmatrix}\frac{\partial}{\partial x}\begin{bmatrix}\rho\\u\\p\end{bmatrix} - \rho\frac{2v}{r_1}\begin{bmatrix}1\\0\\a^2\end{bmatrix} \tag{B.27}$$

or

$$q_t + Aq_x + F = 0 \tag{B.28}$$

The eigenvectors of A are the same as in the previous section, so to rewrite in characteristic form:

$$\begin{aligned} q_t + Aq_x + F &= 0 && \text{(B.29)}\\ Lq_t + LAq_x + LF &= 0 && \text{(B.30)}\\ Lq_t + LAIq_x + LF &= 0 && \text{(B.31)}\\ Lq_t + LARLq_x + LF &= 0 && \text{(B.32)}\\ w_t + \Lambda w_x + LF &= 0 && \text{(B.33)} \end{aligned}$$

B.2 Vibrational-electronic energy conservation

Neglecting chemical source terms, the vibrational-electronic energy conservation equation is:

$$\frac{\partial(\rho e_V)}{\partial t} + \frac{\partial(\rho e_V u)}{\partial x} + p_e\frac{\partial u}{\partial x} = 0 \tag{B.34}$$

In the above, e_V is the mixture vibrational-electronic energy per unit mass with units of $\mathrm{J\,kg^{-1}}$.

B.2.1 Expressing the vibrational-electronic energy conservation equation in terms of T_V

In order to cast the system with T_V as a primitive variable, we must express all e_V terms as functions of T_V and other primitive variables only. In a problem with many species s, e_V may be evaluated as:

$$e_V = \sum_{s=1}^{n} \frac{\rho_s}{\rho} e_{V,s} \tag{B.35}$$

$$\rho e_V = \sum_{s=1}^{n} \rho_s e_{V,s} \tag{B.36}$$

Substituting into Equation B.34:

$$\begin{aligned} \frac{\partial}{\partial t}\left(\sum_{s=1}^{n} \rho_s e_{V,s}\right) + u\frac{\partial}{\partial x}\left(\sum_{s=1}^{n} \rho_s e_{V,s}\right) + \frac{\partial u}{\partial x}\sum_{s=1}^{n} \rho_s e_{V,s} + p_e \frac{\partial u}{\partial x} &= 0 \\ \sum_{s=1}^{n} \frac{\partial \rho_s}{\partial t} e_{V,s} + \sum_{s=1}^{n} \rho_s C_{v,V}^s \frac{\partial T_V}{\partial t} + u\left(\sum_{s=1}^{n} \frac{\partial \rho_s}{\partial x} e_{V,s} + \sum_{s=1}^{n} \rho_s C_{v,V}^s \frac{\partial T_V}{\partial x}\right) & \\ + \frac{\partial u}{\partial x}\sum_{s=1}^{n} \rho_s e_{V,s} + p_e \frac{\partial u}{\partial x} &= 0 \end{aligned} \tag{B.37}$$

Can now subtract the product of the continuity equation with $e_{V,s}$:

$$\sum_{s=1}^{n} \rho_s C_{v,V}^s \frac{\partial T_V}{\partial t} + u\sum_{s=1}^{n} \rho_s C_{v,V}^s \frac{\partial T_V}{\partial x} + p_e \frac{\partial u}{\partial x} = 0 \tag{B.38}$$

$$\rho C_{v,V} \frac{\partial T_V}{\partial t} + u\rho C_{v,V} \frac{\partial T_V}{\partial x} + p_e \frac{\partial u}{\partial x} = 0 \tag{B.39}$$

$$\frac{\partial T_V}{\partial t} + u\frac{\partial T_V}{\partial x} + \frac{p_e}{\rho C_{v,V}} \frac{\partial u}{\partial x} = 0 \tag{B.40}$$

The vibrational-electronic equation is now expressed solely in terms of the primitive variables.

B.2.2 Evaluating $C_{v,V}$

To solve the expression for T_V, $C_{v,V}$ must be known. $e_{V,s}$ may be evaluated as:

$$e_{V,s} = \int_{T_{ref}}^{T_V} C_{v,V}^s dT' \tag{B.41}$$

Where c_s and $e_{V,s}$ are the mass fraction and vibrational-electronic energy of each species, respectively. Here, $C_{v,V}^s$ ($\mathrm{J\,kg^{-1}\,K^{-1}}$) is the specific heat at constant volume for species s for vibrational-electronic energy, T_{ref} is a curve fit reference temperature, typi-

cally 298 K, and T_V is the vibrational-electronic temperature. The vibrational-electronic enthalpy for species s can be evaluated by utilizing the curve fit for specific enthalpy evaluated at temperature T_V and subtracting both the contribution for the translational and rotational enthalpy evaluated at T_V and the enthalpy of formation.

$$C^s_{v,V}(T_V) = C^s_v(T_V) - C^s_{v,t} - C^s_{v,r} \tag{B.42}$$

where

$$C^s_v(T_V) = C^s_p(T_V) - \frac{\bar{R}}{M_s} \tag{B.43}$$

$C^s_{v,v}$, $C^s_{v,t}$ and $C^s_{v,r}$ are the specific heats at constant volume for species s for vibrational, translational, and rotational enthalpy respectively ($\mathrm{J\,kg^{-1}\,K^{-1}}$). C^s_p is the specific heat at constant pressure for species s. $\bar{R}$ is the universal gas constant (8314.3 $\mathrm{J\,mol^{-1}\,K^{-1}}$) and M_s is the molecular weight of species s. $C^s_{v,t}$ and $C^s_{v,r}$ are evaluated simply as:

$$C^s_{v,t} = \frac{3\bar{R}}{2M_s}, C^s_{v,r} = \frac{\bar{R}}{M_s} \tag{B.44}$$

C^s_p and $C^s_{v,v}$ must be evaluated from curve fits/tabulated values from the literature.

$$C^s_p(T) = \frac{\bar{R}}{M_s}\sum_{k=1}^{5} A^s_k T^{k-1} \tag{B.45}$$

The specific heat at constant volume for species s for vibrational-electronic energy is then:

$$C^s_{v,V}(T) = \frac{\bar{R}}{M_s}\left(\sum_{k=1}^{5} A^s_k T^{k-1} - \frac{7}{2}\right) \tag{B.46}$$

The vibrational-electronic energy of a species:

$$e_{V,s} = \int_{T_{ref}}^{T_V} \frac{\bar{R}}{M_s}\left(\sum_{k=1}^{5} A^s_k T^{k-1} - \frac{7}{2}\right) dT' \tag{B.47}$$

And the total vibrational-electronic energy per unit mass:

$$e_V = \sum_{s=i}^{n} c_s \int_{T_{ref}}^{T_V} \frac{\bar{R}}{M_s}\left(\sum_{k=1}^{5} A^s_k T^{k-1} - \frac{7}{2}\right) dT' \tag{B.48}$$

B.2.3 Eigenvector problem with vibrational-electronic energy conservation equation

Neglecting source terms, the governing equations in conservative form are:

$$U = \begin{bmatrix} \rho_1 \\ \vdots \\ \rho_n \\ \rho e_V \\ \rho u \\ \rho E \end{bmatrix} \quad F(U) = \begin{bmatrix} \rho_1 u \\ \vdots \\ \rho_n u \\ \rho u e_V \\ \rho u u + p \\ \rho u E + u p \end{bmatrix} \tag{B.49}$$

In primitive form:

$$q = \begin{bmatrix} \rho_1 \\ \vdots \\ \rho_n \\ T_V \\ u \\ p \end{bmatrix} \quad A(q) = \begin{bmatrix} u & \dots & 0 & 0 & \rho_1 & 0 \\ \vdots & \ddots & \vdots & \vdots & \vdots & \vdots \\ 0 & \dots & u & 0 & \rho_n & 0 \\ 0 & \dots & 0 & u & \frac{p_e}{\rho C_{v,V}} & 0 \\ 0 & \dots & 0 & 0 & u & 1/\rho \\ 0 & \dots & 0 & 0 & \rho a^2 & u \end{bmatrix} \tag{B.50}$$

Let the subscripts $n+1$, $n+2$, $n+3$ represent the vibrational-electronic energy equation, the momentum equation, and the total energy equations respectively. Let subscripts $1-n$ represent the continuity equations. Assume eigenvalues of $\lambda_{1-n,n+1} = u$, $\lambda_{n+2,n+3} = u \pm a$. To find the left eigenvector, $\mathbf{l_{n+1}}$ for λ_{n+1} we must solve $\mathbf{l_{n+1}}(A - \lambda I) = 0$:

$$\mathbf{l_{n+1}}(A-\lambda I) = \begin{bmatrix} \ell_1 & \dots & \ell_n & \ell_{n+1} & \ell_{n+2} & \ell_{n+3} \end{bmatrix} \begin{bmatrix} 0 & \dots & 0 & 0 & \rho_1 & 0 \\ \vdots & \ddots & \vdots & \vdots & \vdots & \vdots \\ 0 & \dots & 0 & 0 & \rho_n & 0 \\ 0 & \dots & 0 & 0 & \frac{p_e}{\rho C_{v,V}} & 0 \\ 0 & \dots & 0 & 0 & 0 & 1/\rho \\ 0 & \dots & 0 & 0 & \rho a^2 & 0 \end{bmatrix} = 0 \tag{B.51}$$

The constraint resulting from the $n+1$ column of A:

$$l_1\rho_1 + \ldots + l_n\rho_n + l_{n+1}\frac{p_e}{\rho C_{v,V}} + l_{n+3}\rho a^2 = 0 \tag{B.52}$$

The eigenvector $\mathbf{l_{n+1}}$ is then:

$$\mathbf{l_{n+1}} = \begin{bmatrix} 0 & \dots & 0 & 1 & 0 & -\frac{p_e}{\rho^2 a^2 C_{v,V}} \end{bmatrix} \tag{B.53}$$

The resulting matrix of left eigenvectors:

$$L = \begin{bmatrix} 1 & \dots & 0 & 0 & 0 & -\frac{\rho_1}{\rho a^2} \\ \vdots & \ddots & \vdots & \vdots & \vdots & \vdots \\ 0 & \dots & 1 & 0 & 0 & -\frac{\rho_n}{\rho a^2} \\ 0 & \dots & 0 & 1 & 0 & -\frac{p_e}{\rho^2 a^2 C_{v,V}} \\ 0 & \dots & 0 & 0 & \rho a & 1 \\ 0 & \dots & 0 & 0 & -\rho a & 1 \end{bmatrix} \tag{B.54}$$

As implemented in the program:

$$L = \begin{bmatrix} 1 & \dots & 0 & 0 & 0 & -\frac{\rho_1}{\rho a^2} \\ \vdots & \ddots & \vdots & \vdots & \vdots & \vdots \\ 0 & \dots & 1 & 0 & 0 & -\frac{\rho_n}{\rho a^2} \\ 0 & \dots & 0 & 1 & 0 & -\frac{p_e}{\rho^2 a^2 C_{v,V}} \\ 0 & \dots & 0 & 0 & 1 & \frac{1}{\rho a} \\ 0 & \dots & 0 & 0 & 1 & -\frac{1}{\rho a} \end{bmatrix} \tag{B.55}$$

B.2.4 Transformation Jacobians for thermochemical source terms

Three sets of state variables arise in SLIME/OCEAN:

$$q_c = \begin{bmatrix} \rho_1 \\ \rho_2 \\ \vdots \\ \rho_n \\ \rho e_V \\ \rho u \\ \rho E \end{bmatrix} \quad q_p = \begin{bmatrix} \rho_1 \\ \rho_2 \\ \vdots \\ \rho_n \\ T_V \\ u \\ p \end{bmatrix} \quad q_w = \begin{bmatrix} \sigma_1 \\ \sigma_2 \\ \vdots \\ \sigma_n \\ T_V \\ T_T \\ u \\ p \end{bmatrix} \tag{B.56}$$

The thermochemical source terms produce by OCEAN are given in terms of q_c, the conserved variables. OCEAN also produces the matrix $\frac{\partial q_c}{\partial q_w}$, the Jacobian of the conserved variables with respect to the working variables. q_w may contain either T or p. To transform the source terms into primitive form so that they may be applied in the program, we require the matrix:

$$J_{pc} = \frac{\partial q_p}{\partial q_c} = \frac{\partial q_p}{\partial q_w}\frac{\partial q_w}{\partial q_c} = \frac{\partial q_p}{\partial q_w}\left(\frac{\partial q_c}{\partial q_w}\right)^{-1} \tag{B.57}$$

Where:

$$J_{pc} = \begin{bmatrix} \frac{\partial q_{p,1}}{\partial q_{c,1}} & \cdots & \frac{\partial q_{p,1}}{\partial q_{c,n}} \\ \vdots & \ddots & \vdots \\ \frac{\partial q_{p,n}}{\partial q_{c,1}} & \cdots & \frac{\partial q_{p,n}}{\partial q_{c,n}} \end{bmatrix} \tag{B.58}$$

Because $\left(\frac{\partial q_c}{\partial q_w}\right)^{-1}$ can be obtained by inverting numerically, we only require the matrices $\frac{\partial q_p}{\partial q_w}$ or J_{pw} and $\frac{\partial q_c}{\partial q_w}$ or J_{cw}.

Appendix C

Reaction Rates

Contents

C.1 Synthetic Air

Values for the characteristic temperature for each molecular species are shown in Table C.1 and are found using the harmonic vibrational frequency found in NIST (2022).

Table C.1: Characteristic temperatures of molecular species for use in Millikan-White approximations

Species	Characteristic Temperature (K)
N_2	3394
N_2^+	3176
O_2	2273
O_2^+	2743
NO	2620
NO^+	4159

These parameters are then used to generate values usable in the Millikan and White equation for translational-vibrational relaxation time (Millikan and White, 1963), using the form:

$$P\tau_{MW,ij} = \exp\left[A_{ij}(T^{-\frac{1}{3}} - b_{ij}) - 18.42\right] \tag{C.1}$$

Where A_{ij} and b_{ij} are specified for each interacting pair ij by:

$$A_{ij} = 0.00116\mu_{ij}^{\frac{1}{2}}\theta_i^{\frac{4}{3}} \tag{C.2}$$

$$b_{ij} = 0.015\mu_{ij}^{\frac{1}{4}} \tag{C.3}$$

Where μ is the reduced molecular mass between the two species and θ_i is the characteristic temperature of the dissociating species. Further detail regarding the summation of the relaxation times can be found in Clarke et al. (2024b). These approximate values are only used where values for specific pairs are not given in Park (1993). The model described by Equation 56 in Gnoffo et al. (1989) is utilised to modify the translational-vibrational relaxation time at high temperatures, which requires a value for the effective cross-section for vibrational relaxation σ_v. The form of σ_v (in m^2) is taken from Park (1993).

$$\sigma_v = 3 \times 10^{-21} \left(\frac{50000}{T}\right)^2 \tag{C.4}$$

Where available, electron-neutral cross sections are taken from Gnoffo et al. (1989) for use in the Appleton and Bray correlation (Appleton, 1966), used to estimate the relaxation time between translational and electronic energy modes. The remaining species are considered as trace species and thus are assumed to have a negligible impact on the energy transfer.

The vibrational-electronic energy lost to dissociation has been modelled using the first approach detailed in Gnoffo et al. (1989) where $\hat{D}_s = \hat{c}_1\tilde{D}_s$. $\hat{c}_1$ is a scalar between 0 and 1. This implies that the rate of energy lost to dissociation for a given species is some fraction of the dissociation energy of the species. $\hat{c}_1 = 0.3$ is used here.

Reaction	Temperature	C	n	T_E
$N_2 + M_1 \rightleftharpoons 2N + M_1$	T_a	7.000E+21	-1.600E+00	1.132E+05
$O_2 + M_2 \rightleftharpoons 2O + M_2$	T_a	2.000E+21	-1.500E+00	5.936E+04
$NO + M_3 \rightleftharpoons N + O + M_3$	T_a	5.000E+15	0.000E+00	7.457E+04
$NO + O \rightleftharpoons O_2 + N$	T_T	8.400E+12	0.000E+00	1.945E+04
$N_2 + O \rightleftharpoons NO + N$	T_T	6.400E+17	-1.000E+00	3.840E+04
$O + N \rightleftharpoons NO^+ + e^-$	T_T	8.800E+08	1.000E+00	3.190E+04
$O + O \rightleftharpoons {O_2}^+ + e^-$	T_T	7.100E+02	2.700E+00	8.060E+04
$N + N \rightleftharpoons {N_2}^+ + e^-$	T_T	4.400E+07	1.500E+00	6.750E+04
$NO^+ + O \rightleftharpoons N^+ + O_2$	T_T	1.000E+12	5.000E-01	7.720E+04
$N^+ + N_2 \rightleftharpoons {N_2}^+ + N$	T_T	1.000E+12	5.000E-01	1.220E+04
${O_2}^+ + N \rightleftharpoons N^+ + O_2$	T_T	8.700E+13	1.400E-01	2.860E+04
$O^+ + NO \rightleftharpoons N^+ + O_2$	T_T	1.400E+05	1.900E+00	2.660E+04
${O_2}^+ + N_2 \rightleftharpoons {N_2}^+ + O_2$	T_T	9.900E+12	0.000E+00	4.070E+04
${O_2}^+ + O \rightleftharpoons O^+ + O_2$	T_T	4.000E+12	-9.000E-02	1.800E+04
$NO + \ + N \rightleftharpoons O^+ + N_2$	T_T	3.400E+13	-1.080E+00	1.280E+04
$NO^+ + O_2 \rightleftharpoons {O_2}^+ + NO$	T_T	2.400E+13	4.100E-01	3.260E+04
$NO^+ + O \rightleftharpoons {O_2}^+ + N$	T_T	7.200E+12	2.900E-01	4.860E+04
$O^+ + N_2 \rightleftharpoons {N_2}^+ + O$	T_T	9.100E+11	3.600E-02	2.280E+04
$NO^+ + N \rightleftharpoons {N_2}^+ + O$	T_T	7.200E+13	0.000E+00	3.550E+04
$O + e^- \rightleftharpoons O^+ + e^- + e^-$	T_V	3.900E+33	-3.780E+00	1.585E+05
$N^+ e^- \rightleftharpoons N^+ + e^- + e^-$	T_V	2.500E+34	-3.820E+00	1.686E+05
$N_2 + e^- \rightleftharpoons 2N + e^-$	T_V	1.200E+25	-1.600E+00	1.132E+05

C.2 N_2–CH_4

Reaction	Temperature	C	n	T_E
$N_2^+ M1 \rightleftharpoons 2 N^+ M1$	T_a	7.00000e+21	-1.60000e+00	1.13200e+05
$CH_4^+ M2 \rightleftharpoons CH_3 + H + M2$	T_a	4.70000e+47	-8.20000e+00	5.92000e+04
$CH_3^+ M3 \rightleftharpoons CH_2 + H + M3$	T_a	1.02000e+16	0.00000e+00	4.56000e+04
$CH_3^+ M4 \rightleftharpoons CH + H_2 + M4$	T_a	5.00000e+15	0.00000e+00	4.28000e+04
$CH_2^+ M5 \rightleftharpoons CH + H + M5$	T_a	4.00000e+15	0.00000e+00	4.18000e+04
$CH_2^+ M6 \rightleftharpoons C + H_2 + M6$	T_a	1.30000e+14	0.00000e+00	2.97000e+04
$CH + M7 \rightleftharpoons C + H + M7$	T_a	1.90000e+14	0.00000e+00	3.37000e+04
$C_2 + M8 \rightleftharpoons C + C + M8$	T_a	1.50000e+16	0.00000e+00	7.16000e+04
$H_2 + M9 \rightleftharpoons H + H + M9$	T_a	2.23000e+14	0.00000e+00	4.83500e+04
$CN + M10 \rightleftharpoons C + N + M10$	T_a	2.53000e+14	0.00000e+00	7.10000e+04
$NH + M11 \rightleftharpoons N + H + M11$	T_a	1.80000e+14	0.00000e+00	3.76000e+04
$HCN + M12 \rightleftharpoons CN + H + M12$	T_a	3.57000e+26	-2.60000e+00	6.28450e+04
$CH_3 + N \rightleftharpoons HCN + H + H$	T_a	7.00000e+13	0.00000e+00	0.00000e+00
$CH_3 + H \rightleftharpoons CH_2 + H_2$	T_a	6.03000e+13	0.00000e+00	7.60000e+03
$CH_2 + N_2 \rightleftharpoons HCN + NH$	T_a	4.82000e+12	0.00000e+00	1.80000e+04
$CH_2 + N \rightleftharpoons HCN + H$	T_a	5.00000e+13	0.00000e+00	0.00000e+00
$CH_2 + H \rightleftharpoons CH + H_2$	T_a	6.03000e+12	0.00000e+00	-9.00000e+02
$CH + N_2 \rightleftharpoons HCN + N$	T_a	4.40000e+12	0.00000e+00	1.10600e+04
$CH + C \rightleftharpoons C_2 + H$	T_a	2.00000e+14	0.00000e+00	0.00000e+00
$C_2 + N_2 \rightleftharpoons CN + CN$	T_a	1.50000e+13	0.00000e+00	2.10000e+04
$CN + H_2 \rightleftharpoons HCN + H$	T_a	2.95000e+05	0.00000e+00	1.13000e+03
$CN + C \rightleftharpoons C_2 + N$	T_a	5.00000e+13	0.00000e+00	1.30000e+04
$N + H_2 \rightleftharpoons NH + H$	T_a	1.60000e+14	0.00000e+00	1.26500e+04
$C + N_2 \rightleftharpoons CN + N$	T_a	5.24000e+13	0.00000e+00	2.26000e+04
$C + H_2 \rightleftharpoons CH + H$	T_a	4.00000e+14	0.00000e+00	1.17000e+04
$H + N_2 \rightleftharpoons NH + N$	T_a	3.00000e+12	5.00000e-01	7.14000e+04
$H + CH_4 \rightleftharpoons CH_3 + H_2$	T_a	1.32000e+04	3.00000e+00	4.04500e+03
$N^+ N \rightleftharpoons N_2^+ + e^-$	T_a	4.40000e+07	1.50000e+00	6.75000e+04
$N^+ C \rightleftharpoons CN^+ + e^-$	T_a	1.00000e+15	1.50000e+00	1.64400e+05
$N^+ e^- \rightleftharpoons N^{++} e\text{-}^+ e^-$	T_a	2.50000e+34	-3.82000e+00	1.68600e+05
$C^+ e^- \rightleftharpoons C^{++} e\text{-}^+ e^-$	T_a	3.70000e+31	-3.00000e+00	1.30720e+05

$H^+ e^- \rightleftharpoons H^{++}$ e-$^+ e^-$	T_a	2.20000e+30	-2.80000e+00	1.57800e+05
$CN^{++} N \rightleftharpoons CN^+ N^+$	T_a	9.80000e+12	0.00000e+00	4.07000e+04
$C^{++} N_2 \rightleftharpoons {N_2}^{++} C$	T_a	1.11000e+14	-1.10000e-01	5.00000e+04
$N^{++} N_2 \rightleftharpoons {N_2}^+ + N$	T_a	1.00000e+12	5.00000e-01	1.22000e+04

C.3 H_2–He

Reaction	Temperature	C	n	T_E
$H + e^- \rightleftharpoons H^+ + 2e^-$	T_a	1.79450e+14	5.00000e-01	1.57822e+05
$He + e^- \rightleftharpoons He^+ + 2e^-$	T_a	1.05230e+15	5.00000e-01	2.85239e+05
$H + e^- \rightleftharpoons H^+ + 2e^-$	T_a	3.25200e+14	5.00000e-01	1.16045e+05
$He + e^- \rightleftharpoons He^+ + 2e^-$	T_a	1.77350e+15	5.00000e-01	2.32090e+05
$2H \rightleftharpoons H^+ + e^- + H$	T_a	4.89500e+11	5.00000e-01	1.16045e+05
$H + He \rightleftharpoons H^+ + e^- + He$	T_a	3.86980e+11	5.00000e-01	1.16045e+05
$H_2 + He \rightleftharpoons 2H + He$	T_a	4.46000e+23	-2.30000e+00	5.23400e+04
$2H_2 \rightleftharpoons 2H + H_2$	T_a	1.11500e+24	-2.30000e+00	5.23400e+04
$H_2 + H \rightleftharpoons 3H$	T_a	6.24400e+24	-2.30000e+00	5.23400e+04
$H_2 + H^+ \rightleftharpoons 2H + H^+$	T_a	6.24400e+24	-2.30000e+00	5.23400e+04
$H_2 + e^- \rightleftharpoons 2H + e^-$	T_a	6.24400e+24	-2.30000e+00	5.23400e+04

Appendix D

Further Analysis of E65

This appendix includes further test cases analysed from the E65 campaign in Titan relevant mixtures

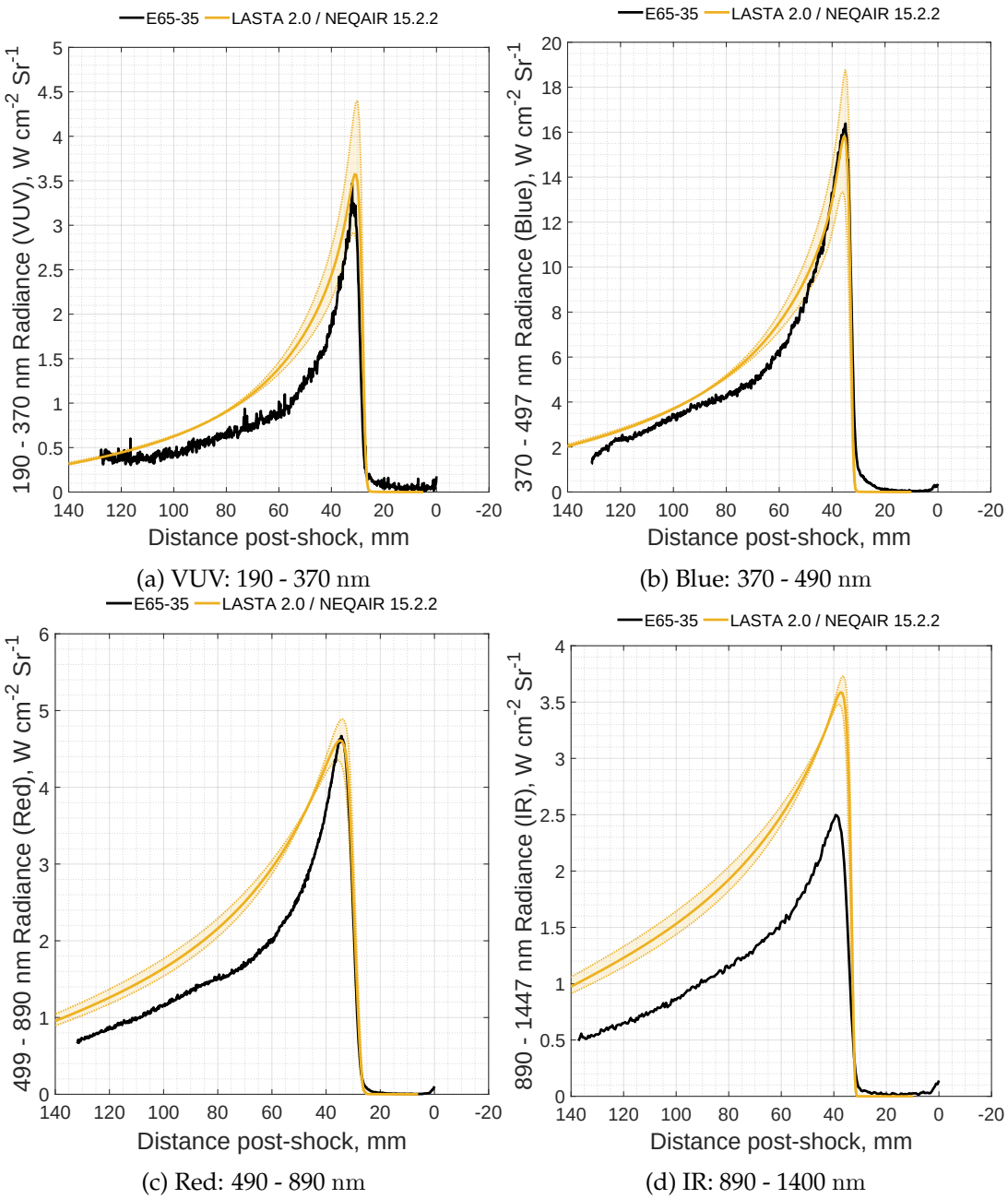

(a) VUV: 190 - 370 nm

(b) Blue: 370 - 490 nm

(c) Red: 490 - 890 nm

(d) IR: 890 - 1400 nm

Figure D.1: Radiance predictions for E65-35. Dashed lines and shaded region represent $\pm 100\ \mathrm{m\,s^{-1}}$ perturbations to the shock trajectory

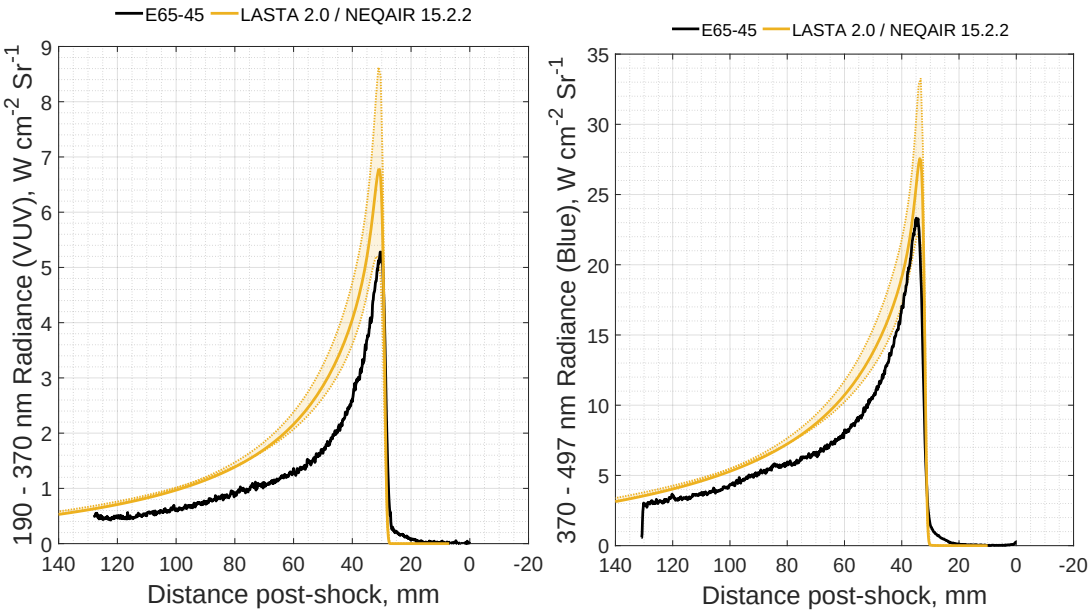

(a) VUV: 190 - 370 nm

(b) Blue: 370 - 490 nm

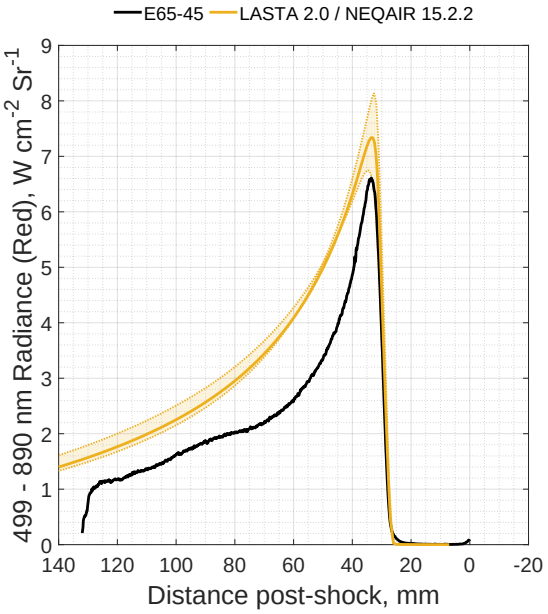

(c) Red: 490 - 890 nm

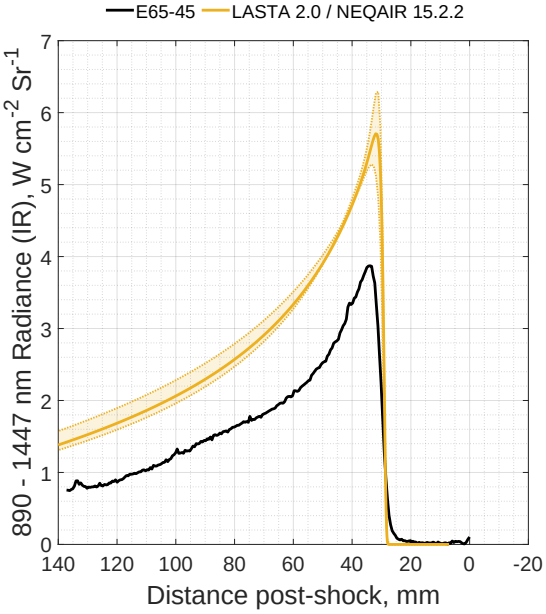

(d) IR: 890 - 1400 nm

Figure D.2: Radiance predictions for E65-45. Dashed lines and shaded region represent $\pm 100\ \mathrm{m\,s^{-1}}$ perturbations to the shock trajectory

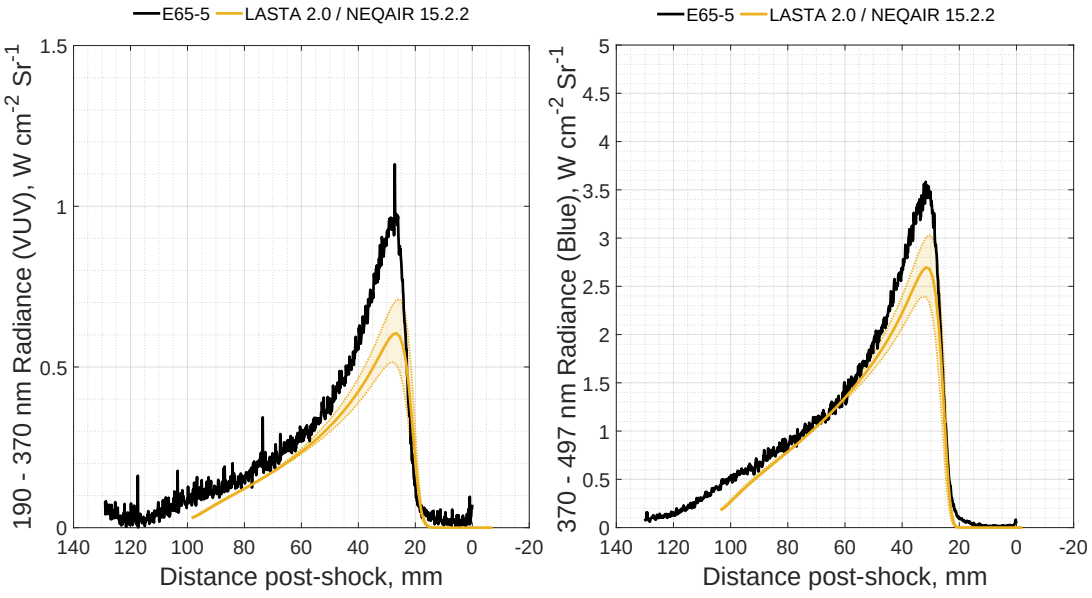

(a) VUV: 190 - 370 nm

(b) Blue: 370 - 490 nm

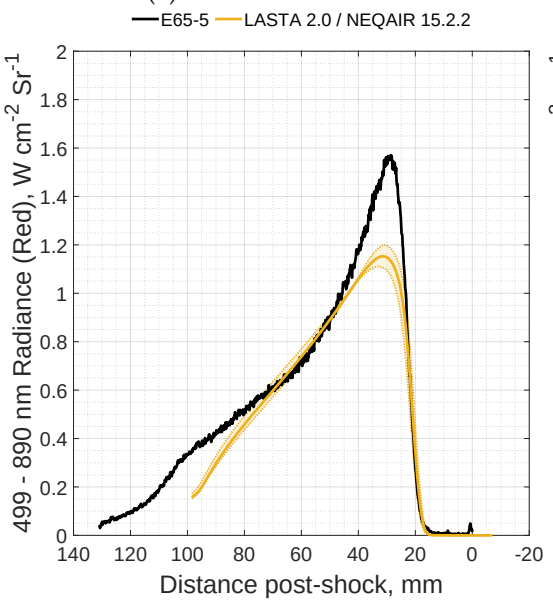

(c) Red: 490 - 890 nm

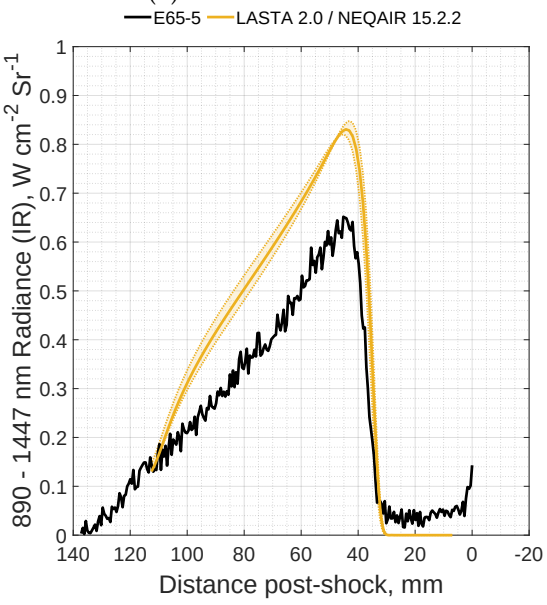

(d) IR: 890 - 1400 nm

Figure D.3: Radiance predictions for E65-5. Dashed lines and shaded region represent $\pm 100\ \mathrm{m\,s^{-1}}$ perturbations to the shock trajectory

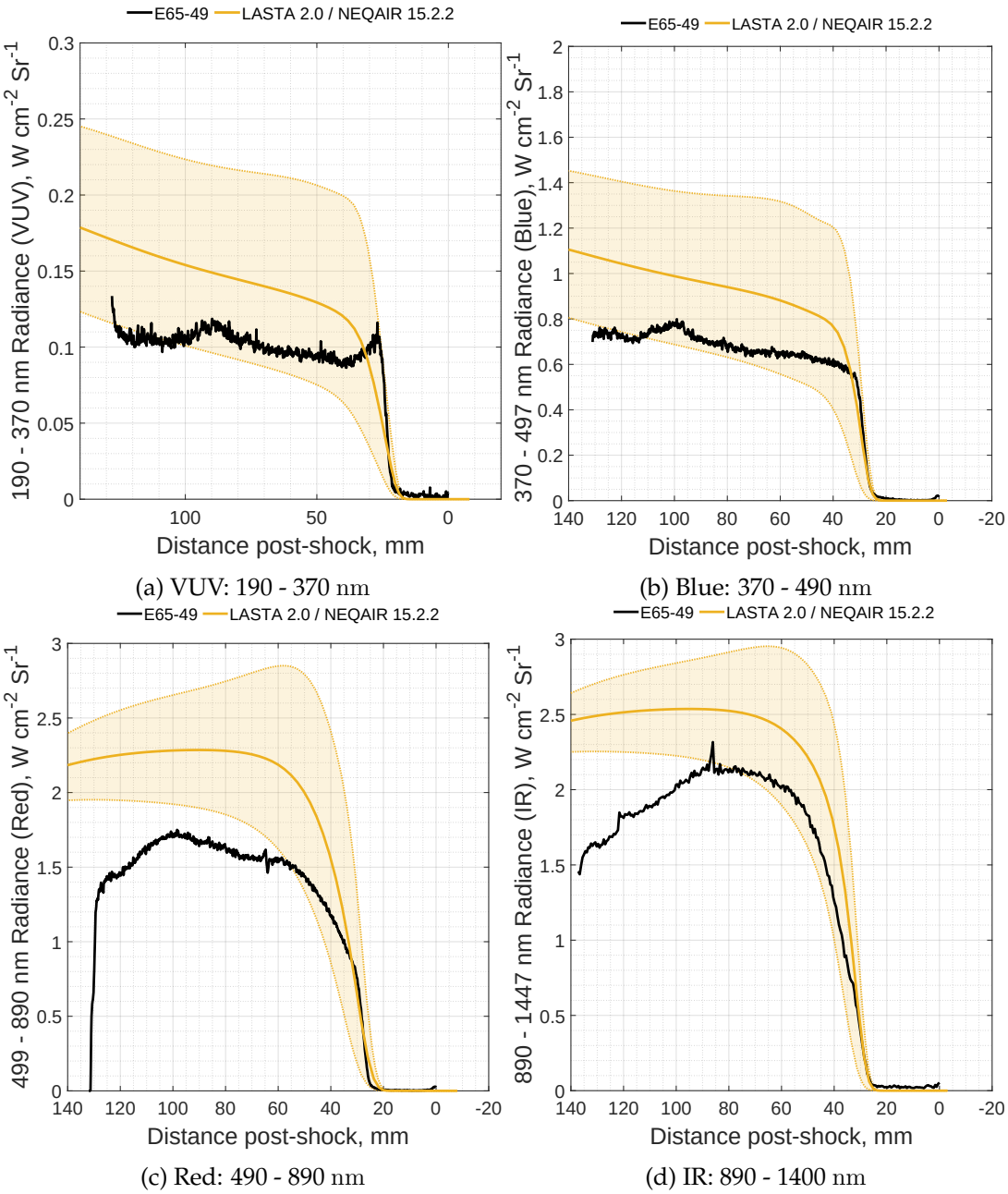

(a) VUV: 190 - 370 nm

(b) Blue: 370 - 490 nm

(c) Red: 490 - 890 nm

(d) IR: 890 - 1400 nm

Figure D.4: Radiance predictions for E65-49. Dashed lines and shaded region represent $\pm 100\ \mathrm{m\,s^{-1}}$ perturbations to the shock trajectory

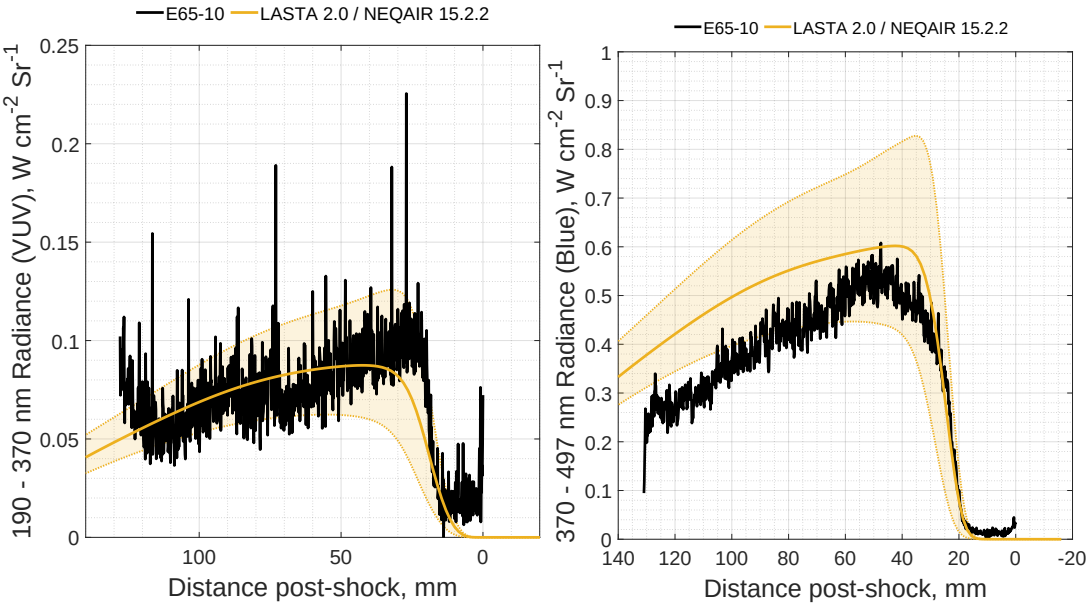

(a) VUV: 190 - 370 nm

(b) Blue: 370 - 490 nm

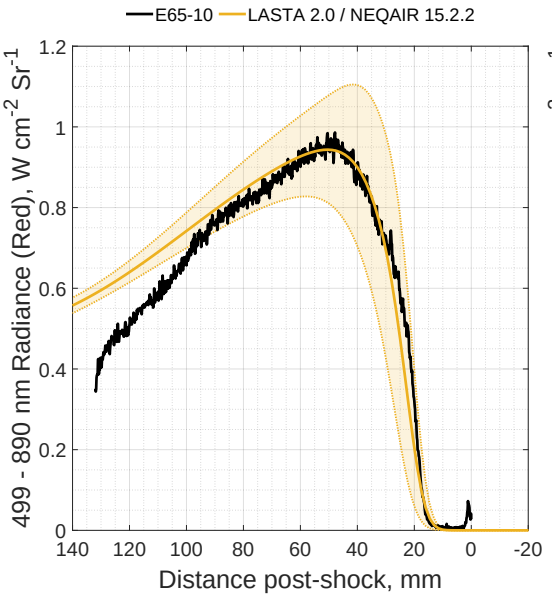

(c) Red: 490 - 890 nm

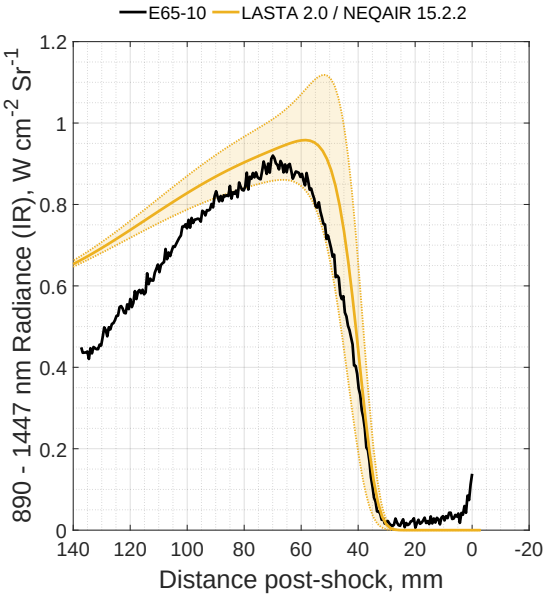

(d) IR: 890 - 1400 nm

Figure D.5: Radiance predictions for E65-10. Dashed lines and shaded region represent $\pm 100\ \mathrm{m\,s^{-1}}$ perturbations to the shock trajectory